MECHANISTIC MODELLING OF ELECTROCHEMICAL AGEING REACTIONS AT THE GRAPHITE ANODE OF LITHIUM-ION BATTERIES

zur Erlangung des akademischen Grades einer

DOKTORIN DER NATURWISSENSCHAFTEN (DR. RER. NAT.)

von der KIT-Fakultät für Chemieingenieurwesen und Verfahrenstechnik des
Karlsruher Instituts für Technologie (KIT)
genehmigte

DISSERTATION

von

M.Sc. Serena Carelli
aus Turin, Italien

Tag der mündlichen Prüfung: 25.01.2021

Erstgutachter: Prof. Dr. Wolfgang G. Bessler
Zweitgutachter: Prof. Dr.-Ing. Hermann Nirschl

ACKNOWLEDGEMENTS

"To the future or to the past, to a time when thought is free,
when men are different from one another and do not live alone -
to a time when truth exists and what is done cannot be undone.
From the age of uniformity, from the age of solitude,
from the age of Big Brother, from the age of doublethink -
greetings!"
(George Orwell, from *1984*)

As I write these acknowledgements - the final page - it's the last days of July outside. I'm in Italy, writing at my parents' house, and ready to leave for some travels around Europe after one of the strangest times in the recent history of the world. This thesis has been written during the Covid-19 pandemic: I've seen my native country (Italy) getting ravaged at the end of February, then I had to live it twice when that touched also my actual city (Strasbourg) and I found myself secluded at home in a suddenly empty building. Music, books, good wine and the support of a few special people helped me getting through the sense of fear and isolation and writing this dissertation that, hopefully, won't be so bad in the end despite the difficult conditions in which it came to life.
So here I am, to thank you all.

First of all, my amazing family - which has always been there, in my best and worst moments, when the path in front of me felt plenty of shadows and insecurities. And my friends - the ones who were there all along the pandemic and kept me virtually company on the other side of a screen (special Zoomy thanks to my friend Lili and our virtual Aperitivo Fridays during the worst lockdown period) and the others who were there when the world opened again with plenty of dinners, parties and nice moments.
You are my Italian and French legion - please never change!

Then, some really important thanks. To Prof. Wolfgang Bessler who, as I said many times, has been the perfect supervisor for me and my rebellious personality: I've never felt abandoned or left alone during this doctoral path and, for the first time in my life, I've been actually able to wake up and come to work every day with a smile on my face (not always I know but well, that's how I am). And so many travels allowed! By the way, that smile was also due to my great colleagues, who I'd like to call also friends: Hanhee, Lutz, Michael, Mehmet and the not-anymore-at-HSO Manik and Christian. Your support has been very important for me, let me say it.

Finally, I'd like to thanks Prof. Steven DeCaluwe and his students for having helped me during my research period in the States (when travelling overseas was still no problem at all) and my co-supervisors, Prof. Hermann Nirschl and Prof. Arnulf Latz, for the support in the PhD defence. Funding from Deutsche Forschungsgemeinschaft (DFG) in the framework of the research training group SiMET is also greatly acknowledged.

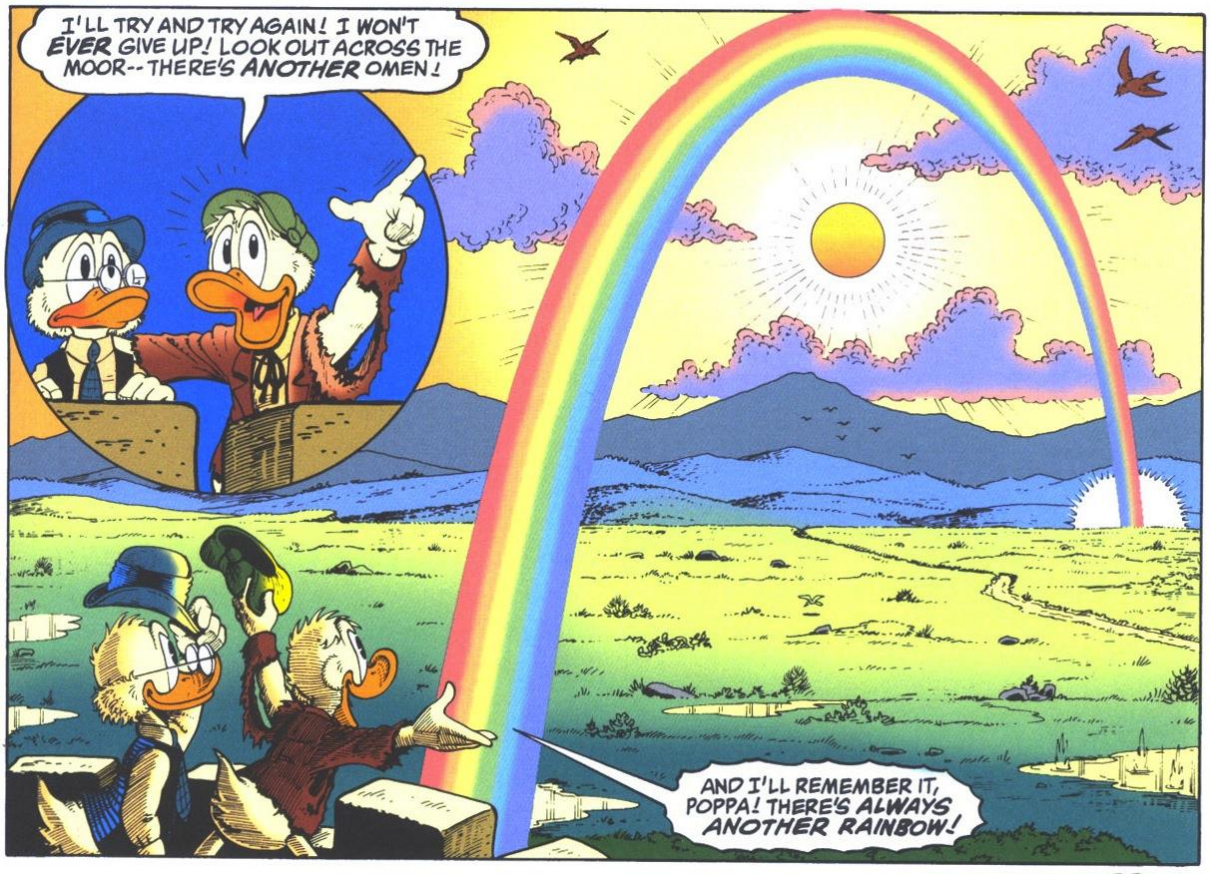

[from Don Rosa, *Walt Disney's The Life and Times of Scrooge McDuck (*2007)]

FEW WORDS ABOUT THE SIMET[1] FRAMEWORK

The work described in the present PhD dissertation has been carried out 100% at the Hochschule Offenburg: experiments, data analysis, modelling and simulations, all of it. Nevertheless, this work is part of a bigger framework, the graduate college SiMET, connecting the Karlsruhe Institute of Technology (KIT), the Helmholtz Institute Ulm and, obviously, the Hochschule Offenburg.

In the Research Training Group "SiMET", an interdisciplinary group of PhD students and Post-Docs is currently working together to achieve a substantial improvement of models and simulation methods for the coupled mechanical-electrical-thermal behaviour of lithium-ion battery cells. The work is characterised by an interdisciplinary approach which fully embraces the engineering sciences, including the methodological competence of the materials sciences, and the natural sciences of mathematics, physics and chemistry.

[1] SiMET stays for "Simulation of Mechanical-Electrical-Thermal Processes in Lithium-Ion Batteries"

ABSTRACT

Lithium-ion batteries play a vital role in a society more and more affected by the spectre of climate change: hence the need of lowering CO_2 emissions and reducing the fossil fuel consumption. At the moment, lithium-ion batteries appear as the ideal candidates for this challenge but further research and development is required to understand their behaviour, predict their issues and therefore improve their performance. In this regard, mathematical modelling and numerical simulation have become standard techniques in lithium-ion battery research and development and have proven to be highly useful in supporting experimental work and increasing the predictability of model-based life expectancy.

This study focuses on the electrochemical ageing reactions at the anode, especially on the topic of lithium plating and its interaction with the solid electrolyte interface (SEI). The purpose of this work is a deeper understanding of these degradation processes through the construction of refined modelling frameworks and the analysis of simulations carried out over a wide range of operating conditions. The governing equations are implemented in the in-house multiphysics software package DENIS, while the electrochemistry model is based on the use of the open-source chemical kinetics code CANTERA.

The development, parameterisation and experimental validation of a comprehensive pseudo-three-dimensional multiphysics model of a commercial lithium-ion cell with blend cathode and graphite anode is presented. This model is able to describe and simulate both multiscale heat and mass transport and complex electrochemical reaction mechanisms, including also as extra feature the capability of reproducing a composite electrode where multiple active materials are subject to intercalation/deintercalation reaction.

A further extension to include reversible lithium plating process and predict ageing behaviour over a wide range of conditions, with a focus on the high currents and low temperatures particularly interesting for the fast charging topic, follows. This extended model is verified by comparison with published experimental data showing *voltage plateau* and *voltage drop* as plating indicators and optionally includes an explicit re-intercalation reaction that is shown to suppress macroscopic plating hints in the specific case of a cell not showing evident plating signs. This model is used to create degradation maps over a wide range of conditions and an in-depth spatiotemporal analysis of the anode behaviour at the mesoscopic and microscopic scales, demonstrating the dynamic and nonlinear interaction between the intercalation and plating reactions.

A deeper outlook on the SEI formation and growth is presented, together with the qualitative description of three different 1D-models with a decreasing level of detail, developed with the purpose of ideally being included in future in more comprehensive multiscale frameworks.

Finally, the extended model is successfully coupled with a previously developed SEI model to result in an original modelling framework able to simulate both degradation processes and their continuous positive feedback.

KURZFASSUNG

Lithium-Ionen-Batterien spielen eine wichtige Rolle in einer Gesellschaft, die immer mehr von den Auswirkungen des Klimawandels betroffen ist. Daher ist es notwendig, die CO_2-Emissionen und den Verbrauch fossiler Brennstoffe zu reduzieren. Gegenwärtig scheinen Lithium-Ionen-Batterien die idealen Kandidaten für diese Herausforderung zu sein, aber es bedarf weiterer Forschung und Entwicklung, um ihr Verhalten zu verstehen, ihre Grenzen zu kennen und dadurch ihre Leistung zu verbessern. Hierbei haben sich mathematische Modelle und numerische Simulation als Standardtechniken in der Forschung und Entwicklung von Lithium-Ionen-Batterien etabliert und als sehr nützlich erwiesen, um experimentelle Arbeiten zu unterstützen und die Genauigkeit von Modellen zur Lebenserwartungsvorhersage zu erhöhen. Diese Arbeit konzentriert sich auf die elektrochemischen Alterungsreaktionen in der Anode, insbesondere auf das Thema Lithium-Plating und dessen Wechselwirkung mit dem Solid-Electrolyte-Interface (SEI). Ziel dieser Arbeit ist ein tieferes Verständnis dieser Degradationsprozesse durch die Verwendung verfeinerter Modellierungsansätze und der Analyse von Simulationen über einen weiten Bereich von Betriebsbedingungen. Die zugrunde liegenden Gleichungen sind im hauseigenen multiphysikalischen Softwarepaket DENIS implementiert, für die elektrochemische Modellbeschreibung wird der Open Source Code für chemische Kinetik CANTERA verwendet. Die Entwicklung, Parametrierung und experimentelle Validierung eines umfassenden pseudo-dreidimensionalen Multiphysik-Modells einer kommerziellen Lithium-Ionen-Zelle mit Mischkathode und Graphitanode wird vorgestellt. Dieses Modell ist in der Lage, sowohl den Wärme- und Massentransport auf mehreren Skalen, als auch komplexe elektrochemische Reaktionsmechanismen zu beschreiben und zu simulieren, einschließlich der Fähigkeit, eine Mischelektrode zu simulieren, in der mehrere Aktivmaterialien einer Interkalations-/Deinterkalations-Reaktion ausgesetzt sind. Es folgt eine Erweiterung, um den reversiblen Lithium-Plating Vorgang darstellen zu können und die Vorhersage des Alterungsverhaltens über einen weiten Bereich von Bedingungen vorher sagen zu können, wobei der Schwerpunkt auf hohen Strömen und niedrigen Temperaturen liegt, die insbesondere im Feld der Schnellladung interessant sind. Dieses erweiterte Modell wird durch Vergleich mit veröffentlichten experimentellen Ergebnissen überprüft, die ein Spannungsplateau und einen Spannungsabfall als Plating-Indikatoren zeigen, und beinhaltet optional eine explizite Reinterkalationsreaktion, die makroskopische Hinweise auf Plating im speziellen Fall einer Zelle, die keine offensichtlichen Plattierungszeichen zeigt, unterdrückt. Dieses Modell wird verwendet, um Degradationskarten über einen weiten Bereich von Bedingungen und eine eingehende raum-zeitliche Analyse des Anodenverhaltens auf der mesoskopischen und mikroskopischen Skala zu erstellen, um die dynamische und nichtlineare Wechselwirkung zwischen der Interkalations-Reaktion und den Plating-Reaktionen zu demonstrieren. Es wird ein vertiefender Ausblick auf die SEI-Bildung und das SEI-Wachstum gegeben, zusammen mit der qualitativen Beschreibung von drei verschiedenen 1D-Modellen mit abnehmendem Detaillierungsgrad, die mit dem Ziel entwickelt wurden, in Zukunft idealerweise in umfassendere Multiskalen-Modelle einbezogen zu werden. Schließlich wird das erweiterte Modell erfolgreich mit einem zuvor entwickelten SEI-Modell gekoppelt, so dass ein umfassendes Modellgerüst entsteht, das in der Lage ist, sowohl Degradationsprozesse als auch deren kontinuierliche positive Rückkopplung zu simulieren.

Table of Contents

1 INTRODUCTION AND MOTIVATION

Lithium-ion batteries have been intensively used for a number of years in a variety of consumer electronic devices and the interest in their cycling and storage has been increasing with their growing importance in the market of electric vehicles and stationary energy storage. Lithium-ion batteries play therefore a vital role in a society more and more affected by the spectre of climate change: hence the need of lowering CO_2 emissions and reducing the fossil fuel consumption.

The presence of batteries in our life is anyway only a relatively recent commodity[1]: it is just at the end of the 19th century that the use of coal or any other hydrocarbon as primary source of electrical energy started to be of utmost importance in the industrial world, raising the need for a secondary storage system. The first prototype of a secondary lead-acid cell had been invented by Gaston Planté only few years before but there was only little use for such a device at that time: all the research was concentrated in finding more efficient primary sources and developing primary batteries with specific purposes. It was only with the advent of the electric starter at the beginning of the 20th century that the lead-acid battery acquired its fundamental role in the automotive field, as the only relatively inexpensive battery with the necessary power density to get ignition[2].

Between the primary batteries, the most common type could be considered the LeClanché cell invented in the same period: the early forms were simple wet cells with zinc as the reducing agent and manganese dioxide as the oxidizer. The modern version (alkaline dry cell - sealed) then comes from an idea of Carl Gassner in 1886, who substituted the previous liquid electrolyte with a more practical moist ammonium chloride paste: its relatively high energy densities and long charge retention times make this cell suitable for many portable applications even today[3]. In 1899 Waldmar Jungner invented the nickel-cadmium rechargeable battery, the first secondary cell to use an alkaline electrolyte, which, in its variant with iron at the anode, inspired the nickel-iron battery of Thomas Edison at the beginning of the 20th century, commonly used in electric and diesel-electric rail vehicles. More powerful and lasting energy sources were then needed to fulfill the demands of the post-war technological boom: the long-lasting alkaline batteries entered the market in the 1950s, when Lewis Urry developed a cell with powdered zinc at the anode, and overcame in popularity all the other primary cells[4].

It was only in 1991 that the lithium-ion battery came finally onto the market, when Sony commercialized it in Japan as a rechargeable and more stable version of the lithium battery (developed few years before in the 1970s[5]). This is not the end of the story though: new challenges are continuously opening for these unique electrochemical devices, pushed - as mentioned above - by the constant increasing urgency for a larger use of green energy sources and the replacement of the classical polluting internal combustion cars with more efficient controlled emissions vehicles, such as hybrid vehicles (HEVs) or electric vehicles (EVs)[6,7]. At the moment, lithium-ion batteries appear as the ideal candidates for this challenge but further research and development is required to understand their behaviour, predict their issues and therefore improve their performance above all in terms of safety, cost, power and energy density. Big problems come actually from the numerous degradation processes affecting the batteries and causing capacity loss or, even worse, safety issues such as the fire hazards coming from unexpected thermal runaway[8,9]. Fast-charging over a wide range of temperatures is above all highly desired

in the sector of electro-mobility and it is exactly at these conditions that the process of lithium plating becomes one of the dominant degradation processes and safety risks during continuous cycling. This degradation process leads to the deposition of lithium metal on the surface of the negative electrode, which can happen reversibly or irreversibly, causing loss of cyclable lithium and the eventual formation of dendrites (i.e. needle-like growths on the surface of lithium metal) able to pierce the battery separator and boost a thermal runaway through the creation of a short circuit[10]. The formation of plated lithium furthers also the growth of the Solid Electrolyte Interphase (i.e. the SEI), which is another degradation process happening at the negative electrode[11].

Hence comes the focus of this doctoral thesis on the electrochemical ageing reactions at the anode, especially on the topic of lithium plating and its interaction with the SEI. The purpose of this work is finally a deeper understanding of these degradation processes through the construction of refined modelling frameworks and the analysis of simulations carried out over a wide range of conditions. At the same time experiments are accurately made and used as comparison to validate our results, in a continuous process of improvement which does not end with this thesis.

After this short introduction, two theoretical chapters will greet us in different but complementary ways. In Chapter 2 we will answer to the question “HOW” by presenting the (previously developed) modelling and simulation framework which will then be used, modified and improved throughout this thesis. In Chapter 3 instead the fundamentals of lithium-ion battery ageing will be proposed and a big “WHY” will be raised by the degradation mechanisms here introduced, with a particular focus on the negative electrode.

Then two “applied” Chapters will follow, as the “WHAT” core of this dissertation. Chapter 4 will discuss the development, parameterisation and experimental validation of a pseudo-three-dimensional multiphysics model of a commercial lithium-ion pouch cell with graphite anode and blend cathode: a model which has been built on the theory explained in Chapter 2 and freshly adapted for the challenge of a composite electrode. In Chapter 5 this physicochemical pseudo-3D model will then be furtherly extended to include the lithium plating process and predict ageing behaviour over a wide range of conditions, with a particular focus on the high currents and low temperatures particularly interesting for the fast charging topic. Experiments, simulations and analysis of the internal states will accompany us through the understanding of our newly improved virtual battery.

Finally, the last two Chapters are part of two ongoing studies and are presented even if incomplete and at the moment still under research. Chapter 6 calls back to the short period overseas as guest scientist at Colorado School of Mines: a deeper outlook on the SEI formation and growth and a different approach on its modelling will be presented, together with the qualitative description of three different 1D-models with a decreasing level of detail. Ongoing Chapter 7, with its unresolved questions, will then close this dissertation: here our extended model from Chapter 5 will meet a previously developed SEI model to originate a modelling and simulation framework able to describe both degradation processes and their continuous positive feedback.

At the end of this thesis and after a short summary, a long table of symbols can be found to help during the reading of the tables and the numerous equations. We hope you will also appreciate the famous quotes opening the different sections.

2 A LITTLE BIT OF THEORY

"Any physical theory is always provisional, in the sense that it is only a hypothesis: you can never prove it.
No matter how many times the results of experiments agree with some theory,
you can never be sure that the next time the result will not contradict the theory."
(Stephen Hawking)

The second Chapter of this dissertation is actually dedicated to what we could call "hard theory", that is the basic knowledge at the mathematical and physical level behind the modelling and simulation process: some concepts about batteries, the multiscale approach, thermodynamics, kinetics, electrochemistry…all of these governing the macroscopically observable behaviour of lithium-ion cells in terms of current, voltage and temperature. In order to understand the impact of the multiscale and multiphysical internal processes on macroscopic cell behaviour, modelling and simulation techniques have proven to be highly useful[12] in supporting experimental work and improving the knowledge in this complex field. The true power of simulations is only real if the model can be also validated experimentally[13]: therefore, modelling, parameterisation and experimental validation are closely linked and part of the same scientific process towards a more comprehensive knowledge.
Let's now start with a bit of theory…or better a couple of questions: what is a battery and how does it work?

2.1 LITHIUM-ION BATTERIES: WHAT AND HOW

"To ask the 'right' question is far more important than to receive the answer.
The solution of a problem lies in the understanding of the problem;
the answer is not outside the problem, it is in the problem."
(Jiddu Krishnamurti, from *The Flight of the Eagle*)

A battery is a device consisting of one or more electrically connected electrochemical cells having terminals/contacts to provide electrical energy[27]. In the most general description, a single cell can be divided in six parts:

- Positive current collector: the conductive flat metallic sheet at one of the extremes of the cell, connected to the positive electrode with external loading[28]. The typical current collector currently used is made of aluminium;
- Positive electrode: the electrode with the higher potential. During discharge, it is associated with chemical reduction (cathode), gaining electrons from the external circuit;
- Electrolyte: the chemical medium that allows the flow of ionic charge between the electrodes. It consists of soluble salts and organic solvents in liquid, gelled or solid forms[29];

- Separator: a physical permeable barrier placed between the electrodes to prevent the otherwise inevitable electrical shorting. It can be a microporous film or any inert porous material filled with electrolyte[30];
- Negative electrode: the electrode with the lower potential. During discharge, it is associated with chemical oxidation (anode), releasing electrons into the external circuit;
- Negative current collector: the conductive flat metallic sheet at the other extreme of the cell, connected to the negative electrode with external loading. The typical current collector currently used is made of copper.

Figure 1 shows the path of lithium ion and electron movement during a lithium-ion battery discharge and charge[31]. During discharge, the oxidation at the negative electrode occurs causing electrons to be lost and take an external path to the positive electrode, where the lithium ions from the negative electrode are finally conducted by the electrolyte through the separator. During charge the process is reversed, with the negative electrode gaining electrons and the lithium ions getting there, reduced and stored. The possibility of "cycling the battery" instead of simply discarding it after the complete discharge, is a prerogative of the so-called "secondary cells", to distinguish them from the cheaper but mono-use "primary cells"[32]. But what happens in detail during these processes? Let's have a deeper look.

As we already mentioned, the electrodes (more specifically, the active materials of which they are partially made) are the physical sites of the oxidation-reduction reactions behind the production of electricity.

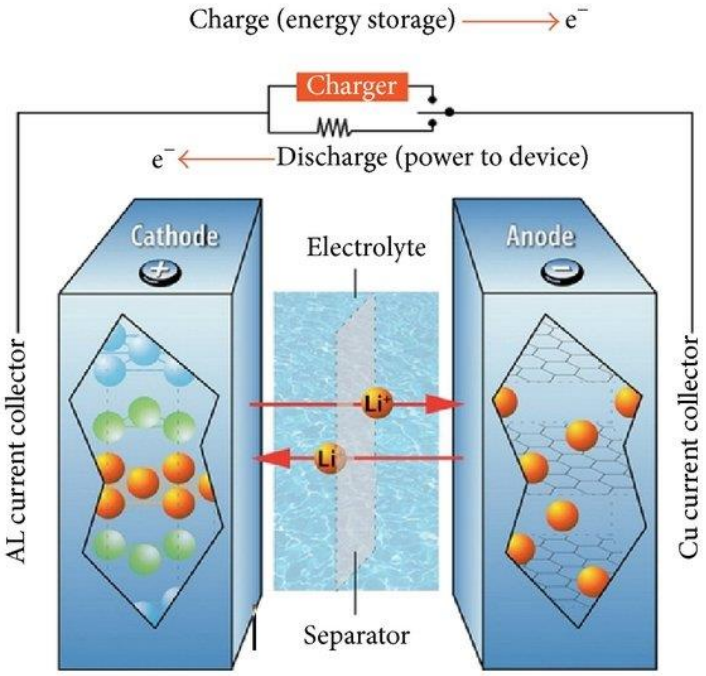

FIGURE 1: LITHIUM-ION BATTERY CHARGE/DISCHARGE DIAGRAM.THE FIGURE IS FROM MEBARKI *ET AL.*[31]

In a lithium-ion battery the active material of the negative electrode is mostly lithiated graphite: during discharge, lithium ions de-intercalate from the parallel carbon layers with a 1:6 proportion according to the following reaction

$$\mathrm{Li_xC_6} \rightleftharpoons \mathrm{xLi^+ + xe^- + C_6}\,, \tag{1}$$

where $0 \leq x \leq 1$ is a mole fraction of the amount of lithium stored within the electrode, normalised by the saturation (maximum) value. During charge, the negative carbon electrode becomes instead the site for reduction in the process of (re-)intercalation of lithium ions.

During discharge, the typical reaction at the positive electrode for a lithium-ion battery is

$$\mathrm{yLi^+ + ye^- + M \rightleftharpoons Li_yM}\,, \tag{2}$$

where y has the same definition as x used previously for the negative electrode and M refers to a general metal oxide. Specifically, in the cell analysed in the following Chapters (starting from Chapter 4) the positive electrode is a blended electrode with two active materials and consequently a more complex electrochemistry, while the electrolyte salt is $LiPF_6$ at an optimal concentration of 1.0 M in a common mixture of carbonates such as ethylene carbonate (EC) and ethyl methyl carbonate (EMC).

The electrical current produced by the redox mechanisms previously described is called Faradaic current (or more simply "external current"): in this thesis, during discharge of the battery (energy supplied by the cell) the current has positive sign, while in case of charge (energy supplied to the battery) the sign convention is negative[33].

When the current is zero and the cell is at rest, an important characteristic of the battery is the open-circuit voltage (OCV) which is the potential difference between the two electrodes at equilibrium. It evolves in function of the state of charge (SOC): the ratio of its current capacity C to the nominal capacity C_N, according to

$$\mathrm{SOC}\,(t) = \frac{C}{C_\mathrm{N}} \cdot 100\,\%\,, \tag{3}$$

where SOC is usually given in percent. The nominal capacity is given by the manufacturer and ideally represents the maximum amount of charge that can be stored in the battery: in fact, the real capacity of a fully-charged battery could be quite different from the nominal value and the measurement of the SOC should evaluate the real state of the battery.

The capacity of an electrochemical cell, at any instant, is defined as the amount of charge that can be delivered within a complete discharge at a specific current value and between specific voltage limits defined by the cell manufacturer. Upon reaching the lower voltage limit, capacity is defined as the integral of current

$$C = \int_0^t I(t)dt\,. \tag{4}$$

The upper voltage limits for lithium-ion cells are usually from 3.6 to 4.2 V, while the lower voltage limits vary from 2.0 to 3.0 V, depending on the cell chemistry. It is recommended to respect these operational limits when running the battery to avoid any harmful side reaction or even explosion. In battery technology, the current is often specified as a multiple of cell capacity, the so-defined "C-rate": being a current magnitude, 1C is taken as the standard current required to fully discharge the cell in a period of one hour, while multiples indicate a faster discharging and fractions a slower one, according to

$$\text{C-rate} = \frac{I \cdot 1\mathrm{h}}{C_\mathrm{N}}\,. \tag{5}$$

All this is about the "real" battery, the one we meet continuously in real life. Now that we had a look at some basic concepts and we know a bit more about it, let's have a look instead at the theory necessary to build a virtual one: hence, all the coupling of scales, mathematics and physics behind our multiscale modelling framework.

2.2 TRANSPORT AND KINETICS: OUR P3D MULTISCALE APPROACH

"It is a capital mistake to theorize before one has data.
Insensibly one begins to twist facts to suit theories, instead of theories to suit facts."
(Sherlock Holmes)

Different approaches have been developed in the modelling community, according to the type of ongoing investigation: the most common is the pseudo-2D (P2D) approach, in which the model covers the mass transport at the particle scale and the mass and charge transport at the electrode-pair scale[14,15]. When the heat transport on the cell scale needs also to be included, we may find the so-called multiscale multi-domain (MSMD) models[16], which can be in the form P2D+1D[17,18], pseudo-3D (P3D)[19–21] or P2D+3D[22] according to how they have been developed. It is also possible to meet computationally efficient 1D-models[23–25], in which only one type of transport is described: 1D simulations are mainly used for a fast determination of specific parameters (kinetics, thermal, stress analysis…)[26].

The computational domain of our multiscale model is shown schematically in Figure 2. Transport processes are well described on three distinct scales, each of which modelled in one dimension and coupled via appropriate boundary conditions and upscaling relationships. We have:

- 1D for heat transport along the through-cell direction (macroscale or *x* scale)
- 1D for mass and charge transport inside the liquid electrolyte (mesoscale or *y* scale)
- 1D for diffusive mass transport in the active materials particles (microscale or *z* scale)

Resulting in a 1D+1D+1D (pseudo-3D or P3D) model, a comprehensive framework able to simulate processes from the centimetre cell scale to the micrometric paths inside the particles.

The P3D model described in this Chapter has actually been developed not during this PhD work but in a previous time for representing a $LiFePO_4$ (LFP) / C_6 (graphite) high-power cylindrical cell[19]. Nevertheless, as will be illustrated in Section 4.1, some changes have been made to adapt it to our reference cell, a high-power lithium-ion pouch cell with $LiNi_{0.8}Co_{0.15}Al_{0.05}O_2$ (NCA) / $LiCoO_2$ (LCO) blend positive electrode (see Figure 10). The necessity of including aluminium holders for the heat transport and the development of a theory framework[34] to determine volume fractions and stoichiometry ranges of active materials in lithium-ion battery cells (see Section 4.3) are just two of the added features present in this new model.

For the moment anyway, let's focus on the common theory and have a look at the modelling structure at the different scales.

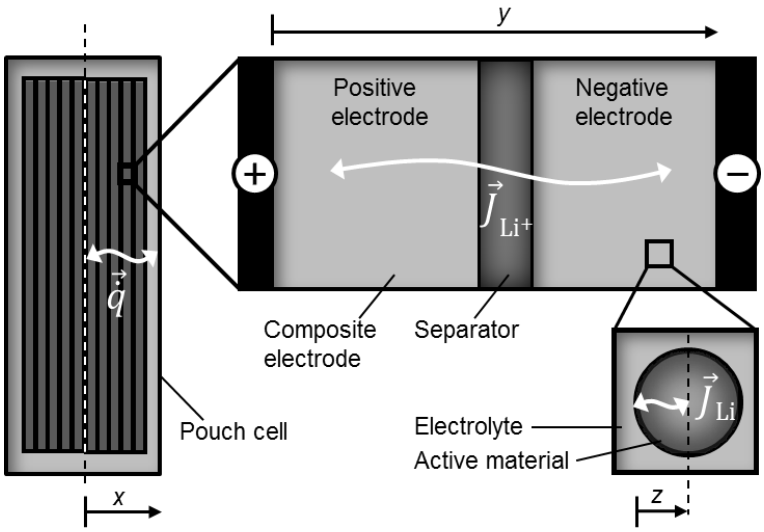

FIGURE 2: SCHEMATIC REPRESENTATION OF 1D+1D+1D (PSEUDO-3D, P3D) MODELLING DOMAIN WITH MACROSCALE (*X*), MESOSCALE (*Y*) AND MICROSCALE (*Z*).

2.2.1 MACROSCALE (CELL)

At the centimetre scale (*x*) our model is devoted to the description of the heat transport. In Figure 2 the heat conduction is assumed to take place along a single dimension (1D), that is the through-cell direction *x* perpendicular to the electrodes. The two axial directions, being much bigger, are neglected for the sake of simplicity and therefore we can describe the heat transport due to conduction as

$$\rho c_p \frac{\partial T}{\partial t} = \operatorname{div}(\lambda \operatorname{grad} T) + \dot{q}^{\mathrm{V}} \tag{6}$$

with $\operatorname{div}(\lambda \operatorname{grad} T) = \frac{\partial}{\partial x}\left(\lambda \frac{\partial T}{\partial x}\right)$ for a pouch cell with cartesian coordinates. If we wanted to represent in full resolution the heat transport and the temperature for the entire geometry, a simple double ended 1D "arrow" would not be enough but we should use instead a 3D thermal model for a 3D space defined by the length, width and thickness of our cell. This goes well beyond the scope of our macroscale modelling anyway, so let's keep our double ended arrow and define the boundary conditions at the cell centre ($x = 0$) and at the cell/ambient interface ($x = d_{\mathrm{cell}}/2$) as

$$j_q = 0 \ , \tag{7}$$

$$j_q = \alpha(T - T_{\mathrm{amb}}) + \epsilon\sigma_{SB}(T^4 - T_{\mathrm{amb}}^4) \ , \tag{8}$$

respectively. We are now ready to step into the next scale, at the hundred-micron level.

2.2.2 MESOSCALE (ELECTRODE PAIR)

The mesoscopic scale (*y) is* focused on the mass and charge transport in the liquid electrolyte as well as the charge transport in the electronic phase. As shown in Figure 2, we neglect again any axial direction and we stay on a 1D representation involving here the working core of our battery: positive electrode-separator-negative electrode. The specific electrolyte model for our reference cell will be explained in detail in Section 4.3.3 while here we will concentrate on the general theory behind the mesoscale.

Let's start by saying that in a closed system, like the liquid electrolyte contained in our cell, both species and charge must be conserved. Here follow respectively for species

$$\frac{\partial(\varepsilon_{\text{elyt}} c_i)}{\partial t} = -\frac{\partial j_i}{\partial y} + \dot{s}_i^{\text{V}} + \dot{s}_{i,\text{DL}}^{\text{V}} \,, \tag{9}$$

and for charge, by multiplying for the "charge factor" $z_i F$

$$0 = -\sum_i z_i F \frac{\partial j_i}{\partial y} + \sum_i z_i F \dot{s}_i^{\text{V}} + \sum_i z_i F \dot{s}_{i,\text{DL}}^{\text{V}} \,, \tag{10}$$

where the three right-hand side terms represent in order the transport fluxes of the species i in the electrolyte, the source term due to electrochemical reactions, and the source term due to double layer charging/discharging. Worth noticing that in Eq. 10 the principle of electroneutrality is fully respected by setting the left-hand side term to 0. About the last of the three right-hand side terms, the electric double layer that is electrostatically forming at the electrode/electrolyte interface, we describe its related charging/discharging current as

$$i_{\text{DL}}^{V} = \sum_i z_i F \dot{s}_{i,\text{DL}}^{\text{V}} = C_{\text{DL}}^{\text{V}} \frac{\text{d}(\Delta\phi)}{\text{d}t} \,, \tag{11}$$

where the electric potential difference between liquid electrolyte and electronic phase is given as[35]

$$\Delta\phi = \phi_{\text{elde}} - \phi_{\text{elyt}} \tag{12}$$

(NB "elyt" and "elde" stand for electrolyte and electrode, respectively). The Faradaic current i_F^{V}, which is the production rate of electrons in the solid phase due to charge-transfer reactions $\dot{s}_{\text{e}}^{\text{V}}$, can be defined as

$$i_F^{\text{V}} = \sum_i z_i F \dot{s}_i^{\text{V}} = F \dot{s}_{\text{e}}^{\text{V}} \,. \tag{13}$$

A rearrangement of all the shown equations will finally lead us to the governing potential equation for the electric potential difference $\Delta\phi$

$$C_{\text{DL}}^{\text{V}} \frac{\partial(\Delta\phi)}{\partial t} = \sum_i z_i F \frac{\partial j_i}{\partial y} - i_F^{\text{V}} \,. \tag{14}$$

All this seems a lot of maths and symbols, but we can imagine Eq. 9 being simply an everchanging sum of species that in total must be conserved and Eq. 10 an everchanging sum of currents that in the end gives a zero result. But what is that first term on the right side of both equations? For that we have to refer to the various ways in which a species can make its way through the electrolyte, which are the three forms of mass transport:

- Diffusion: rises from concentration gradients with entropy as main driving force
- Migration: rises from potential gradients and acts in opposite ways on opposite charges
- Convection: rises from the action of a force on the solution (i.e. small thermal or density differences, if natural convection; a pump, a flow of gas or even gravity, if forced) – neglected here

That first term, once we take away $z_i F$, becomes simply

$$j_i = -D_i^{\text{eff}} \frac{\partial c_i}{\partial y} - D_i^{\text{migr,eff}} \frac{\partial \phi_{\text{elyt}}}{\partial y} \,, \tag{15}$$

where the first and second terms on the right-hand side refer respectively to the fluxes originated by diffusion (see the concentration gradient ∂c_i) and migration (see the potential gradient in the electrolyte $\partial \phi_{\text{elyt}}$). The two effective transport coefficients indicated with D_i^{eff} and $D_i^{\text{migr,eff}}$ follow porous electrode theory and are calculated from bulk properties by correcting for porosity and tortuosity[36]

$$D_i^{\text{eff}} = \frac{\varepsilon_{\text{elyt}}}{{\tau_{\text{elyt}}}^2} D_i \,, \tag{16}$$

in our model with a tortuosity factor $\tau' = \tau^2 = \varepsilon_{\text{elyt}}^{-0.5}$ [37]. In the so-called Diluted Solution Theory (DST), which in its simplest form is applied precisely to dilute solutions, we have

$$D_i^{\text{migr,DST}} = \frac{z_i F}{RT} c_i D_i \,, \tag{17}$$

which reduces to one the number of transport coefficient to calculate for every species i. Electrolytes are not diluted solutions though, so we will have to include a more accurate theory called CST (i.e. Concentrated Solution Theory) in which the interactions between ions are not neglected [38]. In this case

$$D_i^{\text{CST}} = D^0 - \frac{t_i^0}{z_i F c_i} \cdot \frac{2RT}{F} \sigma(c,T) \cdot \nu(c,T) \tag{18}$$

$$D_i^{\text{migr,CST}} = \frac{t_i^0}{z_i F} \cdot \sigma(c,T) \tag{19}$$

where the index i refers to the two ions (for example, Li^+ and PF_6^-). In CST theory every ion can be singularly described through its own parameters, denoted by subscripts + if positive, and – if negative:

- Ion concentration c

$$c = c_+ = c_- \tag{20}$$

- Ion charge z_i

$$z_+ = -z_- \tag{21}$$

- Ion transference number t_i^0 - it defines the fraction of the total electrical current carried in the electrolyte, with a value between 0 and 1

$$t_-^0 = 1 - t_+^0 \ . \tag{22}$$

The CST diffusion coefficient D^0, electrolyte conductivity σ and the lumped activity parameter $\nu = (1 - t_+^0)(1 + \frac{\partial \ln f_\mp}{\partial \ln c})$ need also to be known when applying CST in a modelling framework[39], which makes the parameterisation a difficult and time-consuming process. In Section 4.3.3 we will explain how we used an intelligent combination of DST and CST to parameterise the electrolyte model for our reference cell.

We have now defined the transport equations for the electrolyte. What about the electrodes? If until now we have been talking about ions, it is now time to talk about electrons: electronic phases, electronic conductivities, electronic resistances. Electrode materials are chosen to facilitate the electronic path to the current collector, therefore the electronic resistance is assumed negligible and the ϕ_{elde} is considered spatially constant throughout each electrode. The boundary conditions for the species conservation are $j_i = 0$ at both electrode/current collector interfaces, while for the ionic potential the boundary conditions are $\mathrm{d}(\Delta\phi)/\mathrm{d}x = 0$ at both electrode/current collector interfaces: to put it simply, no species can leave the battery. The electrode-pair voltage

$$E = \phi_{\text{elde,ca}} - \phi_{\text{elde,an}} - i \cdot R_{\text{cc}} \tag{23}$$

is nothing less than the potential difference between positive and negative electrode, furtherly reduced by an additional potential drop due to the electronic resistance R_{cc} of the current collection system. When the cell is not at equilibrium, the applied current density i_{cell} can be expressed as

$$i_{\text{cell}} = \frac{A_{\text{e}}}{V_{\text{cell}}} \cdot \int_{y=0}^{L_{\text{electrode}}} \left(i_{\text{F}}^{\text{V}} + i_{\text{DL}}^{\text{V}}\right) \mathrm{d}y \,, \tag{24}$$

where the geometric factor $\frac{A_e}{V_{cell}}$ is cell specific. The fundamental relationship between the Faradaic current and electric potential difference, $i_F^V = f(\Delta\phi^{eff})$ follows from electrochemistry and will be explained in Section 2.2.5. On the electrode-pair scale temperature gradients are much smaller than at the cell scale, therefore the electrodes are modelled isothermally. Reversible and irreversible heat production is happening at a local level and the area-specific heat is obtained by integrating all these local heat sources over the electrode-pair length

$$\dot{q}^A = \int_0^{L_{EP}} \left(\dot{q}_{chem}(y) + \dot{q}_{ohm}(y)\right) dy + R_{cc} i^2 \,, \tag{25}$$

where

$$\dot{q}_{chem} = \sum_{n=1}^{N_r} (r_n A_n^V (-\Delta H_n + F \nu_{e,n} \Delta\phi_n)) \tag{26}$$

$$\dot{q}_{ohm} = \sigma \cdot \left(\frac{\partial \phi_{elyt}}{\partial y}\right)^2 . \tag{27}$$

The three heating terms on the right-hand side of Eq. 25 are respectively due to the electrochemical reactions and to the ohmic heating of the electrolyte and the current collection system.

Now that we have explored the mesoscale, we can finally step into the micron scale.

2.2.3 MICROSCALE (PARTICLE)

We are now at the micrometre scale (*z*) where diffusive mass transport inside the active materials particles is described through the assumption of spherical particles and Fickian diffusion. A deeper explanation of our microscale modelling will be done in Section 4.1 with the description of the blend electrode model applied to our reference cell positive electrode. But in the simplest case where the electrode (positive or negative) has only one active material AM, the mass conservation for lithium inside the AM particles is given by

$$\frac{\partial c_{Li[AM]}}{\partial t} = \frac{1}{z^2} \frac{\partial}{\partial z} \left(z^2 D_{Li[AM]}(c_{Li[AM]}) \frac{\partial c_{Li[AM]}}{\partial z} \right) . \tag{28}$$

The solid-state diffusion coefficient $D_{Li[AM]}$ may depend on the concentration of intercalated lithium $c_{Li[AM]}$. The boundary conditions are $j_{Li[AM]} = 0$ in particle centre and $j_{Li[AM]} = \frac{r_P}{3\varepsilon_{AM}} \dot{s}_{Li[AM]}^V$ at the particle surface. The geometric factor $\frac{r_P}{3\varepsilon_{AM}}$ is nothing else than $1/A^V$, where A^V is the specific area as function of volume fraction[19]. Remember: the specific area is defined as the total surface area of a material per unit of bulk volume and has a unit of m^{-1}.

2.2.4 UPSCALING

In the previous paragraphs we went from the centimetre macroscale to the micron microscale, that is from the cell dimensions to the small world of the AM particles. A good point of a P3D model is to be able not only to describe one-dimensionally the transport processes on three different scales (1D + 1D + 1D) but also to have them coupled, connected and not isolated. Let's have a look at the coupling of the macroscale and the mesoscale in Figure 3.

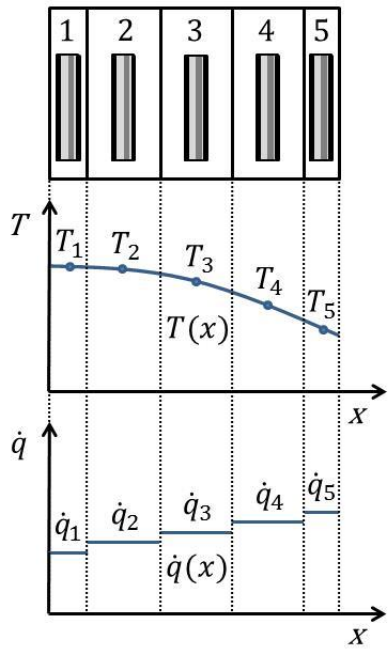

FIGURE 3: COUPLING OF MACROSCALE (CELL) AND MESOSCALE (ELECTRODE PAIR) VIA HOMOGENISATION USING REPRESENTATIVE ELECTRODE PAIRS (HERE, $N_{\mathrm{EP}} = 5$). THE CENTRE OF THE CELL IS AT $x = 0$. THE FIGURE IS FROM KUPPER *ET AL.*[19]

Along the *x* scale we set a N_{EP} (typically, 1…10) number of electrode pair models *m*. In some modelling frameworks (see Chapter 4) the thermal cell behaviour can be simply simulated with only one single volume section, i.e. one single electrode pair ($N_{\mathrm{EP}} = 1$). Talking about heat transport, the coupling is a matter of "give and take": the cell scale passes the local time-dependent *T* (see Section 2.2.1) down to the electrode pair scale, where every single *m* is modelled isothermally and gives back its own calculated volume-specific heat source

$$\dot{q}^{\mathrm{V}} = \frac{A_{\mathrm{e}}}{V_{\mathrm{cell}}}\left(\int_0^{L_{\mathrm{EP}}}\left(\dot{q}_{\mathrm{chem}}(y) + \dot{q}_{\mathrm{ohm}}(y)\right)\mathrm{d}y + R_{\mathrm{cc}} i^2\right), \tag{29}$$

which now enters Eq.6 at the macroscale. In the case of one single electrode pair, it will lead to a temperature gradient under a constant heat source along the *x*-scale. Eq. 29 is also obtained by multiplying Eq. 25 for $\frac{A_{\mathrm{e}}}{V_{\mathrm{cell}}}$, where A_{e} is called "active electrode area" [17]. For example, our reference lithium-ion pouch cell consists of a number of stacked sheets of electrode pairs with a total active electrode area of 0.028833 m^2. The total cell current at a macroscopic level is given as weighted sum over the representative electrode pairs

$$I_{\mathrm{cell}} = \frac{A_{\mathrm{e}}}{V_{\mathrm{cell}}} \sum_{m=1}^{N_{\mathrm{EP}}} V_{\mathrm{m}} \cdot i_m \ , \tag{30}$$

while the cell voltage is identical for all electrode pairs due to their parallel connection[40]

$$E_{\mathrm{cell}} = E_1 = E_2 = \cdots = E_{N_{\mathrm{EP}}} \ . \tag{31}$$

Between the mesoscale (electrode pair) and the microscale (particle) we apply the "standard" pseudo-2D (P2D) approach[15,41] . Every electrode-pair at the mesoscale is composed of three parts, positive electrode-separator-negative electrode, each one of them discretised in a number of finite volume compartments. There a single particle is modelled at every one of them and in turn it is discretised again. Upscaling and discretisation walk side by side in building a solid and refined model, as we will better see when talking about the simulation methodology in Section 2.3.

2.2.5 ELECTROCHEMISTRY AND MULTI-PHASE CHEMISTRY

Until now we have been exploring the transport processes from the macro to the microscale and we learnt how the information at each scale is transferred between them. What is missing is the chemistry framework, the system describing the reactions and consequently the formation/destruction of the species involved in those processes. At the mesoscale, the electrode pair is assumed to consist of up to three layers: positive electrode-separator-negative electrode (as explained in the previous paragraph). Each layer may host an arbitrary number of bulk phases (solid, liquid, or gaseous) characterised by their respective volume fractions ε, and each bulk phase may host an arbitrary number of chemical species. For example, in our model all the said layers contain the phase "electrolyte", which includes different chemical species like the ions derived from the salt ($LiPF_6$) and the solvents in which it is dissolved (EC, EMC). Each layer may furthermore host an arbitrary number of interfaces, where an arbitrary number of reactions takes place (i.e. intercalation/deintercalation at the positive and negative electrode/electrolyte interfaces). Each interface is also defined by a specific area A_n^{V} : for an intercalating electrode it refers to the active material/electrolyte interface and corresponds to the calculated ratio of its total surface area and its total volume. More comprehensive the model is, more layers, phases, species and reactions will be included. All this chemistry framework is managed by Cantera[42], an open-source chemical kinetics code that will be better introduced in the next paragraph.

Now, the reactions. The rate of a single interfacial reaction follows from mass-action kinetics[43,44]

$$r = k_{\mathrm{f}} \prod_{i=1}^{N_{\mathrm{R}}} c_i^{|\nu_i|} - k_{\mathrm{r}} \prod_{i=1}^{N_{\mathrm{P}}} c_i^{|\nu_i|} \ , \tag{32}$$

where the concentrations c_i refer to the concentrations at the electrode/electrolyte interface as given by the transport models. With k_{f} we mean the forward rate constant, which consists of a thermally-activated part (the Arrhenius expression[43,45]) and a potential-dependent part

$$k_{\mathrm{f}} = k_{\mathrm{f}}^0 \cdot \exp\left(-\frac{E_{\mathrm{act,f}}}{RT}\right) \cdot \exp\left(-\frac{\alpha_{\mathrm{f}} zF}{RT} \Delta\phi^{\mathrm{eff}}\right) \ , \tag{33}$$

while k_{r} is the reverse rate constant

$$k_{\mathrm{r}} = k_{\mathrm{f}}^0 \cdot \exp\left(-\frac{E_{\mathrm{act,f}}}{RT}\right) \cdot \exp\left(\frac{\Delta G}{RT}\right) \cdot \exp\left(\frac{(1-\alpha_{\mathrm{f}})zF}{RT} \Delta\phi^{\mathrm{eff}}\right) \cdot \prod_{i=1}^{N_{\mathrm{R}},N_{\mathrm{P}}} {c_i^0}^{-\nu_i} \ . \tag{34}$$

When talking about kinetics in this thesis, we will nevertheless use more extensively the exchange current density i^0 obtained via Butler-Volmer equation. Substituting the effective potential difference $\Delta\phi^{\mathrm{eff}}$ with the activation overpotential $\eta_{\mathrm{act}} = \Delta\phi^{\mathrm{eff}} - \Delta\phi^{\mathrm{eq}}$ and converting the reaction rate to current via $i = zFr$, we obtain the Butler-Volmer form

$$i = i^0 \left[\exp\left(-\frac{\alpha_{\mathrm{f}} zF}{RT}\eta_{\mathrm{act}}\right) - \exp\left(\frac{(1-\alpha_{\mathrm{f}})zF}{RT}\eta_{\mathrm{act}}\right)\right], \tag{35}$$

with the exchange current density

$$i^0 = i^{00} \cdot \exp\left(-\frac{E_{\mathrm{act,f}}}{RT}\right) \cdot \prod_{i=1}^{N_{\mathrm{R}}} \left(\frac{c_i}{c_i^0}\right)^{(1-\alpha_{\mathrm{f}})} \prod_{i=1}^{N_{\mathrm{P}}} \left(\frac{c_i}{c_i^0}\right)^{\alpha_{\mathrm{f}}} \tag{36}$$

and the exchange current density factor

$$i^{00} = zF \cdot k_{\mathrm{f}}^0 \cdot \exp\left(\alpha_{\mathrm{f}} \frac{\Delta G}{RT}\right) \cdot \prod_{i=1}^{N_{\mathrm{R}}} c_i^0 \ . \tag{37}$$

In Section 5.2.2 we will show many different forms of Eq. 36 that can be found in literature: it is important to understand their differences and similarities to be able to compare them. ΔG is the Gibbs reaction energy which,

for an intercalation material in a lithium-ion battery, is a function of SOC and consequently showing concentration dependence. In Cantera, $\Delta G(c_i)$ is calculated from the species molar enthalpies and entropies

$$\Delta G(c_i) = \sum_{i=1}^{N_{\mathrm{R}},N_{\mathrm{P}}} \nu_i (h_i(c_i) - T s_i(c_i)) \,, \tag{38}$$

where $h_{\mathrm{Li}}(c_i)$ and $s_{\mathrm{Li}}(c_i)$ of intercalated lithium species are calculated from experimental half-cell potentials. Having a look back at Eq. 33 for a reaction at the negative electrode/electrolyte interface, the effective potential difference $\Delta\phi^{\mathrm{eff}}$ includes also the correction for the SEI (Solid Electrolyte Interphase) resistance

$$\Delta\phi^{\mathrm{eff}} = \Delta\phi - R_{\mathrm{SEI}}^{\mathrm{V}} i_{\mathrm{F}}^{\mathrm{V}} \,. \tag{39}$$

We will talk more about this important film in Chapter 6. We can now call back from the mesoscale paragraph the mass conservation equation

$$\frac{\partial(\varepsilon_{\mathrm{elyt}} c_i)}{\partial t} = -\frac{\partial j_i}{\partial y} + \dot{s}_i^{\mathrm{V}} + \dot{s}_{i,\mathrm{DL}}^{\mathrm{V}} \tag{40}$$

and the charge neutrality condition

$$C_{\mathrm{DL}}^{\mathrm{V}} \frac{\partial(\Delta\phi)}{\partial t} = \sum_i z_i F \frac{\partial j_i}{\partial y} - i_F^{\mathrm{V}} \quad , \tag{41}$$

and finally define their respective volumetric terms $\dot{s}_i^V$ and i_F^{V} using what seen in this electrochemistry section. $\dot{s}_i^{\mathrm{V}}$ corresponds to the sum of all the interfacial reactions scaled to the specific area of the respective interface (i.e. any AM interface)

$$\dot{s}_i^{\mathrm{V}} = \sum_{n=1}^{N_{\mathrm{r}}} (\nu_{i,n} r_n A_n^{\mathrm{V}}) \,, \tag{42}$$

while i_F^{V} , the Faradaic current, is similarly obtained from the source terms of electrons

$$i_{\mathrm{F}}^{\mathrm{V}} = F \dot{s}_{\mathrm{e}}^{\mathrm{V}} = \sum_{n=1}^{N_{\mathrm{r}}} F\left(\nu_{\mathrm{e},n} r_n A_n^{\mathrm{V}}\right) , \tag{43}$$

both of them connected to the reaction rate from Eq. 32. All these interfacial reactions cause formation and destruction of species, leading to a change of volume fractions from the initial values set at equilibrium. Therefore, additional conservation equations must be added. For all bulk phases[38]

$$\frac{\partial(\rho_j \varepsilon_j)}{\partial t} = \sum_{i=1}^{N_{\mathrm{R},j},N_{\mathrm{P},j}} \dot{s}_i^{\mathrm{V}} M_i \,, \tag{44}$$

while for the gas species, also subjected to changes in pressure and concentration

$$\frac{\partial \rho_{\mathrm{gas}}}{\partial t} = \frac{1}{V_{\mathrm{void}}} \sum_{i=1}^{N_{\mathrm{gas}}} \dot{s}_i^{\mathrm{gas}} M_i \tag{45}$$

$$\frac{\partial(\rho_{\mathrm{gas}} Y_i)}{\partial t} = \frac{1}{V_{\mathrm{void}}} \dot{s}_i^{\mathrm{gas}} M_i \tag{46}$$

under the ideal-gas law

$$p_{\mathrm{gas}} = \rho_{\mathrm{gas}} R T \sum_{i=1}^{N_{\mathrm{gas}}} Y_i / M_i \quad . \tag{47}$$

Y_i here stays for the mass fraction of species i while V_{void} refers to the void space in the cell that is modelled as 0D gas reservoir[46] for the accumulation of the gases eventually produced during the reactions. A good example is the SEI formation and again we refer the interested reader to Chapter 6. The gas-phase species source term $\dot{s}_i^{\mathrm{gas}}$ follows from integration over the complete electrode volume on mesoscale and macroscale, according to

$$\dot{s}_i^{\mathrm{gas}} = \frac{A_{\mathrm{e}}}{V_{\mathrm{cell}}} \sum_{m=1}^{N_{\mathrm{EP}}} \left(V_m \cdot \int_0^{L_{\mathrm{EP}}} \dot{s}_i^{\mathrm{gas,V}} \mathrm{d}y \right) \,. \tag{48}$$

For the sake of simplicity, the gas pressure and composition are assumed constant throughout the cell, including the gas-filled porosity inside the negative electrode.

In summary, with this section we have now a (nearly) complete overview on the theoretical structure of our general modelling framework: a multiscale model subdivided in layer, phases and species defined by electrochemical thermodynamics and kinetics. Charge-transfer (involving electrons and kinetic coefficients) and non-charge-transfer reactions happen at defined interfaces according to values of enthalpy and entropy accurately parameterised. The formation and destruction of species here involved are then subjected to transport processes at different scales, always respecting the principles of electroneutrality and mass balance of a closed system (i.e. the cell). What is missing? Well, the simulation methodology, i.e. the software which allows us to step from theory (modelling) to practice (simulation).

2.3 SIMULATION METHODOLOGY: WELCOME TO CANTERA AND MCDENIS

"The machines do not solve problems with greater insight than men do, only faster.
Only faster!"
(Isaac Asimov)

We have defined the governing equations, the chemistry and the relationships between the different scales, but until now all this is just theoretical knowledge. How can we step into practice from this modelling framework? The illustrated multiscale theoretical structure gets implemented in the in-house multiphysics software package DENIS (Detailed Electrochemistry and Numerical Impedance Simulation)[35,38] and numerically solved using the implicit time-adaptive solver LIMEX. DENIS is a C/C^{++} code with modular structure whose main functionality is to cast the model equations into the form of a differential-algebraic equation system

$$\frac{\mathrm{d}y}{\mathrm{d}t} = f(y,t), \quad 0 = g(y,t)\,, \tag{49}$$

based on conveniently editable text input files (beware! The *y* in Eq. 57 refers to variables like T and c_i – nothing to do with the *y* scale). The equation system can be either solved for I_{cell} when E_{cell} is given as independent variable (potentiodynamic simulation), or vice versa (galvanodynamic simulation). As already mentioned in Section 2.2.4, the partial differential equations at every level of the multiscale are discretised through the application of a finite-volume method and consequently the creation of "compartments" in which every scale is parted. For example, for the modelling of the Kokam cell described in Chapter 4, at the macroscale *x* the cell is discretised in 20 non-equidistant compartments: 10 for the cell itself plus other 10 for the two symmetrically surrounding aluminium plates (5+5). At the mesoscale *y*, 19 compartments for the electrode-pair: 7 for the negative electrode, 5 for the separator, 7 for the positive electrode. Note that, for each layer, the compartments have different width along the *y* axis (the two at the extremes are set to be 1/100 thinner than the ones at the centre). At the microscale *z*, 11 compartments for every AM particle. Then the complete electrochemistry (thermodynamics and kinetics) is based on the use of the open-source chemical kinetics code Cantera[42], a C^{++} code built to obtain the reaction rates r and the Gibbs reaction energies $\Delta G(c_i)$ (see previous Section 2.2.5). Cantera is coupled to the DENIS transport model via the chemistry source terms[47] (i.e. $\dot{s}^{\mathrm{V}}_{\mathrm{Li[AM},i]}$ and $\dot{s}^{\mathrm{V}}_{\mathrm{V[AM},i]}$ for

the AMs at the electrodes). In our modelling framework, we use Cantera's *BinarySolutionTabulatedThermo* class for the three AM (NCA, LCO, graphite), while the electrolyte phase is described through the *IdealSolidSolution* class, with the standard concentration set to a unity value. The gas phases (*ideal_gas* class), the electrons from the charge-transfer reactions (*metal* class) and the "extras" like SEI and lithium metal (*stoichiometric_solid* class) fall into other classes with their own specific features. The internal calculation is supported by a library of thermodynamic and kinetic parameters of all involved phases, species, interfaces and reactions, obtained via accurate literature research and post-experiments data analysis. If you want to know more about the Cantera's classes and their properties, a more detailed insight into the models implemented in Cantera can be found in Mayur *et al*.[47].

In practice, all this means we have to deal with two different files, one for each software, in which we define the needed parameters: one for the multiscale level (".model" file) and one for the electrochemistry (".cti" file). MATLAB (version 2019a) is the chosen interface for controlling all DENIS simulations[2], as well as for data evaluation and visualization. In short, we say M(atlab) c(oupled) DENIS, a.k.a McDENIS.

2.4 CHALLENGES AND CONCLUSIONS

With their growing importance in the market of electric vehicles and energy storage, a more comprehensive evaluation of lithium-ion batteries behaviour has now become necessary for the power sources industry. Mathematical modelling and numerical simulation are now recognized as standard techniques in lithium-ion battery research and development, with the purpose of studying the issues of batteries, including performance and ageing, and consequently increasing the predictability of model-based life expectancy.

It is in this context that this thesis has been developed, starting from the present Chapter with the necessary knowledge used to build the modelling and simulation frameworks discussed in the next pages (see Chapters 4, 5 and 7). The "basic" transport model here exposed, previously described in the fundamental paper from Kupper[19], is based on a P3D multiscale approach where the heat transport in the through-cell direction (1D, macroscale) is modelled as conductive process, mass and charge transport on the electrode-pair scale (1D, mesoscale) as diffusion and migration and intraparticle transport of lithium atoms (1D, microscale) as Fickian diffusion with concentration-dependent diffusion coefficient. A 0D model of the void cell volume was also added, allowing to describe gas-phase species concentration and pressure build-up during ageing processes. The governing equations for this model are implemented in the in-house multiphysics software package DENIS, while the electrochemistry model is based on the use of the open-source chemical kinetics code Cantera, which is coupled to the DENIS transport model via the chemistry source terms.

The next Chapter will be complementary to the "hard theory" here exposed, by introducing us to the problems of ageing in a qualitative way: by knowing more about them, we will then try to translate them from real to virtual with the purpose of modelling and simulating their impact on the battery behaviour.

---

[2] Simulation times are fast indeed! A "standard" simulated cycle [discharge (1C CCCV, C/20 cut-off) – rest (1800 s) – charge (1C CCCV, C/20 cut-off) – rest (1800 s)] would require a computational time of around 360 s.

3 FUNDAMENTALS OF LITHIUM-ION BATTERY AGEING

"We don't stop playing because we grow old.
We grow old because we stop playing."
(George Bernard Shaw)

Batteries, as any other object in the real world, are not eternal and their lifetime is affected by various ageing mechanisms happening at the mesoscale and causing the fatal degradation of the electrodes. The capacity and power fade originate from side reactions occurring at both anode and cathode[3], even if in a significantly different way: it can originate from a loss of electrode active material, from a loss of cyclable lithium, or from increasing internal resistances which could cause an earlier termination of the charging or discharging process[48–50]. A sophisticated evaluation of lithium-ion batteries lifetime and behaviour has become consequently necessary but, unfortunately, batteries are extremely complex systems to understand and even more complex are the ageing processes within them[51].
As already explained in Section 2.1, a lithium-ion battery cell consists of two (composite or not) electrodes and a polymeric separator in-between, which pores are filled with electrolyte (consisting of organic solvents, additives and - the most important - a conductive salt); at the extremes, current collectors provide conduction of electrons from inside the electrochemical reaction to the external part. In this Chapter (a "soft theory" one compared to Chapter 2) we will therefore introduce the ageing phenomena in these different parts of the battery, with a particular attention to the formation of the Solid Electrolyte Interphase (SEI) and the lithium plating; we will also shortly talk about the concept of calendar and cyclic ageing.

3.1 DEGRADATION OF CELL COMPONENTS

"The Old Ones were, the Old Ones are, and the Old Ones shall be.
Not in the spaces we know, but between them.
They walk serene and primal, undimensioned and to us unseen."
(H.P. Lovecraft, from *The Dunwich Horror and Others*)

The different components of a lithium-ion cell are all subject to degradation[52]: the quite complicate figure below (Figure 4) illustrates most of the degradation mechanisms in lithium-ion cells, some of them mainly chemical (i.e. SEI and lithium plating), some rather mechanical (i.e. cracking and exfoliation).

[3] From now on, we will always refer to the negative carbon electrode as "anode" and to the positive electrode as "cathode". In battery science, texts which describe battery anodes or cathodes implicitly consider the case of the discharge, according to a well-established convention.

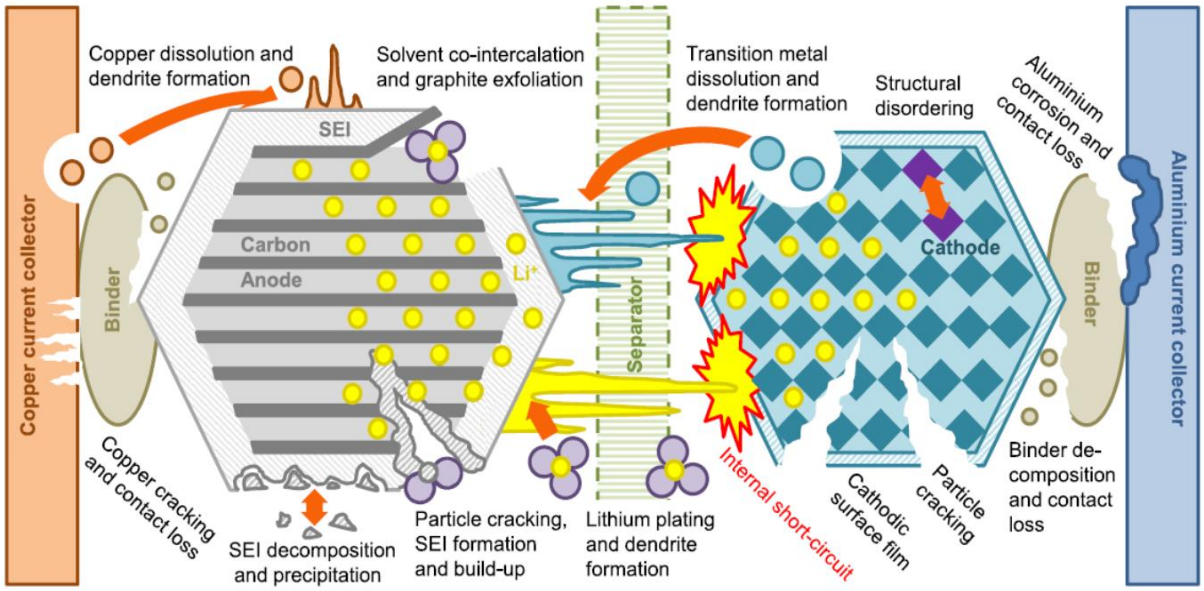

FIGURE 4: AGEING MECHANISMS IN LITHIUM-ION CELL: GRAPHIC REPRESENTATION OF STRUCTURAL DAMAGE, SEI FORMATION AND STABILISATION MECHANISMS AND LI PLATING AT THE ELECTRODE, WITH SUBSEQUENT CORROSION. THE FIGURE IS FROM BIRKL *ET AL.*[50]

The multiple causes, rates and inter-dependencies of these degradation mechanisms make a complete analysis of the ageing phenomena extremely challenging: if time, high temperature and SOC can take to formation, growth and decomposition of SEI, with consequent electrolyte decomposition and graphite exfoliation, low temperature can lead instead to lithium plating and formation of dendrites, with eventual pierce of the separator and possible short circuit (and thermal runaway and explosion), causing loss of lithium inventory (lithium ions are consumed by these parasitic reactions and no longer available for cycling - or even definitely lost if trapped in electrically isolated particles, a.k.a. “dead lithium”) and active anode material (the active mass is no more available for intercalation/deintercalation). Then, the mechanical stress and the low SOC could also lead to damage at the cathode, electrode cracking and metal dissolution, causing loss of active cathode material (same as above). The primary effect of degradation on the cell kinetics is an increase in internal resistance or cell impedance, which can be measured by the voltage drop in response to a load and EIS analysis[53] (see 4.3.5.1 for a short outlook on Electrochemical Impedance Spectroscopy). Voltage cut-off is also reached visibly sooner during charging/discharging in an aged battery.

Now, let’s have a closer look to what happens at the single components of the cell.

3.1.1 ANODE

Main character for the ageing discussion in this dissertation, the anode (prevalently graphite-made) suffers of its ageing issues mainly at the electrode/electrolyte interface, where the formation, growth and dissolution of SEI and the lithium plating (and eventually also dendrites) happen.

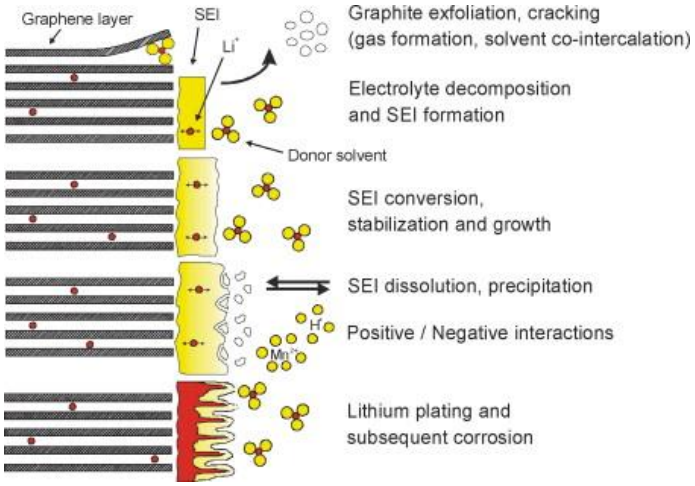

FIGURE 5: CHANGES AT THE ANODE/ELECTROLYTE INTERFACE. THE FIGURE IS FROM VETTER *ET AL.*[51]

As shown in Figure 5, mechanical degradation can also be observed at the anode in the form of graphite exfoliation and cracking due to repeated intercalation/deintercalation in the structure[54] and excessive formation of gases. The repeated uptake and removal of lithium ions along cycling leads to volume changes (around 10 % or less, depending on the material[51]) in the graphite, which can cause structural damage and cracking not only at the electrode but also at the passivating films on the surface in case of high C-rates[55]: hence new active anode material enters in contact with the electrolyte, causing new SEI formation and an increased consumption of cyclable lithium[56,57]. Further degradation is also caused by solvent co-intercalation and electrolyte reduction inside the bulk.

3.1.1.1 Surface film formation: Solid Electrolyte Interphase (SEI)

The most common source of capacity fade and consequent ageing of the battery is the loss of lithium to the SEI, which competes with reversible lithium intercalation. As the graphite anodes of lithium-ion cells operate at voltages beyond the thermodynamic stability of the organic electrolytes, the electrochemical reduction of the electrolyte solvent and decomposition of the conducting salt are inevitable, with the resulting products forming a passivating film at the graphite/electrolyte surface which is permeable for lithium cations, but rather impermeable for electrons and other electrolyte components[51,58]. Thus, the irreversible formation of the SEI passivation layer during the first few charge/discharge cycles of the battery is actually considered a positive mechanism, as it reasonably protects both the electrolyte and the electrode from further lithium losses and degradation[59,60]. This self-passivating ability is indeed extremely important in making a difference between a well and a badly performing lithium-ion battery, even if a real SEI will never be perfectly passivating and the electrolyte reduction will never be completely suppressed. The oxidation of SEI compounds is instead only possible at high voltages not normally met in normal battery operation[61]. Therefore, over time SEI growth and thickening leads to a gradual but important capacity loss[62,63]. With the ageing of the battery, the SEI may also penetrate into the pores of the electrodes and eventually clog the separator, reducing the capacity and increasing the internal resistance.

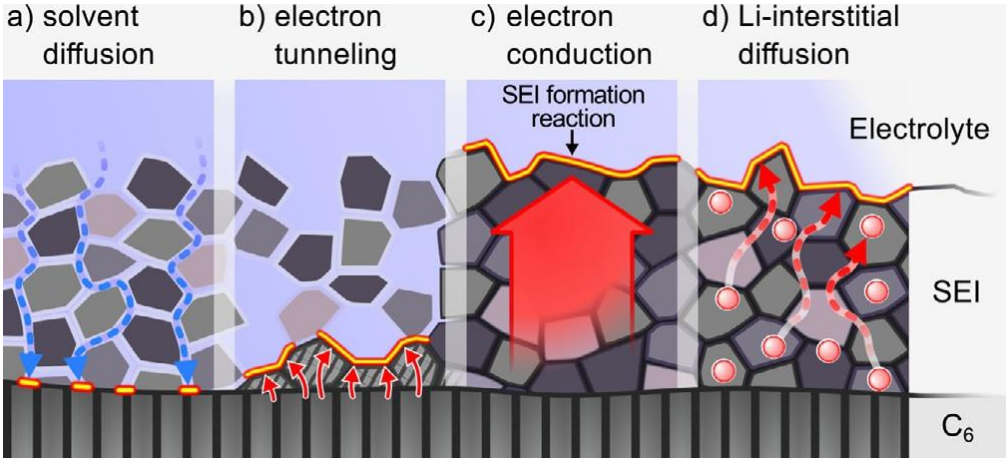

FIGURE 6: SCHEMATIC OF FOUR DIFFERENT TRANSPORT MECHANISMS SUGGESTED TO CAUSE LONG-TERM SEI GROWTH. A) SOLVENT DIFFUSION THROUGH SMALL SEI PORES, B) ELECTRON TUNNELLING THROUGH A THIN AND DENSE INNER SEI LAYER, C) ELECTRON CONDUCTION THROUGH THE SEI, D) DIFFUSION OF NEUTRAL LI THROUGH THE SEI. THE SEI FORMATION REACTION TAKES PLACE AT DIFFERENT INTERFACES DEPENDING ON THE MECHANISM, MARKED YELLOW/RED. THE FIGURE IS FROM SINGLE *ET AL*.[64]

The composition and structure of the SEI varies according to the active materials, the characteristics of the electrolyte (EC is a known first-choice for SEI formation, as "favourite" solvation shell for lithium-ions) and the formation process: it is generally described though as a bilayer structure with a dense inner inorganic core and a soft outer organic layer [55,65–67] (see Chapter 6 to learn more about SEI bilayer structure). At the moment the mechanisms for lithium-ion transport through the SEI, initial SEI formation and its long-term growth are still debated, because of the difficulties in accessing it experimentally and the influence of too many variables preventing a systematic investigation. As exposed in the works from Horstmann[68] and Single[64], the SEI thickness is experimentally observed to grow with the square-root of time $\sqrt{t}$ during long-term storage under open-circuit condition, but some unknown transport process seems to limit its growth after sufficiently long times.

This mechanism has been studied and evaluated by different continuum models, to finally result in four main suggested theories (Figure 6):

- Diffusion of solvent/salt molecules/anions through nanosized SEI pores[61,62,66,69,70]. Even if it matches the square-root-of-time behaviour, the solvent diffusion seems to fail explaining the observed dependence of SEI growth rate on electrode potential and SOC.
- Electron tunnelling through a dense, inner layer of the SEI[55,61]. Differently from the others mechanisms, it predicts capacity fade with the logarithm of time $\ln t$. Electron tunnelling allows the transport of electrons only through 2-3 nm thin SEI layers, a fact which could restrict its role mainly to the initial part of SEI growth (i.e. first cycle), together with nucleation and precipitation mechanisms.
- Electron conduction through the SEI[61,62,66,71–73]. Same as solvent diffusion, it matches the $\sqrt{t}$ behaviour but in this case, it seems to fail explaining the involvement of convection in SEI growth.
- Diffusion of neutral radicals such as lithium interstitials through the SEI, pass through a selected SEI or along nanosized SEI pores[64,74,75]. The diffusion of neutral radicals is considered an alternative mechanism for charge transport through the SEI: in the inorganic inner layer, lithium ions take up an electron at the electrode/SEI interface and diffuse as neutral interstitials to finally release it at the SEI/electrolyte

interface; in the organic outer layer, the radicals formed by electrolyte reduction can act as electron carrier. According to Single *et al.*[64], this mechanism offers a promising agreement with the experiments.

In a recent work from Kolzenberg[76], it is proposed that during battery cycling these different growth mechanisms could dominate at different time scales: at the beginning, SEI growth is limited by the formation reaction of neutral lithium atoms, to then switch to first diffusion and then electromigration of the electrons coordinated to lithium ions with increasing thickness.

Finally, in Kupper *et al.*[19,77] the SEI formation and growth is modelled under both storage and cycling, with its formation rate *r* set $\propto \frac{1}{\delta_{\mathrm{SEI}}}$. For the sake of simplicity, the structure is considered as ideally uniform in morphology and chemical composition (only two components: organic $(\mathrm{CH_2OCO_2Li})_2$ and inorganic $\mathrm{Li_2CO_3}$), with its formation at the anode accompanied by the release of gaseous decomposition products according to the following reaction:

$$2\mathrm{Li^+[elyt]} + 2\mathrm{e^-} + 2\mathrm{C_3H_4O_3[elyt]} \rightleftharpoons (\mathrm{CH_2OCO_2Li})_2\mathrm{[SEI]} + \mathrm{C_2H_4[gas]}. \quad (50)$$

Worth noting, the coupling "SEI - lithium plating" presented in Chapter 7 blossoms from the fusion of this previously developed SEI model from Kupper and the recently published lithium plating model[78] presented in Chapter 5.

3.1.1.2 LITHIUM PLATING

During charging at high currents and low temperatures, a high overpotential is reached and hence a dropping of the anode potential below 0 V vs. Li/Li$^+$ [17,79–81]: in these conditions, the lithium plating reaction becomes favourable over the main reaction of intercalation in the anode particles, as a further source of degradation of the cell. Lithium plating describes the reduction of lithium ions dissolved in the electrolyte to lithium plated at the surface of the anode: this reaction could be reversible (see Chapter 5 to learn more about reversible lithium plating) or irreversible, with the deposition of insoluble side products at the turning point of a sudden capacity drop[49,82,83]. During the stripping process (the opposite of deposition), it can occur that a part of the metal lithium loses contact to the anode, finding itself electrically isolated and taking the suggestive name of "dead lithium"[84]: this is one of the main causes of capacity fade in the battery during cycling ageing at low temperatures (see 3.2). The reduction of the dissolved lithium ions to lithium plated on the anode (see Figure 8) happens generally according to the following reaction:

$$\mathrm{Li^+[elyt]} + \mathrm{e^-[elde]} \rightleftharpoons \mathrm{Li[metal]}\,, \quad (51)$$

and the metallic film can usually be detected by an increasing thickness of the cell[85] , EIS analysis[86] and observation through scanning electron microscopy (SEM)[87] .

Lithium plating can also be identified by some specific "plating hints". The most known is a specific plateau in the cell voltage, observed during relaxation or discharge after charge at low temperatures[86–96]: it is ascribed to the mixed potential associated with simultaneous oxidation of deposited lithium and eventual re-intercalation into the anode active material, hence indicating that lithium has been plated at one point during charging. Worth noting, its duration is affected by the rate capability of re-intercalation into graphite.

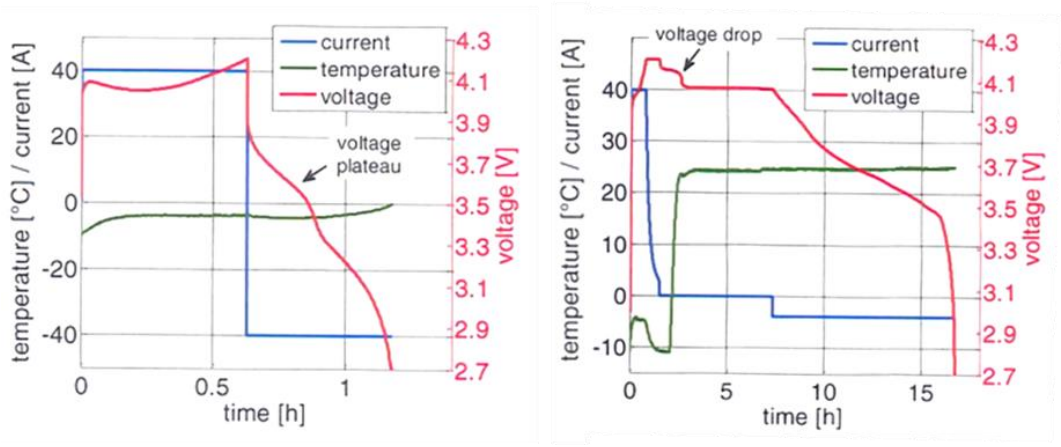

FIGURE 7: EXAMPLES OF PLATING HINTS: VOLTAGE PLATEAU (ON THE LEFT) AND VOLTAGE DROP (ON THE RIGHT). CURRENT AND TEMPERATURE CURVES ARE ALSO SHOWN TOGETHER WITH THE VOLTAGE. THE FIGURE IS FROM ECKER[95]

Another less-known voltage hint is a voltage drop detected when cells are charged at low temperatures and then heated during the following rest[95,97–99]. This fast drop of voltage of about 0.1 V, is not simply due to the temperature rise of the cell but more to a heat-favoured re-intercalation of lithium plated on the anode surface during charge at low temperature.

In Figure 7 an example of voltage plateau and one of voltage drop are shown respectively on the left and on the right. These curves have been extracted from the work of Ecker[95] on a 40 Ah high-power Kokam cell[95] with NMC at the cathode and we will meet them again in Section 5.4.1, where they will be used as experimental comparison for our model.

Worth adding also that thicker electrodes with larger particles and a lower porosity are more subject to lithium plating than thinner electrodes with smaller particles and a higher porosity[100]. Hence multiple factors, both geometric, thermodinamic and kinetic, could influence the voltage behaviour and determining the presence or absence of these plating hints. If you want to know more about this subject, go to Chapter 5.

In conclusion, rapid charging at low temperature can be a main cause of cell degradation, leading to consumption of cyclable lithium through lithium plating, consequent capacity loss and eventual formation of metallic dendrites[84,101] (a potential safety hazard).

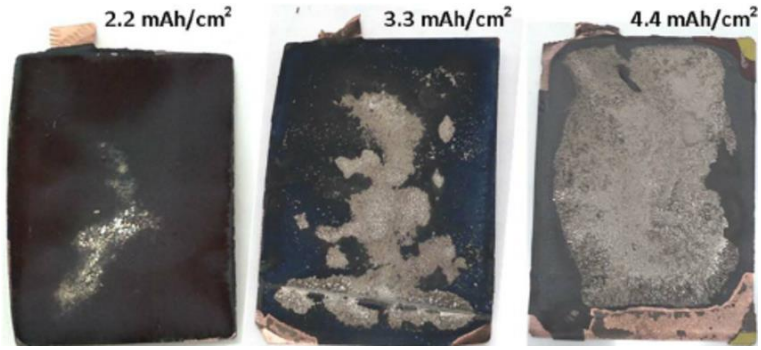

FIGURE 8: IMAGES OF GRAPHITE ELECTRODE AFTER AGEING IN NMC622/GR POUCH CELLS. LITHIUM PLATING APPEARS AS METALLIC DEPOSITS ON THE SURFACE OF THE ELECTRODE. THE FIGURE IS FROM GALLAGHER *ET AL.*[100]

3.1.2 CATHODE

As shown in Figure 4, both the electrodes are subject to degradation: in the case of the cathode, the ageing process works through structural changes, mechanical stresses and metal dissolution during cycling[102], with the eventual formation of a surface film called SPI (Solid Permeable Interphase) similarly to the parallel SEI at the anode[103].

The repeated lithiation/delithiation at the cathode during cycling leads to structural changes which may induce mechanical stress to the active material particles and possible phase transitions which may lead to distortion of the crystal lattice and further mechanical stress. The eventual formation of new compounds due to structural disorder reactions is often accompanied by gas release and electrolyte decomposition, which accelerate the ongoing damage and increase the cathode impedance (and the consequent capacity fade[104]). Then the formation of microcracks at the electrode could lead to fragmentation of isolated particles from the matrix and consequent loss of active cathode mass. At high temperatures the dissolution of the transition metals also adds to the degradation and the dissolved ions have been seen migrating to the anode and aggravating the SEI growth with additional consumption of cyclable lithium[51]. Last but not least, the SPI at the cathode/electrolyte surface, similarly to the SEI, is composed of organic species from the electrolyte oxidation and inorganic species from the conductive salt decomposition[105].

3.1.3 ELECTROLYTE, SEPARATOR AND CURRENT COLLECTORS

We will now have a look at the ageing processes at the other components of the battery beside the electrodes: electrolyte, separator and current collectors. As previously presented, the electrolyte oxidation/reduction and its participating in the formation of films at both the electrodes surfaces contribute to the global capacity fade, with the decomposition of the conductive salt strongly affecting the ohmic resistance of the lithium-ion cell[39,106]. Further effects of this degradation are the release of gaseous reaction products, with consequent increase of the internal cell pressure[107], and a local dry-out of the lithium-ion cell, leading to contact loss of active material particles with the liquid electrolyte and accelerated ageing[77].

Deposits from the electrolyte decomposition can also cause pores clogging in the porous separator, which leads to an increasing ionic impedance and, in extreme cases, even a decrease of the accessible active surface area of the electrodes[51]. Pores closure may also be caused by mechanical stress altering the separator characteristics, leading to inhomogeneous current distribution, local overpotentials and an augmented risk of lithium plating at the anode surface[86].

Finally, the current collectors (aluminium at the cathode and copper at the anode) are subject to electrochemical corrosion and dissolution, due to the presence of acidic species in the electrolyte (i.e. HF) and repeated cycling outside the electrochemical stability window of the collector components[104]. Again, mechanical stress can deform and damage the foils, with local deformations and an evident weakening of the contact with electrodes[108].

3.2 GETTING OLD: CALENDAR AGEING OR CYCLIC AGEING?

"That is the way it is, Ananda.
When young, one is subject to ageing;
when healthy, subject to illness;
when alive, subject to death."
(Buddha, from *Jara Sutta - Old Age*)

Ageing is not only about the different types of ageing processes, but also about the different ways of ageing: shortly, you can age resting quietly at your place or you can age living fully, with all the ups and downs of an exciting existence. If you are a battery, we will call the first type "calendar ageing" (nonoperating conditions) and the second one "cyclic ageing" (charging/discharging operations)[48,77].
Calendar ageing mainly results from the interactions between the electrolyte and the active materials: it depends on resting time, SOC and temperature and it is strongly linked to the electrolyte decomposition and consequent formation of SEI and SPI films on the electrodes surfaces. Cyclic ageing instead is an active ageing, influenced by many parameters as the operating conditions and the structural changes of the battery (see: lithium plating and its growing dendrites). In reality, it is impossible to completely separate the contributions from these two types of ageing, seen that the calendar ageing tends to happen during time and so also during the cyclic ageing, making the two phenomena additive[109].
Finally, after continuous and consuming ageing, the battery, like you and me and everyone else on this planet, will be pronounced dead. If for humans the concept of death is sometimes a debated and ethical issue, for a battery is simply defined by the concept of "End of Life" (EoL), which is generally defined as the reaching of the 70-80 % of the nominal capacity with consequent incapability of performing most of its applications[110].

3.3 AGEING STUDIES: FUTURE CHALLENGES AND CONCLUSIONS

"I wanted a mission, and for my sins, they gave me one."
(Captain Benjamin L. Willard, *Apocalypse Now* by F. F. Coppola)

In the present Chapter, we have introduced the ageing phenomena in different parts of the battery, with a particular attention to the formation of the Solid Electrolyte Interphase (SEI) and the lithium plating at the anode; we have also shortly talked about the concept of calendar and cyclic ageing. By knowing a bit more about the issues a battery is facing during its life, it is in our interest to include their impact on its behaviour with the purpose of "virtually" predicting the life expectancy and avoiding dangerous conditions (i.e. extreme temperatures, improper SOC during storage…).
With the modelling framework introduced in the previous Chapter and the ageing concepts discussed in this present Chapter, we now have the tools and the purpose for the mission behind the title of this thesis: building

a new and more complex model of a reference cell (yet able to be easily modified and re-parameterised to be adapted to similar cells – see Chapter 4) with the innovative inclusion of specific electrochemical ageing reactions at the anode to simulate lithium plating (see Chapter 5) and its coupling with the SEI (see Chapter 7). As we will see in the next pages, adding these ageing extensions needs quite a lot of work and makes the simulations slower and more computationally expensive: hence, there is probably a limit on how many ageing processes a model is able to include. We decided to choose to focus on the two main ones at the anode, keeping out of discussion the analysis of the complex effects from mechanical degradation and structural damage.

4 MODELLING AND SIMULATING THE KOKAM CELL: FROM REAL TO VIRTUAL

"Today's scientists have substituted mathematics for experiments,
and they wander off through equation after equation,
and eventually build a structure which has no relation to reality."
(Nikola Tesla)

The previous Chapters have introduced us to the principles of battery ageing (and batteries themselves) and to the modelling theory. We started from the basics, we went through many equations and complex ideas, we explored the ageing issues and the challenges they bring with them. Now it is time to move on to practice! Chapter 4 refers to the work done in the first part of the PhD and illustrated in the paper "Modelling and experimental validation of a high-power lithium-ion pouch cell with LCO/NCA blend cathode"[111], while Sections 4.1 and 4.3 partly refer to the co-authored (and second) paper "Identification of stoichiometric and microstructural parameters of a lithium-ion cell with blend electrode"[34]. We will go through the parameterisation: experiments, literature research and data analysis. We will understand how a blend electrode can be modelled and in this we will connect to Chapter 2 (so be prepared to jump some pages back). We will show the experimental validation and what is happening in the inside: the internal states at the *y* and *z* scales. First of all, let's introduce the protagonist of this Chapter in Figure 9:

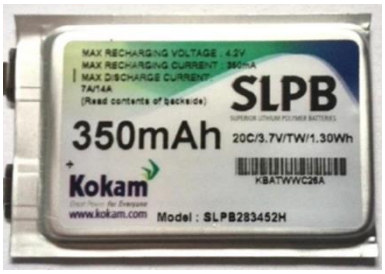

FIGURE 9: A PHOTO OF OUR REFERENCE CELL, 350 MAH HIGH-POWER LITHIUM-ION WITH BLEND CATHODE AND GRAPHITE ANODE.

This is a 350 mAh high-power lithium-ion pouch cell with graphite anode and lithium cobalt oxide/lithium nickel cobalt aluminium oxide (LCO/NCA) blend cathode. We will refer to it as "Kokam cell" (named after the producer) to keep it short. It is a high-power cell, so it can deliver large amounts of energy per unit time. It is a pouch cell, so it has a quite small though-cell direction (*x* scale). Observing Figure 10 you will also notice two differences from the modelling domain shown in Figure 2: the boundary conditions are now both at the cell/ambient interfaces ($x = 0$ and $x = d_{\mathrm{cell}}$) and in the *x* scale are also included two symmetrically surrounding holder plates, added in the experiments for well-defined mechanical boundary conditions.

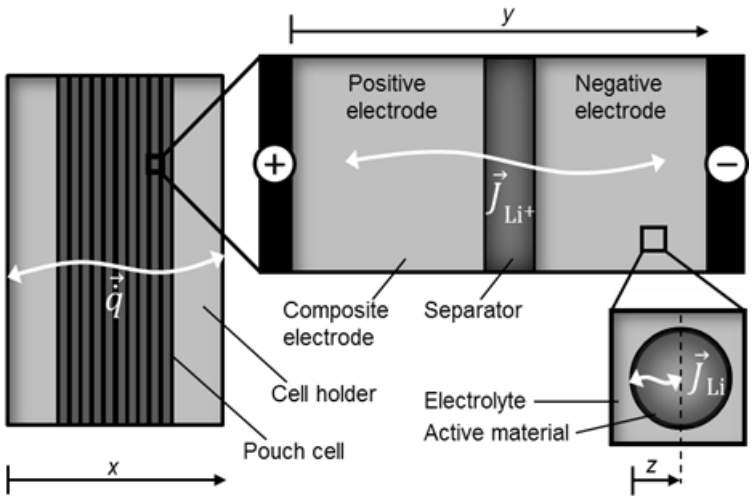

FIGURE 10: SCHEMATIC REPRESENTATION OF THE 1D+1D+1D (PSEUDO-3D, P3D) DOMAIN USED TO MODEL THE KOKAM REFERENCE CELL IN THIS CHAPTER. THE THREE SCALES (MACROSCALE (*X*), MESOSCALE (*Y*) AND MICROSCALE (*Z*)) ARE SHOWN.

The cell has a graphite anode (one active material) and a blend cathode, with two active materials (LCO and NCA). This last point is the most peculiar one. The blending of different AMs at one or both the electrodes is commonly used to tailor the overall performance towards specific requirements[112,113], but its "virtual" modelling happens to be much more complex than the case of single-material electrodes, due to the requirement of implementing competing reactions and the increasing effort for parameter identification. Few models that include blend electrodes were demonstrated before with different combinations of active materials at the cathode: we cite here Albertus[114] (LMO/NCA); Rodriguez and Plett[115] (multiple AMs); Jung[116], Appiah et al.[117], Mao et al.[118] (LMO/NMC). As you can see, we could not find a work treating our combination (LCO/NCA), which means we had to go step by step, building a specific model for the blend electrode and parameterising singularly both the AMs. This has been a long team process (carried out in mutual collaboration with M. Quarti, M. Mayur and M. Yagci) but you will see the results being quite satisfying, with this modelling framework being in the end used as "base" for the extensions in Chapters 5 and 7…but let's start from the beginning with a bit of theory.

4.1 BLEND ELECTRODE MODEL

"A theory is just a mathematical model to describe the observations"
(Karl Popper)

In Section 2.2.3 we have talked about the general theory behind microscale modelling: in the simplest case, where the electrode has only one active material, the mass conservation for lithium inside the AM particles is given by Eq. 28

$$\frac{\partial c_{\mathrm{Li[AM]}}}{\partial t} = \frac{1}{z^2}\frac{\partial}{\partial z}\left(z^2 D_{\mathrm{Li[AM]}}(c_{\mathrm{Li[AM]}})\frac{\partial c_{\mathrm{Li[AM]}}}{\partial z}\right). \quad (52)$$

In our Kokam cell, this would be the case for the anode (1 AM: graphite) but we need to make an extra effort to simulate the blend cathode (2 AMs: LCO and NCA). The first step is be to generalize the base model[19,77] in order to make possible the modelling of any composite electrode with an arbitrary number N_{AM} of different active materials i with their own individual properties. We don't talk anymore about concentration $c_{\mathrm{Li[AM]}}$ but about mole fraction $X_{\mathrm{Li[AM},i]}$, molar mass $M_{\mathrm{Li[AM},i]}$ and density $\rho_{\mathrm{Li[AM},i]}$ for every - lithiated - active material AM (in our model, $N_{\mathrm{AM}} = 3$). We consider the individual particle radii $r_{\mathrm{AM},i}$ (we assume spherical particles and fixed radius for simplicity's sake) and their initial volume fraction $\varepsilon_{\mathrm{AM},i}$ before intercalation (this is not a fixed value because of the natural volume expansion during cycling). We add an extra dependence from the lithium mole fraction $X_{\mathrm{Li[AM},i]}$ to the solid-state diffusion $D_{\mathrm{Li[AM},i]}$, which is now connected to the intercalation stoichiometry range $X_{\mathrm{Li[AM},i]}^{\mathrm{SOC=0}}$ (empty cathode – battery SOC 100 %) … $X_{\mathrm{Li[AM},i]}^{\mathrm{SOC=1}}$(full cathode – battery SOC 0 %), balanced and different for every AM at the cathode. At any SOC, the active material will be described by complementary mole fractions of its lithiated form $\mathrm{Li[AM},i]$ and its delithiated one $\mathrm{V[AM},i]$ defined as a vacancy. In view of all these assumptions, we obtain a new and more flexible form of Eq. 52 in spherical coordinates

$$\frac{\partial \rho_{\mathrm{Li[AM},i]}}{\partial t} = \frac{1}{r^2}\frac{\partial}{\partial r}\left(r^2 D_{\mathrm{Li[AM},i]}(X_{\mathrm{Li[AM},i]})\frac{\partial \rho_{\mathrm{Li[AM},i]}}{\partial r}\right). \tag{53}$$

The boundary flux at the particle/electrolyte interface $r = r_{\mathrm{AM},i}$ is given as[77]

$$j_{\mathrm{Li[AM},i]}\big|_{r=r_{\mathrm{AM},i}} = \frac{1}{A_{\mathrm{AM},i}^{\mathrm{V}}}\cdot\frac{1}{\varepsilon_{\mathrm{AM},i}}\left(\left(1-\frac{\rho_{\mathrm{Li[AM},i]}}{\rho_{\mathrm{AM},i}}\right)\dot{s}_{\mathrm{Li[AM},i]}^{\mathrm{V}}\cdot M_{\mathrm{Li[AM},i]} - \frac{\rho_{\mathrm{Li[AM},i]}}{\rho_{\mathrm{AM},i}}\dot{s}_{\mathrm{V[AM},i]}^{\mathrm{V}}\cdot M_{\mathrm{V[AM},i]}\right), \tag{54}$$

where, the AM specific surface area $A_{\mathrm{AM},i}^{\mathrm{V}}$, already introduced in Section 2.2.3, is now defined as

$$A_{\mathrm{AM},i}^{\mathrm{V}} = \frac{3}{r_{\mathrm{AM},i}}, \tag{55}$$

and $\dot{s}_{\mathrm{Li[AM},i]}^{\mathrm{V}}$ and $\dot{s}_{\mathrm{V[AM},i]}^{\mathrm{V}}$ are the volumetric source terms obtained from Cantera[42] for lithium and vacancies, respectively. How does it work though? Specifically, the local thermodynamic state in terms of temperature, pressure, electrode potential, electrolyte potential, electrolyte composition and lithium mole fraction at the particle surface is passed to Cantera, which will return net formation rates for every species we asked about (i.e. $\dot{s}_{\mathrm{Li[AM},i]}$ from intercalation reaction). Worth noting that, for the sake of simplicity, all the above listed parameters except the lithium mole fraction are set to identical for all AMs in the blend. To know more about Cantera, our dedicated tool for electrochemical thermodynamics and kinetics, have a look at Section 2.3 or, for a detailed theoretical insight, to Mayur *et al.*[47]. At the particle centre we set as always $j_{\mathrm{Li[AM},i]}\big|_{r=0} = 0$. In Eq. 53 the degree of lithiation is described by the change in density during time $\frac{\partial \rho_{\mathrm{Li[AM},i]}}{\partial t}$ which is connected to the lithium mole fraction $X_{\mathrm{Li[AM},i]}$ in the AM through

$$X_{\mathrm{Li[AM},i]} = \frac{\rho_{\mathrm{Li[AM},i]}}{\rho_{\mathrm{Li[AM},i]} + \frac{M_{\mathrm{Li[AM},i]}}{M_{\mathrm{V[AM},i]}}(\rho_{\mathrm{AM},i} - \rho_{\mathrm{Li[AM},i]})}\ . \tag{56}$$

When we talk commonly about battery cells, we are more interested on the level of charge (or discharge) reached either during cycling or at the end of it. The overall SOC of an electrode results from a weighted average of the SOCs of the individual AM

$$\mathrm{SOC}_{\mathrm{elde}} = \frac{\sum_{i=1}^{N_{\mathrm{AM,elde}}}(\mathrm{SOC}_i \cdot c_{\mathrm{AM},i}^{\mathrm{V}})}{\sum_{i=1}^{N_{\mathrm{AM,elde}}}(c_{\mathrm{AM},i}^{\mathrm{V}})}, \tag{57}$$

which can give a different value for anode and cathode according to the presence or absence of parasitic reactions beside the main intercalation/deintercalation at the electrode (i.e. plating at the anode, see Section 5.4.1). For each individual AM

$$\mathrm{SOC}_i = \frac{\bar{X}_{\mathrm{Li[AM},i]} - X_{\mathrm{Li[AM},i]}^{\mathrm{SOC=0}}}{X_{\mathrm{Li[AM},i]}^{\mathrm{SOC=1}} - X_{\mathrm{Li[AM},i]}^{\mathrm{SOC=0}}} \ , \tag{58}$$

which is related to the limits of the stoichiometry range $X_{\mathrm{Li[AM},i]}^{\mathrm{SOC=0}}$ … $X_{\mathrm{Li[AM},i]}^{\mathrm{SOC=1}}$ defined through the theory framework discussed in Section 4.3.1. The average lithium mole fraction $\bar{X}_{\mathrm{Li[AM},i]}$ is calculated through first integrating the density $\rho_{\mathrm{Li[AM},i]}$ over the particle volume ($r_{\mathrm{AM},i}^3$)

$$\bar{\rho}_{\mathrm{Li[AM},i]} = \frac{3}{r_{\mathrm{AM},i}^3} \int_0^{r_{\mathrm{AM},i}} \rho_{\mathrm{Li[AM},i]}(r) r^2 \mathrm{d}r \ , \tag{59}$$

and then using Eq.56. Finally, in Eq. 57 the individual overall capacity $C_{\mathrm{AM},i}^{\mathrm{V}}$ of the AM i in the electrode (in C/m^3) is given as

$$C_{\mathrm{AM},i}^{\mathrm{V}} = z_i F \varepsilon_{\mathrm{AM},i} \frac{\rho_{\mathrm{AM},i}}{M_{\mathrm{Li[AM},i]}} \left| X_{\mathrm{Li[AM},i]}^{\mathrm{SOC=1}} - X_{\mathrm{Li[AM},i]}^{\mathrm{SOC=0}} \right| , \tag{60}$$

where the volume fractions $\varepsilon_{\mathrm{AM},i}$ are also obtained through the theory framework exposed in Section 4.3.1. Based on the comparison of the experimental equilibrium cell voltage curve and the active material half-cell potential curves as function of $X_{\mathrm{Li[AM},i]}$ for every AM, this modelling framework has been of great help for us in the parameterisation of the model for our Kokam cell. Have a look at Section 4.3 and then check Ref. [34] if you want to learn more about it!

4.2 First of all, experiments

"A theory can be proven by experiment; but no path leads from experiment to the birth of a theory."
(Albert Einstein)

The second step, after having implemented the blend electrode model, is running the experiments in order to obtain model parameters and validation data. The cell-level experiments have been carried out by M. Yagci (Hochschule Offenburg) and are shown in 4.4.1. The electrical cycling tests (BaSyTec GSM) have been run on two individual cells at different ambient temperatures (5 °C, 20 °C, 35 °C, CTS T-40/200 Li climate chamber) and at different C-rates between C/20 and 10 C with CCCV protocol (3.0 V and 4.2 V cut-off voltages, C/20 CV cut-off current, 30 min rest). Here in Figure 11 follow the first obtained experimental data, which guided us in finding the best parameterisation for our model.

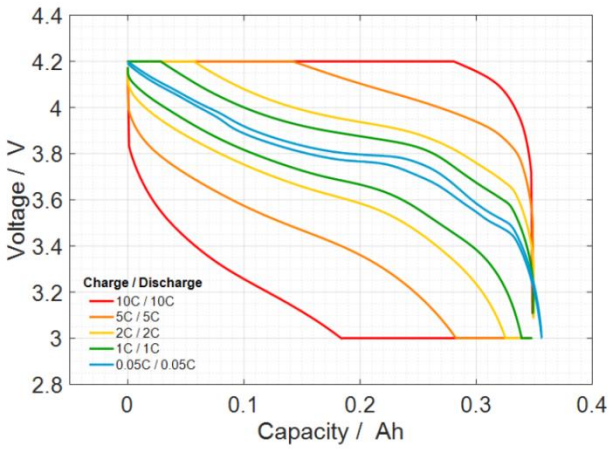

FIGURE 11: CCCV CYCLES AT 20 °C CARRIED OUT AT DIFFERENT C-RATES BETWEEN C/20 AND 10 C. PROTOCOL: 3.0 V AND 4.2 V CUT-OFF VOLTAGES, C/20 CV CUT-OFF CURRENT, 30 MIN REST.

The electrochemical impedance spectra have been recorded (Gamry Reference 3000) at different SOC (20 %, 50 %, 80 % only at 20 °C) and the same ambient temperatures. As shown in Figure 10 , the investigated cell has been placed between two aluminium plates - under mechanical load (50 000 N/m^2) - while the temperature was measured on the surface of the plate itself.

4.3 PARAMETERISATION ON THE MULTISCALE LEVEL

"Either this is madness or it is Hell."
"It is neither," calmly replied the voice of the Sphere, "it is Knowledge; it is Three Dimensions:
open your eye once again and try to look steadily."
(The Square and the Sphere, *Flatland* by Edwin A. Abbott)

As explained in 2.3, our modelling approach takes advantage of a multiscale structure defined by DENIS and an electrochemical library from Cantera, working together with MATLAB as user interface. Now this Section will show us how many parameters are needed (the answer is: quite a lot!) and how have been parameterised.

4.3.1 CELL AT THERMODYNAMIC EQUILIBRIUM

For cell at thermodynamic equilibrium, we mean a state in which there are no net flows of matter or of energy. From this base situation, we can measure the open-circuit voltage V^0 as function of charge throughput Q and consequently derive the other parameters related to nonequilibrium effects such as transport on the multiscale level and reactions kinetics. In order to ensure self-consistency of all input parameters in our model, we therefore need to define temperature-dependent half-cell potentials (if interested, it is all explained in much more details in Mayur *et al.*[34,47] : here we will just give a short summary). Figure 12 shows the molar enthalpies $h^0_{\mathrm{Li[AM},i]}$ and

entropies $s^0_{\mathrm{Li[AM},i]}$ of intercalated lithium as function of $X_{\mathrm{Li[AM},i]}$: these thermodynamic data have been calculated from literature experiments of half-cell potential vs. lithium metal $E^{\mathrm{eq}}_{\mathrm{Li[AM},i]}$ and their temperature dependence $E^{\mathrm{eq}}_{\mathrm{Li[AM},i]}/\mathrm{d}T$, including a correction for the entropy of the lithium metal contribution[47].

Because of the literature half-cell potentials not extending over complete stoichiometry range between 0 and 1, we needed to artificially extend the chosen NCA and LCO curves towards higher and lower stoichiometries than available experimentally – no worries, this process did not affect at all the results but instead it improved the numerical stability during simulations. For LCO, we extracted the potential data from Karthikeyan *et al.*[119] and added +8 mV to the values to match the (true) open-circuit potential plateau of Menetrier *et al.*[120]; entropies were taken from Reynier *et al.*[121], interpolated and corrected for $s^0_{\mathrm{Li[metal]}} = 29.12$ J·mol^{-1}·K^{-1}. For NCA, the original data are from Hall *et al.*[122], but because $X_{\mathrm{Li[NCA]}}$ range was not really specified in the paper, we decided to shift and scale the data the to the known $X_{\mathrm{Li[NCA]}}$ of Karthikeyan *et al.*[119].

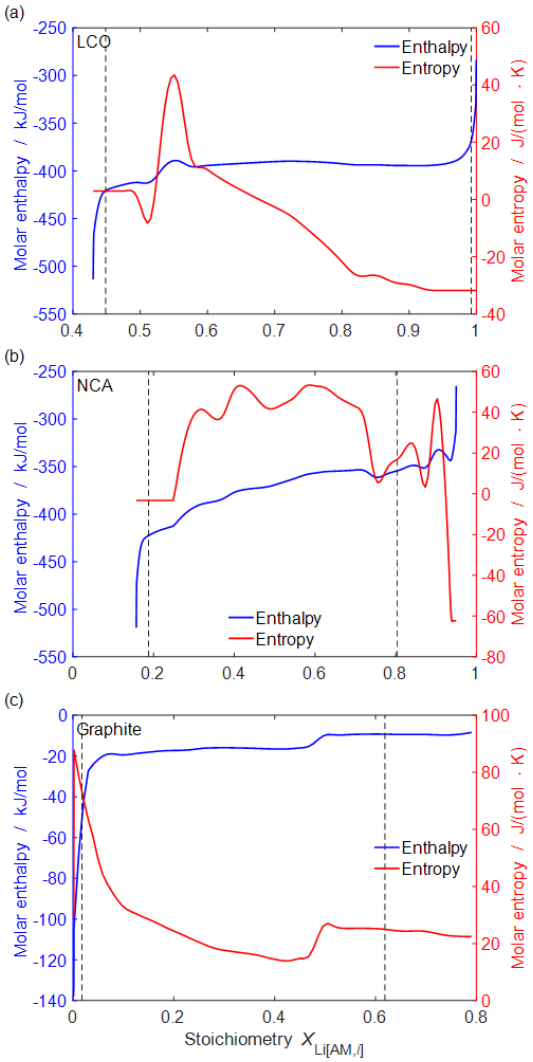

FIGURE 12: MOLAR ENTHALPIES AND ENTROPIES OF INTERCALATED LITHIUM WITHIN THE THREE AM (A) LCO, (B) NCA AND (C) GRAPHITE. THE VERTICAL DASHED LINES INDICATE THE STOICHIOMETRY RANGES FOR EVERY AM, AS OBTAINED THROUGH OPTIMISATION. SEE TEXT AND REF.[34] FOR DETAILS.

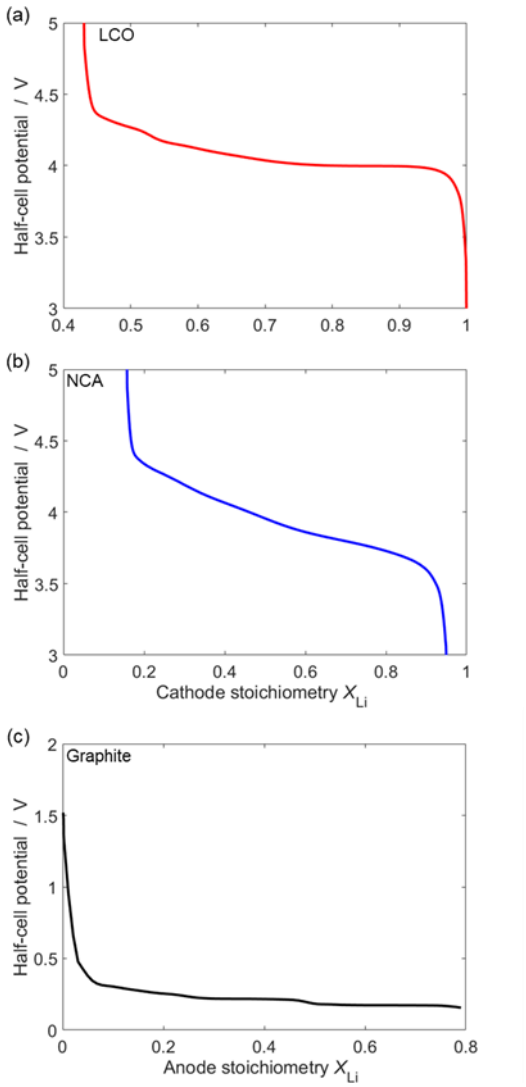

FIGURE 13: HALF-CELL POTENTIALS AT 25 °C FOR (A) LCO, (B) NCA AND (C) GRAPHITE.

Entropies were taken from Basu *et al.*[123], interpolated and corrected as done for LCO. For graphite, the potential data were directly taken from Ecker *et al.*[124] without modifications while the entropies were taken from Reynier *et al.*[125]. Figure 13 shows the resulting half-cell potentials at 25 °C after all these processes.

We furthermore needed to collect molar thermodynamic data for all other species present in the model. These data form the thermochemical basis of the model and are listed in Table 1.

After the chemical thermodynamics, the $V^0(Q)$ behaviour also depends on the available electrode capacity and several microstructural parameters of the electrode, as the volume fraction of the AMs, the densities of AMs, and the stoichiometry ranges the AMs are cycled in. But if unknown, how can we find these "electrode balancing" values in a blend electrode with more than one AM and implement them in the model? Now, this is where the carefully built methodology exposed in Mayur *et al.*[34] comes to help. First, an experimental charge/discharge cycle at low C-rate (for example C/20, to keep the cell voltage close to the reversible equilibrium) must be recorded; then, the cell is opened, the thicknesses of the electrodes and the active electrode area are measured

with simple measurement equipment. Together with the half-cell potential curves, the molar masses and densities of the AMs, these will form the self-consistent input data set required to finally obtain the missing output parameters (stoichiometry ranges of all AMs, volume fractions as function of SOC and corresponding cell capacity) via mathematical optimisation[34]. The equilibrium cell voltage curve is here assumed to be a superposition of the two half-cell potential curves, with the total half-cell capacity being provided by each AM in case of a blend electrode. Hence, the half-cell potential versus charge throughput Q is considered a superposition of the individual AMs potentials, which must be set equal at equilibrium. The AMs are also assumed to have a constant density independent of intercalation stoichiometry. A series of mathematical relationships, together with an intelligent computational framework, will finally allow to calculate the unknown electrode balancing parameters.

Let's have a look at the results shown in Figure 14 for our LCO-NCA/ graphite cell: the simulated $V^0(Q)$ curves are fitted and compared to the experimental cycle data, and volume fractions and stoichiometry ranges of all AMs are identified through mathematical optimisation and here plotted versus charge throughput. Figure 14a shows the cell voltage as obtained from the optimisation procedure: the experimental charge and discharge curves along with their average are also included. In Figure 14b the half-cell potentials of anode and cathode are plotted, demonstrating the capability of the model to calculate the half-cell potential of a blend electrode from the individual AMs ones. Figure 14c and Figure 14d shows respectively the stoichiometries and volume fractions of all three active materials as function of charge throughput. The stoichiometries of the cathode materials exhibit a strongly nonlinear behaviour, as a result of the blend continuously requiring the same half-cell potential for both AMs. The graphite stoichiometry, on the other hand, varies linearly as expected. In Figure 14d it is interesting to note that all three AMs exhibit a significant variation in volume fraction during discharge as a consequence of the expansion/contraction due to lithiation/delithiation.

TABLE 1: THERMODYNAMIC PROPERTIES OF ALL SPECIES INCLUDED IN THE MODEL.

Species	Molar enthalpy h_i / kJ·mol^{-1}	Molar entropy s_i / J·mol^{-1}·K^{-1}	Reference
Li[LCO]	See Figure 12a	See Figure 12a	34,47,119,121
V[LCO]	0	0	Reference value
Li[NCA]	See Figure 12b	See Figure 12b	34,47,122,123
V[NCA]	0	0	Reference value
Li[C_6]	See Figure 12c	See Figure 12c	34,47,124,125
V[C_6]	0	0	Reference value
$C_3H_4O_3$[elyt]	-578 *	175 *	126
$C_4H_8O_3$[elyt]	0	0	Dummy value (not chemically active)
Li^+[elyt]	0	0	Assumed
PF_6^- [elyt]	0	0	Dummy value (not chemically active)

* Values are assumed *T*-dependent [126], here given at 298 K

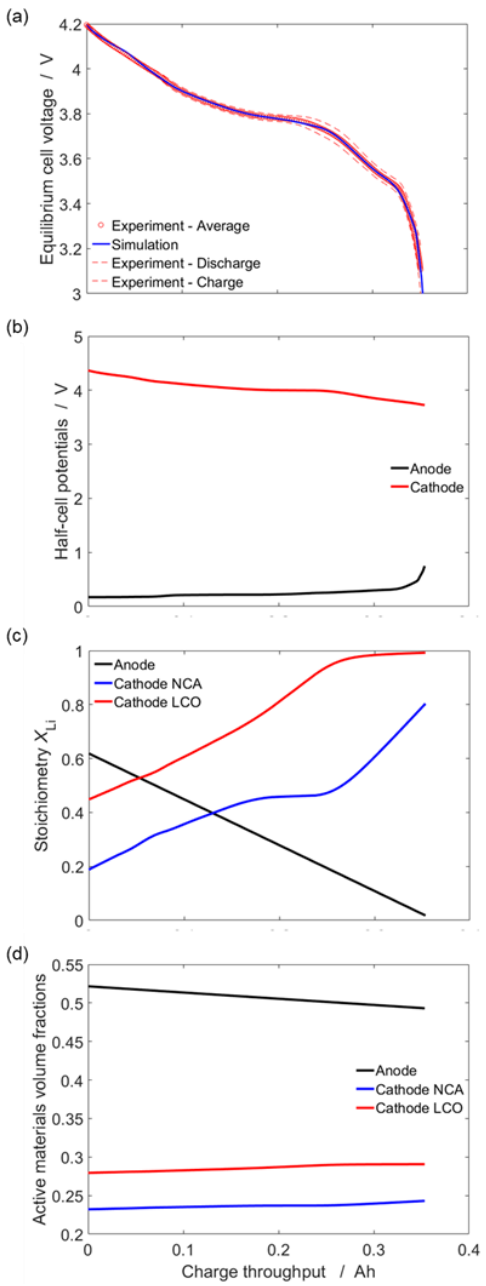

FIGURE 14: NCA-LCO/GRAPHITE CELL: (A) EXPERIMENTAL AND SIMULATED CELL VOLTAGE, (B) HALF-CELL POTENTIALS (C) ACTIVE MATERIAL STOICHIOMETRIES AND (D) VOLUME FRACTIONS AS FUNCTION OF CHARGE THROUGHPUT.

The resulting parameters are included in Table 2, where all phases and species assumed in both electrodes and separator are also defined, and in the following Tables.

Afterwards we had the opportunity to compare our simulated results to the FIB/SEM tomography experiments from Almar et al.[127] . As explained in their work, they discharged the same 350 mAh Kokam cell to 0 % SOC, then opened it and prepared a cathode sample to be investigated it with FIB/SEM and digitalized in a 3D model. Their obtained volume fractions for the blend electrode were $\varepsilon_{\mathrm{LCO}} = 0.32$ and $\varepsilon_{\mathrm{NCA}} = 0.28$. We therefore extracted the values at 0 % SOC from Figure 14d to obtain $\varepsilon_{\mathrm{LCO}} = 0.291$ and $\varepsilon_{\mathrm{NCA}} = 0.243$. By comparing them, we can say that the agreement is remarkable despite the different methodologies behind, and that our theoretical approach has been nevertheless quite successful.

TABLE 2: PROPERTIES OF ALL BULK PHASES INCLUDED IN THE MODEL.

Layer	Phase	Initial volume fraction ε	Density ρ / kg·m^{-3}	Species (initial mole fraction X_i)	Reference
Cathode	LCO	0.2856	4790	Li[LCO], V[LCO] (depends on SOC - see Table 5)	[34]
	NCA	0.2368	3900	Li[NCA], V[NCA] (depends on SOC - see Table 5)	[34]
	Electrolyte	0.2976	1270	$C_3H_4O_3$ [elyt] (0.52), $C_4H_8O_3$ [elyt] (0.34), Li^+ [elyt] (0.07), PF_6^- [elyt] (0.07)	Assumed 1.0 M $LiPF_6$ in EC/EMC=50/50 v/v
	Gas phase	0.030	From ideal gas law	N_2 (1)	Assumed
	Electron conductor	0.150	2000	Carbon, electron	Assumed graphite
Separator	Separator	0.5 [30]	777		Assumed
	Electrolyte	0.470	1270	same as at cathode	
	Gas phase	0.030	From ideal gas law	N_2 (1)	Assumed
Anode	C_6	0.5073	2270	Li[C_6], V[C_6] (depends on SOC - see Table 5)	[34]
	Electrolyte	0.4527	1270	same as at cathode	
	SEI	0.0008	1300 [128]	$(CH_2OCO_2Li)_2$	Assumed*
		0.0092	2100	(Li_2CO_3)	Assumed*
	Gas phase	0.030	1.14 [129]	N_2 (1)	Assumed

* SEI species included as placeholder for future investigations

This concludes the identification of parameters required for describing the equilibrium case. We next determine transport parameters on macro, meso and microscale and finally the reaction kinetic parameters.

4.3.2 MACROSCALE: THE THERMAL PARAMETERS

First scale to be discussed is the macroscale and consequently the geometric and thermal parameters behind the heat transport process.

The main thermal parameters to define are the through-plane thermal conductivity and the heat capacity for both the cell and the aluminium holder plates. In Table 3 you can see them being taken from literature while the geometric parameters have been directly measured (NB this part of the parameterisation process has been done by M. Quarti and therefore it will be described in detail in his PhD thesis).

More details are available in the original paper[111].

Let's now step one scale lower, into the mesoscale.

TABLE 3: MACROSCALE: GEOMETRIC AND THERMAL PARAMETERS.

Parameter	Domain	Value	Reference
Thickness	Left aluminium plate	0.0083 mm	Measured*
Thickness	Cell	3 mm	Measured
Thickness	Right aluminium plate	0.019 mm	Measured*
Active electrode area A_e	Cell	0.02883 m²	Measured [34]
Thermal conductivity λ	Left / right aluminium plate	237 $W \cdot m^{-1} \cdot K^{-1}$	[130]
Thermal conductivity λ	Cell	0.9 $W \cdot m^{-1} \cdot K^{-1}$	[131]
Heat capacity ρc_P	Left / right aluminium plate	0.897 $J \cdot g^{-1} \cdot K^{-1}$	[130]
Heat capacity ρc_P	Cell	0.95 $J \cdot g^{-1} \cdot K^{-1}$	[132]
Heat transfer coefficient α	Aluminium plate surface	157 $W \cdot m^{-2} \cdot K^{-1}$	Measured*
Emissivity ϵ	Aluminium plate surface	0.15	[133]

* Values include correction for 1D computational domain

4.3.3 MESOSCALE: THE ELECTROLYTE MODEL

In this Section we will start by recalling some of the DST and CST equations introduced in 2.2.2. Here follow:

$$j_i = -D_i^{\text{eff}} \frac{\partial c_i}{\partial y} - D_i^{\text{migr,eff}} \frac{\partial \phi_{\text{elyt}}}{\partial y} \tag{61}$$

$$D_i^{\text{eff}} = \frac{\varepsilon_{\text{elyt}}}{{\tau_{\text{elyt}}}^2} D_i \tag{62}$$

$$D_i^{\text{migr,DST}} = \frac{z_i F}{RT} c_i D_i \tag{63}$$

$$D_i^{\text{migr,CST}} = \frac{t_i^0}{z_i F} \cdot \sigma(c, T)\ . \tag{64}$$

Eq. 61 describes the transport fluxes of the species i in the electrolyte via diffusion and migration. Eqs. 62 and 63 use Diluted Solution Theory and a diffusion coefficient D_i for every single species. Eq. 64 refers instead to Concentrated Solution Theory and builds an important species-specific connection to the electrolyte conductivity σ and the transference number t_i^0 .

According to the cell data sheet for our Kokam cell, the electrolyte is composed of EC, EMC, and $LiPF_6$ as salt; the exact composition is nevertheless unknown to us.

TABLE 4: LITERATURE CONDUCTIVITY DATA FOR EC/EMC/$LiPF_6$ ELECTROLYTES AT 1 MOL/L. FOR ZHANG *ET AL.*, ACTIVATION ENERGIES ARE GIVEN FOR DIFFERENT TEMPERATURE RANGES, AS INDICATED IN THE TABLE.

Reference	Electrolyte	Conductivity	Activation energy (E_{act})
Nyman *et al.* (2008) [134]	EC:EMC 3:7 wt	0.95 S/m (25°C)	
Zhang *et al.* (2002) [135]	EC:EMC 3:7 wt	0.80 S/m (21°C)	17.20 kJ/mol (-20°C/62°C)
		0.95 S/m (30°C)	15.30 kJ/mol (0°C/62°C)
			26.70 kJ/mol (-50°C/-10°C)
Ecker *et al.* (2015) [124]	EC:EMC 1:1 wt	0.96 S/m (25°C)	17.12 kJ/mol

Following a literature research on similar electrolyte systems, Table 4 gives an overview of the data of conductivity as function of lithium ion concentration and/or temperature which will be used for parameterisation. We use here a combination of DST and CST to build a electrolyte transport model based on dilute solution theory but with concentration and temperature dependent diffusivities D_i for Li^+ and PF_6^- (accounting for the interaction between the ions in the concentrated solution). Seen our limited knowledge about the exact nature of the present electrolyte, an application of the concentrated solution theory would be not feasible due to the requested higher complexity of parameterisation.

First of all, we define the transference numbers t_+^0 and t_-^0 respectively for the positive and negative ion

$$t_+^0 = \frac{D_{\mathrm{Li}^+}}{\left(D_{\mathrm{Li}^+} + D_{\mathrm{PF}_6^-}\right)} \tag{65}$$

$$t_-^0 = 1 - t_+^0. \tag{66}$$

For transference (or transport) number we mean the fraction of the total electrical current carried in an electrolyte by a given ionic species. According to Capiglia[136], the diffusion coefficient for PF_6^- is higher than the diffusion coefficient for the cationic Li^+, probably due to the larger number of solvent molecules needed in its solvation shell. Consequently, we can expect $t_-^0 > t_+^0$. In our model we set a (concentration-independent) value of t_+^0= 0.30 at 1 mol/l [134] (NB the lithium transport number has been seen decreasing with concentration from 0.37 at 0.2 mol/l to 0.22 at 2.0 mol/l in Nyman *et al.*[134]).

Dependent from the salt $LiPF_6$ concentration as from the temperature of the system, the ionic conductivity σ is well described by the famous Nernst-Einstein equation in the limit of infinite dilution (non-interacting ions)

$$\sigma = \frac{z^2F^2}{RT} \cdot c_{\mathrm{LiPF_6}} \cdot \left(D_{\mathrm{Li}^+} + D_{\mathrm{PF}_6^-}\right), \tag{67}$$

which can be obtained by assuming $D_i^{\mathrm{migr,CST}} = D_i^{\mathrm{migr,DST}}$ and combining Eqs. 63 and 64 with Eq. 65. Being $c_{\mathrm{LiPF_6}} = c_{\mathrm{Li}^+} = c_{\mathrm{PF}_6^-}$, we assume a simple exponential dependence of the diffusion coefficients on ion concentration

$$D_{\mathrm{Li}^+} = a_1 \exp(-a_2 c_{\mathrm{Li}^+}) \quad \text{and} \quad D_{\mathrm{PF}_6^-} = a_3 \exp(-a_2 c_{\mathrm{PF}_6^-}). \tag{68}$$

Eqs. 65 and 67 are used to fit the parameters a_1, a_2 and a_3 in Eq. 68 to the concentration dependence of conductivity measured by Nyman *et al.*[134] at 298 K.

For the temperature dependence we will simply assume an Arrhenius-type dependence

$$\sigma = \frac{1}{T} \cdot \sigma_0 \cdot \exp\left(-\frac{E_{\mathrm{act}}}{RT}\right) , \tag{69}$$

where σ_0 is the pre-exponential factor dependent from temperature. We take an activation energy of E_{act} = 17.20 kJ/mol from Zhang *et al.*[135] in the range of –20/+62 °C (see Table 4), which is very similar to the value found by Ecker *et al.*[124] of about 17.12 kJ/mol.

Finally the resulting expressions are, respectively for Li^+ and PF_6^-:

$$D_{\mathrm{Li}^+} = 2.06{\cdot}10^{-10}\ \mathrm{m^2 s^{-1}} \cdot \exp\left(-\frac{c_{\mathrm{Li}^+}}{1000\ \mathrm{mol\ m^{-3}}}\right) \cdot \exp\left(-\frac{17.20\ \mathrm{kJ\ mol^{-1}}}{R}\left(\frac{1}{T} - \frac{1}{298\ \mathrm{K}}\right)\right) \tag{70}$$

$$D_{\mathrm{PF}_6^-} = 4.81{\cdot}10^{-10}\ \mathrm{m^2 s^{-1}} \cdot \exp\left(-\frac{c_{\mathrm{PF}_6^-}}{1000\ \mathrm{mol\ m^{-3}}}\right) \cdot \exp\left(-\frac{17.20\ \mathrm{kJ\ mol^{-1}}}{R}\left(\frac{1}{T} - \frac{1}{298\ \mathrm{K}}\right)\right). \tag{71}$$

We see them being different, due to the relationship expressed in Eq. 66.

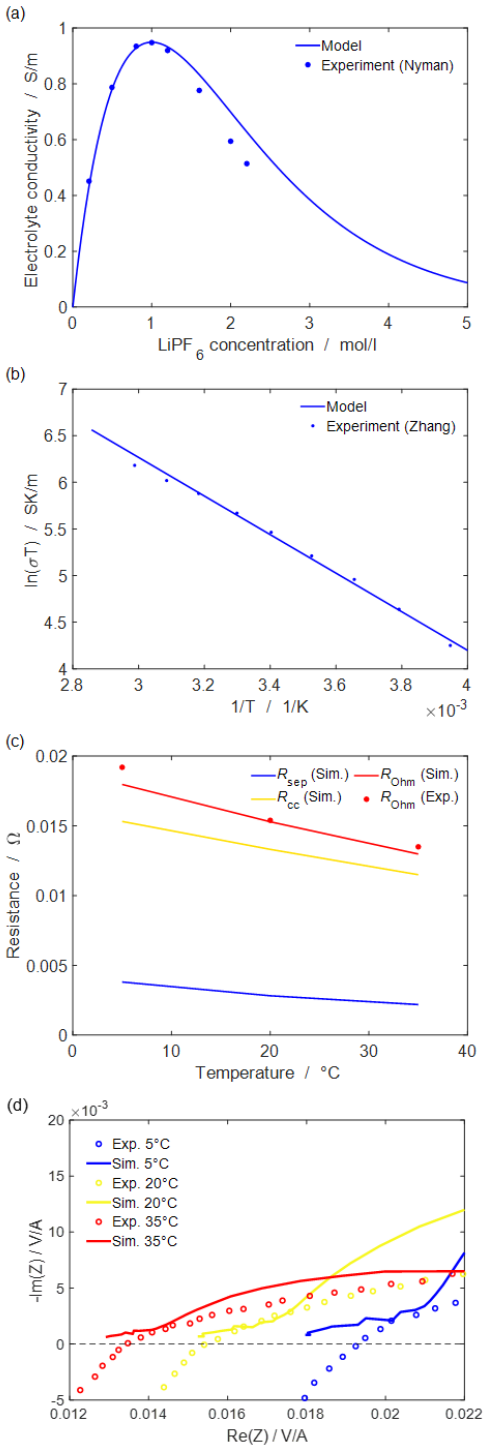

FIGURE 15. ELECTROLYTE CONDUCTIVITY (A) AS FUNCTION OF CONCENTRATION FOR *T* = 298 K (EXPERIMENTS FROM NYMAN *ET AL.*) AND (B) AS FUNCTION OF TEMPERATURE AT *C* = 1 MOL/L (EXPERIMENTS FROM ZHANG *ET AL.*). THE LINES SHOW THE MODEL PREDICTION ACCORDING TO EQS. 70 71 AND 67 (C) OHMIC RESISTANCE R_{Ohm} AS SUM OF R_{sep} AND R_{cc} FOR DIFFERENT TEMPERATURES AT 50 % SOC (D) EXPERIMENTAL AND SIMULATED EIS FOR DIFFERENT TEMPERATURES AT 50% SOC (NYQUIST PLOT). THE EXPERIMENTAL INTERCEPT VALUES AT Y = 0 HAVE BEEN USED TO FIT THE SERIAL RESISTANCE AS FUNCTION OF TEMPERATURE.

Now let's have a look at the results shown in Figure 15. In Figure 15a modelled and experimental electrolyte conductivity is plotted as function of concentration at 298 K: the experimental data were fitted avoiding a polynomial fitting (which would have shown an erroneous increasing of the conductivity at higher

concentrations) and simply modelling D_{Li^+} concentration dependence through application of Eqs. 65 and 67. The fitting is pretty accurate for concentrations < 1.5 mol/l and, as expected, deviates increasingly from experiments for higher concentrations due to the Nernst-Einstein equation being suitable mainly for describing dilute solutions (not the case when c > 1.5 mol/l). The temperature dependence of conductivity at c = 1 mol/l is shown in Figure 15b. The model is able to correctly describe the temperature dependence over a wide range between 253 and 335 K: note this has not been an arbitrary choice, being the most common temperature range for battery use. In the work from Zhang[135], it is actually visible how the slope changes drastically at very low T, due to the heavy changes in battery behaviour at those temperatures. Worth noting that Figure 15b shows here an Arrhenius plot ln(σT) vs 1/T: a linear Arrhenius relation for conductivity is actually correct only if plotting ln(σT) and NOT ln(σ) - as can be erroneously found sometimes in literature. This is due to the proportionality $\sigma \propto \frac{D_i}{RT}$ clearly visible in the Nernst-Einstein equation.

The diffusion coefficients D_i derived until now represent bulk electrolyte properties and must be corrected for porosity $\varepsilon_{\mathrm{elyt}}$ and geometric tortuosity τ_{elyt} as in Eq. 62, with $\tau_{\mathrm{elyt}} = \varepsilon^{-0.25}$ (see 2.2.2). At the separator the initial volume fractions of the three phases (in our model: $\varepsilon_{\mathrm{elyt}}$, $\varepsilon_{\mathrm{separator}}$, $\varepsilon_{\mathrm{gas}}$) have been assumed to be similar to the corresponding volume fractions in Kupper[19,30], with that same value for $\varepsilon_{\mathrm{gas}}$ set equally at both anode and cathode. At the electrodes

$$\varepsilon_{\mathrm{elyt,elde}} = 1 - \sum_i^{i \neq \mathrm{elyt}} \varepsilon_{i,\mathrm{elde}} \ , \tag{72}$$

where $\varepsilon_{i,\mathrm{elde}}$ refers to the volume fractions of the bulk phases included in each electrode (see Table 2).

Now, let's examine the last two panels of Figure 15. Figure 15c shows the simulated and experimental (obtained via EIS - see 4.4.1) resistance R_{Ohm} as well as its contributions R_{sep} and R_{cc} at different temperatures (5 °C, 20 °C and 35 °C). The choice of the correct parameterisation for the ohmic resistance of the current collection system R_{cc} is very important when parameterising the electrolyte model. We assume an empirical temperature dependence according to

$$R_{\mathrm{cc}}(T) = R_{\mathrm{cc}}^0 \cdot [1.0 + \alpha_{\mathrm{cc}} \cdot (T - 293)] \ , \tag{73}$$

where the temperature dependence is described by using a slope α_{cc} with a reference temperature of 293 K. Here the parameters R_{cc}^0 and α_{cc} are obtained by comparing the simulated and experimental ohmic part of the impedance called R_{Ohm} (as a matter of fact, the "real" part of the impedance is called resistance – see 4.3.5.1 to know more about impedance and EIS). In practice, we carried out (both virtually and experimentally) EIS for different temperatures at 50 % SOC, to finally obtain the comparison Nyquist plot shown in Figure 15d (zoom) from which the experimental intercept values at y = 0 have been extracted and used as "guide" to fit the serial resistance R_{cc} as function of temperature. Because R_{Ohm} summarises the losses at the separator R_{sep} due to the electrolyte resistance (with $\lim_{d_{\mathrm{sep}} \to 0} R_{\mathrm{sep}} = 0$) and the losses at the current collection system R_{cc} due to its limited electronic conductivity[137] , to find each of the two contributions we just needed to set the other one equal to 0 according to

$$R_{\mathrm{Ohm}} = R_{\mathrm{sep}} + R_{\mathrm{cc}} \ . \tag{74}$$

The purpose is clearly fitting in the best possible way the experimental R_{Ohm}, with a special attention to the ambient temperature (20 °C) which is set as standard value in our model.

TABLE 5: MESOSCALE: GEOMETRY AND TRANSPORT PARAMETERS OF THE ELECTRODE-PAIR SCALE.

Parameter	Value	Reference
Thickness of cathode	32.9 µm	Measured [34]
Thickness of separator	15.7 µm	Measured [34]
Thickness of anode	49.1 µm	Measured [34]
Tortuosity of cathode τ	1.35	Calculated from Bruggeman relationship
Tortuosity of separator τ	1.21	Calculated from Bruggeman relationship
Tortuosity of anode τ	1.22	Calculated from Bruggeman relationship
Diffusion coefficients $D_{\mathrm{Li^+}}$, $D_{\mathrm{PF_6^-}}$	See Eqs. 70 and 71	See Section 4.3.3
Specific surface area LCO/electrolyte A^{V}	$6.67 \cdot 10^5$ m²/m³	$3\varepsilon_{\mathrm{AM}}/r_{AM}$, r_{AM} from Table 6
Specific surface area NCA/electrolyte A^{V}	$4.28 \cdot 10^6$ m²/m³	$3\varepsilon_{\mathrm{AM}}/r_{AM}$, r_{AM} from Table 6
Specific surface area graphite/electrolyte A^{V}	$2.79 \cdot 10^5$ m²/m³	$3\varepsilon_{\mathrm{AM}}/r_{AM}$, r_{AM} from Table 6
Anode double layer capacitance $C_{\mathrm{DL}}^{\mathrm{V}}$	$1.5 \cdot 10^4$ F·m⁻³	Fitted to EIS data
Cathode double layer capacitance $C_{\mathrm{DL}}^{\mathrm{V}}$	$2.8 \cdot 10^5$ F·m⁻³	Fitted to EIS data
Ohmic resistance of current collection system R_{cc}^0	$3.648 \cdot 10^{-1}$ mΩ·m²	Fitted to EIS data
Slope α_{cc} (ref. T = 293 K)	-0.009	Fitted to EIS data
Electrical conductivity of the SEI layer σ_{SEI}	$1.0 \cdot 10^{-5}$ S/m	Assumed [105]
Graphite stoichiometry range $X_{\mathrm{Li[C_6]}}$ (0…100 % SOC)	0.0180…0.6186	Optimisation [34] – see 4.3.1
LCO stoichiometry range $X_{\mathrm{Li[LCO]}}$ (0…100 % SOC)	0.9922…0.4487	Optimisation [34] – see 4.3.1
NCA stoichiometry range $X_{\mathrm{Li[NCA]}}$ (0…100 % SOC)	0.8033…0.1876	Optimisation [34] – see 4.3.1

Being the separator quite thin (few microns) and having a low tortuosity value, it is not surprising that in Figure 15c R_{sep} looks much lower than R_{cc}. The fitted value of $\alpha_{\mathrm{cc}} = -0.009$ is also slightly negative and all the three resistances tend to decrease with temperature increasing.

All geometrical and transport parameters of the mesoscale (electrode pair) are now summarised in Table 5.

4.3.4 MICROSCALE: THE SOLID-STATE TRANSPORT PARAMETERS

We have now reached the lower of the multiscale levels, the microscale.

The parameters here collected refer to the lithium diffusion inside the three types of AM particles, graphite at the anode and LCO/NCA at the cathode. Hence, two types of parameters are clearly visible in Table 6: the radii and the diffusion coefficients. The radii are geometric parameters and, in the same way as we measured cell dimensions in Table 3, we did similarly with these small quantities, this time using images taken via scanning electron microscopy (SEM)[34] and measuring the average particle size.

Figure 16 shows top-view SEM images of the two electrodes as well as magnified views of two individual particles of the cathode. LCO and NCA particles look very different in their morphology: LCO is totally looking like a "compact stone" while NCA could remind more of a "mixed rice ball" fragmented in very small particles of different sizes, probably as consequence of sample preparation. The variegate morphological dimensions of the

AMs particles led us to ask ourselves if there was a way to reproduce them more accurately, for example by including different radii for each AM, or also if we could somehow reproduce the "fluffy" appearance of NCA. We tried also to vary the tortuosity values beside the classical Bruggeman approach[36], but the results were not improving enough to justify the extra effort and the simulations were at that point much more computationally expensive.

TABLE 6: MICROSCALE: TRANSPORT PARAMETERS OF LITHIUM WITHIN THE AM PARTICLES.

Parameter	Value	Reference
Radius of cathode particles r_{LCO}	$4.5{\cdot}10^{-6}$ m	Measured [34]
Diffusion coefficient of Li in LCO $D_{\mathrm{Li[LCO]}}$	See Figure 16a	Calculated [138] + $E_{\mathrm{act,LCO}}$ =28.95 kJ/mol [139]
Radius of cathode particles r_{NCA}	$0.7{\cdot}10^{-6}$ m	Measured [34]
Diffusion coefficient of Li in NCA $D_{\mathrm{Li[NCA]}}$	See Figure 16b	Measured [140] + $E_{\mathrm{act,NCA}}$ =115.78 kJ/mol [141]
Radius of anode particles $r_{\mathrm{C_6}}$	$1.075{\cdot}10^{-5}$ m	Measured [34]
Diffusion coefficient of Li and graphite $D_{\mathrm{Li[C_6]}}$	See Figure 16c	Measured [142] + $E_{\mathrm{act,C_6}}$ =44.0 kJ/mol [124]

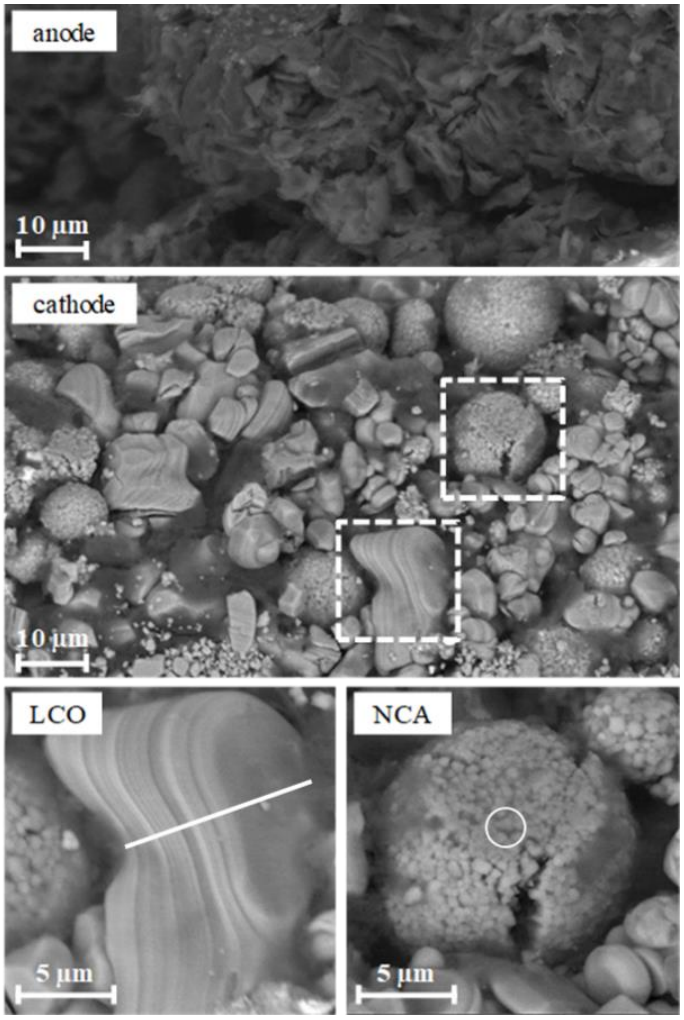

FIGURE 16: SEM MICROGRAPHS OF ELECTRODES HARVESTED FROM THE INVESTIGATED CELL. THE FIGURE IS FROM MAYUR *ET AL.*[34]

Let's concentrate now on the second type of parameters: the bulk diffusion coefficients $D_{\mathrm{Li[AM},i]}$, which are composed of a stoichiometry-dependent part $D^0_{\mathrm{Li[AM},i]}(X_{\mathrm{Li[AM},i]})$ and an Arrhenius-type temperature dependence with activation energy $E_{\mathrm{act,AM}}$

$$D_{\mathrm{Li[AM},i]} = D^0_{\mathrm{Li[AM},i]}(X_{\mathrm{Li[AM},i]}) \cdot \exp\left(-\frac{E_{\mathrm{act,AM}}}{R}\left(\frac{1}{T}-\frac{1}{T_{\mathrm{ref}}}\right)\right). \quad (75)$$

An extended bibliographic research[105,135,141,143–156] was required to choose the suitable parameters and, because values in literature vary strongly, our present choice has been carefully taken after reviewing several sources and considering data completeness. Figure 17 shows diffusion coefficients $D_{\mathrm{Li[AM},i]}$ of intercalated lithium as function of intercalation stoichiometry for the three AMs.

For LCO (Figure 17a) we decided to use as reference the work from Van der Ven[138], in which the LCO diffusion coefficients have been calculated over the complete intercalation stoichiometry range by using first-principles electronic structure methods in combination with Monte Carlo simulations. These data have been obtained at T_{ref} = 27 °C and we set an activation energy of 28.95 kJ/mol as average of the various results obtained from Okubo *et al.*[139].

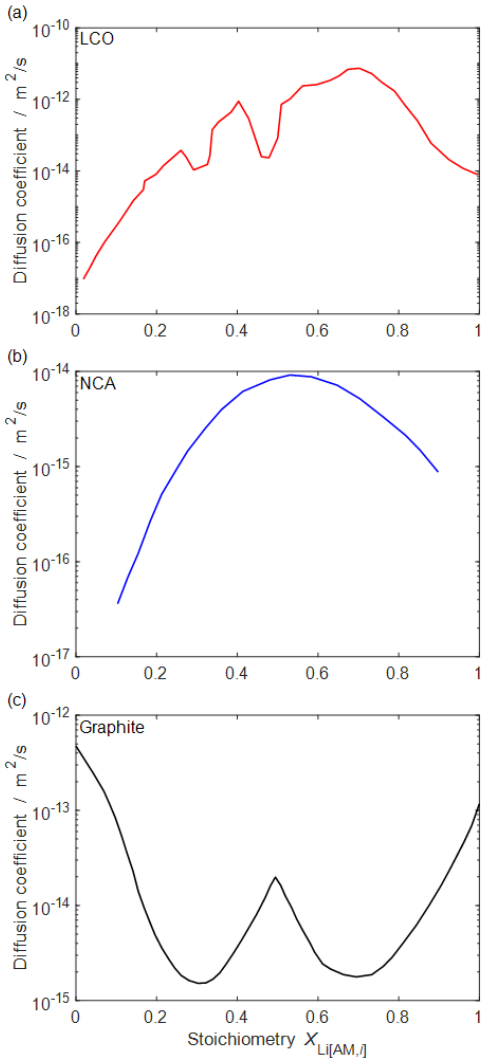

FIGURE 17: SOLID-STATE DIFFUSION COEFFICIENTS OF LITHIUM WITHIN THE THREE AM (A) LCO, (B) NCA, (C) GRAPHITE AT 20 °C.

For NCA (Figure 17b), we chose the work from Dees *et al.*[140], where GITT and EIS experiments at 23 °C have been conducted over a nearly complete intercalation stoichiometry range, and we included the Arrhenius temperature dependence with an activation energy of 115.78 kJ/mol as found by Amin[141].

For graphite (Figure 17c), diffusion coefficients vary greatly according to the characteristics of the material. Finally, we took as reference the work from Levi[142], where the diffusion was investigated using both PITT and EIS techniques, and we went for an activation energy of 44.0 kJ/mol as average between the two values experimentally measured (respectively with GITT - 48.9 kJ/mol - and EIS - 40.8 kJ/mol - methods) in Ecker *et al.*[124].

4.3.5 ELECTROCHEMICAL PARAMETERS

In this short section, we will briefly discuss about the electrochemical parameters (NB this part of the parameterisation has been carried out by M. Quarti).

Three charge-transfer reactions have been implemented in the model, one intercalation/deintercalation reaction for each AM, and they are all shown in Table 7. For each reaction you can here find the exchange current density factor i^{00}, the activation energy $E_{\mathrm{act,f}}$ and the forward reaction symmetry factor α_{f}, according to the following equation already met in Section 2.2.5,

$$i^0 = i^{00} \cdot \exp\left(-\frac{E_{\mathrm{act,f}}}{RT}\right) \cdot \prod_{i=1}^{N_{\mathrm{R}}} \left(\frac{c_i}{c_i^0}\right)^{(1-\alpha_{\mathrm{f}})} \prod_{i=1}^{N_{\mathrm{P}}} \left(\frac{c_i}{c_i^0}\right)^{\alpha_{\mathrm{f}}} . \tag{76}$$

These parameters were obtained by fitting simulated EIS data to experimental values at two different SOC (20 %, 50 %) and three different temperatures (5 °C, 20 °C, 35 °C), while the activation energies were obtained from Arrhenius plots. The resulting values of the double layer capacitances are included in Table 5.

Within the blend cathode, the two electrochemical reactions of LCO and NCA are assumed to take place in parallel, with independent intercalation or deintercalation happening for each one of the individual AM at their own relative rate. Even when the cell is finally put at rest and the overall current gets equal to zero, further inter-particles rearrangement is possible on the *y*-scale to reach equilibrium. We will see that in Section 4.4.2 during our analysis of the P3D distribution of internal states.

TABLE 7: INTERFACIAL CHEMICAL REACTIONS AND RATE COEFFICIENTS, AS OBTAINED FROM FITTING TO EIS EXPERIMENTS. THE SYMMETRY FACTORS ARE ASSUMED.

Interface	Reaction	Exchange current density factor i^{00} / A · m^{-2}	Activation energy $E_{\mathrm{act,f}}$ / kJ·mol^{-1}	Symmetry factor α_{f}
LCO/electrolyte	Li^+[elyt] + e^- + V[LCO] ⇄ Li[LCO]	$8.20 \cdot 10^{12}$	72.32	0.5
NCA/electrolyte	Li^+[elyt] + e^- + V[NCA] ⇄ Li[NCA]	$2.63 \cdot 10^{10}$	61.01	0.5
Graphite/electrolyte	Li^+[elyt] + e^- + V[C_6] ⇄ Li[C_6]	$8.84 \cdot 10^{14}$	77.05	0.5

(NB $\mathrm{Li}[\mathrm{AM}, i]$ represents intercalated lithium and $\mathrm{V}[\mathrm{AM}, i]$ represents vacancies)

4.3.5.1 *Electrochemical Impedance Spectroscopy (EIS)*

We have been mentioning multiple times the EIS until now. But what is EIS, if we had to just explain it simply (if that is possible)? The Electrochemical Impedance Spectroscopy (or just EIS) looks at the impedance characteristics of an electrochemical system over a range of frequencies and, through experimental fitting of the corresponding "equivalent circuit"[137], helps us in obtaining the necessary electrochemical parameters we are looking for. Let's start from the basics.

The electrical resistance *R* is the ability of a circuit element to resist the flow of electrical current and it is defined in the very famous Ohm's law as the ratio between voltage *E* and current *I*

$$R = \frac{E}{I}. \tag{77}$$

That, if we were in an ideal world with ideal resistors which follow Ohm's Law at any conditions and independently from the applied frequency. Very important, the current and voltage signals passing through an ideal resistor are in phase with each other. However, this is the real world and, being the behaviour much more complex, we need to extend the concept of resistance to a more general one, the impedance *Z*. The electrochemical impedance is usually measured by applying an oscillating voltage to an electrochemical cell and then measuring the oscillating current response.

A small excitation signal is sent through the cell

$$E(t) = E_0 \sin(\omega t) \tag{78}$$

where $E(t)$ is the voltage at time t, E_0 is the amplitude of the signal, and ω is the radial frequency. The relationship between radial frequency ω (expressed in radians/second) and frequency f (expressed in hertz) is

$$\omega = 2\pi f\ . \tag{79}$$

As illustrated in Figure 18, in a linear (or pseudo-linear) system, the current response $I(t)$ to a sinusoidal potential will be a sinusoid at the same frequency but shifted in phase φ [157,158]

$$I(t) = I_0 \sin(\omega t + \varphi) \tag{80}$$

and with a different amplitude, I_0. The impedance can therefore be expressed in terms of the magnitude Z_o and the measured phase shift φ as

$$Z = \frac{E(t)}{I(t)} = \frac{E_0 \sin(\omega t)}{I_0 \sin(\omega t+\varphi)} = Z_0 \frac{\sin(\omega t)}{\sin(\omega t+\varphi)}. \tag{81}$$

Now, via Euler's formula

$$e^{(i\varphi)} = \cos\varphi + \mathrm{i}\sin\varphi \tag{82}$$

it is possible to express the impedance using complex numbers (i is the imaginary unit $\sqrt{-1}$). The potential is now described as

$$E(t) = E_0 e^{(\mathrm{i}\omega t)}, \tag{83}$$

and the current response as

$$I(t) = I_0 e^{(i\omega t - \mathrm{i}\varphi)}. \tag{84}$$

The impedance is then represented as a complex number

$$Z(\omega) = \frac{E(t)}{I(t)} = Z_0 e^{(i\varphi)} = Z_0\,(\cos\varphi + \mathrm{i}\sin\varphi), \tag{85}$$

where a real and an imaginary part are both present.

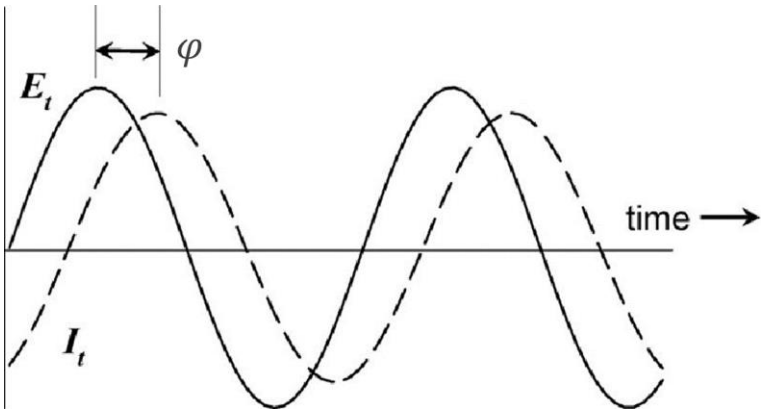

FIGURE 18: PHASE SHIFT φ IN THE OUTPUT CURRENT $I(T)$ WITH RESPECT TO THE INPUT VOLTAGE $E(T)$. THE FIGURE IS FROM DENIZ *ET AL.*[157]

Let's now have a look at Figure 19 (extracted from Ref. [111]). If the real part Re(Z) is plotted on the X-axis and the imaginary part -Im(Z) is plotted on the Y-axis of a chart, we get a "Nyquist Plot" (see Figure 19a), where the low frequency data are plotted on the right side of the plot and the higher frequencies are plotted on the left. In Panel a) you can see multiple EIS curves and for each one of them three distinct features are visible (sometimes semicircles overlap and this can get trickier):

- a small semi-circle at high frequency which corresponds to the anode charge-transfer reaction and double layer
- a larger, overlapping semi-circle at medium frequency which can be assigned to the cathode charge-transfer reaction and double-layer
- a Warburg-type branch at low frequency which indicates the solid-state diffusion of Li^+ in the AM.

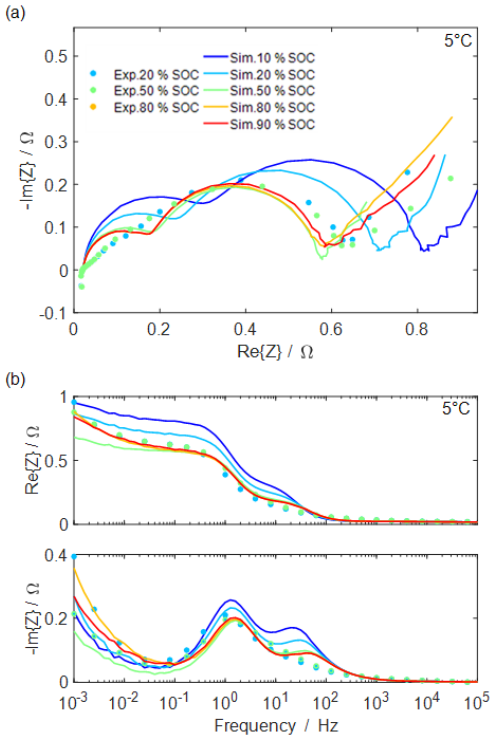

FIGURE 19: EXPERIMENTAL AND SIMULATED ELECTROCHEMICAL IMPEDANCE SPECTRA FOR VARYING SOC AT 5 °C, IN BOTH NYQUIST (A) AND BODE (B) REPRESENTATIONS. THE FIGURE IS FROM REF.[111].

Beside these features, in a Nyquist plot several "points of interest" are also very useful sources of information[159], i.e. R_{Ohm} whose measurement has already been discussed in 4.3.3. Another popular presentation method is the "Bode Plot" (Figure 19b): the impedance is here plotted versus log(*f*) on the X-axis.

4.4 RESULTS AND DISCUSSION

"Curiouser and curiouser!"
(Alice, ***Alice in Wonderland*** by Lewis Carroll)

If until now we have been discussing about parameters and modelling equations, this Section finally will take us into the practical world. We can see how our modelling framework simulates reality, we can compare it with experimental data, we can even step inside the multiscale and have a look at the internal states of the cell during the simulations. This Section, here called "Results and discussion", is always of particularly importance in any study because it could validate all the efforts put in it or simply shatter any hopes of being on the right path. Luckily for us, this last one was not our case.

4.4.1 THERMO-ELECTROCHEMICAL BEHAVIOUR: SIMULATIONS VS EXPERIMENTS

Nothing like a comparison between experiments and simulations can be more of validation for a model. The simulation of the complete thermo-electrochemical behaviour of the cell has therefore been necessary as an ongoing process during parameterisation and as final destination of our journey.

About EIS, simulations were carried out for frequencies from 10^{-3} Hz up to 10^{5} Hz at different SOCs (20 %, 50 % and 80 %) and temperatures (5 °C, 20 °C and 35 °C), then compared with experiments. For each AM, two parameters have been obtained from fitting: the exchange current density factor i^{00} and the activation energy $E_{\mathrm{act,f}}$ for the charge-transfer reaction (see Table 6). In the same way, the double-layer capacitances for both electrodes have been obtained and are listed in Table 5. About the thermo-behaviour of the cell, the temperature of the aluminium plate surface has been recorded during CCCV cycles for different C-rates and temperatures and its fitting has been used to obtain the parameters listed in Table 3.

Note this part of the work has been carried out by M. Quarti, therefore it will be presented in his PhD thesis. The reader is anyway referred to Ref. [111] for a deeper insight (with figures) in the long process behind the EIS and thermo analysis.

What we will show here is the time-domain behaviour. In Figure 20 simulated CCCV discharge-charge cycles are compared with experimental data at three different temperatures (5 °C, 20 °C and 35 °C) and different C-rates. It is worth saying that this has not been a fast process but more than one year was needed to reach these final results, showing a fair agreement with experiments at all C-rates (here 0.05C, 1C, 2C, 5C and 10C) plus a good reproducibility at different temperatures.

But what about the not visible, the internal states?

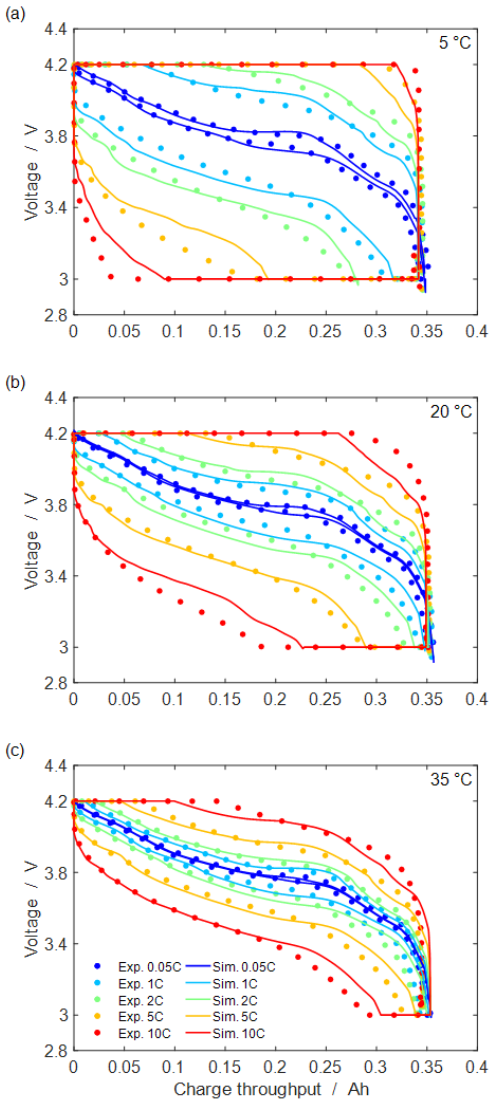

FIGURE 20: EXPERIMENTAL AND SIMULATED CCCV DISCHARGE/CHARGE CYCLES AT (A) 5 °C, (B) 20 °C, (C) 35 °C.

4.4.2 INSIDE THE CELL: P3D DISTRIBUTION OF INTERNAL STATES

Now we will be showing the internal states of the cell, something that cannot be macroscopically seen. All data here shown refer to a specific cycle: 5C CC discharge, 1 h rest, and 5C CCCV (C/20 cut-off) charge at 20 °C ambient temperature, starting from a fully-charged cell.

About the *x* scale, temperature profiles have been obtained and can be found in Ref. [111]. We want instead to focus here more on the *y* and *z* scales, where quite a lot is happening.

Let's start by the mesoscopic scale in Figure 21.

Here we begin analysing what is happening during the CC discharge (here shown in Panels a,b,c) with regard to ion diffusion, ion migration and lithium stoichiometry in the active materials. The concentration of Li^+ and PF_6^- ions (both with identical value, in respect of charge neutrality) in the electrolyte is shown in Figure 21a. During the CC discharge, a gradient is visible between negative electrode (high concentration) and positive electrode (low concentration), which is consistent with the formation and consumption of Li^+, respectively at the anode and at the cathode. A spatial gradient is also visible between the current collector interface and the separator

one for both electrodes, with Li^+ values keeping quite stable during all the CC discharge. Figure 21b shows the normalised electric-potential distribution in the electrolyte. The potential has been normalised to the value at the centre of the separator to make the small gradient (ca. 10-20 mV) visible. The potential is increasing from the positive to the negative electrode, with a spatial gradient visible inside both electrodes and a small temporal gradient towards more negative values present in the most outside layers of the cathode. Added to the diffusive flux originated from the concentration gradient (Figure 21a), Li^+ is here driven by a migration flux in the same direction from the negative to the positive electrode. The potential at the cathode is also slightly getting to more negative values with time, helping the ion migration into the most outside layers of the electrode. For PF_6^- instead, the migration flux due to the potential gradient is and will always be in the opposite direction and cancelled by the diffusive flux, resulting in a net zero flux for the PF_6^- ion. The combined fluxes satisfy both the conditions for charge neutrality and net Li^+ transport. Figure 21c shows the lithium stoichiometry in the active materials (LCO and NCA on the left and graphite on the right). At the positive electrode, the stoichiometry increases (lithium intercalation), while at the negative electrode it decreases (lithium de-intercalation) during all the discharge period. The data show a spatial gradient of the stoichiometry - that is, a spatial distribution of the local SOC - which is more pronounced at the positive electrode for LCO than for NCA, with the highest values close to the separator interface. It is also visible that NCA tends to get charged more slowly than LCO. At the end of the CC discharge, the stoichiometry limits have not yet been reached for all the AMs, as we can see by comparison with the stoichiometry range in Table 5.

A rest phase follows the CC discharge and is illustrated in Figure 21d,e,f. The ion concentration and the electric-potential distribution quickly relax to a spatiotemporally constant value, while slow changes are observed in the lithium stoichiometries in the cathode. These are related to the equilibration of the two blend components (NCA and LCO), which will be further discussed below. At the same time, a small internal spatial rearrangement is visible at the graphite anode from the layers close to the current collector to the ones at the electrode/separator interface.

Figure 21g,h,i shows the behaviour during CCCV charge. For the Li^+ concentration (Figure 21g), the situation is reversed to what seen in Figure 21a, with the high concentration of Li^+ formed at the cathode progressively decreasing to the equilibrium value during the CV phase. A strong spatial gradient is visible between the opposite sides of the electrode, getting smoother with time. At the anode, the low concentration of Li^+ is progressively increasing in a similar way, the current getting lower and the ion consumption rate slowing down to zero. The electric potential (Figure 21h) shows a similar behaviour: the potential gradient progressively returns to zero at both the electrodes, with the Li^+ migration flux from the cathode to the anode adding to the diffusive one observed in Figure 21a. Figure 21i shows the complete de-intercalation of LCO and NCA to the lower stoichiometry limits, while the graphite gets well intercalated at the anode. A spatial gradient is here clearly visible in both electrodes, being present in the graphite anode even at the end of charge, indicating that the cell is not completely equilibrated at end of the CV phase.

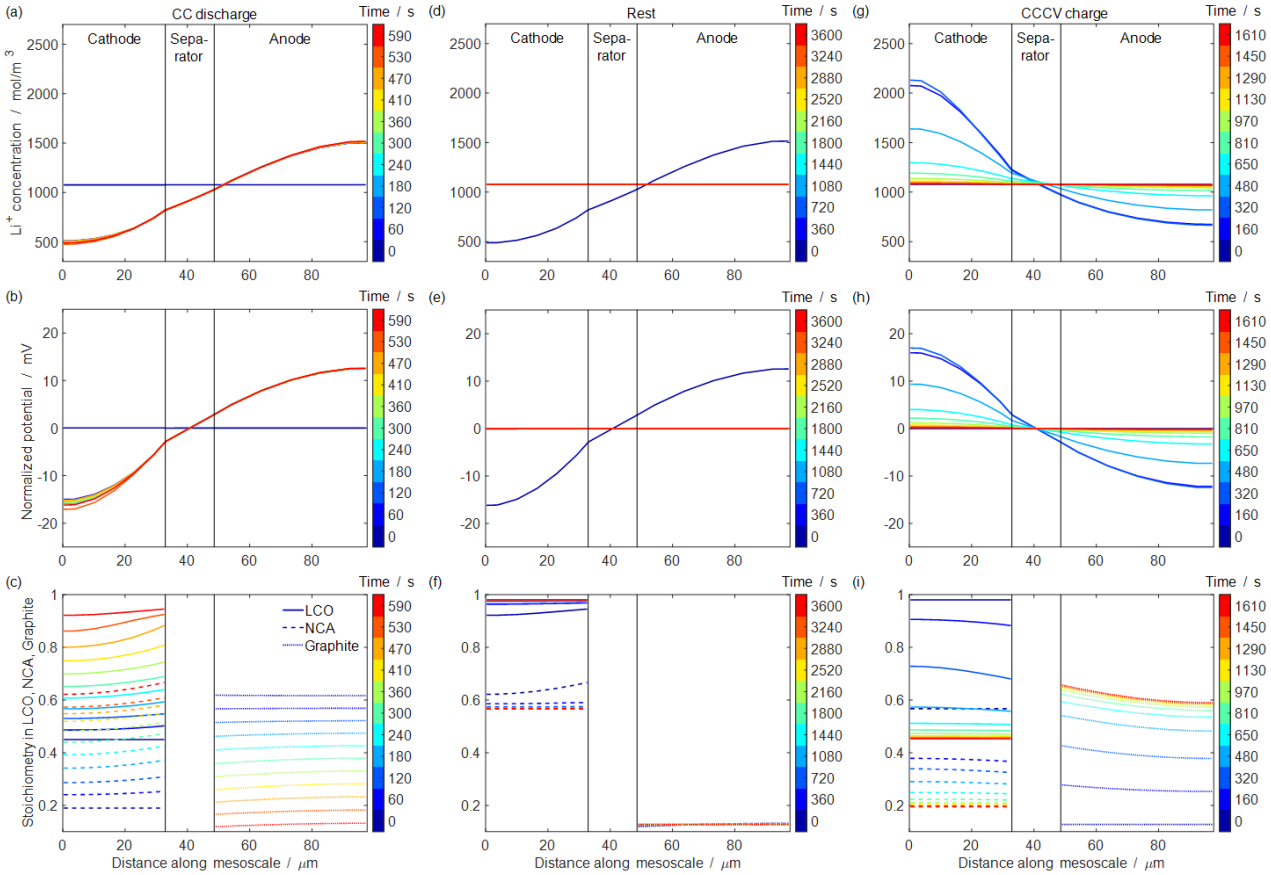

FIGURE 21: MESOSCALE: SIMULATED DISTRIBUTION OF (A) LITHIUM ION CONCENTRATION IN THE ELECTROLYTE, (B) IONIC POTENTIAL OF THE ELECTROLYTE (NORMALISED TO THE CENTRE OF THE SEPARATOR), AND (C) AVERAGE LITHIUM BULK STOICHIOMETRY IN THE AM FOR A 5C CC DISCHARGE, 1 H REST, CCCV CHARGE AT 20 °C.

Let's now have a look at the microscopic scale in Figure 22.

Figure 22 shows the distribution of lithium stoichiometries inside the AM particles. These data were taken for particles close to the electrodes/separator interface (y = 32.9 µm for the cathode and y = 48.6 µm for the anode). During the CC discharge, the distribution of lithium stoichiometry inside LCO (Figure 22a) looks spatially quite uniform for most of the CC discharge but shows some slight gradient with higher values at the particle surface (z = 0 µm) towards the end due to a facile diffusion into the first micrometre. NCA (Figure 22b) also shows a spatially uniform distribution but is only partially intercalated and reaches a maximum stoichiometry of 0.675 at the particle surface, rather inferior to the stoichiometry limits. The stoichiometry of lithium in graphite (Figure 22c) continuously decreases during CC discharge, starting at the particle surface and showing a strong spatial gradient of the stoichiometry with no de-intercalation happening at the centre of the particle (ca. 10 µm).

The rest phase (Figure 22d,e,f) is showing stoichiometry rearrangements both within the particles as well as between the particles in the blend cathode, as similarly seen in Figure 21f at the electrode pair scale. In Figure 22d we see LCO spatial gradient slowly disappearing to reach finally a uniform higher stoichiometry value of 0.98. An equilibrium is reached internally to the positive electrode, with NCA particles (Figure 22e) getting de-intercalated to a spatially uniform lower stoichiometry on behalf of LCO. In graphite (Figure 22f), the lithium

stoichiometry rearranges to reach a spatially uniform value, with a strong decrease in the particle centre on behalf of an increase in the outer regions.

During CCCV charge (Figure 22g,h,i) the behaviour for all the particles is similar to what seen during discharge, however with opposite gradients. Intra- and inter-particle equilibration already starts during the decreasing current of the CV phase. At the end of the CV phase, NCA and LCO are almost under equilibrium, while strong gradients remain within the graphite particles. This spatial gradient and stoichiometry excess happen specifically when cycling at high C-rates and low temperatures, while at milder conditions the intercalated lithium concentration would be distributed more uniformly inside the particles.

A deeper insight into the behaviour of the blend cathode can be found in Ref. [111]. As already noted above while talking about the rest period, LCO and NCA show a complex inter-particle equilibration behaviour. While the graphite shows a linear delithiation/lithiation behaviour upon cycling, the blend cathode shows a dynamic behaviour, with NCA and LCO competing in a sort of "lithiation/delithiation race" (opposite to graphite, obviously) guided by the difference of half-cell potential curves between the two materials. The nonlinear behaviour becomes also more pronounced as the temperature increases.

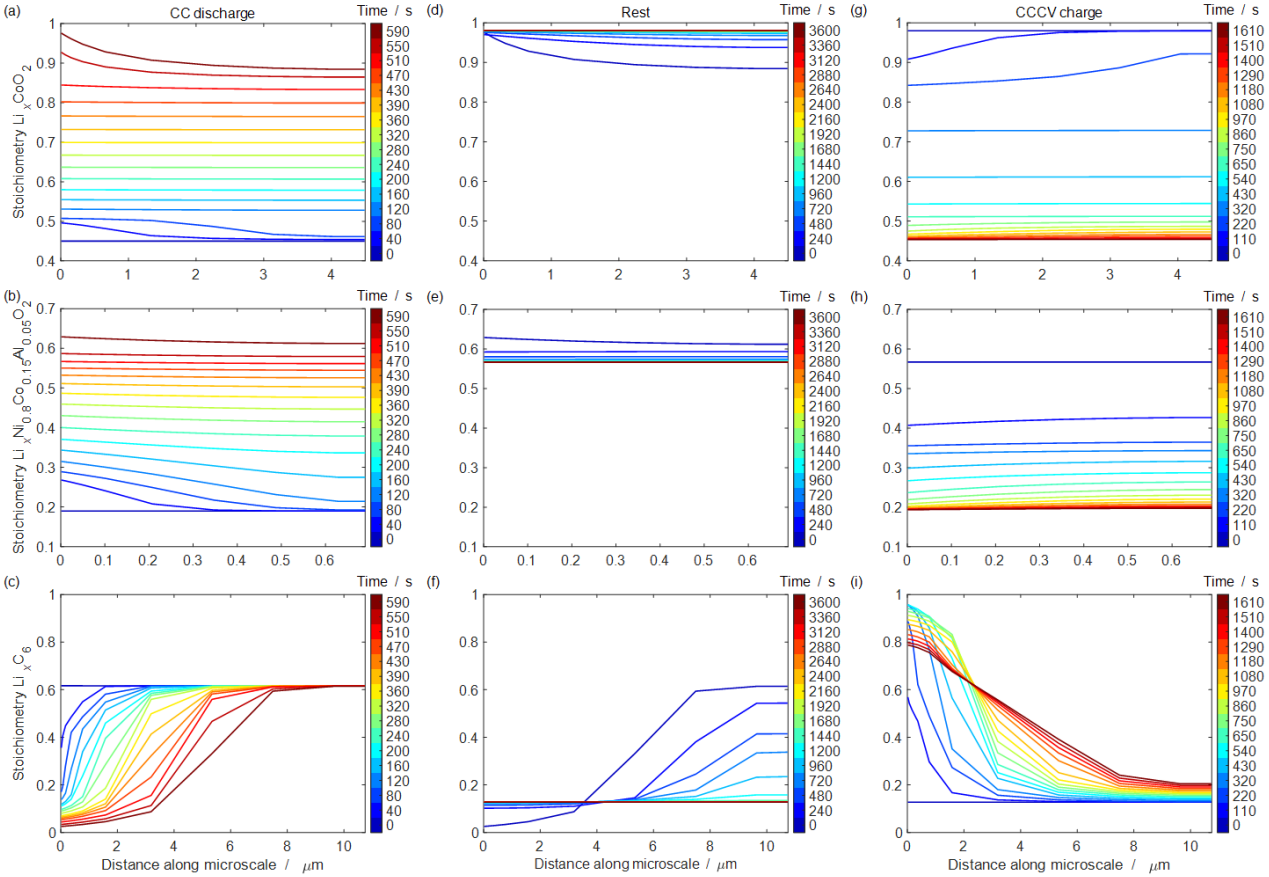

FIGURE 22: MICROSCALE: SIMULATED DISTRIBUTION OF INTERCALATED LITHIUM STOICHIOMETRY INSIDE AM PARTICLES OF (A) LCO, (B) NCA, (C) GRAPHITE FOR A 5C CC DISCHARGE, 1 H REST, CCCV CHARGE AT 20 °C. THE DATA WERE TAKEN FOR PARTICLES CLOSE TO THE ELECTRODE/SEPARATOR INTERFACES.

4.5 CONCLUSIONS AND NEXT STEPS

In the present Chapter, we have discussed the parameterisation and validation of a comprehensive modelling and simulation framework applied to our chosen cell of reference, a commercial 0.35 Ah high-power lithium-ion pouch cell with LCO/NCA blend cathode and graphite anode. This model, built on the theory explained in Chapter 2, is able to describe both multiscale heat and mass transport and complex electrochemical reaction mechanisms, including also as extra feature the capability of reproducing a composite electrode where multiple AMs are subject to intercalation/deintercalation reaction. We used a systematic approach toward parameterisation, starting from equilibrium and then adding transport processes on all three scales as well as electrochemistry, which was accurately validated through experiments in frequency and time domain over a wide range of conditions and explored through detailed simulations of the internal states on the P3D scales.

We have now in our hands a complete "basic" model able to simulate intercalation/deintercalation at the electrodes but we are still far away from reality: as we have seen in Chapter 3, a battery is subject to multiple ageing processes, therefore an "ideal" model, as the one presented here, needs to be furtherly enriched with extensions able to model different electrochemical ageing reactions. Let's go then to the next Chapter, where our model will be extended to include reversible lithium plating (see 3.1.1.2) over a wide range of conditions.

5 UNDERSTANDING LITHIUM PLATING THROUGH A MODELLING APPROACH

"Nothing in life is to be feared.
It is only to be understood."
(Marie Curie)

Chapter 5 refers to the work done in the second part of the PhD and illustrated in the third paper "Prediction of reversible lithium plating with a pseudo-3D lithium-ion battery model"[78]: as better explained later, this Chapter is actually an extension of the previous one and the reactions and mechanisms here presented are an adding to the model illustrated in Chapter 4.
There is a practical reason behind all this extra effort, obviously: the study and comprehension of the formation of metallic lithium (a.k.a. lithium plating, as already introduced in 3.1.1.2) on the anode surface is at the moment one of the key challenges for the energy and automotive industry[101]. This degradation process damages the mechanical and chemical integrity of the electrode, causing capacity fade and heavily affecting the possibility of a fast charging[160]. In case of cumulative plating, dendrites could even form and pierce the separator, creating an electrical short circuit and a consequent fire hazard[79,80].
Worth noting that it is also very difficult to simply detect lithium plating *in situ* without a direct observation of the open electrode via microscopy techniques, hence opening and breaking the battery itself. An analytical and more theoretical approach in this case comes in help, via observation of the changes in the cell voltage behaviour during charge/discharge cycles under plating conditions and detection of some peculiarities commonly considered as "plating hints". On the other hand, as we will see in Section 5.4, "absence of evidence is not evidence of absence"[101], as inhomogeneities in the cell could smear indeed the plating hints up to extinction[95] and, in case of a fast-chemical intercalation (or accelerated side reactions – see 5.2.3) the quantity of plated lithium available for stripping could be under the limits of detection[161]. One of the advantages of the modelling and simulation approach is also the possibility of studying all these mechanisms and having a detailed insight of the spatiotemporal behaviour in the internal states of the battery at the different scales (meso and micro).

5.1 AN OLD MODEL, A NEW MODEL

"Mixing one's wines may be a mistake, but old and new wisdom mix admirably."
(Bertolt Brecht)

The modelling framework here introduced can be considered an extension of the "Kokam model" exposed in the previous Chapter. Let's see what's old and what's new, always keeping an eye on Figure 23.

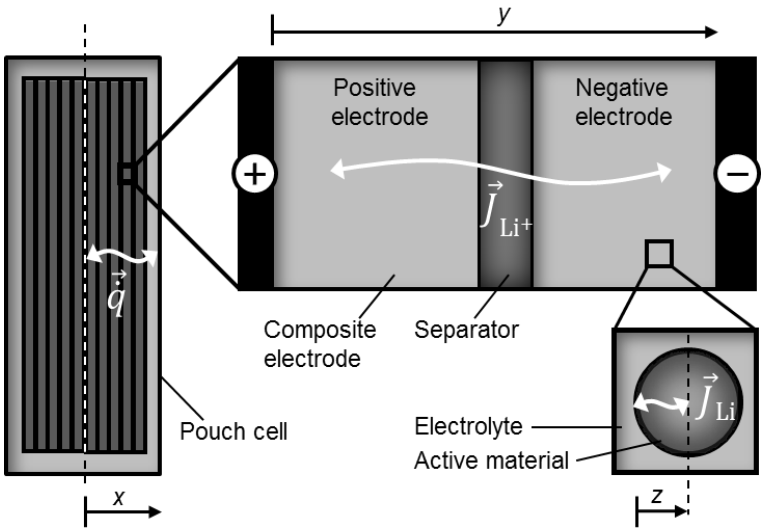

FIGURE 23: SCHEMATIC REPRESENTATION OF 1D+1D+1D (PSEUDO-3D, P3D) MODELING DOMAIN.

OLD

- The transport processes and model equations: see Chapter 2
- The multiscale approach: as shown in Figure 23, it's again a 1D+1D+1D (P3D) multiscale modelling domain. The transport scales combine heat transport through the cell thickness (*x* scale), mass and charge transport inside the liquid electrolyte (*y* scale), and diffusive mass transport in AM particles (*z* scale). Upscaling, boundary conditions and electrochemistry obviously follow
- The cell (a commercial 350 mAh high-power lithium-ion pouch cell with graphite at the anode and NCA/LCO blend at the cathode): see Chapter 4

NEW

- The heat transport is here assumed symmetrical to the centre of the cell ($x = 0$): see Section 2.2
- The cell surface is exposed to ambient air without aluminium holder plates: see Figure 10 for comparison. Thus, the heat transfer coefficient α has been modified on purpose (now 30 $W \cdot m^{-2} \cdot K^{-1}$)
- The "ageing challenge"!

The "ageing challenge" is the main point of this Chapter. We have already introduced the degradation process universally known as lithium plating in Section 3.1.1.2: now it's time to include it in our modelling framework.

5.2 Enter the Plating

"The best scientist is open to experience and begins with romance - the idea that anything is possible."
(Ray Bradbury)

5.2.1 PLATING THERMODYNAMICS

The first step for building an extended model is the adding of all the missing reactions whose effects we want to be included in our modelling framework. In the "Kokam model" described in Chapter 4, only intercalation/deintercalation at the electrodes is happening and no parasitic reactions have been included. Here in Chapter 5 we will now introduce lithium plating in the form of a single-electron charge-transfer reversible reaction[43]

$$\mathrm{Li^+[elyt]} + \mathrm{e^-[elde]} \rightleftharpoons \mathrm{Li[metal]}\ , \tag{86}$$

where Li[metal] represents plated lithium, with a constant density of 534 g/cm^3 [162]. Eq. 86 is formulated as a global reaction, even if microkinetically the formation of plated lithium could more probably consist of a combination of multiple consecutive or parallel elementary reaction steps. The equilibrium potential of this reaction, $\Delta\phi_{\mathrm{Li}}^{\mathrm{eq}}$, is often assigned a canonical value of 0 V vs Li/Li$^+$ [83,84,163] in literature, an easy approach not without several pitfalls. One does not simply choose a value because it is the simplest solution, we could say: firstly, it has to be ensured that the graphite half-cell potential ($\Delta\phi_{\mathrm{LiC6}}^{\mathrm{eq}}$ as function of intercalated lithium stoichiometry) used as model input has the correct potential reference of 0 V vs. Li/Li$^+$, which means it should use lithium metal as reference electrode; secondly, $\Delta\phi_{\mathrm{Li}}^{\mathrm{eq}}$ is not only not always equal to 0 but also it does not stay constant, depending on operating conditions as temperature, pressure, concentration of all involved species and, as we will see later on, cell current (affecting local Li$^+$ concentration). No worries, we will demonstrate and discuss all these points.

The concentration dependence of $\Delta\phi_{\mathrm{Li}}^{\mathrm{eq}}$ in our model is described by the Nernst equation

$$\Delta\phi_{\mathrm{Li}}^{\mathrm{eq}} = -\frac{\Delta G^0(p,T)}{zF} - \frac{RT}{zF}\cdot\ln\left(\prod_{i=1}^{N_{\mathrm{R}},N_{\mathrm{P}}}\left(\frac{c_i}{c_i^0}\right)^{\nu_i}\right)\ , \tag{87}$$

where $\Delta G^0(p,T)$ is the standard Gibbs energy of reaction, which is a function of pressure (here assumed as constantly atmospheric) and temperature, but not of concentration; in fact, it is defined for standard concentrations c_i^0 (consequently, the concentration-dependent term vanishes for $c_i = c_i^0$) while assuming that the activity equals the concentration c_i (activity coefficient of unity for all species). While for $\mathrm{Li^+[elyt]}$ this is likely a simplifying assumption, being well-known that the concentrated electrolytes used in lithium-ion batteries behave non-ideally[44], for Li[metal], the assumption is reasonably valid, with the activity value set to zero in our model if the solid phase vanishes. The Gibbs energy of reaction $\Delta G^0(T)$ can be obtained from the standard-state chemical potentials μ_i^0 of all species i involved in the plating reaction according to

$$\Delta G^0(T) = \sum_{i=1}^{N_{\mathrm{R}},N_{\mathrm{P}}}\nu_i\mu_i^0(T)\ , \tag{88}$$

and the standard-state chemical potentials can be calculated from the molar enthalpies, $h_i^0(T)$, and molar entropies, $s_i^0(T)$, according to

$$\mu_i^0(T) = h_i^0(T) - Ts_i^0(T)\ . \tag{89}$$

Consequently, molar thermodynamic parameters are needed for the involved species Li[metal], $\mathrm{Li^+[elyt]}$, and $\mathrm{e^-[elde]}$. Molar enthalpies, entropies and heat capacities as function of temperature can be found for a large number of compounds in the NASA thermochemical tables[126], which provide the following polynomial functions:

$$\frac{h^0(T)}{RT} = a_1 + a_2\frac{(T/\mathrm{K})}{2} + a_3\frac{(T/\mathrm{K})^2}{3} + a_4\frac{(T/\mathrm{K})^3}{4} + a_5\frac{(T/\mathrm{K})^4}{5} + \frac{b_1}{(T/\mathrm{K})} \tag{90}$$

$$\frac{s^0(T)}{R} = a_1 \ln(T/\mathrm{K}) + a_2(T/\mathrm{K}) + a_3\frac{(T/\mathrm{K})^2}{2} + a_4\frac{(T/\mathrm{K})^3}{3} + a_5\frac{(T/\mathrm{K})^4}{4} + b_2 \quad (91)$$

$$\frac{c_p^0(T)}{R} = a_1 + a_2(T/\mathrm{K}) + a_3(T/\mathrm{K})^2 + a_4(T/\mathrm{K})^3 + a_5(T/\mathrm{K})^4 \quad (92)$$

where, $T^0 = 298.15\ \mathrm{K}$ is the standard temperature and $c_{p,i}^0$ the molar heat capacity. For crystalline metallic lithium Li[metal] [164], $a_1 = 6.10909942 \cdot 10^{-1}$, $a_2 = 1.41041217 \cdot 10^{-2}$, $a_3 = -1.74958170 \cdot 10^{-5}$, $a_4 = -3.33741023 \cdot 10^{-8}$, $a_5 = 7.76629665 \cdot 10^{-11}$, $b_1 = -6.25121208 \cdot 10^2$, $b_2 = -3.26449947 \cdot 10^0$. Once substituted these values in the Eqs. 90, 91 and 92 at a standard temperature of 298.15 K, we finally obtain the respective values of $h^0_{\mathrm{Li[metal]}} = 0$ (thermodynamic reference for pure elements), $s^0_{\mathrm{Li[metal]}} = 29.12\frac{\mathrm{J}}{\mathrm{K\cdot mol}}$, and $c^0_{p,\mathrm{Li[metal]}} = 24.86\frac{\mathrm{J}}{\mathrm{K\cdot mol}}$. Worth noting that these values are given for crystalline "isolated" lithium, while for plated lithium on graphite particles (which is our case) the thermodynamic parameters may differ significantly. The molar thermodynamic properties of dissolved lithium ions in lithium-ion battery electrolytes, $\mathrm{Li^+[elyt]}$, are unavailable in literature, being the absolute thermodynamic values for dissolved ions subject of controversy even for the most simple system, that is protons in aqueous solution[165,166]. We can assume $\mathrm{Li^+[elyt]}$ as reference species and assign $h^0_{\mathrm{Li^+[elyt]}} = 0$ and $s^0_{\mathrm{Li^+[elyt]}} = 0$: the reason is that, being $\mathrm{Li^+[elyt]}$ the only ion involved in the intercalation/deintercalation and plating reactions, its behaviour affects them in the same way and only relative values are needed. A standard entropy of zero is also used in aqueous electrochemistry as reference ($s^0_{\mathrm{H^+[H_2O]}} = 0$) [167], therefore it is reasonable to use a similar reasoning for lithium-ion battery electrolytes and for electrons ($h^0_{\mathrm{e^-[elde]}} = 0$ and $s^0_{\mathrm{e^-[elde]}} = 0$).

Once defined all these parameters, we can now obtain $\Delta\phi^{\mathrm{eq}}_{\mathrm{Li}}$ from Eq. 87 as function of temperature and lithium-ion concentration: the results are shown in Figure 24a for concentrations $c_{\mathrm{Li^+[elyt]}}$ from 0.5 to 2 M and temperatures from -20 to 30 °C, with the values plotted relative to the $\Delta\phi^{\mathrm{eq}}_{\mathrm{Li}}$ value at 25°C and a $\mathrm{Li^+}$ concentration of 1 M (assumed as reference conditions for $\Delta\phi^{\mathrm{eq}}_{\mathrm{Li}} = 0$). As shown here, the $\Delta\phi^{\mathrm{eq}}_{\mathrm{Li}}$ is not constant at 0 V but varies according to the operating conditions, with higher salt concentration heightening the equilibrium potential at which lithium plating occurs: this quite evident behaviour, clearly visible in Figure 24b at T = 30 °C, has also been shown experimentally with a linear behaviour of $\Delta\phi^{\mathrm{eq}}_{\mathrm{Li}}$ vs. $\ln c_{\mathrm{Li^+}}$ observed for concentrations ≤ 1 mol/l [168]. For concentrations between 0.5 and 2 M it varies by 34 mV at 30 °C and by 28 mV at -20 °C, showing how much small is in reality the influence of temperature, with no difference at 0.5 M for temperatures between -20 and 30 °C and the spread increasing to a maximum of only 5.2 mV at 2 M.

Although the results show that the plating thermodynamics significantly depend on operating conditions, even more important is the interplay between plating and intercalation, the last included in our model according to

$$\mathrm{Li^+[elyt]} + \mathrm{e^-[elde]} + \mathrm{V[C_6]} \rightleftharpoons \mathrm{Li[C_6]}\ . \quad (93)$$

Here the thermodynamics of the intercalation reaction depends on lithium ion concentration, temperature and, differently from plating, also intercalated lithium stoichiometry.

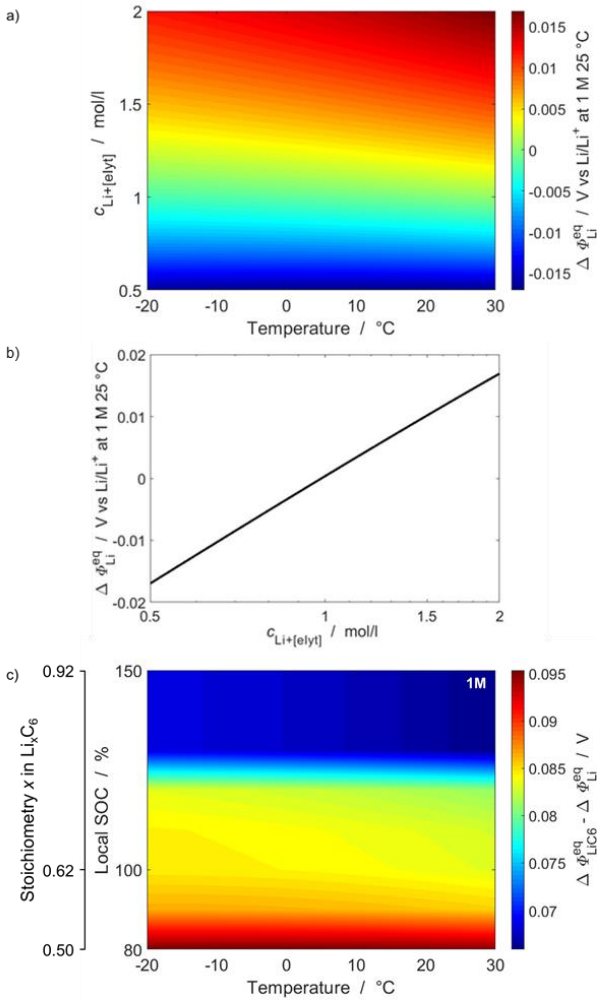

FIGURE 24: A) EQUILIBRIUM POTENTIAL $\Delta\Phi_{Li}^{eq}$ FOR $c_{Li^+[elyt]}$ FROM 0.5 TO 2 M AND TEMPERATURES FROM -20 TO 30 °C. THE VALUES ARE PLOTTED RELATIVE TO THE VALUE AT 25 °C AND 1 M (REFERENCE CONDITIONS FOR $\Delta\Phi_{Li}^{eq} = 0$); B) EQUILIBRIUM POTENTIAL $\Delta\Phi_{Li}^{eq}$ FOR $c_{Li^+[elyt]}$ FROM 0.5 TO 2 M AT 30 °C: HIGHER SALT CONCENTRATION HEIGHTENS $\Delta\Phi_{Li}^{eq}$ VALUE; C) EQUILIBRIUM POTENTIAL DIFFERENCE $\Delta(\Delta\Phi) = \Delta\Phi_{LiC6}^{eq} - \Delta\Phi_{Li}^{eq}$ FOR TEMPERATURES VARYING FROM -20 TO 30 °C AND SOC FROM 80 TO 150 %.

As previously discussed in 4.3.1, experimental half-cell curves from literature (voltage as function of lithium stoichiometry using lithium metal as counter electrode) have been used to derive molar enthalpies and entropies of the intercalation compound, with the same thermodynamic data of Li[metal] used to subtract out the influence of the lithium counter electrode[47] (that is subtracting $s^0_{Li[metal]} = 29.12$ J·mol^{-1}·K^{-1}). This modelling and parameterisation of $h^0_{Li[C_6]}$, $s^0_{Li[C_6]}$, $h^0_{V[C_6]}$ and $s^0_{V[C_6]}$ is explained in details in Ref. [47] while the used self-consistent parameters can be found in Section 4.3.

As plating and intercalation are competing reactions, Figure 24c shows the equilibrium potential difference $\Delta(\Delta\phi) = \Delta\phi^{eq}_{LiC6} - \Delta\phi^{eq}_{Li}$ as function of temperature varying from -20 to 30 °C and as function of state of charge (SOC) of the graphite from 80 to 150 % (and stoichiometry, where $X_{Li[C6]} = 0.619$ corresponds in our model to SOC 100 % - see Table 5). The choice of this SOC range is well motivated by overlithiation being one of the conditions in which lithium plating is most likely to happen. $\Delta(\Delta\phi)$ shows a high dependence on SOC (hence dependence on concentration and applied C-rate) and is always positive, varying between approx. 65 and 95 mV

within the investigated parameter ranges (84 mV at SOC 100 %) which tells us that, under equilibrium conditions, intercalation will always be favoured over plating. Again, the dependence on temperature looks quite small. Finally, $\Delta(\Delta\phi)$ has proven to be independent of the lithium ion concentration, because of $c_{\mathrm{Li}^+[\mathrm{elyt}]}$ affecting the thermodynamics of both reactions in the same way[168,169]: this means that even if the data shown in Figure 24c have been calculated for $c_{\mathrm{Li}^+[\mathrm{elyt}]}$ = 1 M (the reference concentration in our model), we could obtain the same colourmap at any other $c_{\mathrm{Li}^+[\mathrm{elyt}]}$ value.

5.2.2 PLATING KINETICS

In the last Section we have been exploring the thermodynamics of the plating reaction and we demonstrated how the commonly accepted condition $\Delta\phi_{\mathrm{Li}}^{\mathrm{eq}}$= 0 V vs Li/Li$^+$ for the plating has proven to be very simplistic. Actually, the fact of using only a thermodynamic condition for plating ignores the kinetics of the reaction, as the assumption $\Delta\phi_{\mathrm{an}} < \Delta\phi_{\mathrm{Li}}^{\mathrm{eq}}$ (hence in literature $\Delta\phi_{\mathrm{an}} \leq 0$) does not necessarily induce plating if it is kinetically hindered. As we will see later on, at low temperatures, which are usually seen to support plating, both the intercalation and the plating reactions are kinetically affected and the competition between them becomes much more complex than expected. Both the electrochemical reactions in our model are in fact expressed in the (already met in 2.2.5) Butler-Volmer form

$$i = i^0 \left[\exp\left(\frac{\alpha_{\mathrm{c}} zF}{RT}\eta_{\mathrm{act}}\right) - \exp\left(-\frac{(1-\alpha_{\mathrm{c}})zF}{RT}\eta_{\mathrm{act}}\right)\right] \tag{94}$$

with the exchange current density

$$i^0 = i^{00} \exp\left(-\frac{E_{\mathrm{act}}}{RT}\right) \cdot \prod_{i=1}^{N_R}\left(\frac{c_i}{c_i^0}\right)^{(1-\alpha_{\mathrm{c}})} \prod_{i=1}^{N_P}\left(\frac{c_i}{c_i^0}\right)^{\alpha_{\mathrm{c}}} , \tag{95}$$

where i^{00} is assumed constant. Similar as for the Nernst equation (Eq. 87) this formulation is based on the simplifying assumption that activities are equal to concentrations (unity activity coefficients). By looking at these equations, we can see that both the intercalation and the plating reactions are potential-driven (i.e. reaction rates increase with decreasing potential – look at the overpotentials η_{act} in Eq. 94), thermally-activated (i.e reaction rates decrease with decreasing temperature – this is regulated by the Arrhenius part in Eq. 95), and concentration-influenced (i.e. reaction rates depend on $\mathrm{Li}^+[\mathrm{elyt}]$ and $\mathrm{Li}[\mathrm{C}_6]$ concentrations – the last terms of Eq. 95). In the model both reactions take place in parallel, one as the main reaction and the other as the parasitic one, the two competing for electrons and lithium ions: the relative kinetics therefore decide which one will dominate. An accurate parameterisation of the new mass-action kinetics parameters i^{00}, E_{act} and α_{c} for the plating reaction is therefore required in order to simulate the competition mechanism, while the parameters of the intercalation reaction stay the same of the "Kokam model" discussed in Chapter 4. An extended bibliographic research was required to choose suitable parameters for the plating kinetics, having only few papers been published with a full set of values for both the intercalation and plating reactions.

Table 9 offers a (hopefully comprehensive enough!) collection of the available plating parameters in literature, which seem to vary strongly depending on different measurement techniques, used materials, or modelling purposes. The exchange current density, the activation energy, and the cathodic symmetry factor for the plating reaction are shown together with the different forms of the Butler-Volmer equation used (NB these BV forms

are fruit of a long "conversion job" from the original forms in the respective cited studies to facilitate the comparison with our chosen BV form – that's how most of the parameters values, not explicitly written down in those papers, could be obtained and then listed in this table). Where available, the intercalation kinetics are also included, because the ratio of intercalation vs. plating rate is an additional indicator on the consistency of the parameters. A detailed analysis of the strong relationship between different electrolyte compositions and lithium deposition kinetics can be found in some of the works[170–172] here listed . As you can see, some of the studies are based on modelling, others are purely experimental and used a wide range of different measurement techniques: worth noting that the plating kinetics is strongly influenced not only by these last ones, but also by the electrode characteristics in terms of dimensions[173] and morphology[174]. Hence, we can see that the wide range of values reported in the table covers a wide range of conditions and cases. About the cathodic symmetry factor $\alpha_{c,Li}$, Table 9 shows that only two values are mainly used: a value of approx. 0.7 with reference to the experimental work of Verbrugge[173] and the renowned mathematical modelling work of Arora[82], and a value of approx. 0.5 in many experimental works. The exchange current densities, however, scatter over many orders of magnitude, from 0.001 A/m^2 to 1200 A/m^2, with the most extreme values coming from modelling work (so extreme that are defined there as "assumed", or as we could better say here "specially created for that purpose"), while experimental data range "only" from 0.084 A/m^2 to 316 A/m^2. Arora[82] explains the large variation in the values reported in literature with the difference in the surface conditions of the Li/Li cells under study and chooses as exchange current density the "standard" value of 10 A/m^2 reported in Jasinski[175] and Meibuhr[171] in the 1970s. Excluding the high value found in Verbrugge[173] for an ultrahigh-rate lithium deposition on a microelectrode, the highest values found experimentally were obtained by Tao[170] and Ecker[95] (approx. 20 A/m^2).

It is also interesting to compare the plating and the intercalation kinetics. In most of the studies where the exchange current density is available for both reactions (most but not all: see the exception in Ge[176]), the exchange current density of the plating reaction at room temperature happens to be around 10-25 times higher than that of intercalation, while the activation energies are in a similar range. In Table 9 only two works, very different from each other, are listed in which a full set of parameters is available, both for plating and intercalation reactions: the first is from Ge[176] and the second one is from Ecker[95] . Let's have a look at them.

In Ge[176] the plating reaction exchange current has been seen gradually increasing with the SOC mainly due to the decreasing equilibrium potential of graphite, with its absolute value generally being smaller than that of intercalation current because of its smaller exchange current density (0.17 A/m^2 vs 1.17 A/m^2 at 25 °C). The ratio i^0_{Li}/i^0_{LiC6} gets affected by the temperature: i^0_{LiC6} is actually bigger than i^0_{Li} with a ratio of about 0.15 at 25 °C, but at lower temperatures i^0_{LiC6} experiences a faster decrease than i^0_{Li} reaching a ratio of about 0.36 at -30 °C. The smaller activation energy of the plating exchange current density makes the plating reaction remarkably more competitive at low temperatures and favours the unwanted formation of lithium metal.

The second work is the one from Ecker[95]. A Li/Li coin cell, which consisted of two metallic lithium foils and a separator coming from a 7.5 Ah high-energy Kokam cell together with 1M $LiPF_6$ in EC/EMC (1:1 wt) electrolyte, has been used for the model parameterisation in the study. Because of these similarities with our reference cell, we found these plating kinetic parameters the most appropriate to be chosen; hence we decided to virtually build a simple "flat Li/cathode model" to simulate Ecker's experimental set-up.

The following features:

- At the anode, $\varepsilon_{\mathrm{elyt}} = 0.5$ and $\varepsilon_{\mathrm{Li}} = 0.5$, with the single plating reaction restricted at the electrode/separator interface
- Flat electrode surface with A^{V} = 1 m^{-1}
- Electrode area $A = 2.01 \cdot 10^{-4}$ m^2 (from Ecker, for a Li/Li coin cell with d = 16mm)
- Intercalation reaction at the anode switched off (extremely slow and not competitive)
- Deintercalation reaction at the cathode set as extremely fast (set as reference electrode)

have been included in this basic modelling framework. The value of i_{Li}^{00} to be inserted for the plating reaction $\mathrm{Li}^+ + \mathrm{e}^- \rightleftharpoons \mathrm{Li}$ was obtained from Eq. 95, according to

$$i_{\mathrm{Li}}^{0} = i_{\mathrm{Li}}^{00} \exp\left(-\frac{E_{\mathrm{act,Li}}}{RT}\right) \cdot \left(\frac{c_{\mathrm{Li}^+}}{c_{\mathrm{Li}^+_{\mathrm{ref}}}}\right)^{(1-\alpha_{\mathrm{c,Li}})} \left(\frac{c_{\mathrm{e}^-}}{c_{\mathrm{e}^-_{\mathrm{ref}}}}\right)^{(1-\alpha_{\mathrm{c,Li}})} \left(\frac{c_{\mathrm{Li}}}{c_{\mathrm{Li}_{\mathrm{ref}}}}\right)^{\alpha_{\mathrm{c,Li}}} \tag{96}$$

where $\left(\frac{c_i}{c_{i_{\mathrm{ref}}}}\right) = 1$ for $\mathrm{e}^-$and Li. Note that $c_{\mathrm{Li}^+_{\mathrm{ref}}}$ is also equal to 1 and c_{Li^+} value is equal to its molar fraction $X_{\mathrm{Li}^+} = 0.07$. Thus, once substituted the values above (given by Cantera) and the values in Table 9 for Ecker at 23°C, we have $20.4\ \mathrm{A/m^2} = i_{\mathrm{Li}}^{00} \exp\left(-\frac{65000\ \mathrm{J/mol}}{8.314 \frac{\mathrm{J}}{\mathrm{K\ mol}} \cdot 296.15\ \mathrm{K}}\right) \cdot (0.07)^{(1-0.492)}$ and $i_{\mathrm{Li}}^{00} = 2.2932 \cdot 10^{13}$ A/m^2. Once inserted i_{Li}^{00} in our "flat Li/cathode model", the R_{ct} value extracted from the simulated EIS Nyquist plot finally enters the following "practical" equation

$$i_{\mathrm{Li}}^{0} = \frac{R \cdot T}{z \cdot F \cdot A_{\mathrm{e}} \cdot R_{\mathrm{ct}}}, \tag{97}$$

which is nothing else than a mathematically approximated derivation of Eq.94 for $(\frac{zF}{RT}\eta_{\mathrm{act}}) = x$ and $\mathrm{e}^x = (1 + x)$. The resulting i_{Li}^{0} equals 20.4 A/m^2 , i.e. the value found by Ecker in Table 9, and also validates the use of this simple modelling framework for simulating an experimental Li/Li coin cell.

With a similar process but without having to look for new parameters, we can calculate i_{LiC6}^{0} for the intercalation reaction in our model $\mathrm{Li}^+ + \mathrm{e}^- + \mathrm{V[C_6]} \rightleftharpoons \mathrm{Li[C_6]}$ from Eq. 95, according to

$$i_{\mathrm{LiC6}}^{0} = i_{\mathrm{LiC6}}^{00} \exp\left(-\frac{E_{\mathrm{LiC6}}^{\mathrm{act}}}{RT}\right) \cdot \left(\frac{c_{\mathrm{Li}^+}}{c_{\mathrm{Li}^+_{\mathrm{ref}}}}\right)^{(1-\alpha_{\mathrm{c}})} \left(\frac{c_{\mathrm{e}^-}}{c_{\mathrm{e}^-_{\mathrm{ref}}}}\right)^{(1-\alpha_{\mathrm{c}})} \left(\frac{c_{\mathrm{V[C_6]}}}{c_{\mathrm{V[C_6]_{ref}}}}\right)^{(1-\alpha_{\mathrm{c}})} \left(\frac{c_{\mathrm{Li[C_6]}}}{c_{\mathrm{Li[C_6]_{ref}}}}\right)^{\alpha_{\mathrm{c}}} \tag{98}$$

where $c_{\mathrm{Li}^+_{\mathrm{ref}}}$, $c_{\mathrm{V[C_6]_{ref}}}$, $c_{\mathrm{Li[C_6]_{ref}}}$, $\left(\frac{c_{\mathrm{e}^-}}{c_{\mathrm{e}^-_{\mathrm{ref}}}}\right) = 1$.

Consequently, according to Cantera and using the parameters already set in the model (see Table 7) at 23 °C:

$$i_{\mathrm{LiC6}}^{0} = 8.83836 \cdot 10^{14} \exp\left(-\frac{77055\ \mathrm{J/mol}}{8.314 \frac{\mathrm{J}}{\mathrm{K\ mol}} \cdot 296.15\ \mathrm{K}}\right) \cdot (0.07)^{0.5} (0.674)^{0.5} (0.326)^{0.5} = 2.81\ \mathrm{A/m^2} \tag{99}$$

as in Table 9. Hence, we can now calculate i^0 for both plating and intercalation reactions at any temperature. Obviously our present model and Ecker's[95] show identical values for i_{Li}^{0} at 25 °C (24.3 A/m^2) and -10 °C (0.74 A/m^2), being the parameters for the plating reaction the same. Nevertheless, i_{LiC6}^{0} values happen to be quite different at 25 °C (3.47 and 0.81 A/m^2) and quite similar at -10 °C (0.06 and 0.05 A/m^2), with the respective ratios $i_{\mathrm{Li}}^{0}/i_{\mathrm{LiC_6}}^{0}$ varying from 7 and 30 at 25 °C, to 12 and 15 at -10 °C. Worth noting that, at low temperatures, the values of the ratio are much closer due to the choice of a larger activation energy for the intercalation reaction in our model (77.05 kJ/mol) than in Ecker (53.4 kJ/mol).

In summary, the exchange current density of plating is in our model always faster than that of intercalation but at low temperatures both the plating and intercalation reactions are considerably slowed down as compared to room temperature. Now that we have defined all the necessary thermodynamic and kinetic parameters and included them in our extended model, we can finally run our simulations and see if it works out. Or not?

5.2.3 TO PLATE OR NOT TO PLATE?...

Until now, an additional side reaction has been added at the anode with the purpose of simulating reversible lithium plating: plating and intercalation now act in parallel and compete for electrons and lithium ions. Is that enough? As we will see later on, sometimes an extra reaction is needed to reinforce the reversibility of the plating and the consequent re-intercalation

$$\mathrm{Li[metal]} + \mathrm{V[C_6]} \rightleftharpoons \mathrm{Li[C_6]}\,. \tag{100}$$

This reaction takes place at the contact interface between plated lithium and graphite, while the "classic" re-intercalation due to the reversibility of the plating reaction (Eq. 86) is solution-mediated (see 5.4.1.5).

At this point, it is time to summarise the final electrochemistry in our model: let's have a look at Table 8. All reactions and their kinetic coefficients are here listed: all the charge-transfer reactions follow Butler-Volmer kinetics (Eq. 95) and they are area-specific, with the reaction surface area assumed constant and independent of lithium volume fraction. At the graphite/electrolyte interface, three reactions (intercalation, plating and re-intercalation) take place while, at the cathode, each AM intercalation reaction happens at its respective AM/electrolyte interface. All the three AMs (graphite at the anode, LCO and NCA at the cathode) are characterised by their lithium stoichiometry $X_{\mathrm{Li[AM},i]}$ ranges, which have been already defined in Table 5.

TABLE 8: INTERFACIAL CHEMICAL REACTIONS AND RATE COEFFICIENTS USED IN THE PRESENT MODEL

Interface	Reaction	Label	Rate coefficient	Activation energy $E_{\mathrm{act,f}}$ / kJ/mol	Symmetry factor α_{f}
Graphite/electrolyte (anode)	$\mathrm{Li^+[elyt] + e^- + V[C_6] \rightleftarrows Li[C_6]}$	Intercalation	i^{00} = 8.84·10^{14} A/m^2	77.1	0.5
Graphite/electrolyte (anode)	$\mathrm{Li^+[elyt] + e^- \rightleftarrows Li[metal]}$	Plating	i^{00} = 2.29·10^{13} A/m^2	65.0	0.492
Graphite/electrolyte (anode)	$\mathrm{Li[metal] + V[C_6] \rightleftarrows Li[C_6]}$	Re-intercalation	k_{f} = 1·10^{-6} m^3/(mol·s) *	0 *	-
LCO/electrolyte (cathode)	$\mathrm{Li^+[elyt] + e^- + V[LCO] \rightleftarrows Li[LCO]}$	Intercalation	i^{00} = 8.20 ·10^{12} A/m^2	72.3	0.5
NCA/electrolyte (cathode)	$\mathrm{Li^+[elyt] + e^- + V[NCA] \rightleftarrows Li[NCA]}$	Intercalation	i^{00} = 2.63 ·10^{10} A/m^2	61.0	0.5

* Arbitrary values, set fast

TABLE 9: LITERATURE OVERVIEW OF EXPERIMENTAL AND MODELING STUDIES OF LITHIUM PLATING

Reference	Type of study	Kinetic expressions for plating reaction	Exchange current density i_{Li}^{0}	Activation energy $E_{\mathrm{act,Li}}$	Cathodic symmetry factor $\alpha_{\mathrm{c,Li}}$	Intercalation kinetics i_{LiC6}^{0}	Activation energy $E_{\mathrm{LiC6}}^{\mathrm{act}}$
Arora (1999)[82] [at 21 °C]	Modelling (physics-based)	$i_{\mathrm{Li}} = i_{\mathrm{Li}}^{0}\left[\exp\left(\frac{\alpha_{\mathrm{a,Li}} zF}{RT}\eta_{\mathrm{act}}\right) - \exp\left(-\frac{\alpha_{\mathrm{c,Li}} zF}{RT}\eta_{\mathrm{act}}\right)\right]$ $i_{\mathrm{Li}}^{0} = F(k_{\mathrm{a}})^{\alpha_{\mathrm{c,Li}}}(k_{\mathrm{c}})^{\alpha_{\mathrm{a,Li}}}(c_{\mathrm{Li}})^{\alpha_{\mathrm{a,Li}}}$	10 A/m² [175]		0.7 [173]	2.1 A/m²	
Verbrugge (1994)[41] [at 25 °C]	Experimental (Li/Li cell + voltammetry)	$i_{\mathrm{Li}} = i_{\mathrm{Li}}^{0}\left[\exp\left(\frac{(1-\alpha_{\mathrm{c,Li}})zF}{RT}\eta_{\mathrm{act}}\right) - \exp\left(-\frac{\alpha_{\mathrm{c,Li}} zF}{RT}\eta_{\mathrm{act}}\right)\right]$	316 A/m²		0.67		
Perkins (2012)[177] [at 25 °C]	Modelling (PDE + P2D models)	$j_{\mathrm{V,Li}}(t) = a_{\mathrm{sn}} i_{\mathrm{Li}}^{0}\left[\exp\left(\frac{\alpha_{\mathrm{a,Li}} zF}{RT}\eta_{\mathrm{act}}(t)\right) - \exp\left(-\frac{\alpha_{\mathrm{c,Li}} zF}{RT}\eta_{\mathrm{act}}(t)\right)\right]$ $i_{\mathrm{Li}}^{0} = k_{\mathrm{Li}}(c_{\mathrm{Li^+[elyt]}})^{\alpha_{\mathrm{a,Li}}}$	10 A/m²		0.7	0.96 A/m² *	
Ge (2017)[176] [at 25 °C]	Experimental (NMR) + P2D Modelling	$i_{\mathrm{Li}} = \min\left\{0, i_{\mathrm{Li}}^{0}\left[\exp\left(\frac{\alpha_{\mathrm{a,Li}} zF}{RT}\eta_{\mathrm{act}}\right) - \exp\left(-\frac{\alpha_{\mathrm{c,Li}} zF}{RT}\eta_{\mathrm{act}}\right)\right]\right\}$ $i_{\mathrm{Li}}^{0} = Fk_{\mathrm{Li}}(c_{\mathrm{Li^+[elyt]}})^{\alpha_{\mathrm{a,Li}}}$	0.17 A/m² *	35.3 kJ/mol	0.7 [82,177]	1.17 A/m² *	45 kJ/mol
Ecker (2016)[95] [at 23 °C]	Experimental (Li/Li cell + EIS)	$i_{\mathrm{Li}} = i_{\mathrm{Li}}^{0}\left[\exp\left(\frac{\alpha_{\mathrm{c,Li}} zF}{RT}\eta_{\mathrm{act}}\right) - \exp\left(-\frac{(1-\alpha_{\mathrm{c,Li}})zF}{RT}\eta_{\mathrm{act}}\right)\right]$ $i_{\mathrm{Li}}^{0} = \frac{R \cdot T}{z \cdot F \cdot A_{\mathrm{e}} \cdot R_{\mathrm{ct}}}$	20.4 A/m²	65 kJ/mol	0.492	0.705 A/m²	53.4 kJ/mol

Lueth (2015)[178] [at 25 °C]	Experimental (Li/Li cell + EIS)	$i_{\mathrm{Li}} = i_{\mathrm{Li}}^{0}\left[\exp\left(\frac{\alpha_{\mathrm{a,Li}}zF}{RT}\eta_{\mathrm{act}}\right) - \exp\left(-\frac{\alpha_{\mathrm{c,Li}}zF}{RT}\eta_{\mathrm{act}}\right)\right]$	1.758 A/m^2		0.7		
Tao (2017)[170] [at 23 °C]	Experimental (Li/Li cell + voltammetry)	$\log\frac{i_{\mathrm{Li}}}{\exp\left(\frac{zF}{RT}\eta_{\mathrm{act}}\right)-1} = \log i_{\mathrm{Li}}^{0} - \frac{(1-\alpha_{\mathrm{c,Li}})zF}{2.3RT}\eta_{\mathrm{act}}$	21.7±0.05 A/m^2		0.43±0.05		
Lee (2002)[172] [at 25 °C]	Experimental (RDE + voltammetry)	$\frac{i_{\mathrm{Li}}}{i_{\mathrm{Li}}^{0}} = \left(1-\frac{i_{\mathrm{Li}}}{i_{\mathrm{lim,c}}}\right)\exp\left(-\frac{\alpha_{\mathrm{c,Li}}zF}{RT}\eta_{\mathrm{act}}\right)$	0.943 A/m^2		0.51		
Tippmann (2016)[179] [at -10 °C]	Modelling (P2D Newman-type)	$i_{\mathrm{Li}} = i_{\mathrm{Li}}^{0}\left[\exp\left(\frac{\alpha_{\mathrm{a,Li}}zF}{RT}\eta_{\mathrm{act}}\right) - \exp\left(-\frac{\alpha_{\mathrm{c,Li}}zF}{RT}\eta_{\mathrm{act}}\right)\right]$	1200 A/m^2 **		0.7 [82]		
Danner (2016)[26] [at 28 °C]	Modelling (3D microstructural)	$i_{\mathrm{Li}} = i_{\mathrm{Li}}^{0}\left[\exp\left(\frac{\alpha_{\mathrm{c,Li}}zF}{RT}\eta_{\mathrm{act}}\right) - \exp\left(-\frac{(1-\alpha_{\mathrm{c,Li}})zF}{RT}\eta_{\mathrm{act}}\right)\right]$ $i_{\mathrm{Li}}^{0} = i_{\mathrm{Li}}^{00}(c_{\mathrm{Li^+[elyt]}})^{\alpha_{\mathrm{c,Li}}}(c_{\mathrm{Li}})^{\alpha_{\mathrm{c,Li}}}(c_{\mathrm{Li}}^{\max}-c_{\mathrm{Li}})^{1-\alpha_{\mathrm{c,Li}}}$	10 A/m^2 [171]				
Meibuhr (1970)[171] [at 28 °C]	Experimental (Li/Li cell + polarization)	$i_{\mathrm{Li}}^{0} = \frac{i_{\mathrm{Li}}RT}{\eta_{\mathrm{iR-free\ polarization}}}F$ $\eta_{\mathrm{iR-free\ polarization}} = E_{\mathrm{exp}} - E_{\mathrm{OC}} - i_{\mathrm{Li}}R$	9.5±0.5 A/m^2		0.67		

Hein (2016)[180] [at 25 °C]	Modelling (3D microstructural)	$i_{\mathrm{Li}} = i_{\mathrm{Li}}^{0}\left[\exp\left(\frac{F}{2RT}\eta_{\mathrm{act}}\right) - \exp\left(-\frac{F}{2RT}\eta_{\mathrm{act}}\right)\right]$ $i_{\mathrm{Li}}^{0} = i_{\mathrm{Li}}^{00}(c_{\mathrm{Li^+[elyt]}})^{0.5}$	12.6 A/m^2 [181,182]		0.5	0.40 A/m^2 [41,155]	68 kJ/mol [183]
Sequeira (1983)[184] [at 25 °C]	Experimental (Li/Li cell + polarization)	$i_{\mathrm{Li}} = i_{\mathrm{Li}}^{0}\left[\exp\left(\frac{(1-\alpha_{\mathrm{c,Li}})zF}{RT}\eta_{\mathrm{act}}\right) - \exp\left(-\frac{\alpha_{\mathrm{c,Li}}zF}{RT}\eta_{\mathrm{act}}\right)\right]$	12.6 A/m^2				
Yang (2018)[185] [at 0 °C]	Modelling (ECT model)	$j_{\mathrm{V,Li}} = a_{\mathrm{sn}}i_{\mathrm{Li}}^{0}\left[\frac{c_{\mathrm{Li}}}{c_{\mathrm{Li}}^{0}}\exp\left(\frac{\alpha_{\mathrm{a,Li}}zF}{RT}\eta_{\mathrm{act}}\right) - \frac{c_{\mathrm{Li^+[elyt]}}}{c_{\mathrm{Li^+[elyt]}}^{0}}\exp\left(-\frac{\alpha_{\mathrm{c,Li}}zF}{RT}\eta_{\mathrm{act}}\right)\right]$ $i_{\mathrm{Li}}^{0} = Fk_{\mathrm{Li}}(c_{\mathrm{Li}}^{0})^{\alpha_{\mathrm{c,Li}}}(c_{\mathrm{Li^+[elyt]}}^{0})^{\alpha_{\mathrm{a,Li}}}$	50 A/m^2 ***		0.7 [82]	2.1 A/m^2	
Bieker (2015)[174] [at 20 °C]	Experimental (Li/Li cell + EIS)	Not available	0.084 A/m^2 *				
Yang (2017)[186] [at 25 °C]	Modelling (ECT model)	$j_{\mathrm{V,Li}} = -a_{\mathrm{sn}}i_{\mathrm{Li}}^{0}\exp\left[-\frac{\alpha_{\mathrm{c,Li}}zF}{RT}\left(\phi_{\mathrm{s}} - \phi_{\mathrm{elyt}} - \frac{j_{\mathrm{tot}}}{a_{\mathrm{sn}}}\mathrm{R_{film}}\right)\right]$	0.001 A/m^2 ***		0.5		
Carelli (2020)[78] [values at 23 °C]	Modelling (P3D)	$i_{\mathrm{Li}} = i_{\mathrm{Li}}^{0}\left[\exp\left(\frac{\alpha_{\mathrm{c,Li}}zF}{RT}\eta_{\mathrm{act}}\right) - \exp\left(-\frac{(1-\alpha_{\mathrm{c,Li}})zF}{RT}\eta_{\mathrm{act}}\right)\right]$ $i_{\mathrm{Li}}^{0} = i_{\mathrm{Li}}^{00}\exp\left(-\frac{E_{\mathrm{act,Li}}}{RT}\right)\cdot\prod_{i=1}^{N_{\mathrm{R}}}\left(\frac{c_i}{c_i^{0}}\right)^{(1-\alpha_{\mathrm{c,Li}})}\prod_{i=1}^{N_{\mathrm{P}}}\left(\frac{c_i}{c_i^{0}}\right)^{\alpha_{\mathrm{c,Li}}}$	20.4 A/m^2 [95]	65 kJ/mol [95]	0.492 [95]	2.81 A/m^2 [111]	77.05 kJ/mol [111]

* calculated from values given in the reference

** assumed value for modelling

*** adjusted value for modelling purposes (fitting parameter in absence of experimental data)

5.2.4 TO EXIST OR NOT TO EXIST?...

In the case of the plating reaction (initial $\varepsilon_{\mathrm{Li[metal]}}$ set as 10^{-11}), we decided also to set a lower limit (10^{-10}) below which the decomposition rate is set to zero. This means that, for a stoichiometric phase like lithium metal, the activity of lithium is equal to unity as long as this phase is present, but once the reversible reaction has caused the $\varepsilon_{\mathrm{Li[metal]}}$ to drop below that limit, the activity gets automatically switched to zero and the decomposition stops: this little trick considerably increases the numerical stability of the simulation. Worth saying, the formation of plated lithium also reduces the electrode porosity represented in the model by the gas phase: because of the mechanical expansion of the battery during use not being included yet, the $\varepsilon_{\mathrm{gas}}$ could even go negative during plating (but no worries, it is just a mathematical thing).

Well, our model is now complete and ready to run but how do we know if it actually simulates reality?

5.3 IT'S THE TIME FOR EXPERIMENTS!

"The true method of knowledge is experiment."

(William Blake)

An adequate way to validate our multiscale model is for sure by comparison to macroscopic cell experiments.

We started our parameterisation using Ecker's experimental data for a 40 Ah high-power Kokam cell[95] and, for a long period, these have been our only experiments available: therefore, the first version of our model (including only the plating reaction, Eq. 86) was created to fit and simulate these data and their particular features. According to the manufacturer, this cell comprises graphite at the anode, NMC at the cathode and an EC/EMC mixture with $LiPF_6$ as electrolyte. Even if our modelled cell had a different format and cathode chemistry, the graphite anode could be sufficiently similar (same manufacturer, same high-power characteristics) to allow for comparison. At one point, we finally had the possibility of running our own experiments in order to obtain further validation for our model: we carried them out on our reference cell[111] (0.35 Ah high-power Kokam pouch cell with LCO/NCA blend cathode) inside a climate chamber (CTS T- 40/200 Li) in our own laboratory. As you will see in the next Section, the adding of a new reaction (Eq. 100, the re-intercalation) to our model became necessary to simulate the results obtained.

In this story, experiments have been used to parameterise and validate in a continuous ongoing process.

5.4 RESULTS AND DISCUSSION

"It is common sense to take a method and try it;
if it fails, admit it frankly and try another.
But above all, try something."

(Anthony Burgess)

As we have seen, the parameterisation of electrochemical models is one of the key factors in building up a reliable and working model: thermodynamics, kinetics but also the physical data and the structural parameters need to be defined in the most self-consistent and comprehensive way. Sometimes this process is done via literature research, sometimes via electrode balancing, sometimes they are just extracted from or fitted to accurately built experiments. For example, this multiapproach has been used to build the model discussed in Chapter 4, hence the base of the two versions of the present model we will be using to respectively simulate the two different set of experiments shown in this Section.

5.4.1 SIMULATIONS VS EXPERIMENTS: DIFFERENT CELLS, DIFFERENT MODELS

In this first part of Section 5.4, two different sets of experiments (let's call them "Kokam 40 Ah" and "Kokam 0.35 Ah") are shown and compared to simulations. As we will see, the two cells behave quite differently and the presence/absence of the plating hints (introduced in 3.1.1.2) determinates which of the two models (respectively without and with extra re-intercalation reaction) is the best fitting one. Both a voltage drop and a voltage plateau are actually very evident for "Kokam 40 Ah", while only a voltage drop seems lightly visible for "Kokam 0.35 Ah". In this second case, a parametric study of the rate coefficients has also been carried out in order to understand the mutual influence of the three competing reactions.

5.4.1.1 KOKAM 40 AH - CHARGE/DISCHARGE AT CONSTANT TEMPERATURE

In Figure 25 our simulations and Ecker's experimental data for a CC charge-discharge cycle (1C/1C) at constant ambient temperature (+10 °C and -10 °C, experiments available for -10 °C only) are compared.

The left part of Figure 25 shows data at +10 °C.

Panel a) shows simulated cell voltage and cell surface temperature, and Panel b) shows the corresponding C-rate (positive for charge) and average SOC of the anode (graphite here), defined as

$$\mathrm{SOC_{avg}} = \frac{\bar{\bar{X}}_{\mathrm{Li,an}} - X_{\mathrm{Li,an}}^{\mathrm{SOC=0}}}{X_{\mathrm{Li,an}}^{\mathrm{SOC=1}} - X_{\mathrm{Li,an}}^{\mathrm{SOC=0}}} \quad , \tag{101}$$

where the stoichiometry $\bar{\bar{X}}_{\mathrm{Li,an}}$ is averaged over both the anode thickness and the particle diameters (y and z scales, respectively, see Figure 23), and the nominal stoichiometry ranges $X_{\mathrm{Li,an}}^{\mathrm{SOC=0}}$ and $X_{\mathrm{Li,an}}^{\mathrm{SOC=1}}$ are given in Table 5. The voltage curve represents the typical charge/discharge behaviour of the cell, and the temperature shows self-heating/cooling effects as combination of reversible and irreversible heat sources. In particular, the discharge voltage curve does not show any particular plateau that might be indicative of plated lithium. Figure 25c shows the simulated volume fraction of metallic lithium (averaged over the anode thickness): it remains equal to zero. Panel d) compares the reaction rates of the intercalation and the plating reactions: the plating reaction has a rate of zero. The data in the two panels show clearly that no plating takes place: +10 °C/1C is not a favourable condition for plating and only the intercalation reaction is happening.

This changes when lowering the temperature to -10 °C, as shown in the right part of Figure 25.

In Panel e), both the simulation and the experiment show characteristic voltage plateaus both during the charge and during the discharge. Self-heating of the cell leads to nearly a 7 °C rise during the cycle.

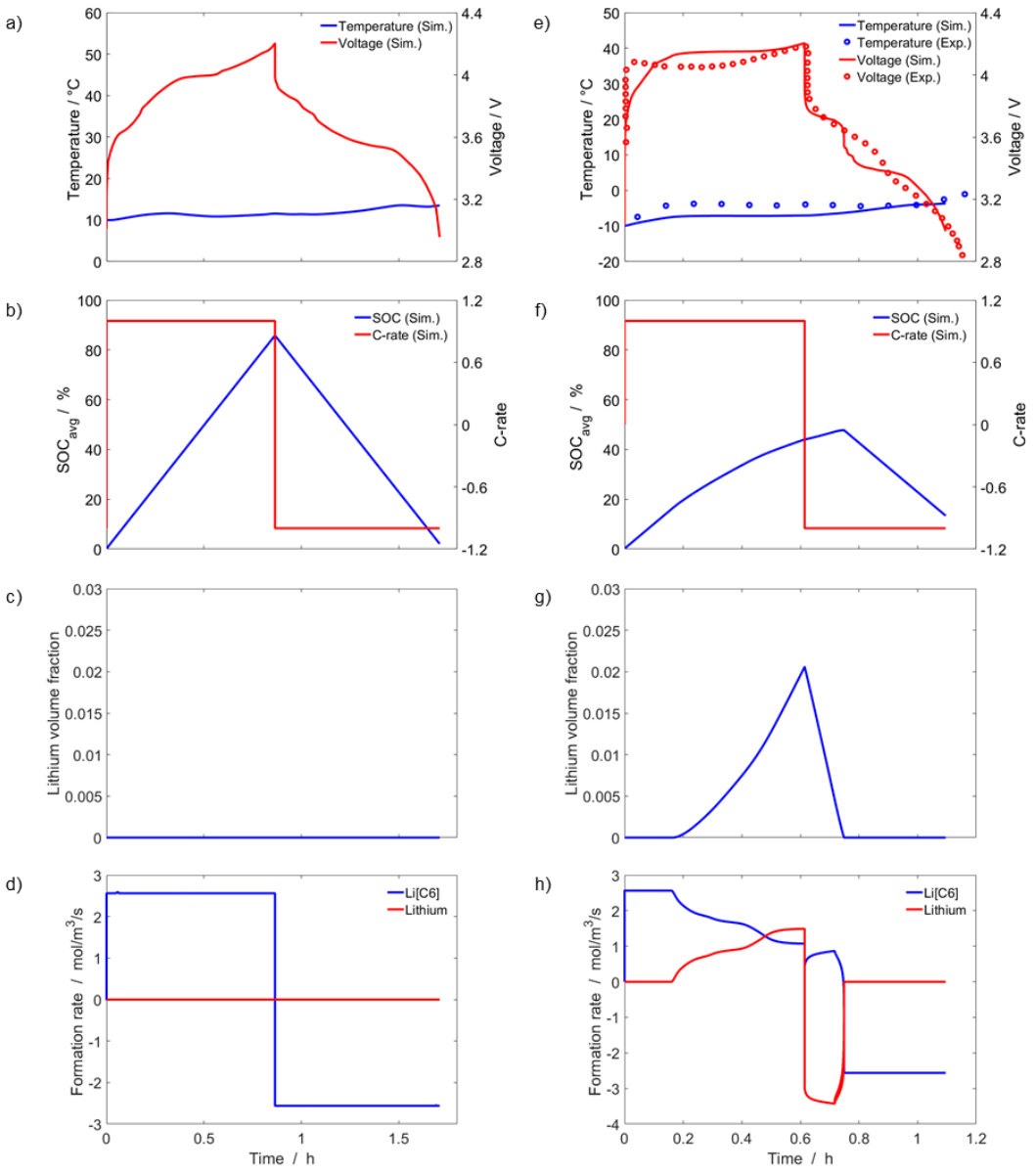

FIGURE 25: SIMULATIONS (THIS WORK) AND EXPERIMENTAL DATA (ECKER[95]) FOR A CHARGE-DISCHARGE CYCLE (1C/1C) AT CONSTANT AMBIENT TEMPERATURE OF +10 °C (ON THE LEFT: A) VOLTAGE AND TEMPERATURE, B) SOC AND C-RATE, C) LITHIUM VOLUME FRACTION, D) FORMATION RATES $\dot{s}_{\mathrm{LiC6}}$ AND $\dot{s}_{\mathrm{Li}}$) AND -10 °C (ON THE RIGHT: E) VOLTAGE AND TEMPERATURE, F) SOC AND C-RATE, G) LITHIUM VOLUME FRACTION, H) FORMATION RATES $\dot{s}_{\mathrm{LiC6}}$ AND $\dot{s}_{\mathrm{Li}}$).

Both voltage and temperature show qualitative agreement between model and experiment, although the discharge plating plateau in the experiments extends towards larger times than in the model. Quantitative differences between experiment and model are expected due to the different chemistry and size of the investigated cells (0.35 Ah NCA/LCO cathode simulated and 40 Ah NCM cathode experimental); taken this difference into account, the qualitative agreement is rather remarkable.

The observed plateau at discharge is one of the plating hints often found in cells after charge at low temperatures. Our model actually allows an in-depth analysis of the processes inside the cell during this plateau. Figure 25f shows the average SOC of the anode and the C-rate: we observe that the anode SOC continues

increasing even after we switch from charge to discharge, and only continues decreasing after having bypassed the plateau zone. It is interesting to note the nonlinearity of the SOC and its asymmetry with respect to charge and discharge, both caused by the presence of plating. Panel g) shows the metallic lithium volume fraction: plating starts at around 0.15 h (simultaneously with the occurrence of the charge voltage plateau), peaks at end of charge at 2.1 vol.-%, which is quite significant, and then decreases during the discharge plateau. Panel h) shows intercalation and plating reaction rates, showing again the onset of plating: after switching to discharge, the plating rate becomes negative, while the intercalation rate remains positive, consistent with the continuous increase of anode SOC. The absolute value of the plating reaction rate is larger than that of intercalation, showing that metallic lithium is simultaneously oxidized ($\mathrm{Li} \rightarrow \mathrm{Li}^{+} + \mathrm{e}^{-}$) and re-intercalated ($\mathrm{Li} + \mathrm{C}_6 \rightarrow \mathrm{LiC}_6$). Note that, although the explicit re-intercalation reaction (Eq. 100) is not explicitly included in the model, here it follows implicitly from a combination of the intercalation and the plating reactions.

5.4.1.2 KOKAM 40 AH - REST WITH TEMPERATURE CHANGE

In Figure 26 our simulations and Ecker's experimental data for a CCCV charge (1C) at low temperature, followed by a rest period with temperature rise to room temperature, and subsequent CC discharge (0.1C) are compared. The CCCV charge was carried out either at +10 °C (Figure 26 left) or at -10 °C (Figure 26 right): in either case the rest phase consisted of first a 0.5 h wait phase at the same temperature, then heating of the cells to 25 °C with an additional 5.5 h and final CC discharge.

The left part of Figure 26 shows data at +10 °C.

Panel a) shows simulated and experimental cell voltage and cell surface temperature, and Panel b) shows the corresponding C-rate (positive for charge) and average SOC of the anode, as defined in Eq. 101. The voltage curves represent a typical charge/rest/discharge behaviour, with a small relaxation drop at the beginning of the first rest phase, and the temperature shows similar self-heating/cooling effects during the CCCV charge for both the experiment and the simulation. In particular, the voltage curves are not affected by the temperature change and do not show any particular hints that might be indicative of plated lithium. Figure 26c shows the simulated volume fraction of metallic lithium (averaged over the anode thickness): it remains equal to zero. Panel d) compares the reaction rates of the intercalation and the plating reactions: the plating reaction has a rate of zero. The data in the two panels show clearly that no plating takes place: only intercalation is happening.

This changes when lowering the temperature to -10 °C, as shown in the right part of Figure 26.

In Panel e), both the experiment and the simulation show a second voltage drop (about 0.1 V) during the heating of the cells, more enhanced in the simulated data and exactly 0.5 h after the first drop corresponding to the beginning of the rest phase. A small voltage plateau in the last part of the CC charge is also clearly visible in the simulation and corresponds to the same plateau that is visible in Figure 25e. Again, quantitative differences between experiment and model are due to the different characteristics of the investigated cells (0.35 Ah simulated and 40 Ah experimental).

The observed voltage drop is one of the plating hints detected when cells are charged at low temperatures and then heated during the following rest. This voltage drop is not due to the temperature rise of the cell, but to the re-intercalation of the plated lithium formed during charge, which is frozen out at low temperatures.

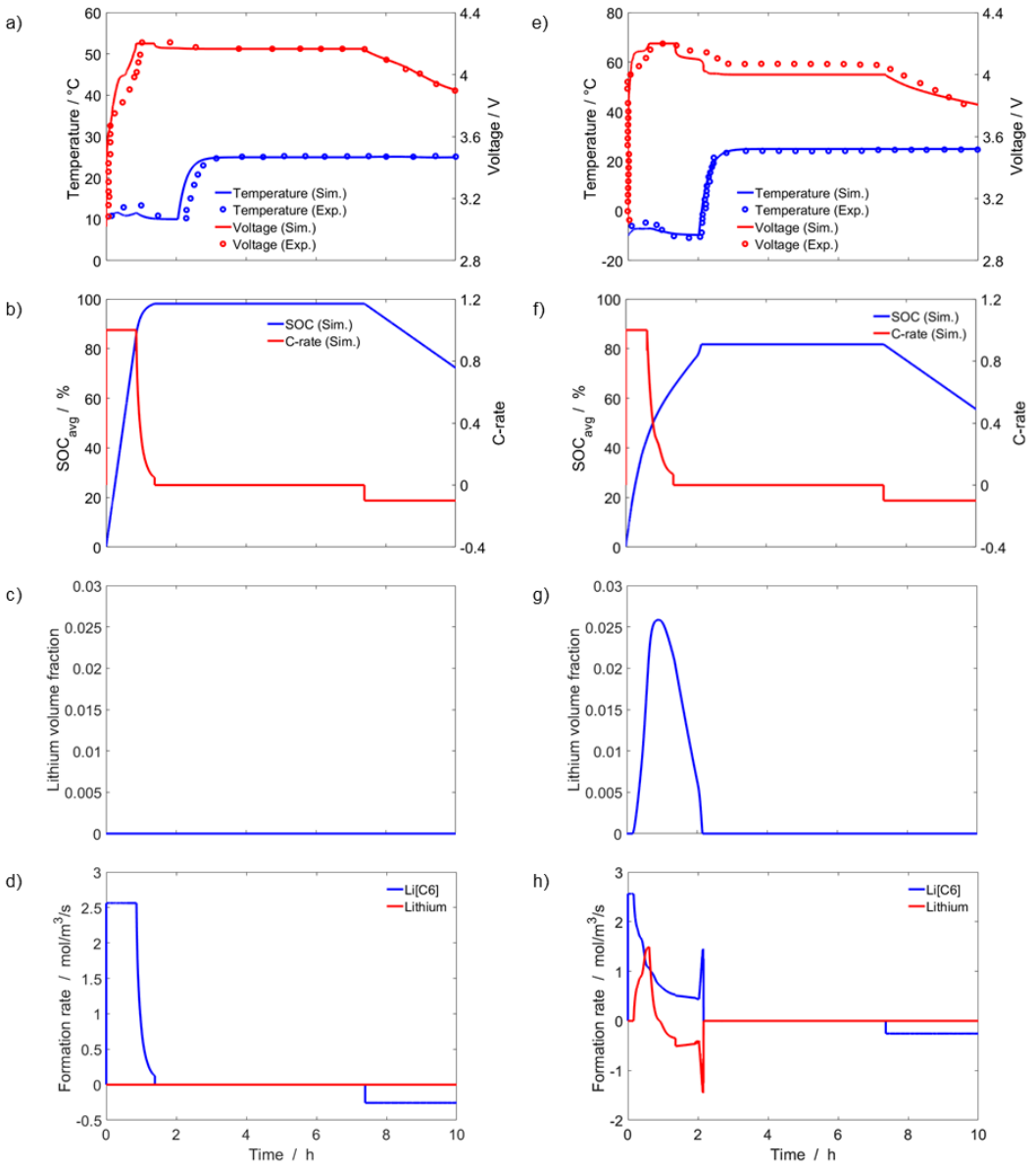

FIGURE 26: SIMULATIONS AND EXPERIMENTAL DATA (ECKER[95]) FOR A CHARGE (1C CCCV) – REST (6 H INCLUDING TEMPERATURE RISE TO 25°C) – DISCHARGE (0.1C CC, HERE ONLY PARTIALLY SHOWN) CYCLE AT DIFFERENT INITIAL TEMPERATURES OF +10 °C (ON THE LEFT: A) VOLTAGE AND TEMPERATURE, B) SOC AND C-RATE, C) LITHIUM VOLUME FRACTION, D) FORMATION RATES $\dot{s}_{\mathrm{LiC6}}$ AND $\dot{s}_{\mathrm{Li}}$) AND -10 °C (ON THE RIGHT: E) VOLTAGE AND TEMPERATURE, F) SOC AND C-RATE, G) LITHIUM VOLUME FRACTION, H) FORMATION RATES $\dot{s}_{\mathrm{LiC6}}$ AND $\dot{s}_{\mathrm{Li}}$).

Again, our model allows us to analyse the internal states of the cell. Figure 26f shows the average SOC of the anode and the C-rate: we can actually observe that the SOC continues increasing even during the first rest phase and accelerates when heating to 25 °C, to then stay stable once all the plated lithium has been re-intercalated (corresponding to the second voltage drop) and normally decrease during CC discharge. It is interesting to note the nonlinearity of the SOC and its asymmetry with respect to charge and discharge, both caused by the presence of plating. Panel g) shows the metallic lithium volume fraction: plating starts at around 0.15 h (simultaneously with the occurrence of the small charge voltage plateau), reaches the peak at 2.7 vol.-% during the CV charge and then starts decreasing to 0, with increased rate during the heating of the cell and the corresponding voltage drop. This is clearly visible in Figure 26h, which shows intercalation and plating reaction rates: after reaching the

maximum, the plating rate drops quickly to negative values, staying stable during the first rest phase and then reaching the maximum negative during the voltage drop, while the intercalation rate remains positive and shows a sharp peak equal and inverse to plating. This is consistent with the anode SOC and shows clearly how the re-intercalation tends to happen already in the CV phase and to be accelerated by warm temperatures.

5.4.1.3 KOKAM 0.35 AH - CHARGE/DISCHARGE AT CONSTANT TEMPERATURE

As previously said in Section 5.3 while talking about experiments, at one point in time we had the possibility of running our own "plating experiments" on our reference cell, a 0.35 Ah high-power Kokam pouch cell with blend cathode. Checking the validity of our model through comparison with the correct experiments was a necessary step to do, having been the model specifically built and parameterised for that cell.
Let's have a look at the results.

In Figure 27 simulations with different plating kinetics are compared with our experimental data for a charge (1C CC, 45 min CV) – rest (30 min) – discharge (1C CC) at a constant temperature of -10 °C. The base value of the exchange current density (multiplying rate factor 1) is shown in Table 8, while the other rate factors here plotted (multiplying rate factors 0.01, 0.1, 10, 100) help us understanding how the plating kinetics strongly influence the different phases of the cycle. Because of the duration of the CC charge phase being strongly affected by the choice of the rate factor, we have decided to set the time scale to 0 at the beginning of the CV phase to allow a better visual comparison for the different phases.
The left part of Figure 27 shows simulations obtained with a modelling framework with the re-intercalation reaction switched off. Panel a) shows the cell voltage: except for 0.01, all the other rates show a more or less pronounced voltage plateau, while this plating hint looks totally absent in the experiments. It is worth noting also how the different rates affect the CC phase and the voltage during the rest. Panel b) shows the current density (negative for charge) while Panel c) shows the SOC of the cell, which matches the SOC at the cathode where no parasitic reactions are included in this model and only the main intercalation/deintercalation reaction is happening. Being a blended cathode, the $\mathrm{SOC_{ca}}$ corresponds to the weighted average of the SOCs of the individual active materials and is defined as

$$\mathrm{SOC_{cell}} = \mathrm{SOC_{ca}} = \frac{\sum_{i=1}^{N_{\mathrm{AM,ca}}} \left(\mathrm{SOC}_i \cdot c_{\mathrm{AM},i}^{\mathrm{V}}\right)}{\sum_{i=1}^{N_{\mathrm{AM,ca}}} \left(c_{\mathrm{AM},i}^{\mathrm{V}}\right)} \quad , \tag{102}$$

where

$$\mathrm{SOC}_i = \frac{\bar{\bar{X}}_{\mathrm{Li[AM},i]} - X_{\mathrm{Li[AM},i]}^{\mathrm{SOC=0}}}{X_{\mathrm{Li[AM},i]}^{\mathrm{SOC=1}} - X_{\mathrm{Li[AM},i]}^{\mathrm{SOC=0}}} \quad . \tag{103}$$

The stoichiometry $\bar{\bar{X}}_{\mathrm{Li[AM},i]}$ is averaged over the cathode thickness, the different active materials concentrations and the particle diameters (y and z scales, respectively, see Figure 23), and the nominal stoichiometry ranges $X_{\mathrm{Li[AM},i]}^{\mathrm{SOC=0}}$ and $X_{\mathrm{Li[AM},i]}^{\mathrm{SOC=1}}$ can be found in Table 5. Panel c) shows the macroscopic SOC of the cell: see how the maximum SOC of the cell strongly depends on plating kinetics, with faster plating leading to a higher apparent SOC.

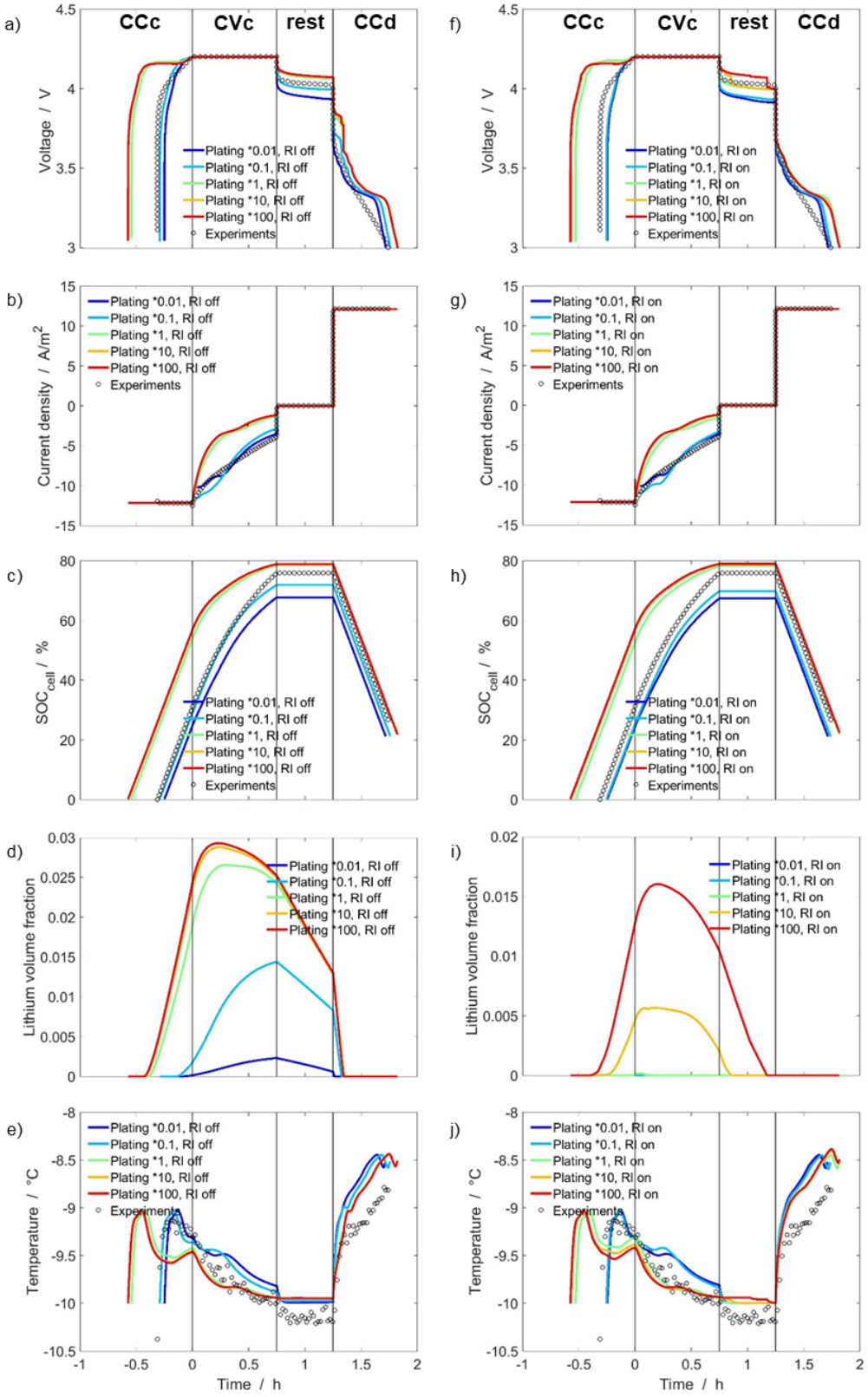

FIGURE 27: SIMULATIONS AND EXPERIMENTAL DATA FOR CHARGE (1C CC, 45 MIN CV) – REST (30 MIN) – DISCHARGE (1C CC) AT CONSTANT AMBIENT TEMPERATURE OF -10 °C AND MULTIPLYING RATE FACTORS FOR THE PLATING KINETICS VARYING FROM 0.01 TO 100. ON THE LEFT, WITH RE-INTERCALATION REACTION OFF: A) VOLTAGE, B) CURRENT DENSITY, C) CELL SOC, D) LITHIUM VOLUME FRACTION, E) TEMPERATURE. ON THE RIGHT, WITH RE-INTERCALATION REACTION ON: F) VOLTAGE, G) CURRENT DENSITY, H) CELL SOC, I) LITHIUM VOLUME FRACTION, J) TEMPERATURE.

Figure 27d shows the simulated volume fraction of metallic lithium (averaged over the anode thickness): easy to see how much plating is affected by the kinetics, with Li formation starting in the last part of the CC phase (corresponding to the CC voltage "bump" for the factors from 1 to 100), the peak in different moments of the CV charge (with 0.01 and 0.1 pushed towards the end of this phase) and then the decrease to 0 during the discharge plateau. Finally, the temperature in Panel e) shows self-heating/cooling effects as combination of reversible and irreversible heat sources.

As already noted, the experimental discharge voltage curve does not show any particular plateau while this is clearly visible in 4/5 of the plotted simulations: this is why we decided to add an extra reaction to reinforce the re-intercalation (Eq. 100) and the results are finally shown in the right part of Figure 27. In Panel f), the simulations don't show anymore voltage plateaus during the CC discharge (but the voltage plateau during CC charge is still present) and the voltage during the rest phase looks lower, showing the best match with the experiments at the standard plating rate. Panel g) and h) show respectively the current density and the average SOC: in both panels only 0.1 and 1 look slightly affected by the re-intercalation reaction, with the standard rate keeping a good match with the experiments. In Panel i), showing the simulated volume fraction (averaged over the anode thickness), only 100 and 10 (and much less evidently 1) seem to allow the formation of plated lithium, with the decrease happening during the CV and the rest phase: this is probably the reason behind the absence of a voltage plateau even at the highest rates. Finally, Panel j) shows no important differences with corresponding Panel e).

For a better understanding of two cases (without and with re-intercalation reaction), we need to consider the rate of progress of the involved reactions and how they influence the results. In Figure 28 we have a deeper look into the simulations at standard plating rate (rate factor 1), which has been seen to be the best match with our experimental data.

On the left with re-intercalation switched off, Panel a) and b) show respectively the voltage, where an unwanted plateau is visible in the simulation during the discharge, and the simulated lithium volume fraction (max 2.7 vol.-%). In Panel c) the rates of progress for the intercalation and plating reaction are plotted: the plating rate peaks at the end of the CC charge, starting its decrease during the CV phase and becoming negative at 0.3h while the intercalation rate remains positive until the end of the voltage plateau at 1.3h. It is very interesting to observe how the intercalation goes on also during the rest phase, with the same magnitude but opposite rate to the plating: being the explicit re-intercalation reaction not included in the model, we can deduce it simply happening from a combination in time of the intercalation and the plating reactions, with a visible negative peak during the voltage plateau.

On the right of Figure 28 we consider instead the modelling framework with the reversible re-intercalation reaction included. In Panel d) showing the voltage, the absence of a plateau in the experiments is successfully reproduced and the simulation is well matching the experiment in the rest and discharge phase. In Panel e) the simulated lithium volume fraction shows a value 142 times smaller than in the corresponding Panel b), with plated lithium starting at the end of the CC charge, peaking at 0.019 vol.-% and decreasing during the CV phase. Finally, Panel f) shows very clearly the influence of the newly added re-intercalation reaction on the simulation through the display of the rates of progress for all the three reactions. The intercalation rate drops to 0 at the

end of the CV charge and the plating rate never becomes negative, which means the plated lithium formed during the charge gets quickly re-intercalated through the extra reaction: this is easily visible in the plot, where the re-intercalation looks completely superimposed to the plating rate.

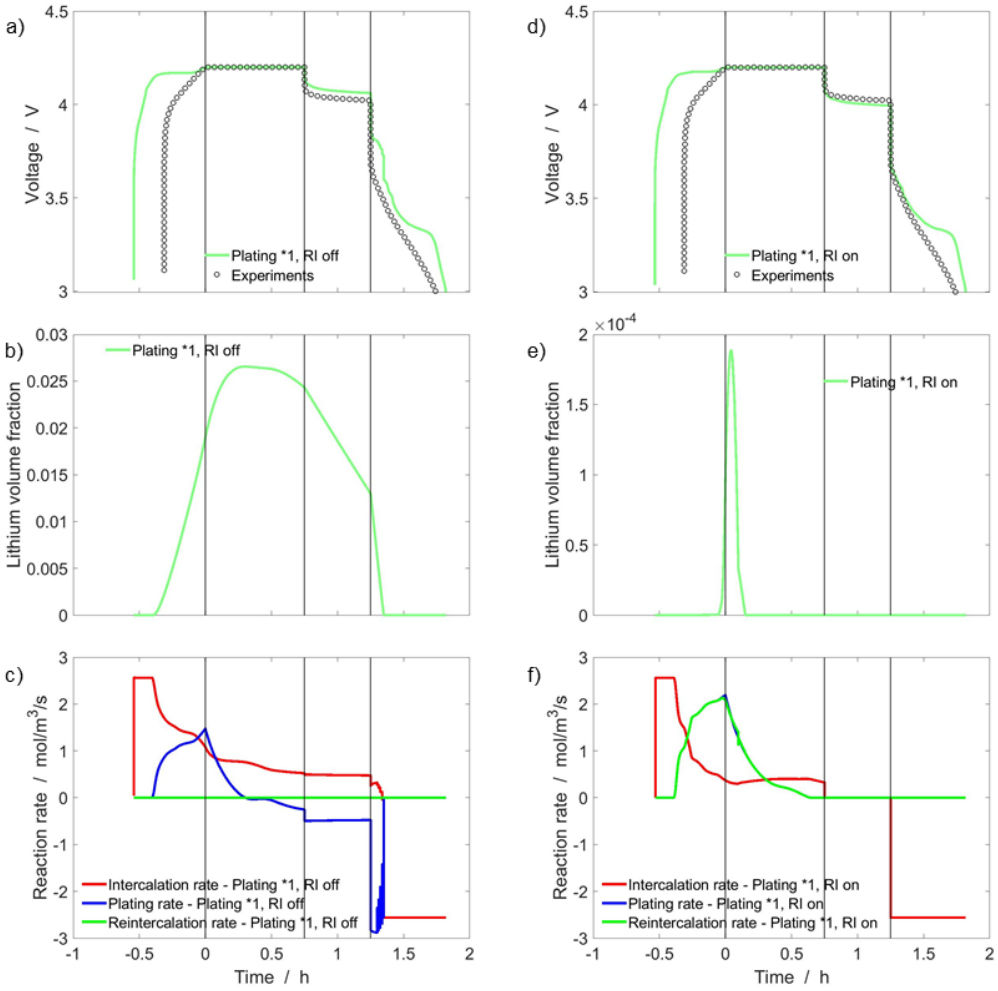

FIGURE 28: SIMULATIONS AND EXPERIMENTAL DATA FOR A CHARGE (1C CC, 45 MIN CV) – REST (30 MIN) – DISCHARGE (1C CC) AT CONSTANT TEMPERATURE OF -10 °C AND STANDARD PLATING RATE (RATE FACTOR 1). ON THE LEFT, WITH RE-INTERCALATION REACTION OFF: A) VOLTAGE, B) LITHIUM VOLUME FRACTION, C) RATE OF PROGRESS OF THE TWO REACTIONS. ON THE RIGHT, WITH RE-INTERCALATION REACTION ON: D) VOLTAGE, E) LITHIUM VOLUME FRACTION, F) RATE OF PROGRESS OF THE THREE REACTIONS.

5.4.1.4 KOKAM 0.35 AH – REST WITH TEMPERATURE CHANGE

In Figure 29 simulations with different plating kinetics are compared with our experimental data for a rest (30 min) - charge (1C CC, 45 min CV) – rest (3.5 h including temperature rise to 25°C) – discharge (1C CC) at initial temperature of -10 °C. The CCCV charge was carried out at -10 °C. The rest phase follows: first a 30 min wait phase at the same temperature, then heating of the cells to 25 °C with an additional 3.5 h. Last, the final CC discharge takes place at constant temperature of 25 °C. The kinetics of reference (multiplying rate factor 1) is shown in Table 8 and the same parameter variation was carried out as in 5.4.1.3.

The left part of Figure 29 shows simulations obtained with a modelling framework with the re-intercalation reaction switched off.

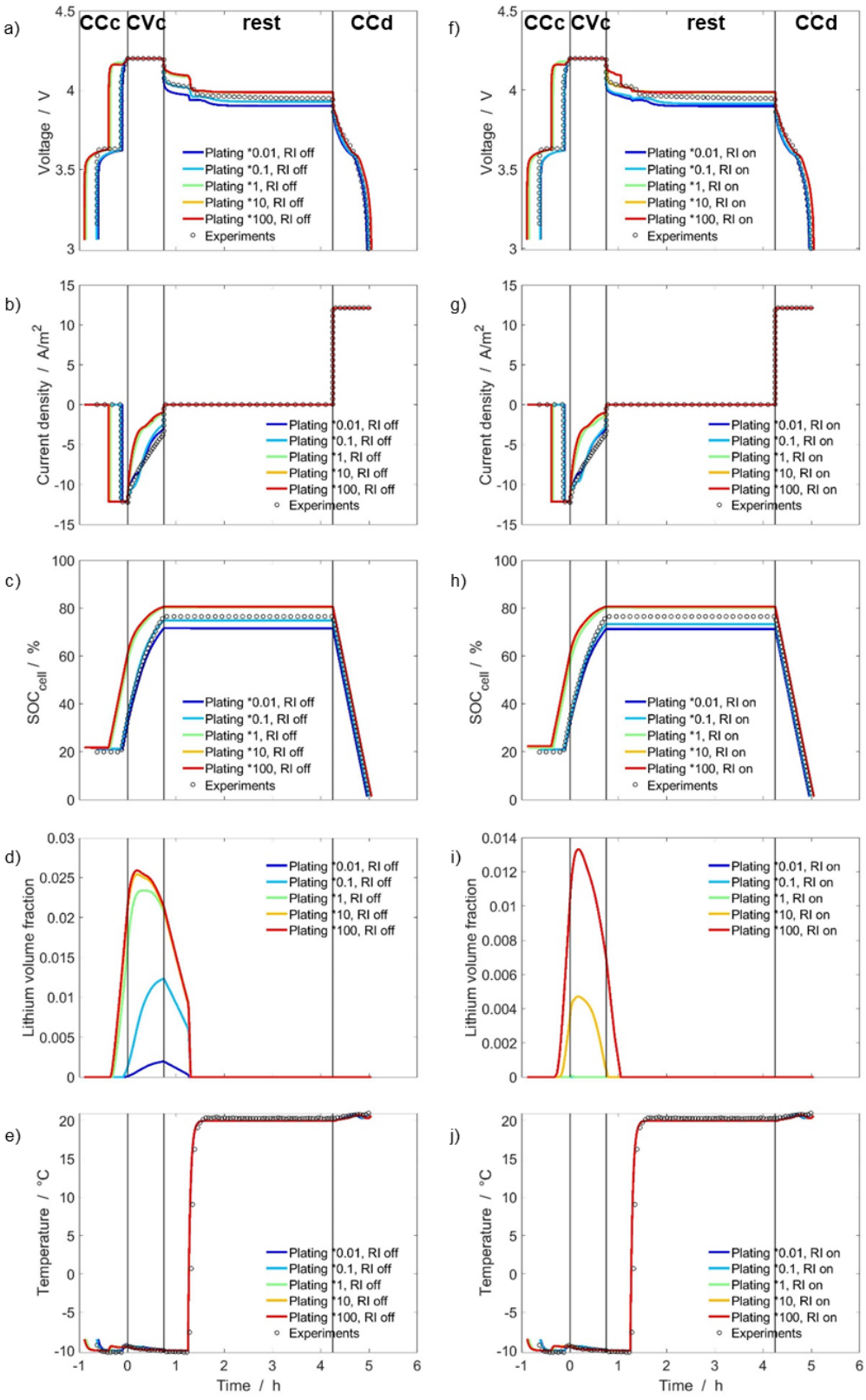

FIGURE 29: SIMULATIONS AND EXPERIMENTAL DATA FOR A REST (30 MIN) – CHARGE (1C CC, 45 MIN CV) – REST (3.5 H INCLUDING TEMPERATURE RISE TO 25°C) – DISCHARGE (1C CC) CYCLE AT INITIAL TEMPERATURE OF -10 °C AND VARYING PLATING RATE FACTORS FROM 0.01 TO 100. ON THE LEFT, WITH RE-INTERCALATION REACTION OFF: A) VOLTAGE, B) CURRENT DENSITY, C) CELL SOC, D) LITHIUM VOLUME FRACTION, E) TEMPERATURE. ON THE RIGHT, WITH RE-INTERCALATION REACTION ON: F) VOLTAGE, G) CURRENT DENSITY, H) CELL SOC, I) LITHIUM VOLUME FRACTION, J) TEMPERATURE.

In Panel a) both the experiment and the simulations show a small voltage drop during the heating of the cells (about 50 mV in the experiments, therefore less evident as the one seen in 5.4.1.2), exactly 30 min after the first drop corresponding to the beginning of the rest phase. This drop is more or less enhanced in the simulations accordingly to plating kinetics, with the best match with the experimental data happening to be with a factor of 0.1: it could actually be mainly due to the temperature rise of the cell. Worth noting also how again the different rates affect the CC phase and the voltage during the rest. Panel b) shows the current density (negative for charge) and Panel c) shows the SOC of the cell, as defined in Eq. 102. Figure 29d shows the simulated volume fraction of metallic lithium (averaged over the anode thickness): easy to see how much plating is affected by the kinetics, with Li formation starting in the last part of the CC phase (corresponding to the CC voltage "bump" for the factors from 1 to 100), the peak in different moments of the CV charge (with 0.01 and 0.1 pushed towards the end of this phase) and then the decrease to 0 at the voltage drop, 30 min in the rest phase. In Panel e) the temperature behaviour is dominated by the temperature rise at around 1.2 h.

On the right side of Figure 29, simulations obtained with the same modelling framework but with the re-intercalation reaction switched on are shown. In Panel f), the simulated voltage drops seem flattened but still visible, with the best match with the experiments for the standard plating rate (rate factor 1). For the highest rate factor (100), the drop keeps the same height seen in Panel a) but looks shifted in time, which can be explained with the simulated re-intercalation happening now earlier and not anymore connected to the time of the temperature rise. Panel g) and h) show respectively the current density and the average SOC: in both panels only 0.1 and 1 look slightly affected by the re-intercalation reaction, with the standard rate keeping a good match with the experiments. In Panel i), showing the simulated volume fraction, only 100 and 10 (and much less evidently 1) seem to allow the formation of plated lithium, with the decrease happening during the CV (factor 10) and the rest phase (factor 100). Panel j) shows no differences with corresponding Panel e).

Same as we did in 5.4.1.3, we now have a look into the simulation at standard plating rate (rate factor 1) in Figure 30. On the left with re-intercalation switched off, Panel a) and b) show respectively the voltage, where a very evident voltage drop is visible in the simulation, and the simulated lithium volume fraction (max 2.4 vol.-%). In Panel c) are plotted the rate of progress for the intercalation and plating reaction: after reaching the maximum, the plating rate drops quickly to negative values, staying stable during the first rest phase and then reaching the maximum negative during the voltage drop, while the intercalation rate remains positive and shows a sharp peak equal and inverse to plating. On the right of Figure 30 we consider instead the modelling framework with the reversible re-intercalation reaction included. In Panel d) showing the voltage, the plateau looks flattened, still matching quite well the experimental data. In Panel e) the simulated lithium volume fraction shows a value 267 times smaller than in the corresponding Panel b), with plated lithium starting at the end of the CC charge, peaking at 0.009 vol.-% and decreasing during the CV phase. Finally, Panel f) shows very clearly how much adding the re-intercalation reaction in the model has an influence on the other reactions rates of progress. The intercalation rate drops to 0 at the end of the CV charge and the plating rate never becomes negative, which means the plated lithium formed during the charge gets simply re-intercalated through the extra reaction, thus the re-intercalation looks completely superimposed to the plating rate. From the observation of the panels on the right of Figure 30, it is then possible to speculate this small drop seen in our experiments being likely due to the temperature rise

and corresponding equilibration of the intra-particle lithium gradients. Worth adding that the cells have been successively opened after the experiments for a post-mortem analysis at the electronic microscope and no signs of plating have been found[187]. The data shown in Figure 29 and Figure 30 demonstrate therefore the challenges in interpreting the plating hints when multiple reactions and external factors like the temperature are involved. The absence of a voltage plateau as seen in 5.4.1.3 and the characteristics of the voltage drop analysed here in 5.4.1.4 are therefore indicative of a cell less likely to be affected by plating, whose modelling requires the adding of an explicit re-intercalation reaction to suppress the otherwise expected plating hints.

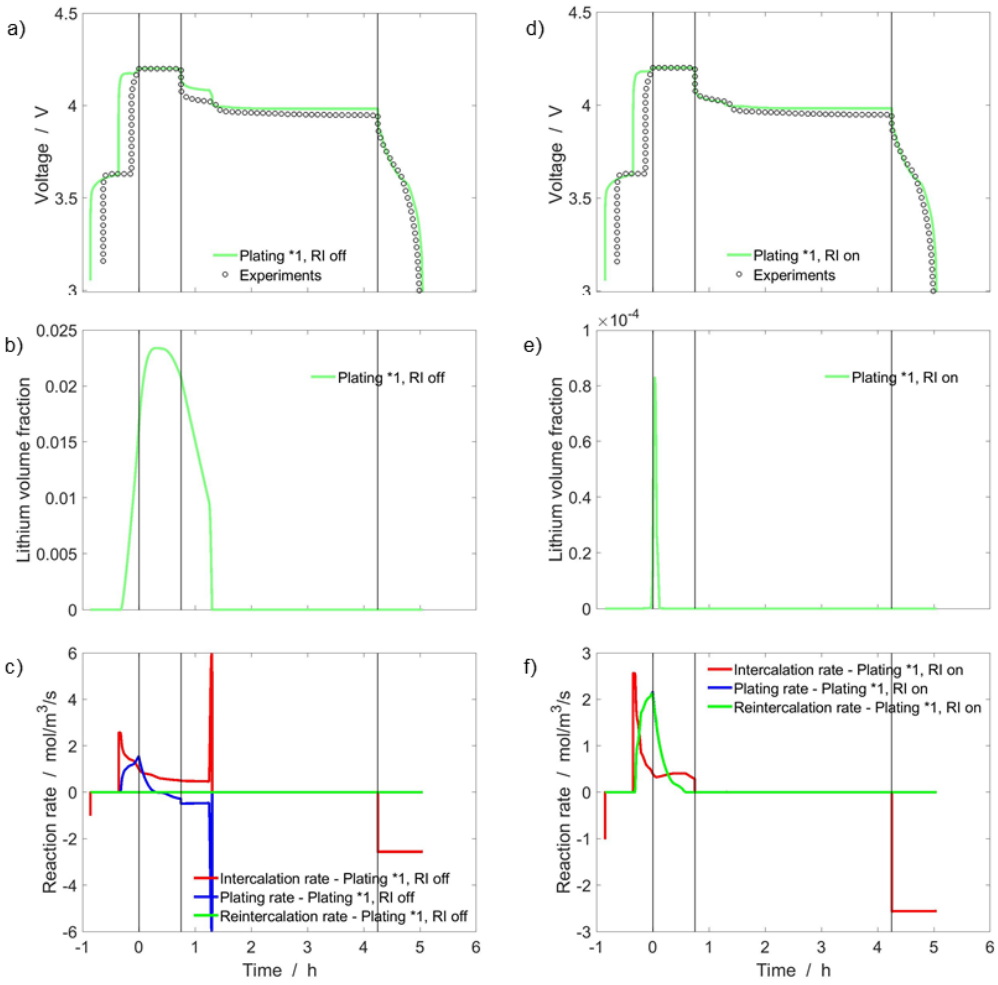

FIGURE 30: SIMULATIONS AND EXPERIMENTAL DATA. FOR A REST (30 MIN) - CHARGE (1C CC, 45 MIN CV) – REST (3.5 H INCLUDING TEMPERATURE RISE TO 25°C) – DISCHARGE (1C CC) CYCLE AT INITIAL TEMPERATURE OF -10 °C AND STANDARD PLATING RATE (RATE FACTOR 1). ON THE LEFT, WITH RE-INTERCALATION REACTION OFF: A) VOLTAGE, B) LITHIUM VOLUME FRACTION, C) RATE OF PROGRESS OF THE TWO REACTIONS. ON THE RIGHT, WITH RE-INTERCALATION REACTION ON: D) VOLTAGE, E) LITHIUM VOLUME FRACTION, F) RATE OF PROGRESS OF THE THREE REACTIONS.

5.4.1.5 …To plate!

We have seen through this long Section how the highly complex competition of intercalation, plating and potential re-intercalation reactions may lead to the presence or absence of the distinctive plating hints. If the "Kokam 40Ah" proved to be well matched by a model with only two reactions, the "Kokam 0.35Ah" needed the adding of an extra explicit reaction to simulate the absence of the voltage plateau and the only partial evidence

of the voltage drop. We knew somehow plating was happening at one point during charge but it was much less evident than in the first case…what could be the reason of this behaviour?

We can try to make some hypothesis connected to the two different ways in which the reversible plating (Eq. 86) and the explicit re-intercalation (Eq.100) are formulated in the model and to the different features of the two analysed cells. The plating reaction is expressed as reversible

$$\mathrm{Li^+[elyt]} + \mathrm{e^-[elde]} \rightleftharpoons \mathrm{Li[metal]} \ , \tag{104}$$

which means that it can run both forward, with formation of plated lithium

$$\underline{\mathrm{Li^+[elyt]}} + \mathrm{e^-[elde]} \rightarrow \mathrm{Li[metal]} \ , \tag{105}$$

and reverse, with decomposition of plated lithium

$$\mathrm{Li[metal]} \rightarrow \underline{\mathrm{Li^+[elyt]}} + \mathrm{e^-[elde]} \ . \tag{106}$$

Subsequent re-intercalation of the formed $\mathrm{Li^+[elyt]}$ into the active material may follow

$$\underline{\mathrm{Li^+[elyt]}} + \mathrm{e^-[elde]} + \mathrm{V[C_6]} \rightarrow \mathrm{Li[C_6]} \ . \tag{107}$$

We can call this process a "solution-mediated re-intercalation", because electrolyte-dissolved $\mathrm{Li^+[elyt]}$ are formed as intermediates: this mechanism actually requires a large lithium/electrolyte interfacial area and is therefore more likely to occur in dendrite-like structures. This could be the case of the big Kokam 40 Ah cell. When we add the explicit re-intercalation reaction

$$\mathrm{Li[metal]} + \mathrm{V[C_6]} \rightleftharpoons \mathrm{Li[C_6]} \ , \tag{108}$$

we open up to the possibility of a "surface-mediated re-intercalation", in which the Li[metal] directly re-intercalates taking advantage of its close position to the graphite, without any intermediates involved: this mechanism is more likely to occur in film-like structures where not too much plated lithium is formed. This could be the case of our small Kokam 0.35Ah.

Now let's play a bit. Our two cells are now a sort of two limiting cases for lithium morphology, but what if the re-intercalation reaction had an intermediate value between 0 (Kokam 40Ah) and 1 (Kokam 0.35Ah)?

In Figure 31 a parametric analysis has been carried out for the explicit re-intercalation reaction, using multiplying factors from 0.001 to 10. It would be useless and repetitive to describe every single panel, having already discussed the effects of this reaction in the previous paragraphs; it is interesting though to observe how the increasing rate of the re-intercalation reaction increasingly smooths the plating hints (Panels a and f) and lowers the plated lithium volume fraction (Panels d and i), till having them disappearing for any factor equal or higher than 0.1. The current density (Panels b and g) and the SOC (Panels c and h) are not affected by the parametric variation instead, while the effect on temperature is visible on Panel e) (but not in j), where the competition between the three reaction causes, with an increasing re-intercalation rate, a consequent heating up of the cell. As example, in Figure 32 the rate of progress for the three reactions are shown at the standard plating rate and multiplying factor of 0.01 for the re-intercalation. Differently from Panels f) from Figure 28 and Figure 30 ("on"), here the re-intercalation curve is not completely superimposed to the plating one, meaning that only a part of the plated lithium is re-intercalated through the surface-mediated mechanism. The reversibility of the plating reaction will then take care of the metallic lithium "leftovers", by solution-mediated re-intercalation (see the plating rate also going negative), as happening in Panels c) from Figure 28 and Figure 30 ("off").

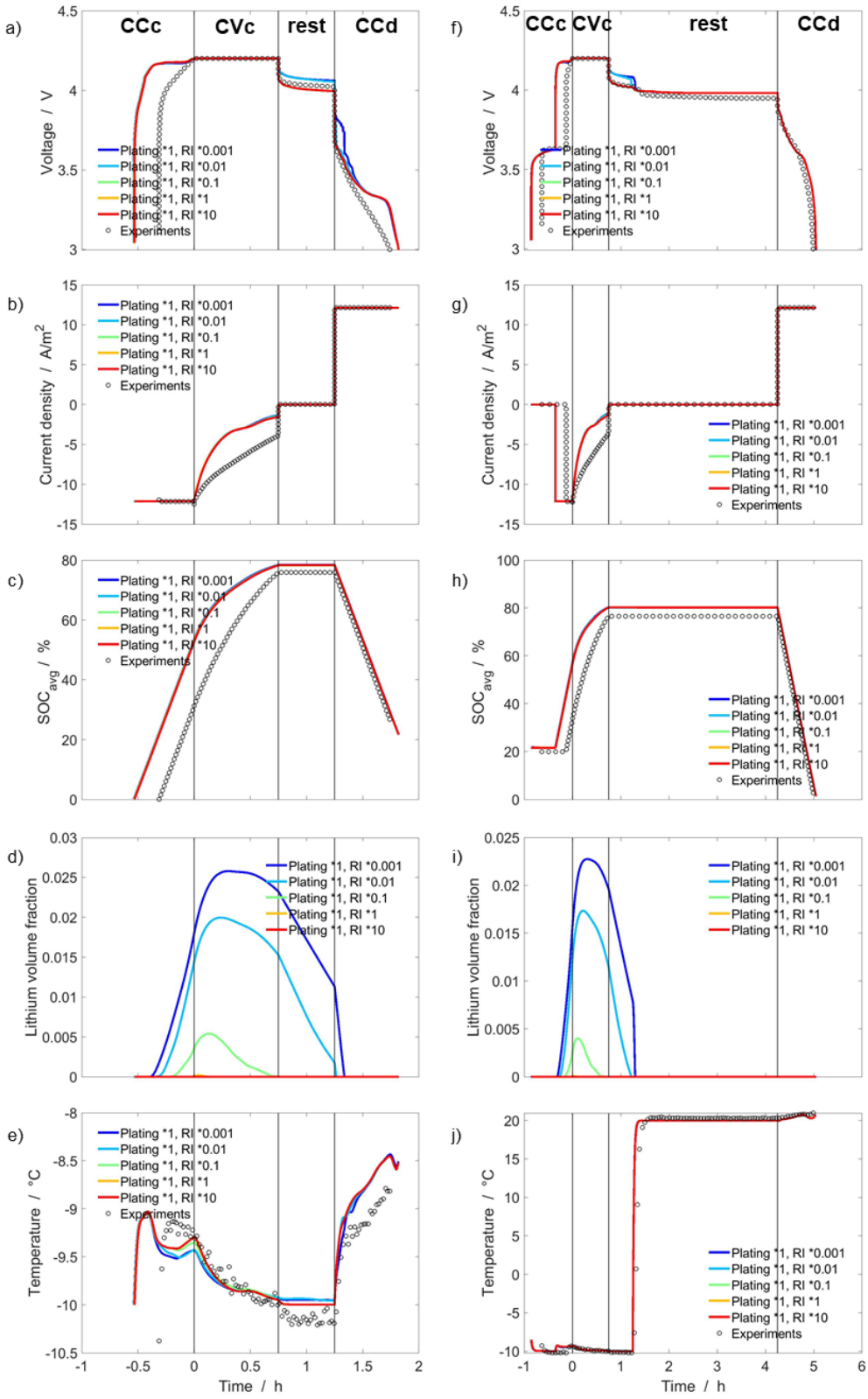

FIGURE 31: SIMULATIONS AND EXPERIMENTAL DATA. ON THE LEFT, CHARGE (1C CC, 45 MIN CV) – REST (30 MIN) – DISCHARGE (1C CC) AT CONSTANT AMBIENT TEMPERATURE OF -10 °C AND MULTIPLYING RATE FACTORS FOR THE RE-INTERCALATION KINETICS VARYING FROM 0.001 TO 10: A) VOLTAGE, B) CURRENT DENSITY, C) CELL SOC, D) LITHIUM VOLUME FRACTION, E) TEMPERATURE. ON THE RIGHT, REST (30 MIN) – CHARGE (1C CC, 45 MIN CV) – REST (3.5 H INCLUDING TEMPERATURE RISE TO 25°C) – DISCHARGE (1C CC) CYCLE AT INITIAL TEMPERATURE OF -10 °C AND MULTIPLYING RATE FACTORS FOR THE RE-INTERCALATION KINETICS VARYING FROM 0.001 TO 10: A) VOLTAGE, B) CURRENT DENSITY, C) CELL SOC, D) LITHIUM VOLUME FRACTION, E) TEMPERATURE.

As said before, we know this combination of mechanisms not being our case, but it could be of some use to understand the behaviour of other cells in the market with intermediate plating characteristics between our small Kokam 0.35Ah and the big Kokam 40Ah.

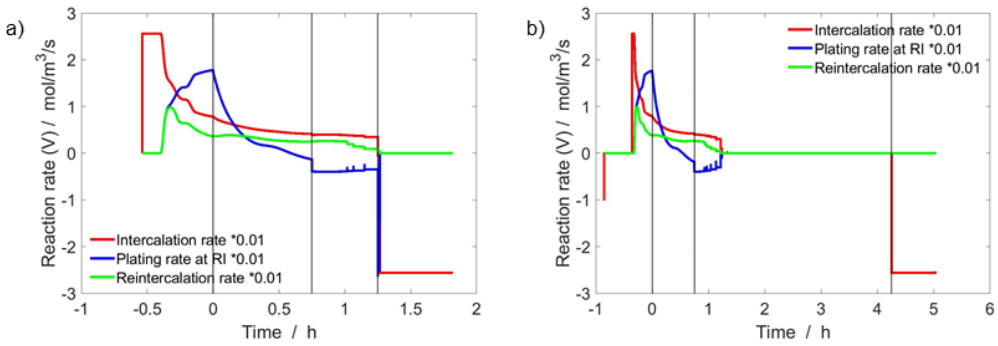

FIGURE 32: RATE OF PROGRESS OF THE THREE REACTIONS AT STANDARD PLATING RATE (RATE FACTOR 1) AND RE-INTERCALATION RATE FACTOR 0.01. ON THE LEFT, CHARGE (1C CC, 45 MIN CV) – REST (30 MIN) – DISCHARGE (1C CC) AT CONSTANT TEMPERATURE OF -10 °C. ON THE RIGHT, REST (30 MIN) - CHARGE (1C CC, 45 MIN CV) – REST (3.5 H INCLUDING TEMPERATURE RISE TO 25°C) – DISCHARGE (1C CC) CYCLE AT INITIAL TEMPERATURE OF -10 °C.

5.4.2 INSIDE THE CELL

In this Section we will have a look inside the cell, not by opening it physically but through simulated internal cell states at the meso and microscale and a comprehensive analysis of the equilibrium potentials behaviour during different operating conditions and cycling protocols. Most of what we have been seeing until now will be better understood in the light of the following Subsections.

5.4.2.1 SPATIOTEMPORAL ANALYSIS AT THE MESOSCALE

We now discuss the effect of temperature on the simulated internal cell states during 1C CC charge and 1C CC discharge: the spatiotemporal analysis is carried out at +10 °C and -10 °C using the "Kokam 40 Ah" model (see 5.4.1.1). The decision of taking this 2-reactions framework instead of the other one used in 5.4.1.3, is due to the presence of an evident voltage plateau as plating hint in the Kokam 40 Ah cell at -10 °C, while the comparison at +10 °C in absence of plating has been also added to understand the effects of temperature in the internal states.

At the macroscale, not much is happening. As explained before, here the cell surface is exposed to ambient air without aluminium holder plates and, due to the small dimension of the cell on the *x*-scale, the temperature is nearly uniform.

But on the mesoscopic scale the situation is quite different. The spatiotemporal behaviour of metallic lithium volume fraction and local SOC is shown in Figure 33 and Figure 34, with the local SOC here defined as

$$\mathrm{SOC}_{\mathrm{local}}(y) = \frac{\bar{X}_{\mathrm{Li,an}} - X_{\mathrm{Li,an}}^{\mathrm{SOC=0}}}{X_{\mathrm{Li,an}}^{\mathrm{SOC=1}} - X_{\mathrm{Li,an}}^{\mathrm{SOC=0}}} \tag{109}$$

and the stoichiometry $\bar{X}_{\mathrm{Li,an}}$ averaged over the particle diameters (z scale, see Figure 23).

Let's have a look first at what is happening at +10 °C (Figure 33).

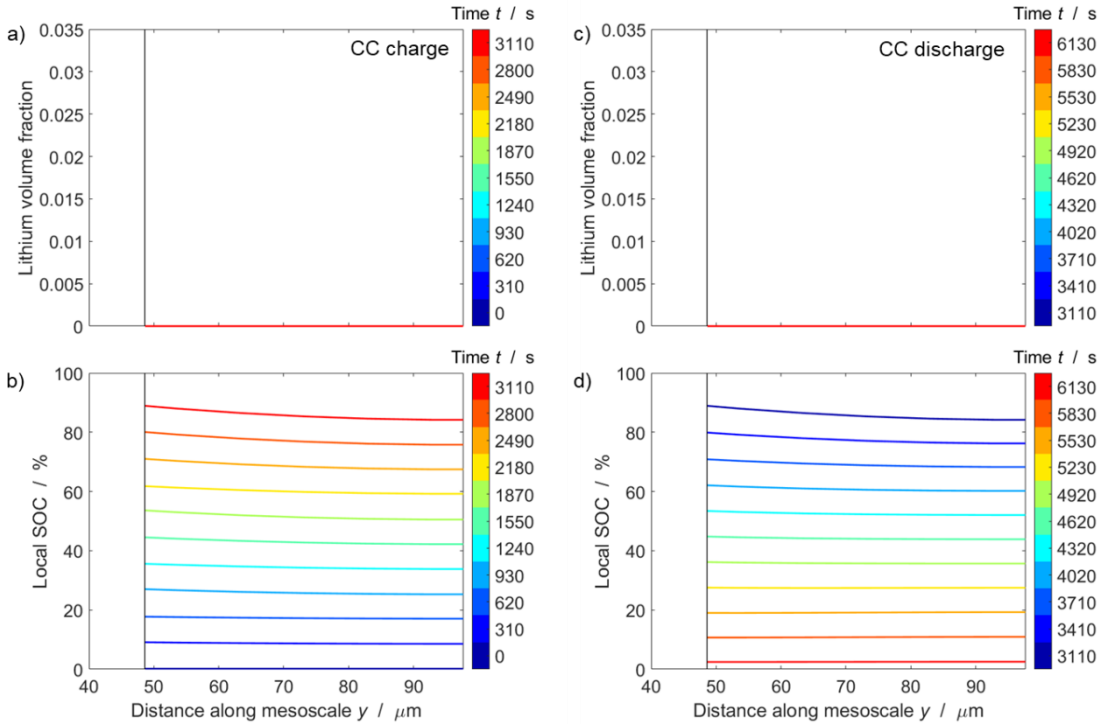

FIGURE 33: SPATIOTEMPORAL BEHAVIOR ALONG THE NEGATIVE ELECTRODE THICKNESS AT +10 °C FOR A 1C CC CHARGE (ON THE LEFT: A) LITHIUM VOLUME FRACTION, B) LOCAL SOC) AND FOR A 1C CC DISCHARGE (ON THE RIGHT: C) LITHIUM VOLUME FRACTION, D) LOCAL SOC). THE LOWER END OF THE MESOSCALE AXIS CORRESPONDS TO THE SEPARATOR, THE UPPER END TO THE CURRENT COLLECTOR.

If you remember, this temperature is not favouring the formation of plated lithium: hence, the metallic lithium volume fraction stays at 0 and the $\mathrm{SOC}_{\mathrm{local}}$, which reflects the intercalated lithium stoichiometry, reaches 90 % as maximum value at the anode/separator interface at the end of the CC charge. This value slightly decreases when moving away from the separator with a 4 % difference between the opposite sides of the electrode. The CC discharge also doesn't show any peculiar features, with the $\mathrm{SOC}_{\mathrm{local}}$ nearly uniformly decreasing and reaching a minimum value of 2.5 % at the end.

This changes when lowering the temperature to -10 °C (Figure 34). Here we have the right conditions for plating and we can observe it starting already at around 660 s, peaking at the end of charge at the maximum value of 3.2 vol.-% at the separator interface where the plated lithium tends to form faster. Compared to what observed at +10 °C, here the cell is less performant: the maximum $\mathrm{SOC}_{\mathrm{local}}$ reaches a much lower value, only 44 % due to the competition between the main and the side reaction. During the CC discharge, the metallic lithium is consumed in the time interval 2190-2700 s, corresponding to the voltage plateau in Figure 25e. What is really interesting is the $\mathrm{SOC}_{\mathrm{local}}$, which shows an increase during this period by nearly 3 % due to (solution-mediated) re-intercalation and then a final decrease to a minimum value of 13.5 % at the end of the CC discharge: a much higher value compared to what observed at +10 °C.

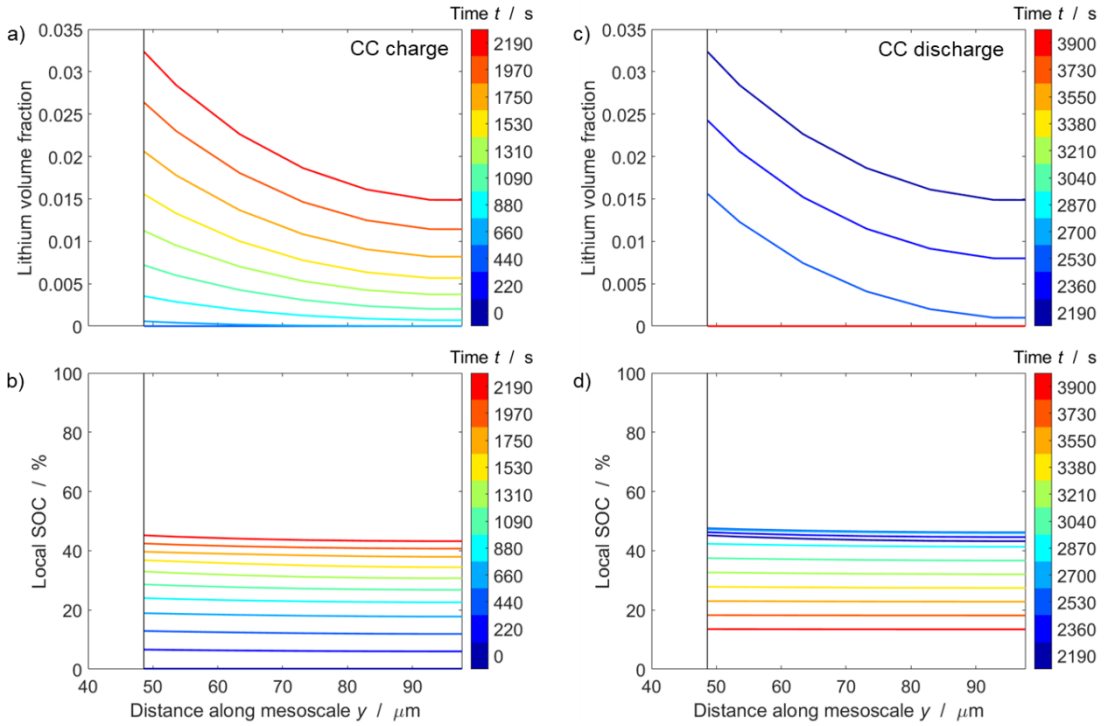

FIGURE 34: SPATIOTEMPORAL BEHAVIOR ALONG THE NEGATIVE ELECTRODE THICKNESS AT -10 °C FOR A 1C CC CHARGE (ON THE LEFT: A) LITHIUM VOLUME FRACTION, B) LOCAL SOC) AND FOR A 1C CC DISCHARGE (ON THE RIGHT: C) LITHIUM VOLUME FRACTION, D) LOCAL SOC). THE LOWER END OF THE MESOSCALE AXIS CORRESPONDS TO THE SEPARATOR, THE UPPER END TO THE CURRENT COLLECTOR.

5.4.2.2 SPATIOTEMPORAL ANALYSIS AT THE MICROSCALE

We now turn to the microscopic scale. Figure 35 shows the distribution of lithium stoichiometry inside the graphite particles at +10 and -10 °C for a representative particle close to the anode/separator interface (y = 48.6 µm). As shown in Figure 23, the particle surface is at z = 0 µm.

Figure 35a shows the spatiotemporal behaviour for a 1C CC charge-discharge at +10 °C. During the CC charge, we can see the stoichiometry increasing with time and the lithium ions bypassing the particle surface and diffusing along z, with stoichiometry values exceeding the nominal upper limit (0.619 at 100 % SOC): the lithium is clearly accumulating (no plating happening though) and the graphite particle is locally overcharged (SOC > 100 %). During the CC discharge, the stoichiometry is rapidly decreasing in the most accessible zones close to the surface but still increasing in the particle bulk, with the diffusive flux still directed towards the particle centre. Finally, the de-intercalation is complete at the end of the cycle. Figure 35b shows the spatiotemporal behaviour for a 1C CC charge-discharge at -10 °C. Due to the lower temperature the (thermally-activated) diffusion along z is much slower and consequently the lithium stoichiometry reaches lower values compared to the ones observed at +10 °C. Again, the accumulation of lithium close to the particle surface is clearly visible, with stoichiometry in this case only slightly exceeding the nominal range even if - we know it from what discussed until now - plating is happening. The surface concentration remains high during the first 500 s of the CC discharge because of the re-intercalation of plated lithium (this period corresponding to the plateau in Figure 25e), with a drop in the stoichiometry around 2600 s indicating its full consumption.

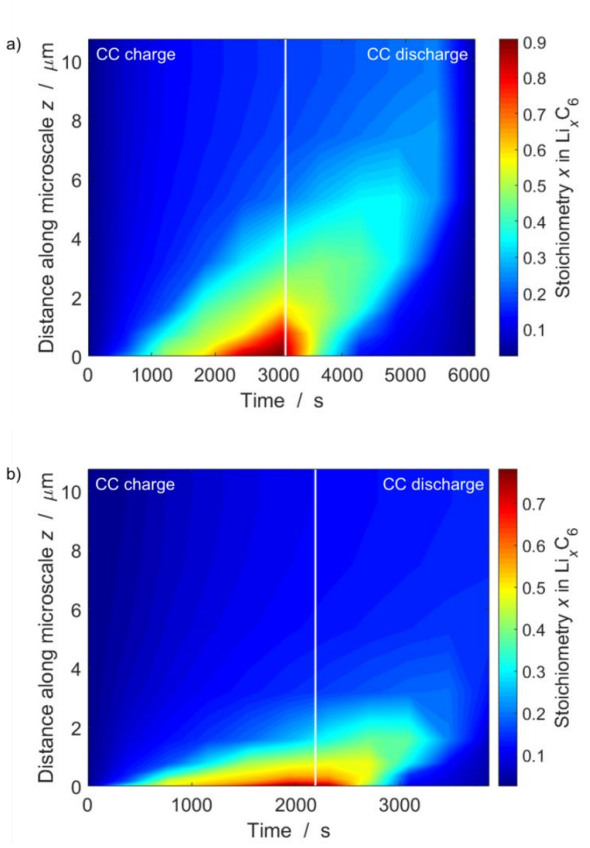

FIGURE 35: LITHIUM MOLE FRACTION AS FUNCTION OF PARTICLE DIAMETER (Z SCALE). HERE SHOWN A 1C CC CHARGE-DISCHARGE CYCLE AT A) +10 °C AND B) -10 °C.

5.4.2.3 PLATING CONDITIONS

In Section 5.2 we have seen how both thermodynamics and kinetics have a dominant influence on plating: this parasitic process shows dependence on temperature and C-rate, with low temperatures slowing down not only the plating but also the intercalation reactions and therefore feeding the competition between them. In this case, the intercalation overpotentials can be high and drive the anode potential below the thermodynamic plating limit. This is what we will investigate here, by using the 2-reactions chemical framework: the simulations shown here start at 100 % SOC with a constant-current (CC) discharge to 3.0 V and a constant-voltage (CV) phase with C/20 cut-off current, followed by a 30 min rest and a CCCV charge to 4.2 V with C/20 final current and 30 min rest to reach equilibrium.

Figure 36 gives us an insight into the potential dynamics during a 5C CCCV cycle at 0 °C. Panel a) shows the voltage and the current density while in b) the equilibrium potentials $\Delta\phi^{\mathrm{eq}}$ of the two competing reactions (intercalation and plating) are plotted together with the half-cell potential $\Delta\phi_{\mathrm{an}}$ at the anode: you can see how the $\Delta\phi_{\mathrm{an}}$ is above the intercalation $\Delta\phi_{\mathrm{LiC6}}^{\mathrm{eq}}$ during the CCCV discharge and below during the CCCV charge (remember! when $\Delta\phi_{\mathrm{an}} > \Delta\phi^{\mathrm{eq}}$ we have an anodic reaction with oxidation, when $\Delta\phi_{\mathrm{an}} < \Delta\phi^{\mathrm{eq}}$ it is a cathodic one with reduction – our reactions are formulated in this way, i.e. $\mathrm{Li}^{+}[\mathrm{elyt}] + \mathrm{e}^{-}[\mathrm{elde}] + \mathrm{V}[\mathrm{C}_6] \rightleftharpoons \mathrm{Li}[\mathrm{C}_6]$). Figure 36c contains a zoom of the last part of the CC charge, where $\Delta\phi_{\mathrm{an}}$ gets also lower than the plating $\Delta\phi_{\mathrm{Li}}^{\mathrm{eq}}$ and this is where the plating reaction is finally favoured to intercalation ($\Delta\phi_{\mathrm{an}} < \Delta\phi_{\mathrm{Li}}^{\mathrm{eq}}$, with $\Delta\phi_{\mathrm{Li}}^{\mathrm{eq}} \neq 0$ V vs Li/Li^{+}).

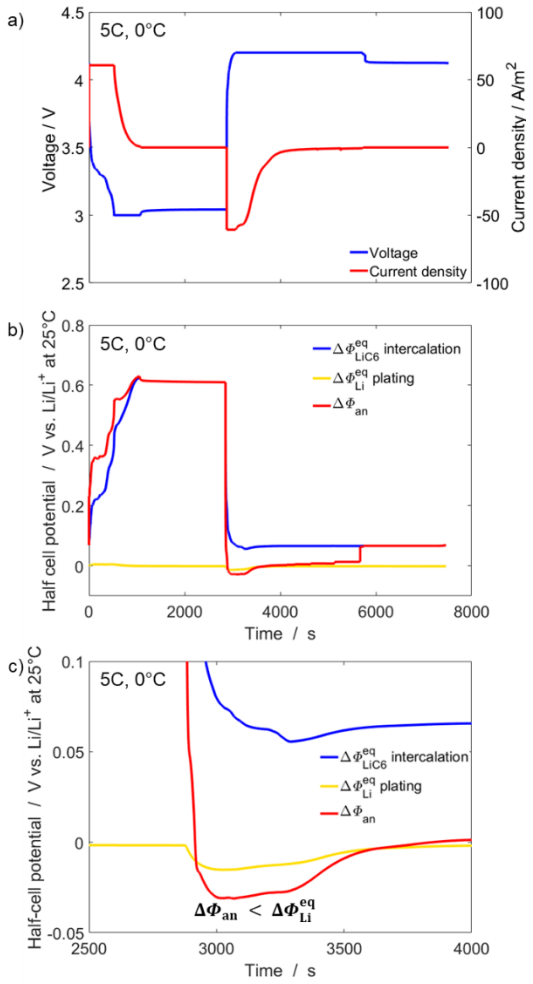

FIGURE 36: POTENTIAL DYNAMICS FOR A 5C CCCV CYCLE AT 0 °C. HERE SHOWN IN A) VOLTAGE AND CURRENT DENSITY, B) EQUILIBRIUM POTENTIALS OF THE COMPETING REACTIONS (INTERCALATION AND PLATING), TOGETHER WITH THE ANODE HALF-CELL POTENTIAL, C) ZOOM IN: THE PLATING ZONE, WHERE $\Delta\Phi_{an} < \Delta\Phi^{eq}_{Li}$ IS SATISFIED.

An insight into the effects of temperature on $\Delta\phi^{eq}_{Li}$ variation along the CCCV cycles is given in Panels a) and b) of Figure 37, respectively for 1C and 5C and for a temperature range -20 °C…30 °C (note that the value at 25 °C and a Li^+ concentration of 1 M are the reference conditions for which $\Delta\phi^{eq}_{Li} = 0$): you can see how most of the $\Delta\phi^{eq}_{Li}$ curves display negative values especially at low temperatures during charge, with the coldest temperatures clearly showing the lowest values. Because of the dependence on Li^+ concentration, $\Delta\phi^{eq}_{Li}$ also depend on the spatial position within the anode. In Figure 37c this lithiation dependence is clearly visible, with the most negative values during CC charge at the anode/separator interface (49 µm on the *y* scale), which is obviously the most involved zone for plating. Same but opposite can be said for the CC discharge, where at 49 µm we have the most positive values (hence, a favoured decomposition of plated lithium). The choice of plotting these specific seven positions, from the separator interface at 49 µm to the current collector at 98 µm, is due to the anode being discretised in seven compartments with different width along the *y* axis (the two at the extremes are 1/100 thinner than the five at the centre), while for "average" we mean the calculated average along the entire anode.

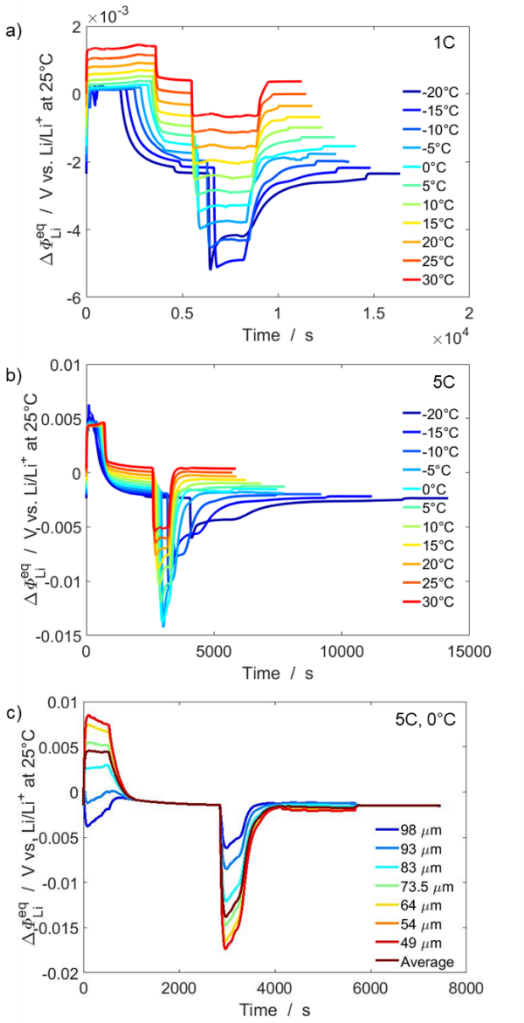

FIGURE 37: EQUILIBRIUM POTENTIAL OF THE PLATING REACTION. HERE SHOWN A) 1C AT DIFFERENT TEMPERATURES, B) 5C AT DIFFERENT TEMPERATURES, C) 5C AT 0 °C AS FUNCTION OF POSITIONS WITHIN THE ANODE (49 µM AT THE SEPARATOR INTERFACE, 98 µM AT THE CURRENT COLLECTOR INTERFACE AND "AVERAGE" AS MEAN VALUE OVER THE TOTAL WIDTH OF THE ANODE).

As you can see, this type of plots are extremely useful to understand the spatiotemporal profiles previously shown in 5.4.2.1.

5.4.3 SIMULATING DEGRADATION: OPERATION MAPS

We all know how fast charging of lithium-ion batteries remains one of the most delicate challenges for the automotive industry, because of the formation of lithium metal at the anode: thus, a semi-qualitative calculation and representation of the electrode degradation caused by the plating process would be highly desirable. At this point of our analysis this can be easily achieved and, in this paragraph, we will discuss four different methods of simulating and representing through intuitive colourmaps the "risk zones" and the "safe havens" for fast charging over a wide range of operating conditions. We use the same cycling protocol as described in Section 5.4.2.3, that is CCCV cycles from 10C down to 0.05C in a temperature range from -20 °C to +30 °C. For the results shown in Figure 38, it should be kept in mind that the present 2-reactions model represents a high-power cell; high-energy cells are expected to have an even lower plating threshold.

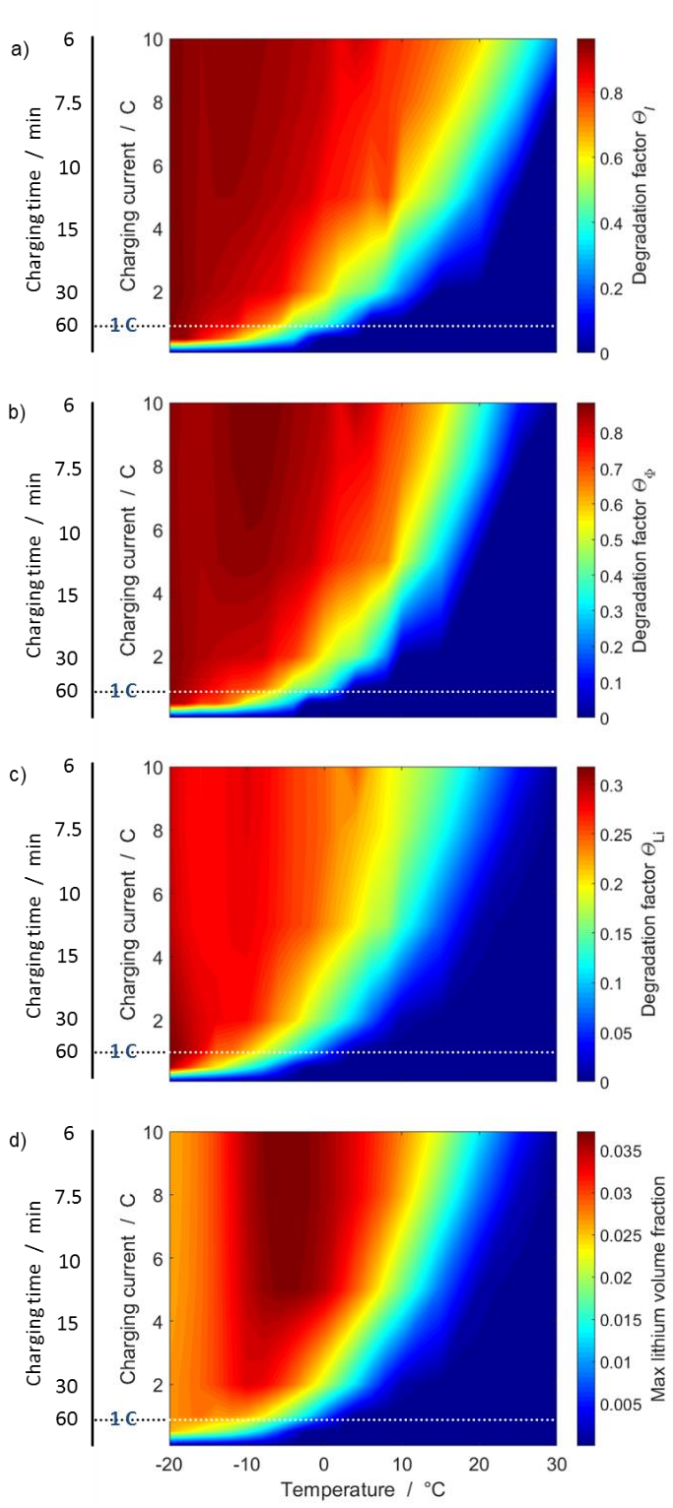

FIGURE 38: OPERATION COLORMAPS OF A CCCV CYCLE WITH CONVERSION C-RATE/CHARGING TIME ON THE SIDE (DASHED LINE SET AT 1C = 60 MIN CHARGING TIME). IN A) THE Θ_I DEGRADATION FACTOR REPRESENTS THE RATIO OF CHARGE INPUT WHEN THE POTENTIAL CONDITION FOR PLATING $\Delta\Phi_{an} < 0$ IS SATISFIED (0 = NEVER, 1 = ALWAYS). IN B) THE Θ_Φ DEGRADATION FACTOR IS BASED ON THE POTENTIAL CONDITION FOR PLATING $\Delta\Phi_{an} < \Delta\Phi_{Li}^{eq}$. IN C) THE Θ_{Li} DEGRADATION FACTOR IS DEFINED AS RATIO OF THE INTEGRATED PLATING RATE OVER THE INTEGRATED TOTAL REACTION RATE. IN D) THE PEAK VALUE OF PLATED LITHIUM VOLUME FRACTION FORMED DURING CYCLING IS USED AS DEGRADATION INDICATOR, WHERE A VALUE OF ZERO MEANS NO METALLIC LITHIUM WAS FORMED.

In Figure 38, four types of degradation factors are represented in four different colourmaps as function of temperature and charging current:

- Panel a) Degradation factor Θ_I (condition for plating: $\Delta\phi_{\mathrm{an}} < 0$)
- Panel b) Degradation factor Θ_Φ (condition for plating: $\Delta\phi_{\mathrm{an}} < \Delta\phi_{\mathrm{Li}}^{\mathrm{eq}}$)
- Panel c) Degradation factor Θ_{Li} (condition for plating: $\dot{s}_{\mathrm{Li}} > 0$)
- Panel d) Maximum lithium volume fraction.

Even if the four colourmaps look quite similar, the ideas behind their realisation come from very different concepts: the first two are based on thermodynamic assumptions, while the third considers also the kinetics of the plating reaction and the fourth works on the direct relationships between maximum quantity of plated lithium formed and damage at the anode. Let's see them in detail.

The degradation factor Θ_I in Panel a) has been previously developed by Tippmann[17] and it is obtained by integration of the current value during charge, using the following assumption:

$$\Theta_I = \frac{\int_{\Delta\phi_{\mathrm{an}}<0} I\,\mathrm{d}t}{\int I\,\mathrm{d}t} \quad . \tag{110}$$

This expression assumes that plating begins when $\Delta\phi_{\mathrm{an}}$ simply drops below 0 V, with the integrals extending over the charging time only. As the charged capacity (that is, the current integrated) differs for the applied conditions, the degradation factor Θ_I must be normalised to the total charge. According to this map, a harming situation (with highly probable plating formation and consequent electrode degradation) can be found at $T < 0$ °C for most of the C-rates, while "safe" conditions for fast charging are present only when $T > 25$ °C.

The degradation factor Θ_Φ is plotted in Panel b) uses the same approach but with a substantial difference: here the plating reaction has been included in the model, thus the thermodynamic limit for plating is not fixed to 0 V as for Θ_I, but varies along the CCCV cycle. Hence

$$\Theta_\Phi = \frac{\int_{\Delta\phi_{\mathrm{an}}<\Delta\phi_{\mathrm{Li}}^{\mathrm{eq}}} I\,\mathrm{d}t}{\int I\,\mathrm{d}t} \ , \tag{111}$$

where the integrals again extend over the charge only and the factor must be consequently normalised to the total charge. $\Theta_\Phi = 1$ means that the anode potential stays below the equilibrium potential $\Delta\phi_{\mathrm{Li}}^{\mathrm{eq}}$ during the whole charging process. If plating is absent, as we can see for the warmer temperatures and lower C-rates, the anode potential will always be over the critical value and $\Theta_\Phi = 0$. According to this map, a harming situation can be found at most of the conditions when temperatures are under 0 °C but, if we stay at ambient temperature, the risk of plating can be easily avoided even at high C-rates and the fast charging becomes definitely possible (at 10C the charging time is equal to only 6 minutes). This more accurate map has a more positive outlook than the first one: worth noting anyway that for both Θ_Φ and Θ_I the maximum values go up to around 0.9, meaning that, for the most critical conditions, the largest part of the charging phase is within the thermodynamic plating limit.

Panel c) shows a colourmap about the degradation factor Θ_{Li} : here we use $\dot{s}_i$ (mol m^{-3} s^{-1}) to indicate the rate of formation of the species i (here intercalated lithium $\mathrm{Li}[\mathrm{C}_6]$ and plated lithium Li). Considering the plating reaction as parasitic towards the intercalation reaction, we obtain a normalised degradation factor Θ_{Li} by

integrating $\dot{s}_{\mathrm{Li}}$ and dividing it by the sum of the integrated $\dot{s}_{\mathrm{LiC6}}$ and $\dot{s}_{\mathrm{Li}}$, both only for positive rates of formation, according to

$$\Theta_{\mathrm{Li}} = \frac{\int_{\dot{s}_{\mathrm{Li}}>0} \dot{s}_{\mathrm{Li}}\, \mathrm{d}t}{\int_{\dot{s}_{\mathrm{LiC6}}>0} \dot{s}_{\mathrm{LiC6}}\, \mathrm{d}t + \int_{\dot{s}_{\mathrm{Li}}>0} \dot{s}_{\mathrm{Li}}\, \mathrm{d}t}\ , \tag{112}$$

which actually gives us the ratio of plated lithium to the total amount of lithium involved in the reactions at the anode (intercalated + plated), physically representing a ratio between quantities in $\mathrm{mol} \cdot \mathrm{m}^{-3}$.

Worth noting that for Θ_{Li} the integral is calculated when the formation rate is positive and not only during the charge process, which allows this degradation factor to include in the calculation the eventual (solution-mediated) re-intercalation happening during rest or discharge. Panel c) shows a possibly more realistic overview of the degradation at the anode, being the kinetics now included: we see Θ_{Li} peaking at much lower values than before, with a maximum of only 0.3 at temperatures below -10 °C and high C-rates above 1C, while no plating or very low values are detected over 10 °C for most of the currents. Thus, Θ_{Φ} and Θ_{I} strongly overpredict the plating propensity as compared to Θ_{Li}: this is quite coherent with our simulations and what discussed in the previous sections.

Finally, the last panel. Panel d) shows an alternative and quite intuitive way of representing degradation at the anode, using the simulated lithium volume fraction according to the (logical) assumption that higher the fraction, higher the resulting degradation. Therefore, the maximum lithium volume fraction reached during the cycle is here plotted as function of temperature and C-rate. The first thing catching the eye is a strongly marked "risk zone" not at the lowest *T* but in the temperature zone between -10 and 0 °C: as we know, both plating and intercalation reactions are slowed down at these temperatures, but the interplay between the two finds here plating in a more competitive position due to its smaller activation energy. Looks like a cold winter day in Northern Italy could not be the best one to fast charge your battery and that you could surprisingly have it better in Lapland!

By looking at these colourmaps, it is definitely clear that the plating mechanism is not just a matter of thermodynamic limits or kinetics, but is comes instead from a combination of both, including also the transport processes and the competition between the parallel and counteracting reactions at the anode.

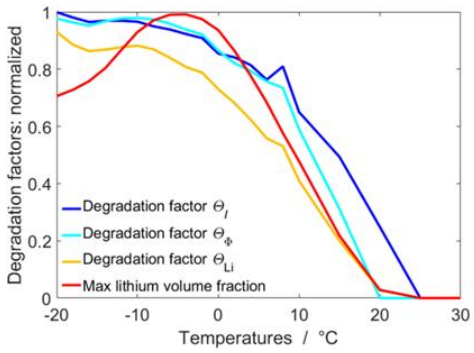

FIGURE 39: DEGRADATION FACTORS FROM THE COLORMAPS IN FIGURE 38, NORMALISED TO THEIR RESPECTIVE MAXIMUM VALUES. HERE ARE SHOWN THE CURVES FOR 5C. THE PLOT HIGHLIGHTS THE DIFFERENCES BETWEEN THE FOUR DIFFERENT METHODS AND HELPS IN THEIR COMPARISON.

Figure 39 shows therefore a comparison of the four approaches at 5C: the values from the four degradation factors, normalised to their individual maximum value reached over the full colormap range, are plotted versus temperature to highlight the similarities and differences between them. Above 20 °C the outlook is quite positive for all the degradation factors except Θ_I that tends to be most pessimistic (but we also know Θ_I to be the least accurate). For temperatures under 0 °C Θ_I , Θ_Φ and Θ_{Li} have similar curves (with Θ_{Li} showing lower values) and the highest degradation peak is reached at the most critical conditions at the left top of the plot. The fourth curve, representing the maximum plated lithium volume fraction, in this behaves differently with the most harming values in the zone between -10 and 0 °C, as expected from our discussion above.

5.5 Conclusion and next challenges

"Very nice! Great success!"
(from *Borat: Cultural Learnings of America for Make Benefit Glorious Nation of Kazakhstan*)

In the present Chapter, we have introduced a successful extension of the "ideal" model from Chapter 4 with the purpose of simulating reversible lithium plating over a wide range of conditions. Here the equilibrium potential of the plating reaction, now included at the anode, is not always equal to 0 V, as commonly assumed in literature, but varies according to the local temperature and lithium-ion concentration. A systematic approach towards parameterisation and validation of the plating reaction was applied: we started with an extensive literature research to choose a coherent set of thermodynamic and kinetic parameters and then we went through a comparison respectively with experiments on our reference cell (where no macroscopic plating hints were present and an extra re-intercalation reaction was included) and published experimental data (where instead voltage plateau and voltage drop were clearly visible). The simulations showed a good qualitative agreement with experiments but still some quantitative differences, probably related to morphological features of the plated lithium, which are not yet included in the present model, and to some imprecisions in the general parameterisation of the model which have now become visible at low temperatures (i.e. the CC charge plateau and the discharge "bump" not found in the experiments). We concluded with the construction of different definitions of "degradation factors" which have been colourfully converted into operational maps as an intuitive way to assess reversible plating propensity during CCCV cycles over a wide range of conditions. Inclusion of irreversible plating and consequent formation of dendrites and so-called "dead lithium" are still missing but expected to be added in the future to predict long-term ageing and capacity loss.
What is also missing at the moment is the interaction between the Solid Electrolyte Interphase (SEI, see 3.1.1.1) and the plated lithium: this will be discussed in a preliminary way (being a work in progress) in Chapter 7, but before let's take a flight to the other side of the Atlantic Ocean and learn a bit more about SEI and its characteristics.

6 SOLID ELECTROLYTE INTERPHASE (SEI): A BACK-STABBING FRIEND

"Betrayal answers betrayal, the mask of love is answered by the disappearance of love."
(Albert Camus)

With this Chapter we finally enter the last part of this dissertation, about SEI. We have already been talking about it in Chapter 3 while discussing the fundamentals of lithium-ion battery ageing, together with lithium plating and the other degradation mechanisms. We know the electrolyte reduction products can form SEI at the anode surface: a layered structure ionically conductive but electrically resistive, the SEI is self-passivating and therefore prevents further electrolyte degradation, even if its continuous growth in case of extended cycling could lead to capacity fade and a shortening of battery lifetime. While this subject has been studied and elaborated in our team by Kupper[19,77,188] and then included in a modelling framework, a different approach was going on at the same time in Prof. DeCaluwe's team at Colorado School of Mines (USA) - where I personally had the opportunity to work for a six-weeks period in 2019 as guest scientist. Needless to say, most of the research, both theoretical and experimental, had already been done before my arrival, hence the job was mainly to understand and properly parameterise the three different models here exposed. As we will see, all of them are 1D models with the purpose of describing SEI formation and growth on a non-intercalating anode, ideally with the purpose of being included in future in bigger and more comprehensive multiscale frameworks as the one exposed in Chapter 4. At the moment, there is truly a need for a greater chemical and spatial understanding of this very special interfacial layer, which can easily transform from a helpful friend to a damaging enemy of our battery.
It is important again to emphasize that what is exposed here is just a small part of a bigger study still in a preliminary phase: yet, it is interesting to be discussed as a different approach on the SEI modelling subject. Last but not least, the plots in this Chapter have been obtained via Python at CSM and were kindly provided by Prof. DeCaluwe, therefore they differ in style from the standard plotting style of this dissertation (obtained instead via Matlab at HSO).

6.1 FROM EXPERIMENTS TO MODELLING

"Life is short and information endless:
nobody has time for everything."
(Aldous Huxley, from *Brave New World*)

6.1.1 THE EXPERIMENTS

First of all, we need experiments. In this case the study of reference is from Lee *et al.*[189] , in which the SEI on a non-intercalating tungsten anode was measured by operando neutron reflectometry (NR) and electrochemical quartz crystal microbalance with dissipation monitoring (EQCM-D). Without going into details, NR measures the

reflected intensity of a highly collimated neutron beam as a function of the grazing angle (or scattering vector): neutrons are highly penetrating and weakly interacting hence they do not alter the chemicals, which makes them particularly fit for analysing the SEI layers. The obtained high-resolution 1D depth profiles of the neutron scattering length density are a function of the local composition, with a resolution in the order of the nanometre scale. Talking about EQCM-D, it measures the vibration frequency and dissipation of a piezoelectric crystal under a sinusoidal voltage input and it is used to determine the SEI mass with high sensitivity. Finally, the choice of studying a non-intercalating electrode is due to a lack of knowledge about the chemistry of the electrolyte and, consequently, a better focus on the electrochemical signals derived from the only SEI growth without the influence of any intercalation-related artefacts. More details about the protocols and the electrochemical measurements can be found in the said paper[189] , while here we will more focus on the analysis of the results and on how they have been used to parameterise and build the 1D-model(s) this Chapter is about.

Nine cyclic voltamograms (CV) at 10 mV/s between 0.05 and 1.5 V vs. Li/Li^+ and at a controlled temperature of 30 °C were used to grow the SEI on the surface: before that, a so-called "Pre-SEI", a liganding layer with nearly organic composition, is actually detected. This layer, probably formed from preliminary electrolyte degradation products, is then either totally or partially removed when the SEI gets added, and in the last case it gets incorporated in the final SEI composition. The newly formed SEI is then observed via NR and EQCM-D, to show a dual-layer structure composed of a thin (around 3.7 nm) but highly dense inorganic inner core and a thicker (around 15.4 nm) outer layer with organic composition and porous structure. The SEI layer mass was found to be around 1207.2 ng/cm^2 at the end of the nine potential cycles. Finally, the results reveal two main reduction processes during the SEI growth: the first one at ~0.75 V and the second one at < 0.25 V (vs. Li/Li^+), with the current and the mass deposition decreasing with increasing number of cycles as proof of the passivating characteristics of the SEI. For a deeper outlook, Monte Carlo simulations were developed for this study to identify SEI chemical compositions, by using data about the layers thickness and the volume fractions of the most common SEI compounds for both the inner and outer layers. The inner SEI is expected to contain mostly inorganic compounds, in particular Li_2O, LiOH, Li_2CO_3, and LiF, while the outer SEI is expected to be composed mostly of organic compounds, above all lithium ethylene dicarbonate (aka LEDC - $(CH_2OCO_2Li)_2$) and lithium ethyl carbonate (aka LEC - $CH_3CH_2OCO_2Li$) and simple electrolyte - due to its porous structure. Anyway, the division between layers is not so rigid and the simulations contemplate the possibility of "intruders" in both layers, as pure Li or compounds normally not expected in case of a rigid segregation. A summary of the results can be seen in Figure 40: here the two histograms show the volume fraction distribution of each component for respectively the inner and outer layer. These profiles are not strictly fitted and have to be taken qualitatively, with the model being unable to discriminate between components with similar property values, such as Li_2CO_3 and LEDC or LiOH and Li_2O. The electrolyte salt used ($LiPF_6$) is known to have also a large impact on SEI composition and performance: LiF, here found above all in the inner layer, is another major SEI compound originated from salt decomposition[190]. If we observe the outer SEI histogram on the right, the organic molecules show relatively uniform values in the volume fraction range of 0–25 %, while the probability of finding the inorganics obviously appears much lower, with the pure Li even touching the 0 %.

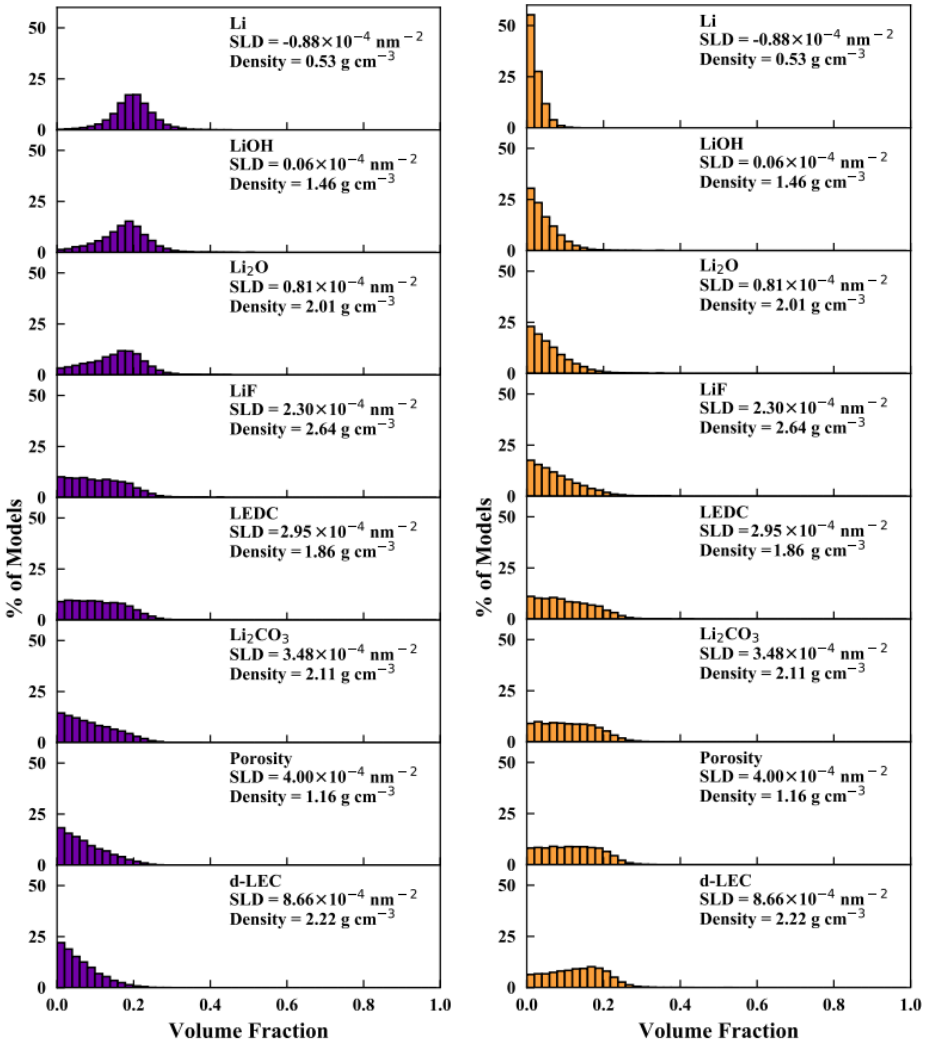

FIGURE 40: HISTOGRAMS OF (LEFT) INNER AND (RIGHT) OUTER SEI COMPONENT VOLUME FRACTIONS WHICH ARE CONSISTENT WITH BOTH THE NR AND EQCM-D. THE FIGURE IS FROM LEE *ET AL.*[189]

The results here shown have then been used as a "guide" in the parameterisation of 1D-SEI model(s) presented below, which is inspired to a previous Newman-type framework developed by Colclasure *et al.*[191] .

6.1.2 THE MODEL(S) BASICS

In this paragraph we discuss the basics of the 1D-SEI model(s): as we will see in the following Section, three models have been elaborated with a decreasing level of detail ("detailed", "homogeneous", "reduced") but the theory behind stays the same for all of them. Let's start with some assumptions.

First, the SEI is actually modelled here as a laterally homogeneous mixture of species, with activity equal to mole fraction. In reality, the SEI is more a laterally inhomogeneous mixture with activity = 1 and reaction rates scaling with surface area, but this current approximation gives anyway qualitatively correct results in a computationally-tractable manner. Second, the electrolyte composition is currently assumed constant and uniform, without transport equations and temporal composition variations. Third, charge neutrality is assumed and applied, to

calculate the potential difference at all phase interfaces. The validity of all these assumptions can be obviously questioned, but this is a reasonable approach to the problem with likely only minor impacts on the results.

Figure 41 shows a schematic representation of the 1D-SEI modelling domain. With discretisation applied, the SEI grows in the *z* direction from an initial thickness δ_{SEI} of 0.01 nm (set as computational lower limit), with each control volume *j* (here N_j= 5 as example) having a Δz thickness.

The rate of progress for a given reaction n is modelled via elementary electrochemistry (as already seen in 2.2.5)

$$r_{n,\mathrm{SEI}} = k_{\mathrm{f}} \prod_i^{N_{\mathrm{R}}} c_i^{|\nu_{i,n}|} - k_{\mathrm{r}} \prod_i^{N_{\mathrm{P}}} c_i^{|\nu_{i,n}|} \ , \tag{113}$$

where c_i refers to the concentrations of the single species i. The forward and reverse rate constants for the different reactions *n* are respectively defined as

$$k_{\mathrm{f}} = k_{\mathrm{f}}^0 \cdot \exp\left(-\frac{\alpha_{\mathrm{f}} zF}{RT}\Delta\phi\right) \tag{114}$$

$$k_{\mathrm{r}} = k_{\mathrm{r}}^0 \cdot \exp\left(\frac{(1-\alpha_{\mathrm{f}}) zF}{RT}\Delta\phi\right). \tag{115}$$

Because the SEI is not a smooth film growing continuously but rather discrete phases mixed together, in this model the microstructure evolution is approximated by describing the growth process as that of a series of spherical particles with diameter d_{SEI} (in this model $\Delta z = d_{\mathrm{SEI}}$), similarly to what done in a previous work from Single *et al.*[66] .

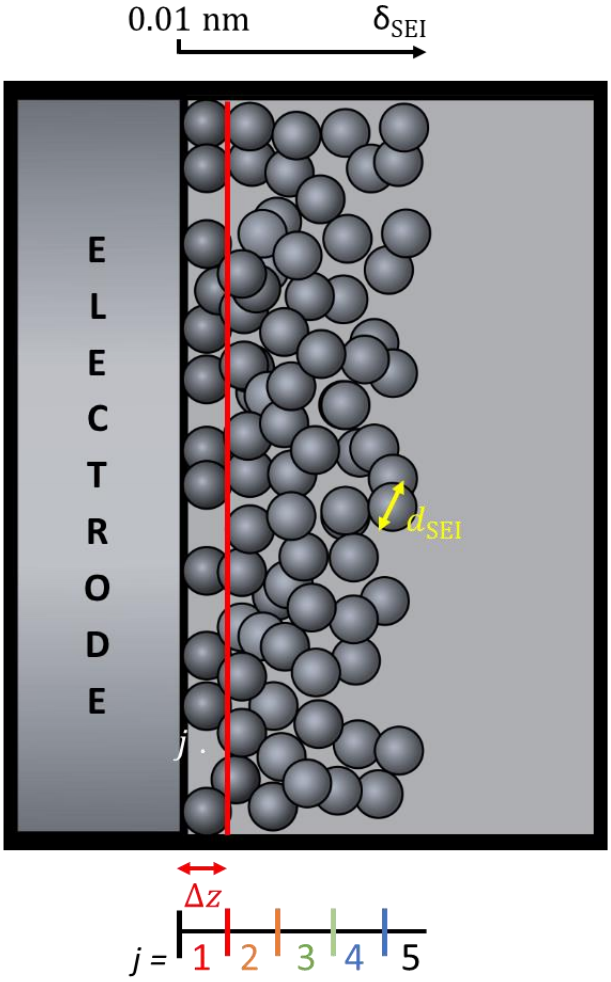

FIGURE 41: SCHEMATIC REPRESENTATION OF 1D-SEI MODELLING DOMAIN. HERE N_j= 5.

Hence, we assume a representative spherical SEI particle with fixed diameter d_{SEI} and we define a local surface area $A_{\mathrm{surf},j}$ for a volume *j* according to

$$A_{\mathrm{surf},j} = (1-\varepsilon_{\mathrm{SEI},j})\left(\frac{\varepsilon_{\mathrm{SEI},j-1}}{\Delta z}+\frac{4\,\varepsilon_{\mathrm{SEI},j}}{d_{\mathrm{SEI}}}\right), \tag{116}$$

depending on the local volume fraction $\varepsilon_{\mathrm{SEI},j}$ and that of the adjacent one $\varepsilon_{\mathrm{SEI},j-1}$. Looking at $\left(\frac{\varepsilon_{\mathrm{SEI},j-1}}{\Delta z}+\frac{4\,\varepsilon_{\mathrm{SEI},j}}{d_{\mathrm{SEI}}}\right)$ on the right, the first term $\frac{\varepsilon_{\mathrm{SEI},j-1}}{\Delta z}$ refers to the volume fraction of the previous control volume (*j*-1) in the direction of the electrode. If this control volume has a volume fraction $\varepsilon_{\mathrm{SEI},j-1}$ occupied by SEI, then that same percentage of the interface between volume (*j*-1) and volume *j* has SEI surface present, which is active in volume *j* for SEI surface reactions. The second term $\frac{4\,\varepsilon_{\mathrm{SEI},j}}{d_{\mathrm{SEI}}}$ refers to the specific surface area of these particles due to the SEI phase growing inside of volume *j*, with $\frac{\varepsilon_{\mathrm{SEI},j-1}}{\Delta z}$ being therefore the surface area per volume (*j*-1). Worth noting, in reality the first term should shrink as the second becomes larger (as the volume fills up with SEI, the surface area exposed in the previous volume (*j*-1) will no longer be accessible), but this is handled qualitatively by the $(1-\varepsilon_{\mathrm{SEI},j})$ pre-factor which reduces the overall available surface area available as $\varepsilon_{\mathrm{SEI},j}$ approaches 1.0.

When $\varepsilon_{\mathrm{SEI},j}$ is equal to 1.0, the volume is "full" (this is required for the model to move the growth process to the next volume *j*+1): the last control volume $j_{\max}$ has $\varepsilon_{\mathrm{SEI},j} \leq 1.0$ and it is where δ_{SEI} is calculated (see Eq. 133).

The SEI growth rate follows as

$$\frac{\partial \varepsilon_{\mathrm{SEI}}}{\partial t} = \sum_{i,\mathrm{SEI}} \frac{M_i A_{\mathrm{surf}}}{\rho_i \Delta z}\dot{s}_{\mathrm{i}}\ , \tag{117}$$

where M_i refers to the molar mass of the single species i and $\dot{s}_i$ to their formation rate in 1D according to

$$\dot{s}_{\mathrm{i}} = \sum_n (\nu_{i,n} r_{n,\mathrm{SEI}})\ . \tag{118}$$

This model is built on a non-intercalating anode, as follows from the experiments discussed in 6.1: therefore, there is no lithium ion flux through the SEI. The electronic conductivity is defined as a volume-weighted average of the individual species local conductivities for a volume *j* (as we will see, these are fitted parameters from literature), which are here defined as

$$\sigma_{\mathrm{elec},j} = \sum_i \varepsilon_{\mathrm{SEI},i}\sigma_{\mathrm{elec},i}\ . \tag{119}$$

Worth remembering, for every control volume *j*

$$\varepsilon_{\mathrm{SEI},j} = \sum_i \varepsilon_{\mathrm{SEI},i}\ , \tag{120}$$

where $\varepsilon_{\mathrm{SEI},i}$ is the volume fraction of i in the total SEI, summed then over all species i in the SEI. Because the species have different molar volumes, $\varepsilon_{\mathrm{SEI},i}$ is calculated as

$$\varepsilon_{\mathrm{SEI},i} = \frac{V_i X_{\mathrm{i}}}{\sum_i V_i X_i}\ , \tag{121}$$

where $V_i = \frac{M_i}{\rho_i}$ is the molar volume of species i and, following species conservation at any given point in time,

$$X_i = \frac{c_i}{\sum_i c_i}\ . \tag{122}$$

About the conservation of charge for electric potentials, charged double layers are integrated in the model at both the electrode-SEI and SEI-electrolyte interfaces.

Both potential differences are governed by

$$\frac{\partial \Delta\phi_{\mathrm{DL}}}{\partial t} = \frac{i_{\mathrm{DL}}}{C_{\mathrm{DL}}}\ , \tag{123}$$

where for the relevant $\Delta\phi_{\mathrm{DL}}$ we have respectively at the electrode-SEI interface

$$\Delta\phi_{\mathrm{DL}} = \phi_{\mathrm{elde}} - \phi_{\mathrm{SEI}} \ , \tag{124}$$

and at the SEI-electrolyte interface

$$\Delta\phi_{\mathrm{DL}} = \phi_{\mathrm{SEI}} - \phi_{\mathrm{elyt}} \ . \tag{125}$$

6.1.3 CANTERA MEETS PYTHON

Once we defined the theoretical basics and coded them in Python, the next step is to couple the 1D-SEI model(s) with something we are familiar with, a .cti file describing all the species/phases and reactions there included. Values like the d_{SEI} (equal to $2{\cdot}10^{-9}$ m), the initial SEI thickness δ_{SEI} (0.01 nm - computational lower limit) and the thermodynamics (Table 10) are fixed at the beginning and common at all the three different models ("detailed", "homogeneous", "reduced") but other parameters, such as the reaction rates and the electrical conductivities, vary and need to be fitted using the SEI layers thickness (inner, outer and total) and their species volume fractions (from Figure 40) as qualitative guide. These means the chosen values are not "real" but assumed to obtain the best fit for each of the models.

TABLE 10: PROPERTIES OF ALL PHASES INCLUDED IN THE 1D-SEI MODEL.

Phase	Density ρ / kg·m^{-3}	Species	Initial mole fraction X_i	Molar enthalpy h_i / kJ·mol^{-1}	Molar entropy s_i / J·mol^{-1}·K^{-1}	Reference
SEI						
	2110	LEDC[SEI]	0.8	-1374.3	88.8	[19]
	2013	Li_2CO_3[SEI]	0.1	-1214.1	90.1	[19]
	1321	Li_2O[SEI]	0.1	-597.9	37.6	[97]
Electrolyte	1208.2					
		$C_3H_4O_3$[elyt]	0.52	$f(T)$	$f(T)$	[126]
		$C_4H_8O_3$[elyt]	0.3398	0	0	Dummy value
		Li^+ [elyt]	0.07	0	0	Assumed
		PF_6^-[elyt]	0.07	0	0	Dummy value
		$C_2H_6O_2$[elyt]	0	-460	163.2	[97]
		H_2O[elyt]	0.0001	-285.8	70	[97]
		C_2H_4	0	$f(T)$	$f(T)$	[126]
		CO, CO_2	0	$f(T)$	$f(T)$	[126]
Tungsten	1925					
		Electron	1.0	0	0	Assumed
Conductor	1925					
		e^-(SEI)	1.0	0	0	Assumed

6.2 ONE SEI, THREE MODELS

"To define is to limit."
(Oscar Wilde)

As shown in 6.1.2, the transport in the 1D-SEI model(s) is quite simple. Since this study is validating against data on a non-intercalating anode, only electron (and not Li^+ ion) transport is included, where the electronic conductivity σ_{elec} is typically calculated as an average of the main SEI components conductivities weighted by their local mole fractions. Being this only a preliminary study, only three SEI components have been chosen and their formation reactions included: the organic LEDC[SEI] for the outer layer, the inorganic Li_2O[SEI] for the inner layer and Li_2CO_3[SEI] as "jolly species" present in both, which conductivities are then fitted within a reasonable range according to σ_{elec} LEDC[SEI] ≤ σ_{elec} Li_2CO_3[SEI] < σ_{elec} Li_2O[SEI] [58]. The electronic conductivities of the said SEI species and the reaction rates of the included electrochemical reactions visibly change between the three different versions of the SEI model, which mainly differ in the level of SEI detail.
The process of finding the correct choice of parameters that correctly balanced each other for all the three models has actually been a lot of work. First of all, the conductivities had to be of the correct magnitude to allow electron transport away from the anode, while also giving passivation. Then the thermodynamics and kinetics had to be properly tuned so that species were deposited at the correct voltages and in the correct ratios: for example, if kinetics were too fast, LEDC would dominate and porosity would reach zero value before LEDC had enough time to degrade to Li_2O and Li_2CO_3. Finally, the meshing of the discretisation impacted both of the above: too fine a mesh and the simulation would not be stable, too thick and the required detail would be lost.

Now, let's have a look a bit more in detail to our three models. We have:

- "Detailed" model: here the SEI is discretised in 1D, and the SEI volume fraction and composition (mole fractions of each species i) are tracked as a function of time t and depth z, for every volume j according to the following species conservation equation

$$\frac{\partial c_{i,\text{SEI},j}}{\partial t} = \dot{s}_{i,\text{SEI},j} A_{\text{surf},j} \,. \tag{126}$$

  Given that, this model resolves the composition as a function of the SEI "depth" starting from the anode interface. At the SEI-electrolyte interface

$$i_{\text{DL}} = -i_{F,\text{SEI}} - \nabla i_{\text{elec}} \,, \tag{127}$$

  with $i_{F,\text{SEI}}$ is the Faradaic current proportional to the rate of production of electrons in the SEI from charge transfer reactions, and i_{elec} the electronic current in the SEI, calculated from Ohm's law

$$i_{\text{elec}} = -\sigma_{\text{elec}} \nabla \phi_{\text{SEI}} \,. \tag{128}$$

  At the electrode-SEI interface

$$i_{\text{DL}} = i_{F,\text{elde}} - i_{\text{elec}} \,, \tag{129}$$

  where $i_{F,\text{elde}}$ is the Faradaic current proportional to the rate of creation of electrons in the working electrode.

- "Homogeneous" model: the SEI thickness and composition are here tracked as a function of *t*, but the SEI is considered to have homogeneous composition – which means that when components are added or removed to/from the SEI, the entire composition consequently changes. This is equivalent to assuming that species transport (i.e. "mixing") within the SEI is infinitely fast.

  Following species conservation

  $$\frac{\partial c_{i,\mathrm{SEI}}}{\partial t} = \frac{\dot{s}_{i,\mathrm{SEI}}}{\delta_{\mathrm{SEI}}} \ , \tag{130}$$

  where $\dot{s}_{i,\mathrm{SEI}}$ is fully dependent on the composition and the SEI electric potential at the electrolyte interface. At the SEI-electrolyte interface

  $$i_{\mathrm{DL}} = \ i_{\mathrm{elec}} - \ i_{F,\mathrm{SEI}} \ , \tag{131}$$

  where now there is just a single electronic current across the homogeneous SEI.

  At the electrode-SEI interface i_{DL} is modelled as in Eq. 129.

- "Reduced" model: the simplest approach inspired by the paper from Kupper[19], with the SEI passivation approximated by dividing the SEI reaction rates by the SEI thickness δ_{SEI}.

  Following species conservation

  $$\frac{\partial c_{i,\mathrm{SEI}}}{\partial t} = \frac{\dot{s}_{i,\mathrm{SEI}} / \delta_{\mathrm{SEI}}}{\delta_{\mathrm{SEI}}} \ , \tag{132}$$

  where $\dot{s}_{i,\mathrm{SEI}}$ depends on the working electrode electric potential and is scaled by the inverse SEI thickness δ_{SEI} (in addition to the $1/\delta_{\mathrm{SEI}}$factor). In the reduced model ϕ_{SEI} is not tracked at both SEI-electrolyte and electrode-SEI interfaces.

The purpose of building three models with three different levels of complexity is to step-by-step reaching a well-parameterised reduced-order model (such as the last one) still able to describe SEI properties but computationally faster and at the same time simple enough to be included in a multiscale modelling framework as the ones shown in Chapters 4 and 5. The electrolyte is here assumed constant in composition and its transport is not yet included in the model to simply focus on the chemistry and passivation of the inner and outer SEI layers. Unfortunately, this is one of the weakest points of this preliminary study, as already addressed at the beginning of the Chapter, and its inclusion will be one of the first logical extension of this work in the future.

Let's now try the three models and have a comparison between the results.

In the following Sections, a specific operating protocol has been set to simulate the conditions of the NR experiments discussed in Section 6.1.1: sweep from an initial working electrode potential of 1.0 V (vs. Li/Li^+) to 0.5 V at a rate of 10 mV/s (50 s sweep), followed by a final hold at 0.5 V for 3600 s.

6.2.1 DETAILED MODEL

The detailed model is the most complete between the three.

TABLE 11: DETAILED MODEL. FITTED PARAMETERS: ABOVE, CHEMICAL REACTIONS AND RATE COEFFICIENTS USED IN THE PRESENT MODEL; BELOW, ELECTRONIC CONDUCTIVITIES FOR THE THREE MAIN SEI SPECIES.

SEI reactions	**Rate coefficient k_f / m³/(mol·s)**	**Activation energy $E_{act,f}$ / kJ/mol**	**Symmetry factor α_f**
Li^+[elyt] + $C_3H_4O_3$[elyt] + e^-(SEI) ⇄ 0.5 C_2H_4 + 0.5 LEDC[SEI]	$k_f = 9 \cdot 10^6$	55.5 [77]	0.5
2 Li^+[elyt] + $C_3H_4O_3$[elyt] + 2 e^-(SEI) ⇄ Li_2CO_3[SEI] + C_2H_4	$k_f = 6 \cdot 10^3$	0	0.5
2 Li^+[elyt] + Li_2CO_3[SEI] + 2 e^-(SEI) ⇄ 2 Li_2O[SEI] + CO	$k_f = 1.8 \cdot 10^4$	0	0.5
LEDC[SEI] + H_2O[elyt] ⇄ Li_2CO_3[SEI] + CO_2 + $C_2H_6O_2$[elyt]	$k_f = 5.4 \cdot 10^{-8}$	0	-
e^-(SEI) ⇄ electron	$k_f = 1 \cdot 10^{-14}$	-	-
Main SEI species	**Electronic conductivity σ_{elec} / S/m**		
LEDC[SEI]	$1.5 \cdot 10^{-8}$		
Li_2CO_3[SEI]	$4 \cdot 10^{-8}$		
Li_2O[SEI]	$9 \cdot 10^{-8}$		

Table 11 lists all the reactions included in the 1D-SEI detailed model and their fitted kinetic coefficients, together with the electronic conductivities for the three main SEI species. At the SEI/electrolyte interface, four reactions take place: the first three describe the formation of the three main species composing the SEI (LEDC[SEI], Li_2CO_3[SEI] and Li_2O[SEI], all with gas production) while the fourth describes the conversion of LEDC[SEI] to Li_2CO_3[SEI]. A fifth one, included in the model, describes the electronic interchange between the metal support (the "tungsten") and the SEI.

Figure 42 shows the SEI thickness as function of time: with the time passing, the SEI continues its growth and reaches a final value of 18 nm. For this model, the calculation of the thickness is not automatic but needs to propose a minimum volume fraction where the SEI is considered to "exist" (i.e. in the range of 2.5 – 5 %) for a particular volume *j*. At any given time, there is a number j_{max} of volumes which exceeds this minimum volume fraction and the thickness is calculated as the thickness up to volume (j_{max} -1), plus the thickness of a single volume (equal to Δz), times the volume fraction of the final such volume j_{max}:

$$\delta_{SEI} = \Delta z(j_{max} - 1) + \Delta z \cdot \varepsilon_{SEI,jmax} . \quad (133)$$

[Example: coming back to Figure 41 with N_j= 5, if at any given time we have $\varepsilon_{SEI,jmax=5} = 0.3$, the final thickness δ_{SEI} will be equal to ($4\Delta z + 0.3\Delta z$) = $4.3\Delta z$. Remember, every "full" volume has $\varepsilon_{SEI,j} = 1.0$]

Figure 43 shows the three main species volume fractions (plus the porosity) as function of the SEI depth: it is possible to see how in the first nanometres the highest volume fraction of inorganic Li_2O[SEI] is present, which then rapidly decreases leaving room for a thick highly organic layer mainly built of LEDC[SEI] (reaching 80 % in

volume between 5 and 15 nm depth). Li_2CO_3[SEI] volume fraction stays nearly constant (between 10 and 20 % in volume) and works as "jolly" component present in both layers. At a depth of 15 nm we can finally notice an increase in porosity, with the electrolyte reaching 100 % in volume (hence, the solid limit of the SEI) at ~19 nm. Qualitatively, those results are consistent with the dual-layer structure composed of a thin (around 3.7 nm) but highly dense inorganic inner core and a thicker (around 15.4 nm) organic outer layer with porous structure shown by experiments. Note that to simulate a truly porous outer layer a proper modelling of electrolyte transport should also be included (and at the moment, it is not yet).

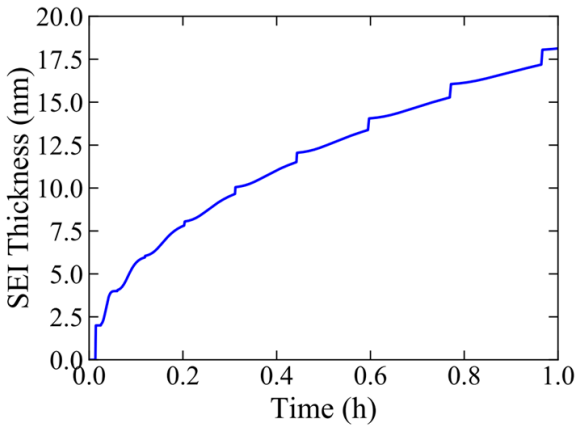

FIGURE 42: DETAILED MODEL. SEI THICKNESS AS FUNCTION OF TIME.

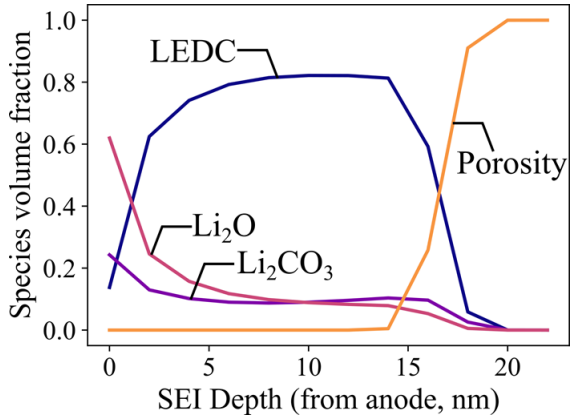

FIGURE 43: DETAILED MODEL AT T = 3650 S. SPECIES VOLUME FRACTIONS (PLUS THE POROSITY) AS FUNCTION OF SEI DEPTH.

6.2.2 HOMOGENEOUS MODEL

The homogeneous model is less complex than the detailed one, therefore more approximate in its results (NB this model provides already a speed-up of more than 50x compared to the detailed one). Here the SEI thickness and composition are tracked as a function of time, without the spatial detail found in the detailed model: the SEI thickness δ_{SEI} is tracked as a state variable

$$\frac{\partial \delta_{\mathrm{SEI}}}{\partial t} = \sum_i \dot{s}_i V_i \ , \tag{134}$$

where V_i is the molar volume of species i.

TABLE 12: HOMOGENEOUS MODEL. FITTED PARAMETERS: ABOVE, CHEMICAL REACTIONS AND RATE COEFFICIENTS USED IN THE PRESENT MODEL; BELOW, ELECTRONIC CONDUCTIVITIES FOR THE THREE MAIN SEI SPECIES.

SEI reactions	**Rate coefficient k_f / m³/(mol·s)**	**Activation energy $E_{act,f}$ / kJ/mol**	**Symmetry factor α_f**
Li^+[elyt] + $C_3H_4O_3$[elyt] + e^-(SEI) ⇄ 0.5 C_2H_4 + 0.5 LEDC[SEI]	$k_f = 2.8 \cdot 10^8$	55.5 [77]	0.5
2 Li^+[elyt] + $C_3H_4O_3$[elyt] + 2 e^-(SEI) ⇄ Li_2CO_3[SEI] + C_2H_4	$k_f = 1.05 \cdot 10^7$	0	0.5
2 Li^+[elyt] + Li_2CO_3[SEI] + 2 e^-(SEI) ⇄ 2 Li_2O[SEI] + CO	$k_f = 1.4 \cdot 10^7$	0	0.5
LEDC[SEI] + H_2O[elyt] ⇄ Li_2CO_3[SEI] + CO_2 + $C_2H_6O_2$[elyt]	$k_f = 2.1 \cdot 10^{-8}$	0	-
e^-(SEI) ⇄ electron	$k_f = 2 \cdot 10^{-11}$	-	-
Main SEI species	**Electronic conductivity σ_{elec} / S/m**		
LEDC[SEI]	$1 \cdot 10^{-10}$		
Li_2CO_3[SEI]	$2 \cdot 10^{-9}$		
Li_2O[SEI]	$3.2 \cdot 10^{-9}$		

All reactions included in the 1D-SEI homogeneous model and their fitted kinetic coefficients are listed in Table 12 together with the electronic conductivities for the three main SEI species. As you can see, all the rate coefficients and the electronic conductivities differ from Table 11.

Figure 44 shows the SEI thickness as function of time: with the time passing, the SEI continues growing but slows down as the passivation effect kicks in, reaching a thickness of ~19 nm after 3600 s. Anyway, the growth, which is proportional to $\sqrt{t}$, does not seem to reach finally a plateau. Figure 45 shows instead the three main species volume fractions as function of time: here the SEI is considered to have homogeneous composition, hence the curves shows how the averaged volume fractions change with time. In the first moments LEDC[SEI] volume fraction drops dramatically to nearly 65 % of the total while Li_2CO_3[SEI] and Li_2O[SEI] volume fractions increase to reach their final average values between 15 and 20 %. Worth noting that here the porosity is not included and the SEI is described as a compact structure mainly formed by organic LEDC[SEI].

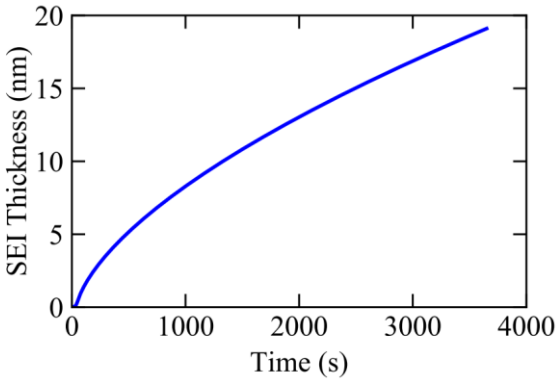

FIGURE 44: HOMOGENEOUS MODEL. SEI THICKNESS AS FUNCTION OF TIME.

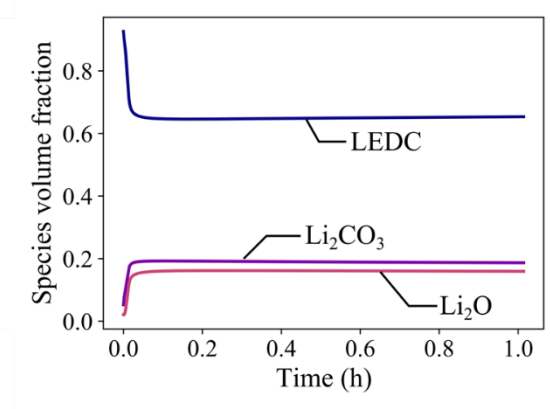

FIGURE 45: HOMOGENEOUS MODEL. SPECIES VOLUME FRACTIONS AS FUNCTION OF TIME.

6.2.3 REDUCED MODEL

The reduced model is the simplest one: the SEI passivation is approximated by dividing the SEI reaction rates by the SEI thickness δ_{SEI}, which is tracked again as a state variable (Eq. 134).

All reactions included in the 1D-SEI reduced model and their kinetic coefficients are listed in Table 13: as you can see, some of the values are the same of Table 12, being the electronic conductivities not anymore included in the calculation. The reduced model is therefore more computationally simple than the homogeneous although able to give similar simulation results (NB this model provides a speed-up of 150x compared to the detailed one).

TABLE 13: REDUCED MODEL. FITTED PARAMETERS: ABOVE, CHEMICAL REACTIONS AND RATE COEFFICIENTS USED IN THE PRESENT MODEL; BELOW, ELECTRONIC CONDUCTIVITIES FOR THE THREE MAIN SEI SPECIES.

SEI reactions	**Rate coefficient k_{f} / m³/(mol·s)**	**Activation energy $E_{\mathrm{act,f}}$ / kJ/mol**	**Symmetry factor α_{f}**
Li^+[elyt] + $C_3H_4O_3$[elyt] + e^-(SEI) ⇄ 0.5 C_2H_4 + 0.5 LEDC[SEI]	k_{f} = $7.65\cdot10^{-4}$	55.5 [77]	0.5
2 Li^+[elyt] + $C_3H_4O_3$[elyt] + 2 e^-(SEI) ⇄ Li_2CO_3[SEI] + C_2H_4	k_{f} = $1.275\cdot10^{-7}$	0	0.5
2 Li^+[elyt] + Li_2CO_3[SEI] + 2 e^-(SEI) ⇄ 2 Li_2O[SEI] + CO	k_{f} = $1.87\cdot10^{-7}$	0	0.5
LEDC[SEI] + H_2O[elyt] ⇄ Li_2CO_3[SEI] + CO_2 + $C_2H_6O_2$ [elyt]	k_{f} = $2.55\cdot10^{-20}$	0	-
e^-(SEI) ⇄ electron	k_{f} = $2\cdot10^{-11}$	-	-
Main SEI species	**Electronic conductivity σ_{elec} / S/m**		
LEDC[SEI]	$1\cdot10^{-10}$		
Li_2CO_3[SEI]	$2\cdot10^{-9}$		
Li_2O[SEI]	$3.2\cdot10^{-9}$		

Figure 46 shows the SEI thickness while Figure 47 illustrates the three main species volume fractions, both as function of time: turns out that the plots look very similar to the ones obtained with the homogeneous model. Again, a passivation effect is visible, with the SEI reaching a thickness of ~19 nm after 3500 s.

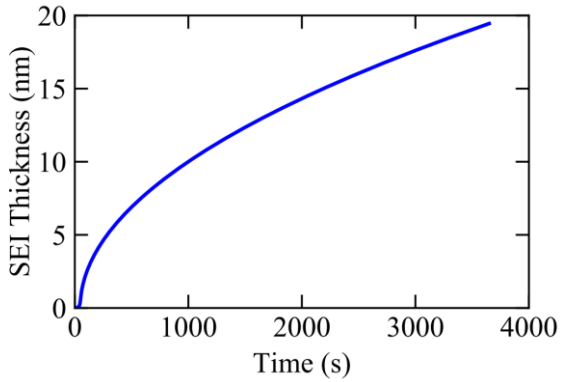

FIGURE 46: REDUCED MODEL. SEI THICKNESS AS FUNCTION OF TIME.

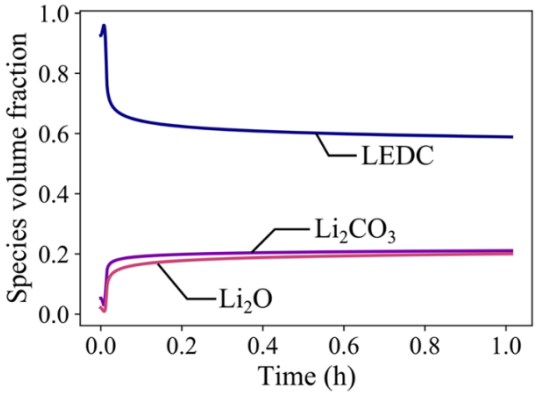

FIGURE 47: REDUCED MODEL. SPECIES VOLUME FRACTIONS AS FUNCTION OF TIME.

6.3 CONCLUSIONS AND OPEN QUESTIONS

In the present Chapter, we have presented the different approach on 1D-SEI modelling developed at Colorado School of Mines (USA), to which parameterisation I had the opportunity to contribute for a six-weeks period in 2019 as guest scientist. Specifically, three 1D-models with a decreasing level of detail ("detailed", "homogeneous" and "reduced") have been developed with the purpose of describing SEI formation and growth on a non-intercalating anode and ideally being included in future in bigger and more comprehensive multiscale frameworks as the ones exposed in the previous Chapters. The most suitable clearly is the well-parameterised reduced model, still able to describe SEI properties despite its computational simplicity: yet a working transport model for the electrolyte is still missing, which is one of the weakest points of this preliminary study. Its inclusion, together with a further development of the SEI passivation effect and the adding of more species in the SEI composition, are expected to be logical extension of this work in the future.

7 THE COUPLING

"Now join your hands, and with your hands your hearts."
(William Shakespeare)

We have now arrived at the last Chapter of this dissertation. We started with the hard theory behind our modelling and simulation framework and then we gave some basics of battery ageing, with a specific focus on SEI and lithium plating; we went through the development of the Kokam model and then we built a working extension able to simulate plating; finally, we introduced SEI with a preliminary model which gave us a deeper outlook on the subject. In this last Chapter we will now couple our plating model with an SEI model previously developed and now partially modified to include the pushing effect of the plating formation on the SEI growth and their complex interactions. Note that we decided to not use the 1D-SEI reduced model presented in Chapter 6, being the model still incomplete and its integration in our P3D framework not so immediate. The prediction of thermal and ageing effects is actually fundamental for a comprehensive understanding of batteries performance and behaviour: several research groups[192–194] have already addressed the need of a comprehensive model for the SEI growth at the electrodes, strongly linked to the unwanted deposition of metallic lithium on the anode surface. Remember, what shown here is at the moment a work in progress: hence, this Chapter has to be considered preliminary, not definitive in its analysis and, above all, open for discussions.

7.1 WHEN LITHIUM PLATING MEETS SEI

"The meeting of two personalities is like the contact of two chemical substances:
if there is any reaction, both are transformed."
(Carl Jung)

In Chapter 3.1.1.1 we anticipated the fusion of the previously developed Kupper's SEI model[77] with the Kokam models (without and with lithium plating) extensively presented in Chapter 4 and 5. In practice, this has been made by including the SEI formation reaction for LEDC[SEI] in our modelling frameworks[78,111], together with the mechanical particle expansion due to volume changes of the graphite particles during cycling. This approach, inspired by the work of Laresgoiti *et al.*[56], assumes that the breaking of the particle-covering SEI layer during charging (originated from the tangential stress due to intercalation) leads to exposition of fresh particle surface to the electrolyte, causing accelerated formation of new SEI. The compressive stress upon deintercalation instead does not lead to ageing. If interested, a detailed explanation can be found in Kupper *et al.*[77].
What is important now, is that two models originated from this operation:

- Model 1: the Kokam model, from Chapter 4, including only the SEI formation reaction (see Table 14).

- Model 2: the Li plating Kokam model, from Chapter 5, including both the "classical" SEI formation reaction and the SEI formation induced by lithium plating (see Table 15)

TABLE 14: INTERFACIAL CHEMICAL REACTIONS AND RATE COEFFICIENTS USED IN MODEL 1 (SEI)

Interface	Reaction	Label	Rate coefficient	Activation energy $E_{act,f}$ / kJ/mol	Symmetry factor α_f
Graphite/electrolyte (anode)	$Li^+[elyt] + e^- + V[C_6] \rightleftarrows Li[C_6]$	Intercalation	i^{00} = 8.84·10^{14} A/m^2	77.1	0.5
Graphite/electrolyte (anode)	$Li^+[elyt] + C_3H_4O_3[elyt] + e^- \rightleftarrows 0.5\ LEDC[SEI] + 0.5\ C_2H_4$	SEI formation[19,77] (electrolyte-driven)	i^{00} = 8.65·10^{-11} A/m^2	55.5	0.5
LCO/electrolyte (cathode)	$Li^+[elyt] + e^- + V[LCO] \rightleftarrows Li[LCO]$	Intercalation	i^{00} = 8.20 ·10^{12} A/m^2	72.3	0.5
NCA/electrolyte (cathode)	$Li^+[elyt] + e^- + V[NCA] \rightleftarrows Li[NCA]$	Intercalation	i^{00} = 2.63 ·10^{10} A/m^2	61.0	0.5

TABLE 15: INTERFACIAL CHEMICAL REACTIONS AND RATE COEFFICIENTS USED IN MODEL 2 (SEI + LI PLATING)

Interface	Reaction	Label	Rate coefficient	Activation energy $E_{act,f}$ / kJ/mol	Symmetry factor α_f
Graphite/electrolyte (anode)	$Li^+[elyt] + e^- + V[C_6] \rightleftarrows Li[C_6]$	Intercalation	i^{00} = 8.84·10^{14} A/m^2	77.1	0.5
Graphite/electrolyte (anode)	$Li^+[elyt] + e^- \rightleftarrows Li[metal]$	Plating	i^{00} = 2.29·10^{13} A/m^2	65.0	0.492
Graphite/electrolyte (anode)	$Li[metal] + V[C_6] \rightleftarrows Li[C_6]$	Re-intercalation	k_f = 1·10^{-6} m^3/(mol·s) *	0 *	-
Graphite/electrolyte (anode)	$Li^+[elyt] + C_3H_4O_3[elyt] + e^- \rightleftarrows 0.5\ LEDC[SEI] + 0.5\ C_2H_4$	SEI formation[19,77] (electrolyte-driven)	i^{00} = 8.65·10^{-11} A/m^2	55.5	0.5
Graphite/electrolyte (anode)	$Li[metal] + C_3H_4O_3[elyt] \rightleftarrows 0.5\ LEDC[SEI] + 0.5\ C_2H_4$	SEI formation (LP-driven)	k_f =8.65·10^{-2} m^3/(mol·s) **	55.5	-
LCO/electrolyte (cathode)	$Li^+[elyt] + e^- + V[LCO] \rightleftarrows Li[LCO]$	Intercalation	i^{00} = 8.20 ·10^{12} A/m^2	72.3	0.5
NCA/electrolyte (cathode)	$Li^+[elyt] + e^- + V[NCA] \rightleftarrows Li[NCA]$	Intercalation	i^{00} = 2.63 ·10^{10} A/m^2	61.0	0.5

* Arbitrary values, set fast

** SEI growth promoted by lithium plating: calculated value to simulate a formation rate ~4 times faster (compared to electrolyte-driven SEI growth)[49]

Model 1 is actually a pure intercalation/deintercalation model enriched with an SEI formation approach while Model 2 has visibly a higher degree of complexity. In Model 2 not only lithium plating and re-intercalation reactions are included, but SEI formation happens via two different paths: one is "electrolyte-driven", forming LEDC[SEI] via reaction of Li^+ ions with the EC electrolyte; the other, "LP-driven" (i.e. LP stays for lithium plating) is induced by lithium plating and it works via direct reaction of Li[metal] with EC without charge-transfer. In both cases we have gas formation (C_2H_4, initially set as 1 % of the gas phase). We use $h^0_{\mathrm{LEDC[SEI]}} = -1383\ \frac{\mathrm{kJ}}{\mathrm{mol}}$ and $s^0_{\mathrm{LEDC[SEI\}}} = 90.1 \frac{\mathrm{J}}{\mathrm{K \cdot mol}}$, here recalculated assuming SEI formation potential of 0.8 V vs. Li/Li^+. The rate coefficient in the LP-driven SEI formation reaction has been calculated to simulate a formation rate happening ~4 times faster than the electrolyte-driven one, as suggested in Ansean *et al.*[49] about the impact of lithium plating on the SEI growth and the consequent capacity fade. Worth remembering this is just a preliminary study: we plan in the future to deepen the simulation of the capacity loss by including proper irreversible plating and different species for the SEI with specific features according to their formation and growth paths.
There is a long and winding road in front of us!

7.2 WITH OR WITHOUT PLATING

"'Same same, but different!"
(Tinglish expression – every street seller in Thailand)

To better understand the influence of plating on SEI formation and consequently how much having one or two paths (electrolyte and LP-driven) could impact on it, the easiest way is clearly to compare the two models (Model 1 and Model 2) introduced in the previous paragraph.
In Figure 48 this is done for 1C at two temperatures, -10 °C (left column) and 10 °C (right column). Panels a) and f) show simulated cell voltage and Panels b) and g) the current density (negative for charge). The average SOC of the anode, defined as in Eq. 101, is shown in Panels c) and h), while the volume fractions of Li[metal] and LEDC[SEI] are visible respectively in Panels d), i) and e), j). The protocol discharge (1C CC) – rest (15 s) – charge (1C CCCV, C/20 cut-off) – rest (15 s) is a bit different from the one previously used in 4.4.1, with no CV phase during discharge and a much shorter rest phase, and it reproduces the approach used in the study from Waldmann *et al.*[195] . Let's have a look at the left column at -10 °C, where plating is expected to be part of the game: first thing to note, the presence of plated lithium in Panel d) for Model 2 accompanies a correspondent higher volume fraction of LEDC[SEI] formed in Panel e), compared to the values obtained using Model 1. Worth remembering that all the curves started at the same initial volume fraction of $8 \cdot 10^{-4}$ set in the model and the first charge-discharge-charge cycle is simply not included here. On the right column at 10 °C, where no plating is happening, the two models look identical: what we see on the right column is the pure SEI formation and growth via classical electrolyte-driven reaction.

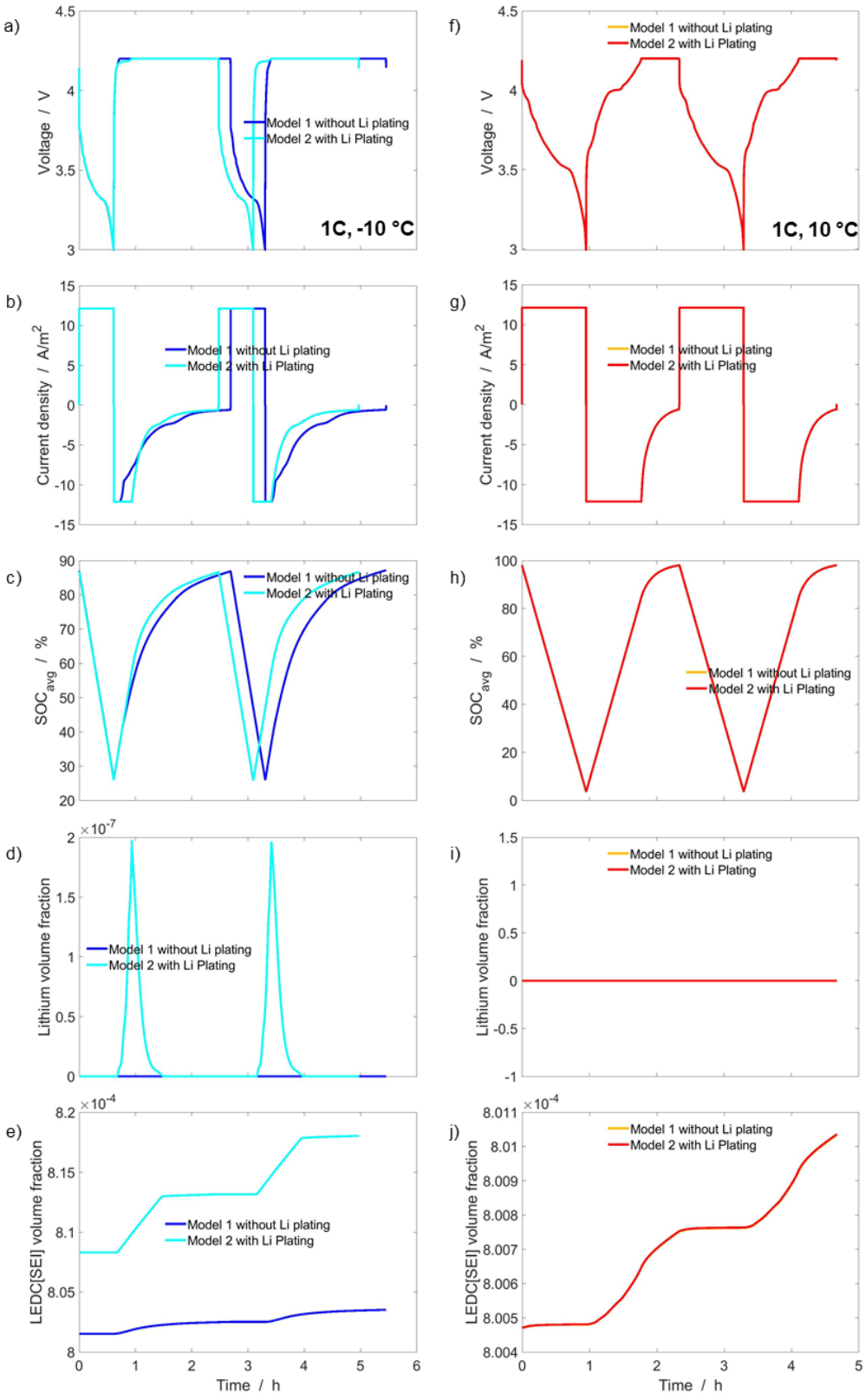

FIGURE 48: COMPARISON BETWEEN MODEL 1 (LI PLATING NOT INCLUDED) AND MODEL 2. SIMULATIONS (2 CYCLES) FOR DISCHARGE (1C CC) – REST (15 S) – CHARGE (1C CCCV, C/20 CUT-OFF) – REST (15 S). ON THE LEFT, AT -10 °C: A) VOLTAGE, B) CURRENT DENSITY, C) SOC, D) LITHIUM VOLUME FRACTION, E) LEDC[SEI] VOLUME FRACTION. ON THE RIGHT, AT 10 °C : F) VOLTAGE, G) CURRENT DENSITY, H) SOC, I) LITHIUM VOLUME FRACTION, J) LEDC[SEI] VOLUME FRACTION.

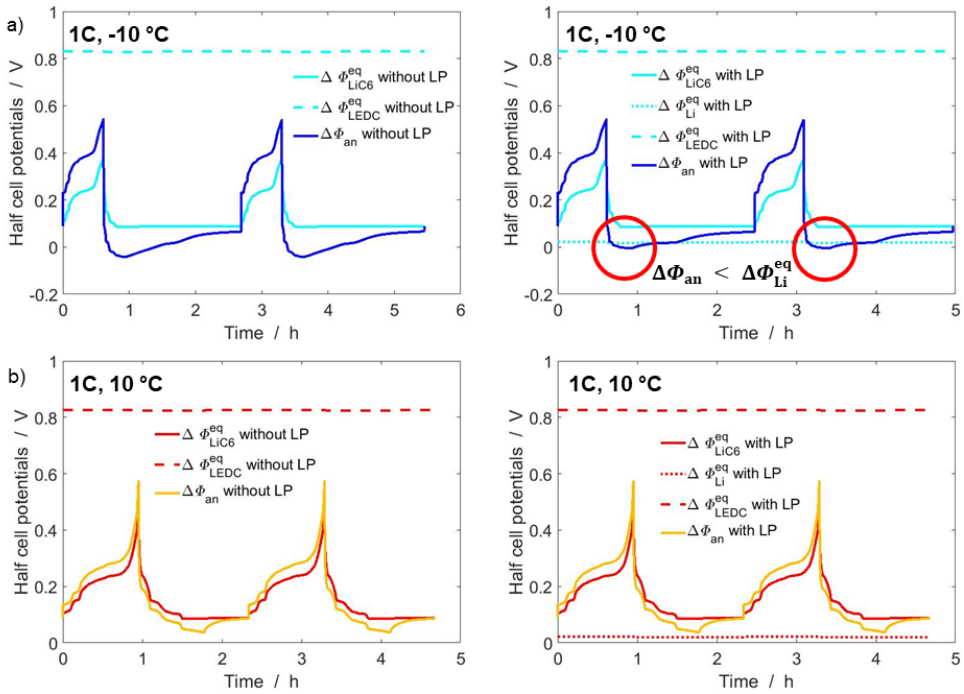

FIGURE 49: COMPARISON BETWEEN MODEL 1 (LEFT) AND MODEL 2 (RIGHT). POTENTIAL DYNAMICS (2 CYCLES) FOR DISCHARGE (1C CC) – REST (15 S) – CHARGE (1C CCCV, C/20 CUT-OFF) – REST (15 S). HERE SHOWN THE EQUILIBRIUM POTENTIALS OF THE COMPETING REACTIONS INCLUDED IN THE MODELS (INTERCALATION, PLATING AND LEDC[SEI] FORMATION), TOGETHER WITH THE ANODE HALF-CELL POTENTIAL: AT A) 1C, -10 °C , B) 1C, 10 °C. HERE LP = LITHIUM PLATING.

Figure 49 gives us an insight into the potential dynamics at the two different temperatures and for the two models (Model 1 on the left and Model 2 on the right). Panels a) and b) show the equilibrium potentials $\Delta\phi^{\mathrm{eq}}$ of the competing charge-transfer reactions (intercalation, electrolyte-driven SEI and plating - if included) together with the half-cell potential $\Delta\phi_{\mathrm{an}}$ at the anode, respectively at -10 °C and 10 °C. Looking at Panel a), you can see how the $\Delta\phi_{\mathrm{an}}$ is above the intercalation $\Delta\phi^{\mathrm{eq}}_{\mathrm{LiC6}}$ during the CC discharge and below during the CCCV charge: in the last part of the CC charge, where $\Delta\phi_{\mathrm{an}}$ gets also lower than the plating $\Delta\phi^{\mathrm{eq}}_{\mathrm{Li}}$, that is where the plating reaction is finally favoured to intercalation ($\Delta\phi_{\mathrm{an}} < \Delta\phi^{\mathrm{eq}}_{\mathrm{Li}}$). It is actually during the CC charge and the first part of the CV phase that we have the steeper increase in LEDC[SEI] volume fraction (see Panel e) from Figure 48): the oxidation of plated lithium during the first part of the CV phase frees Li^+ ions which can now be used for the electrolyte-driven SEI growth. Worth noting, $\Delta\phi_{\mathrm{an}}$ in Model 2 goes less negative than in Model 1 because of the effect of plating on the voltage at the anode during charge. Hence, we observe also longer CC phases - because of the CC charge plateau during plating formation - and shorter CV phases, because of the higher current densities due to the contribution of the parallel reactions $i = i_{\mathrm{LiC6}} + i_{\mathrm{Li}} + i_{\mathrm{LEDC}}$. In absence of plating at 10 °C, the potential dynamics for the two models in Panel b) look instead absolutely identical.

Let's now have a look at how things change when we go from 1C to 5C (same protocol applied but at 5C).
In Figure 50, -10 °C is plotted on the left column: we can observe a quite small volume fraction of formed plated lithium in Panel d) but enough to help making a difference in e), when we compare the two models.

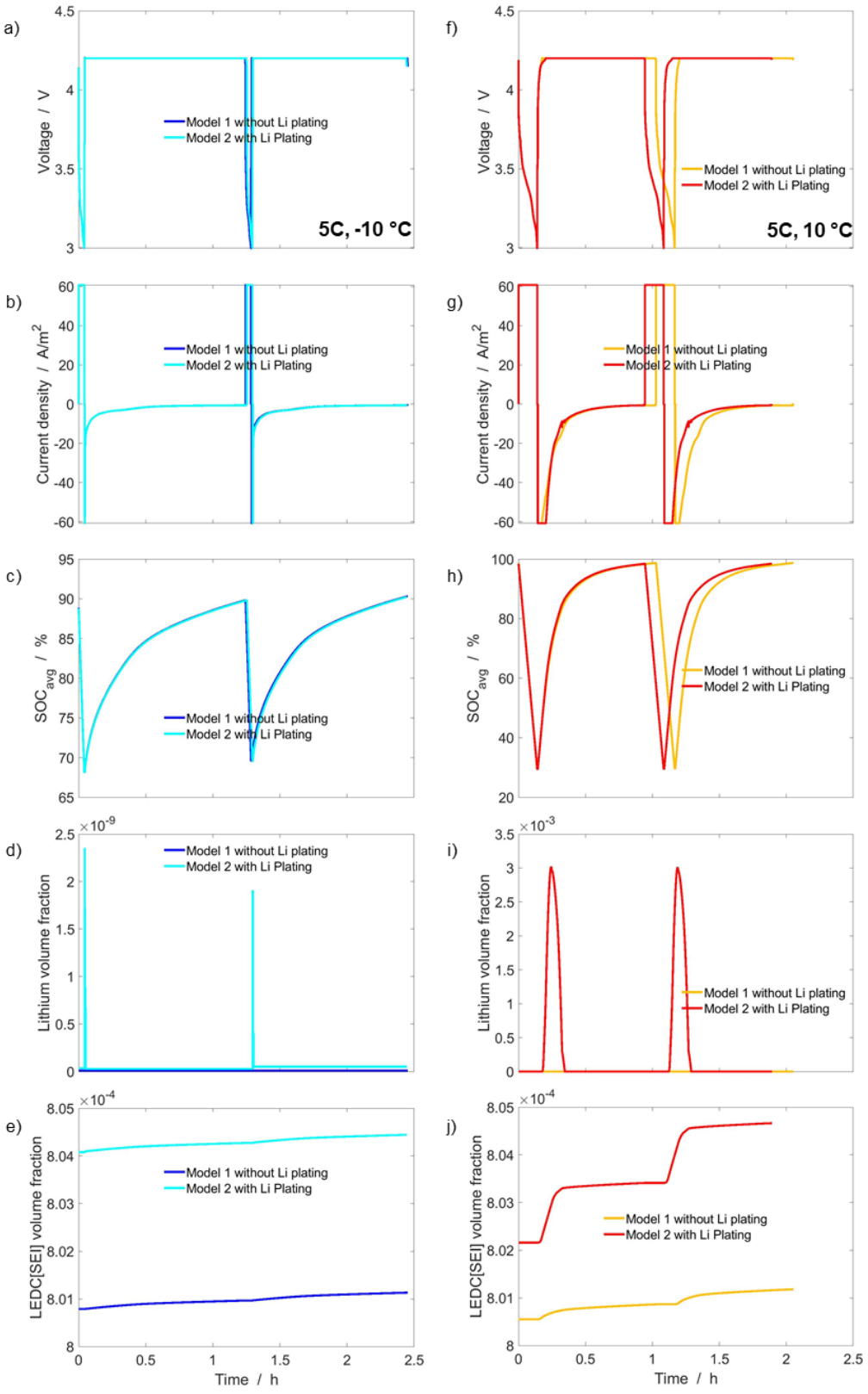

FIGURE 50: COMPARISON BETWEEN MODEL 1 (LI PLATING NOT INCLUDED) AND MODEL 2. SIMULATIONS (2 CYCLES) FOR DISCHARGE (5C CC) – REST (15 S) – CHARGE (5C CCCV, C/20 CUT-OFF) – REST (15 S). ON THE LEFT, AT -10 °C: A) VOLTAGE, B) CURRENT DENSITY, C) SOC, D) LITHIUM VOLUME FRACTION, E) LEDC[SEI] VOLUME FRACTION. ON THE RIGHT, AT 10 °C : F) VOLTAGE, G) CURRENT DENSITY, H) SOC, I) LITHIUM VOLUME FRACTION, J) LEDC[SEI] VOLUME FRACTION.

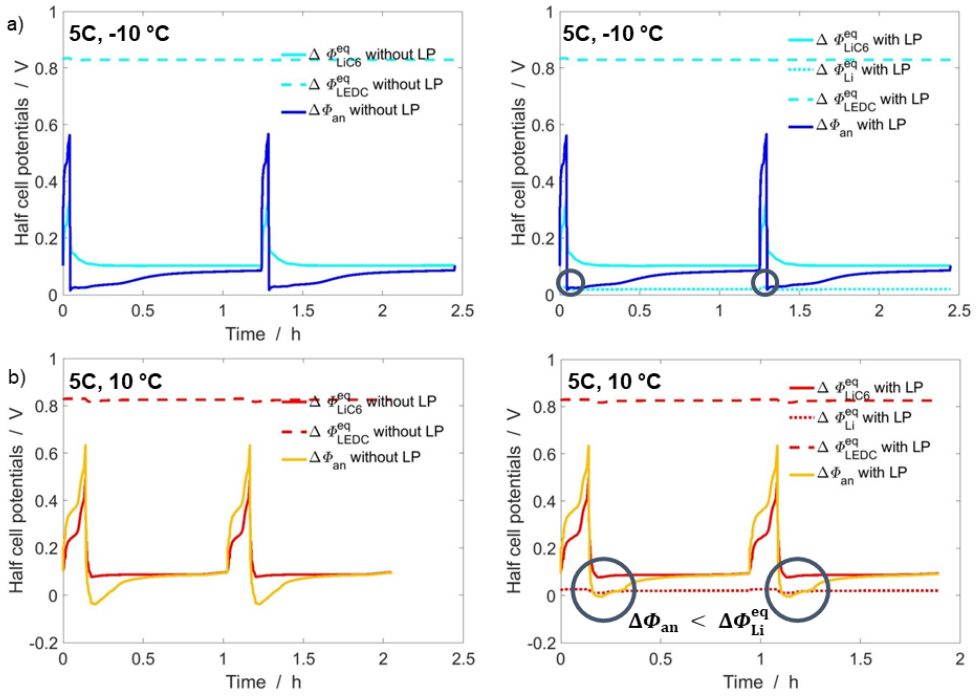

FIGURE 51: COMPARISON BETWEEN MODEL 1 (LEFT) AND MODEL 2 (RIGHT). POTENTIAL DYNAMICS (2 CYCLES) FOR DISCHARGE (5C CC) – REST (15 S) – CHARGE (5C CCCV, C/20 CUT-OFF) – REST (15 S). HERE SHOWN THE EQUILIBRIUM POTENTIALS OF THE COMPETING REACTIONS INCLUDED IN THE MODELS (INTERCALATION, PLATING AND LEDC[SEI] FORMATION), TOGETHER WITH THE ANODE HALF-CELL POTENTIAL: AT A) 5C, -10 °C , B) 5C, 10 °C. HERE LP = LITHIUM PLATING.

Here there is no steep increase in LEDC[SEI] volume fraction during charge phases and the battery is not able to properly cycle, with the SOC oscillating between 90 % and 70 % in Panel c): the lack of a deep charge-discharge strongly influences not only the plating but also the SEI growth. Once we move to the column on the right, where 10 °C is plotted, we observe deeper cycles and a more visible difference between the two models, in a similar way to what seen in Figure 48 at 1C /-10 °C. Consequently, what said for Panel a) (1C /-10 °C) in Figure 49 can be repeated for Panel b) (5C / 10 °C) in Figure 51.

For a deeper understanding, let's now investigate how our most complete framework, Model 2, behaves in simulating SEI formation and growth at different temperatures and C-rates.

In Figure 52 two simulated CCCV discharge-charge cycles are plotted at 1C and different temperatures (same protocol as in Figure 48): on the left, we can see -20 °C, 0 °C and 20 °C, while on the right we have 10 °C, 40 °C and 70°C. This gives us quite a comprehensive outlook on how the model behaves over a wide range of temperatures and how they could impact the SEI formation and growth. Let's start from the left column. We can notice straight away in Panel c) that the temperature has actually a huge impact on the SOC, with a complete discharge/charge only happening at 20 °C and the SOC of the simulated battery just oscillating between 77 and 40 % at -20 °C. If we look at the lower panels we can understand what is happening: in d) at -20 °C and 0 °C we have formation of Li[metal], even if in small quantities (0 °C > -20 °C, as we know from our study on thermodynamics and kinetics of lithium plating in Chapter 5) and in e) we see the SEI growing with time with -20 °C > 0 °C, probably because of the plating becoming more reversible with the increasing temperature and consequently less inclined in binding with EC to form LEDC[SEI].

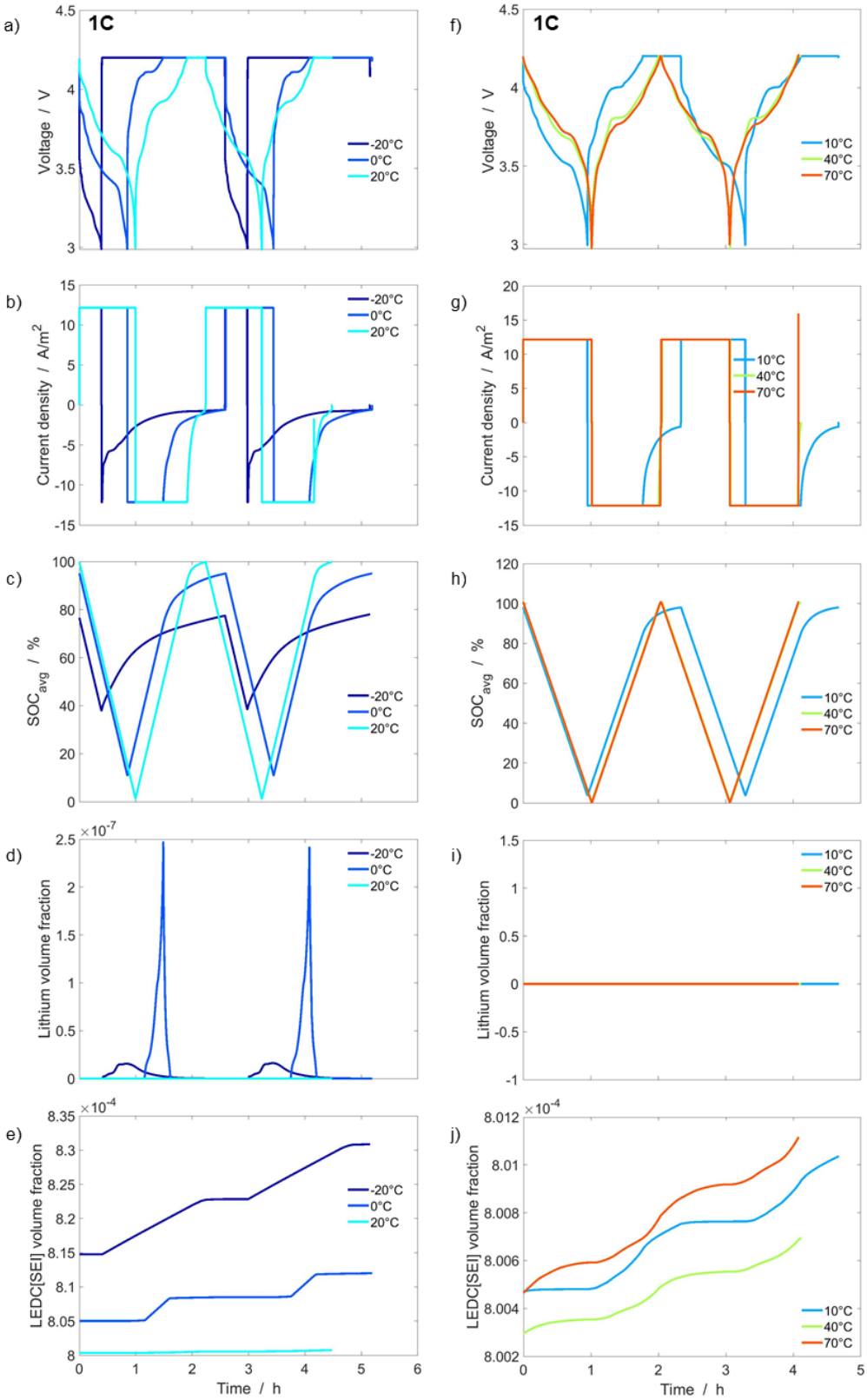

FIGURE 52: MODEL 2 (LI PLATING INCLUDED). SIMULATIONS (2 CYCLES) FOR DISCHARGE (1C CC) – REST (15 S) – CHARGE (1C CCCV, C/20 CUT-OFF) – REST (15 S) AT DIFFERENT TEMPERATURES. ON THE LEFT, AT -20, 0 AND 20 °C: A) VOLTAGE, B) CURRENT DENSITY, C) SOC, D) LITHIUM VOLUME FRACTION, E) LEDC[SEI] VOLUME FRACTION. ON THE RIGHT, AT 10, 40 AND 70 °C: F) VOLTAGE, G) CURRENT DENSITY, H) SOC, I) LITHIUM VOLUME FRACTION, J) LEDC[SEI] VOLUME FRACTION.

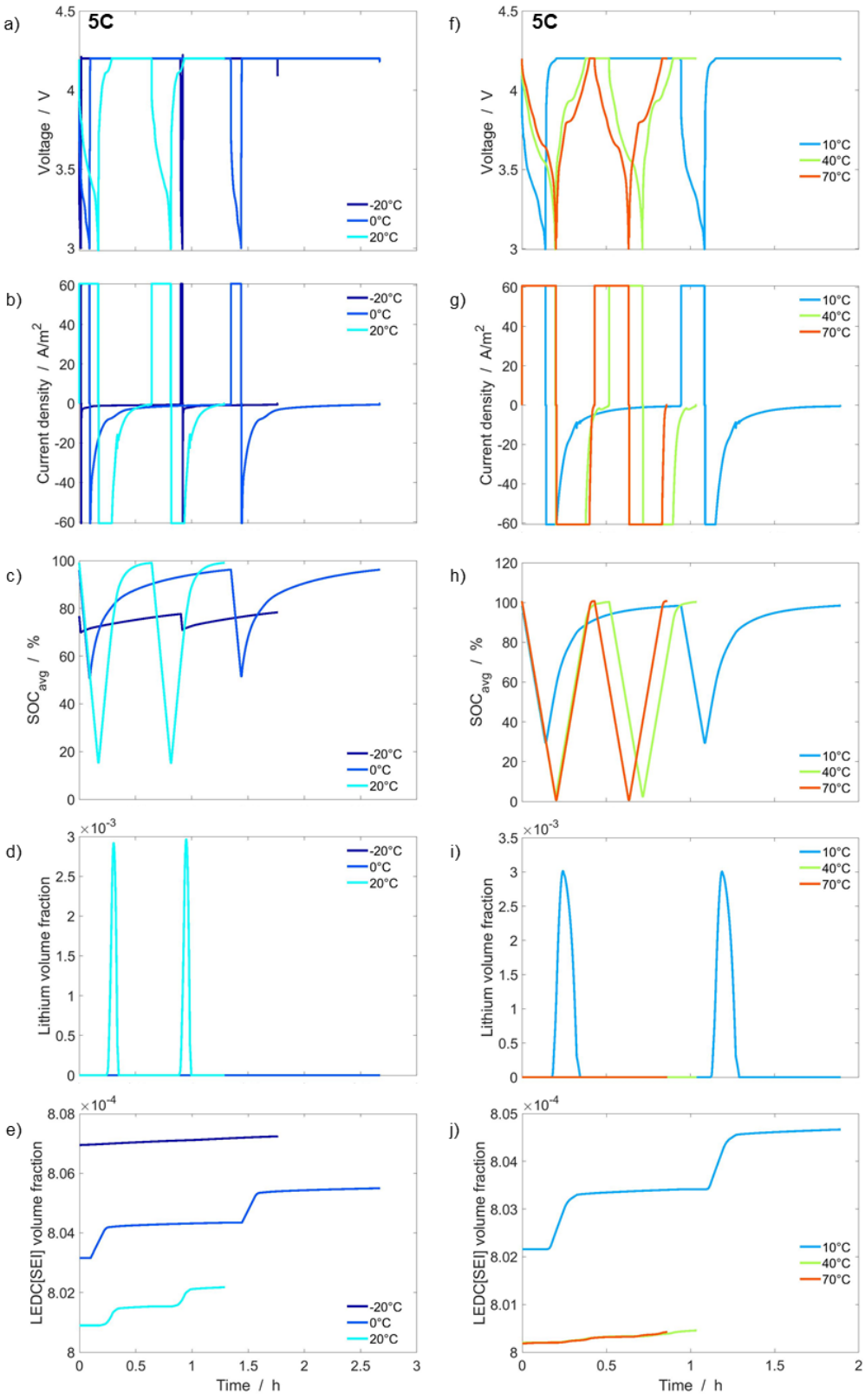

FIGURE 53: MODEL 2 (LI PLATING INCLUDED). SIMULATIONS (2 CYCLES) FOR DISCHARGE (5C CC) – REST (15 S) – CHARGE (5C CCCV, C/20 CUT-OFF) – REST (15 S) AT DIFFERENT TEMPERATURES. ON THE LEFT, AT -20, 0 AND 20 °C: A) VOLTAGE, B) CURRENT DENSITY, C) SOC, D) LITHIUM VOLUME FRACTION, E) LEDC[SEI] VOLUME FRACTION. ON THE RIGHT, AT 10, 40 AND 70 °C: F) VOLTAGE, G) CURRENT DENSITY, H) SOC, I) LITHIUM VOLUME FRACTION, J) LEDC[SEI] VOLUME FRACTION.

Looks like a complex interplay between reactions is happening at these low temperatures. If we look at the column on the right, we see a much better performance of the simulated battery, with good results in terms of SOC and, as expected, no formation of lithium plating. Panel j) gives us an interesting information though: LEDC[SEI] volume fraction is increasing with this trend 70 °C > 10 °C > 40 °C. Somehow this is in accordance with the general principle that chemical reactions (and so the SEI formation too) are accelerated with increasing temperature[43] , while the higher value at 10 °C could be due to the presence of a longer CV phase (i.e. longer time at low anode potential) compared to what observed at 40 °C.

What about the effect of the C-rate instead?

In Figure 53 the same protocol and temperatures from Figure 52 are plotted but at higher C-rate (5C). Looking at the column on the left, we see how a higher C-rate impacts negatively the SOC and moves the "plating zone" towards higher temperatures (here 20 °C), even if in Panel e) LEDC[SEI] volume fraction follows the same trend seen at 1C: -20 °C > 0 °C > 20 °C. The values at 5C are much lower than the ones seen at 1C, though. Looks like the SEI formation, similarly to what seen about plating, is not just a matter of thermodynamic limits or kinetics but derives instead from multiple factors, which include the transport processes and the competition between all the parallel and counteracting reactions at the anode. When plating is present (i.e. at 20 °C) it accelerates SEI growth via the LP-driven reaction while in its absence, whatever the reasons behind it, only the electrolyte-driven path can happen and visibly smaller quantities are produced. This can be equally seen by looking at the column on the right and especially at Panel j), where the highest LEDC[SEI] volume fraction can be found at 10 °C, which is not casually also the temperature showing the highest Li[metal] volume fraction in i).

7.3 Introducing: the "Qualitative Ageing"

In Waldmann[195] the speed of ageing has been quantitatively described using ageing rates *r* derived from capacity fade curves and then plotted in an Arrhenius plot ln(*r*) vs. $1/k_{\mathrm{b}}T$ (see Figure 54).

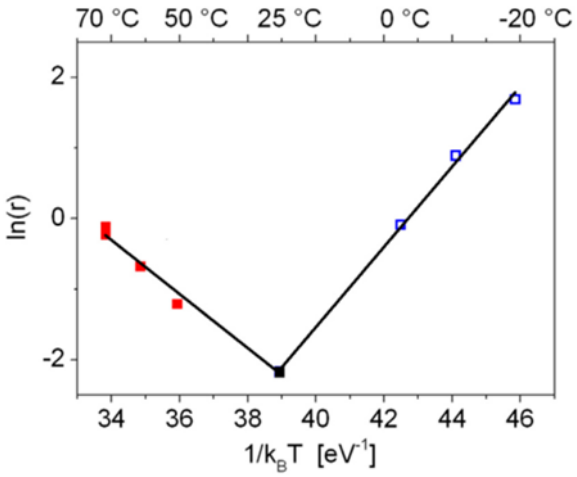

FIGURE 54: ARRHENIUS PLOT FOR THE AGEING BEHAVIOUR OF 18650 CELLS CYCLED AT 1 C IN A TEMPERATURE RANGE OF 20 °C TO 70 °C. THE SOLID LINES CORRESPOND TO LINEAR FITS OF THE DATA POINTS OF THE RESPECTIVE TEMPERATURE RANGES BELOW (LT) AND ABOVE (HT) 25 °C. THE FIGURE IS FROM WALDMANN *ET AL.*[195]

A change of the slope in an Arrhenius plot is known to be an indication for a mechanism change and two different ageing mechanisms have been detected, that is plating at T < 25 °C, with ageing rates increasing with decreasing temperature (positive slope), and SEI at T > 25 °C, with ageing rates increasing with increasing temperature (negative slope).

In the modelling works of Yang[186,196], where only irreversible plating is included, the ageing rate of the cell is defined as the total capacity loss (in %) per full cycle and similarly plotted in logarithmic scale vs. $1/k_{\mathrm{b}}T$: here the change of Arrhenius slope is detected at 20 °C for a C-rate equal to 1C, but the transition from linear to nonlinear ageing, which signals the onset of irreversible lithium plating, tends to appear in higher temperatures with increasing charge rate (i.e. 40 °C for 2C and over 50 °C for 3C). The SEI growth is still found to be the dominant ageing mechanism in the linear ageing stage but, with the appearance of lithium metal, the augmented decrease of local anode porosity sets a positive feedback with the lithium plating rate and leads to a consequent transit from linear to nonlinear ageing.

Inspired by these studies, we introduce in Figure 55 a simple degradation factor called "Qualitative Ageing" (QA). QA is nothing else than the volume fraction of LEDC[SEI] formed during the cycle, according to

$$\mathrm{QA} = \varepsilon_{\mathrm{LEDC[SEI]},t} - \varepsilon_{\mathrm{LEDC[SEI]},0} \ , \tag{135}$$

which logarithm is here plotted on the left against $1/k_{\mathrm{b}}T$, to highlight eventual Arrhenius dependencies, and on the right against T, for clarification purposes. Being $\varepsilon_{\mathrm{LEDC[SEI]}}$ originated via both electrolyte and LP-driven reactions in Model 2, the QA factor gives a qualitative information about the interaction of plating and SEI. The followed protocol for both Model 1 and Model 2 is the same used in the rest of the Chapter: two simulated discharge (1C CC) – rest (15 s) – charge (1C CCCV, C/20 cut-off) – rest (15 s) cycles, over a wide range of temperatures (-20 °C…80 °C) and two different C-rates, 1C and 5C respectively in Panel a) and b).

Let's focus on the right column, where ln(QA) is plotted against T.

In Panel a) on the right, Model 1 and 2 are superimposed in all the range between 10 °C and 80 °C: what we deduce is the absence of plating all over this range (no surprises!) and what we see is an expected increase in SEI growth at T > 30 °C in accordance with the general principle that chemical reactions are accelerated with increasing temperature. The minimum can be found here at 30 °C. At lower temperatures than 10 °C the two models separate: QA becomes evidently higher for Model 2 in presence of plating, peaking at -20 °C where the smaller activation energies for plating and SEI growth (respectively 65 and 55 kJ/mol) make these mechanisms more competitive than intercalation (77.1 kJ/mol). We can somehow see three zones in this plot, even if not well defined as in the works of Waldmann[195] and Yang[196]:

- T < 0 °C: LEDC[SEI] formation and growth above all via LP-driven mechanism (negative slope) due to evident plating formation: maximum at - 20 °C.
- 0 < T < 30 °C: combination of multiple reactions at the anode, thermodynamics and kinetics (negative slope). When T < 10 °C, plating happens and LEDC[SEI] is produced via both electrolyte and LP-driven reactions; when T > 10 °C, all the parallel reactions at the anode are kinetically accelerated and we see intercalation improving - slight decreasing in QA with increasing T
- T > 30 °C: LEDC[SEI] formation and growth via electrolyte-driven mechanism (positive slope). Model 1 and 2 superimpose, plating not present (minimum at 30 °C)

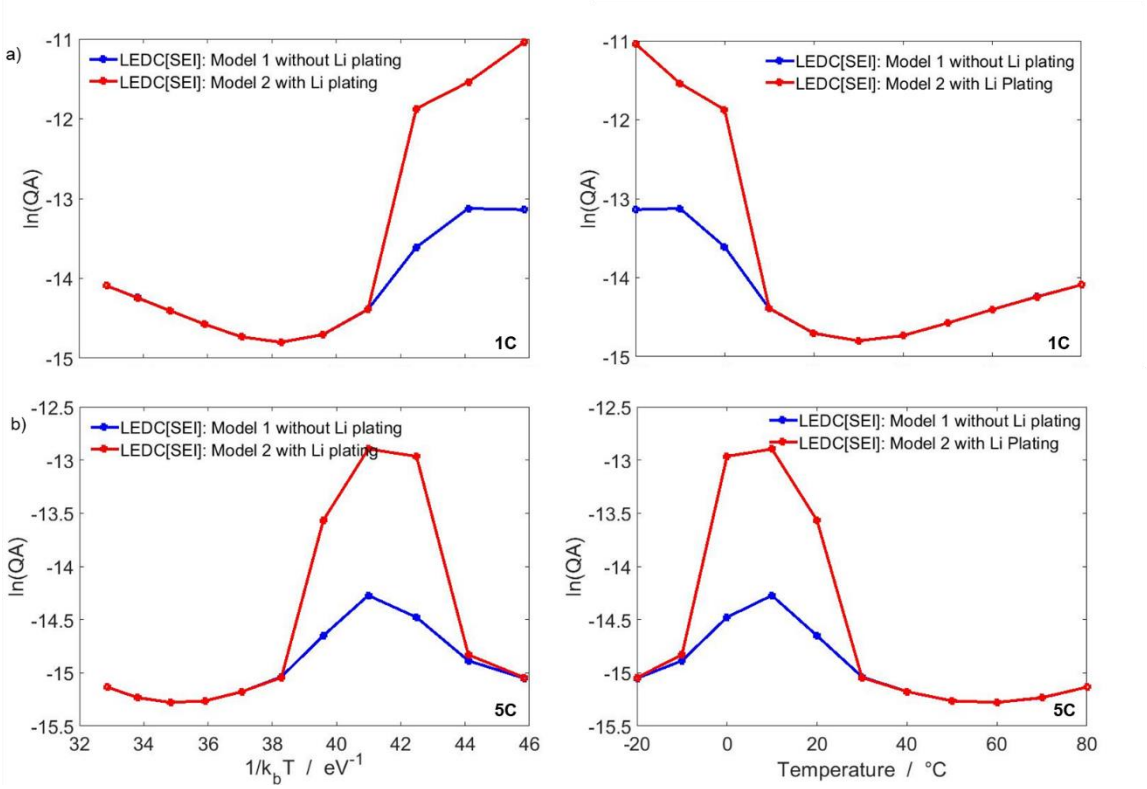

FIGURE 55: ARRHENIUS PLOTS FOR QUALITATIVE AGEING (QA). ON THE LEFT LN(QA) VS $1/K_BT$; ON THE RIGHT, LN(QA) VS T. QA SIMULATED DATA FOR (2 CYCLES) CC DISCHARGE – REST (15 S) – CCCV CHARGE (C/20 CUT-OFF) – REST (15 S) IN THE TEMPERATURE RANGE -20…80 °C: MODEL 1 AND 2 COMPARED AT A) 1C, B) 5C.

If things were not enough complicated as they are, the effect of fast charging adds even more complexity.

In Panel b) on the right, illustrating the same protocol but at 5C, the two models superimpose perfectly for T > 30 °C, where we could therefore expect LEDC[SEI] formation and growth only via electrolyte-driven mechanism. Coherently with Yang's work though, the minimum moves towards higher temperatures with increasing C-rate and here we see it at 60 °C. At T < 30 °C the two models separate, both peaking at 10 °C which looks the favoured temperature for QA in this plot…to then somehow meet again at T < -10 °C where a combination of thermodynamic limits and slow kinetics inhibits the plating and consequently the LEDC[SEI] LP-driven growth. This is quite coherent with our discussion in 5.4.3. Hence, we can here identify five zones in this plot:

- T < -10 °C: Model 1 and 2 superimpose, plating inhibited and LEDC[SEI] formation and growth happening only via electrolyte-driven mechanism (positive slope).
- -10 < T < 10 °C: combination of multiple reactions at the anode, thermodynamics and kinetics (positive slope). LEDC[SEI] is produced via both electrolyte and LP-driven reactions: with increasing temperature, proper cycling is easier for the battery and with higher SOC comes higher QA
- 10 < T < 30 °C: combination of multiple reactions at the anode, thermodynamics and kinetics (negative slope). LEDC[SEI] is produced via both electrolyte and LP-driven reactions: maximum at 10 °C
- 30 < T < 60 °C: LEDC[SEI] formation and growth via electrolyte-driven mechanism (negative slope). Model 1 and 2 superimpose, plating not present: all the parallel reactions at the anode are kinetically accelerated and we see intercalation improving - slight decreasing in QA with increasing T

- T > 60 °C: LEDC[SEI] formation and growth via electrolyte-driven mechanism (positive slope). Model 1 and 2 superimpose, plating not present (minimum at 60 °C)

To conclude our short peek on the QA world, an operation map cannot be missing. In Figure 56 the QA factor is represented as function of temperature and charging current for Model 1 (without plating, Panel a) and Model 2 (with plating included, Panel b). This time the colourmaps illustrate one single cycle done with the same protocol previously described, that is CC discharge – rest (15 s) – CCCV charge (C/20 cut-off) – rest (15 s), from 5C down to 0.05C in a temperature range from -20 °C to +80 °C. A first look tells us that the model with plating experiences remarkably higher QA values at low temperatures, especially for 1C and 2C at T < 0 °C: this is due to the effect of the LP-driven reaction, which adds to the classical electrolyte-driven SEI growth. As already noticed, the minimum values tend to move towards higher temperatures with increasing C-rates and so does the limit between plating/no plating zones. Very low temperatures inhibit the kinetics of all reactions and consequently we have surprisingly low QA values in the harshest conditions - see the blue zone on the top left of Panel b).

Interesting for both models is the behaviour at 0.05 C, which we could consider a sort of representation of (very short-term) calendar ageing: the highest values are reached at T > 40 °C in Panel b) and already T > 20 °C in Panel a). The activation energy of the SEI growth exchange current density, the smallest between the reactions happening at the anode, makes the electrolyte-driven reaction remarkably more competitive at high temperatures and favours in this way the formation of LEDC[SEI], which therefore happens to be the first cause of ageing during storage. A more accurate map to avoid possible artefacts and a more in-depth study are clearly needed to understand all these complex interactions.

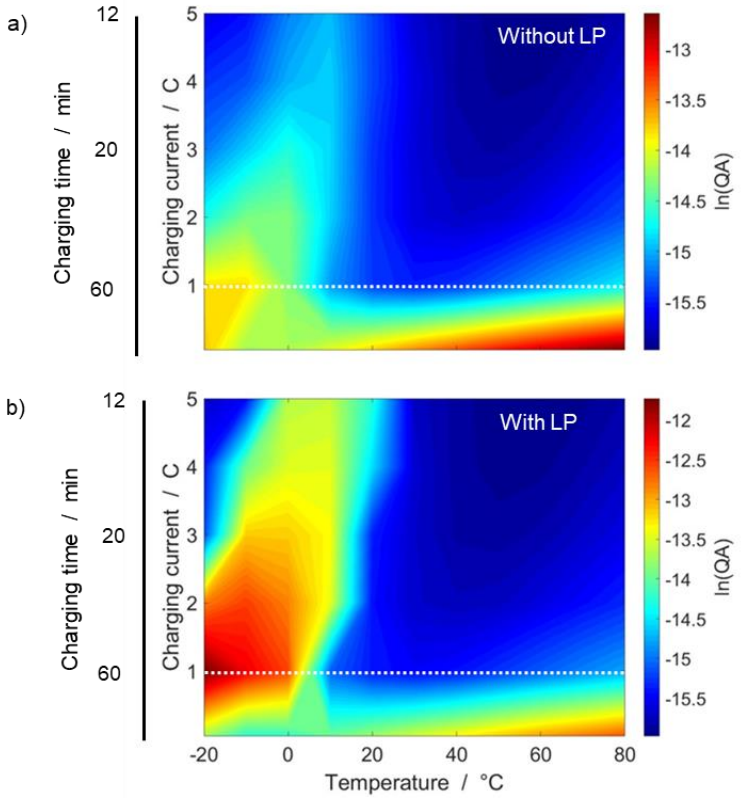

FIGURE 56: OPERATION COLOURMAPS OF A CC DISCHARGE – REST (15 S) – CCCV CHARGE (C/20 CUT-OFF) – REST (15 S) WITH CONVERSION C-RATE/CHARGING TIME ON THE SIDE (DASHED LINE SET AT 1C = 60 MIN). IN A) MODEL 1 WITHOUT PLATING; B) MODEL 2 WITH PLATING.

7.4 A LOOK AT THE FUTURE: CONCLUSIONS

"The future is uncertain but the end is always near."
(Jim Morrison)

In this last and final Chapter, we have coupled our plating model from Chapter 5 with a SEI model previously developed by Kupper[77] and then partially modified to include the positive feedback effect of the plating formation on the SEI growth. The interactions between the two ageing processes are quite complex and the results can be quite unexpected, as we have seen in our study about the effect of the C-rate on the SEI growth during cycling: it is commonly accepted that fast charging has a negative impact on the battery ageing and the unexpected results from the simulated colourmaps of the QA factor rise many open questions and ask for more investigation. Worth noting, in this Chapter validation against experiments is missing and therefore we do not know at the moment how the coupled model will respond to this fundamental test.
For sure, what will improve our results and help us in understanding these complex behaviours is a more refined modelling of reversible lithium plating, capable of distinguishing and describing the different morphological features of the plated lithium during the phases of formation and growth; the inclusion of irreversible lithium plating, characterised by the breaking of dendrites and the formation and isolation of dead lithium from the graphite; and finally, the development of a SEI model in which not one (as in this Chapter: LEDC[SEI]) but two defined species of SEI are created, one in the classical way and the other via lithium plating, with different features and own specific thermodynamics and kinetics. All these missing points will require a more in-depth literature research and parameterisation and therefore are not treated here but will be addressed in the future work (next project about fast-charging starting on September 2020).

8 SUMMARY AND OUTLOOK

Lithium-ion batteries are key components for future technologies such as electro-mobility or energy supply from fluctuating resources: a theoretical understanding and model-based simulation of the batteries mechano-electro-thermal behaviour are consequently a prerequisite for their technology success, hence the development of cell models with the purpose of an increase of predictability of model-based life expectancy.

The present dissertation focused on the important ageing mechanisms at the anode, based on numerous electrochemical side reactions: here in particular the lithium plating, particularly evident in presence of high currents or low temperatures, and its interaction with the Solid Electrolyte Interphase (SEI), which growth is considered one of the most important irreversible loss mechanisms. The ageing reactions were all developed in a consistent kinetic formalism using the open-source chemical kinetics code Cantera[42] implemented in the in-house multiphysics software package DENIS[35,38] and interfaced with MATLAB. The purpose of this work was an in-depth understanding of these two degradation processes through the construction of more and more refined modelling frameworks and the successive analysis of simulations carried out over a wide range of conditions (currents, temperatures and SOCs). Experiments, accurately made in our laboratory or extracted from relevant literature, were used as guide during the parameterisation and comparison to finally validate our results, following the scientific method in a continuous process of improvement.

The first part of the thesis gave the necessary theoretical background to understand the modelling and simulation frameworks discussed in the following Chapters: the transport model with its governing equations, previously illustrated in a fundamental paper from Kupper[19], described a P3D multiscale approach where the heat transport in the through-cell direction (1D, macroscale) was modelled as conductive process, mass and charge transport on the electrode-pair scale (1D, mesoscale) as diffusion and migration and intraparticle transport of lithium atoms (1D, microscale) as Fickian diffusion with concentration-dependent diffusion coefficient. A 0D model of the void cell volume was also included, allowing to describe gas-phase species concentration and pressure build-up during ageing processes. An introduction of the ageing phenomena in different parts of the battery followed, with a particular attention to the formation and growth of the SEI and the lithium plating at the anode.

The core of the thesis focused on the development of a new and more complex P3D multiscale model[111] of a 350 mAh high-power lithium-ion pouch cell with graphite anode and LCO/NCA blend cathode and its successive extension[78] to include and simulate the lithium plating process. The parameterisation and validation of this comprehensive modelling and simulation framework was discussed in detail: a systematic approach was followed, starting from equilibrium[34] and successively adding transport processes on all three scales, then accurately validated through experiments in frequency and time domain over a wide range of conditions and explored through detailed simulations of the internal states on the P3D scales.

A successful extension with the purpose of simulating reversible lithium plating over a wide range of conditions was developed. The equilibrium potential of the plating reaction, now included at the anode, is not always equal

to 0 V but varies according to the local temperature and lithium-ion concentration. Again, a systematic approach towards parameterisation and validation of the plating reaction was applied: an extensive literature research was presented and used to choose a coherent set of thermodynamic and kinetic parameters. It is very difficult to detect lithium plating in situ without a direct observation of the open cell, but it is possible to deduce its presence by analysing the cell behaviour during cycles of charge/discharge in critical conditions and detecting some peculiarities which have been shown to indicate plating (i.e. voltage plateau and voltage drop). A comparison between simulations and experiments followed, respectively with experiments on our reference cell (where no macroscopic plating hints were present) and published experimental data[95] (where the plating hints were instead clearly visible). An extra third reaction, simulating explicitly the re-intercalation of the plated lithium, was also included in the model and could be freely switched on to simulate a case in which the cell was likely not showing voltage plateau and voltage drop. The simulations showed a good qualitative agreement but some quantitative differences, probably related to morphological features of the plated lithium, which were not yet included in the present model, and to some imprecisions in the general parameterisation of the model at low temperatures. It is clear anyway that the plating mechanism is not just a matter of thermodynamic limits or kinetics, but it comes instead from a combination of both, including also the transport processes and the competition between the parallel and counteracting reactions at the anode. Particularly interesting was finally the construction of different definitions of "degradation factors", here colourfully converted into operational maps as an intuitive way to assess reversible plating propensity during CCCV cycles over a wide range of conditions. Inclusion of irreversible plating and consequent formation of dendrites and so-called "dead lithium" are still missing but expected to be added in the future to predict long-term ageing and capacity loss.

The final part of the thesis was about two different topics, both parts of ongoing studies at the present time.
The first introduced a different approach[189] - developed with Python at Colorado School of Mines (USA) - on 1D-SEI modelling, to which parameterisation I had the opportunity to contribute for a six-weeks period in 2019 as guest scientist. Specifically, three 1D-models with a decreasing level of detail ("detailed", "homogeneous" and "reduced") were presented with the purpose of describing SEI formation and growth on a non-intercalating anode and ideally being included in future in bigger and more comprehensive multiscale frameworks. The most suitable turned out to be the well-parameterised reduced-order model, still able to describe SEI properties despite its computational simplicity. Being an ongoing and therefore still incomplete study, a working transport model for the electrolyte is still missing and its inclusion, together with a further development of the SEI passivation effect and the adding of more species in the SEI composition, is expected to be a logical extension of this work in the future.
The second topic focused on the coupling of the above discussed plating model[78] with an SEI model developed in the past by Kupper[77] and then extended to include the positive feedback effect of the plating on the SEI growth. New reactions were added, new interesting results were obtained and will be furtherly explored in a future work; validation against experiments is still missing. A new "Qualitative Ageing" (QA) factor was also introduced[195]. The interactions between the two ageing processes happen to be quite complex and the qualitative results call for further research: it is commonly accepted that fast charging has a negative impact on the battery ageing and the

unexpected results from the simulated QA colourmaps rise many open questions...hence we are open for ideas and suggestions!

For a better understanding and an improvement of the accuracy of our simulations, hence the future to-do steps include a more refined modelling of reversible lithium plating, capable of distinguishing and describing the different morphological features of the plated lithium during the phases of formation and growth; the inclusion of irreversible lithium plating, characterised by the breaking of dendrites and the formation and isolation of dead lithium from the graphite; and finally, the development of an SEI model in which not one but two defined species of SEI are created, one in the “classical” way and the other via lithium plating, with different features and own specific thermodynamics and kinetics.

9 LIST OF SYMBOLS

Symbol	Unit	Meaning
A	1	Pre-exponential factor
A_{e}	$\mathrm{m^2}$	Active electrode area
A^{V}	$\mathrm{m^2 \cdot m^{-3}}$	Volume-specific surface area
A_n^{V}	$\mathrm{m^2 \cdot m^{-3}}$	Volume-specific surface area of reaction *n*
$A_{\mathrm{AM},i}^{\mathrm{V}}$	$\mathrm{m^2}$	AM specific surface area
$A_{\mathrm{surf},j}$	$\mathrm{m^{-1}}$	Local surface area for a volume *j* (Chapter 6)
a_j	$\mathrm{mol \cdot m^{-1}}$	Concentrations of the single volumes *j* (Chapter 6)
a_{n}	1	Equation parameters
a_{n} b_{n}	1	NASA polynomial coefficients
α_{sn}	$\mathrm{m^{-1}}$	Specific surface area
α_{cc}	1	Slope in Eq. 71
C	F	Capacity
$C_{\mathrm{AM},i}^{\mathrm{V}}$	F	Individual overall capacity of the active material
c_i	$\mathrm{mol \cdot m^{-3}}$	Concentration of species *i* in a bulk phase
c_+	$\mathrm{mol \cdot m^{-3}}$	Concentration of cation
c_-	$\mathrm{mol \cdot m^{-3}}$	Concentration of anion
c_{Li^+}	$\mathrm{mol \cdot m^{-3}}$	Concentration of solved Li-ions
$c_{\mathrm{Li[AM},i]}$	$\mathrm{mol \cdot m^{-3}}$	Concentration of lithium in the active material
$c_{\mathrm{Li}^+\mathrm{[elyt]}}$	$\mathrm{mol \cdot m^{-3}}$	Concentration of solved Li-ions
c_{Li}	$\mathrm{mol \cdot m^{-3}}$	Concentration of lithium in the active material
$c_{\mathrm{Li}}^{\mathrm{max}}$	$\mathrm{mol \cdot m^{-3}}$	Maximum amount of lithium stored in the active material
$c_{p,i}^0$	$\mathrm{J \cdot mol^{-1} \cdot K^{-1}}$	Molar heat capacity of species *i*
c_{P}	$\mathrm{J \cdot kg^{-1} \cdot K^{-1}}$	Specific heat capacity
c_i^0	$\mathrm{mol \cdot m^{-3}}$	Standard concentration of species
$C_{\mathrm{DL}}^{\mathrm{V}}$	$\mathrm{F \cdot m^{-3}}$	Volume-specific double-layer capacity
c_{P}	$\mathrm{J \cdot kg^{-1} \cdot K^{-1}}$	Specific heat capacity
d_{cell}	m	Thickness/diameter of the cell
d_{SEI}	m	Diameter for a representative SEI particle (Chapter 6)
D^0	$\mathrm{m^2 \cdot s^{-1}}$	Diffusion coefficient used in CST
D_i^{CST}	$\mathrm{m^2 \cdot s^{-1}}$	Individual ion CST diffusion coefficient
D_i	$\mathrm{m^2 \cdot s^{-1}}$	Diffusion coefficient of species *i*
D_i^{eff}	$\mathrm{m^2 \cdot s^{-1}}$	Effective diffusion coefficient of species *i*

$D_i^{\mathrm{migr,DST}}$	mol·V^{-1}·m^{-1}·s^{-1}	Migration coefficient of species *i* for DST
$D_i^{\mathrm{migr,eff}}$	mol·V^{-1}·m^{-1}·s^{-1}	Effective migration coefficient of species *i*
$D_{\mathrm{Li[AM},i]}$	m^2·s^{-1}	Diffusion coefficient of lithium in active material
E	V	Electrode-pair voltage
$E_{\mathrm{AM},i}^{\mathrm{eq}}$	V	Half-cell potential vs. lithium metal
E_{cell}	V	Cell voltage
$E_{N_{\mathrm{EP}}}$	V	Cell voltage of the n$^{\mathrm{th}}$ electrode pair
$E_{\mathrm{act,f}}$	J·mol^{-1}	Activation energy of forward reaction
$E_{\mathrm{exp}}, E_{\mathrm{OC}}$	V	Experimental and open circuit voltage
F	C·mol^{-1}	Faraday's constant
$f_{\mp}$	mol^{-1}	CST activity coefficient
h_i	J·mol^{-1}	Molar enthalpy of species *i*
$h^0_{\mathrm{Li[AM},i]}$	kJ·mol^{-1}	Molar enthalpy of intercalated lithium in active material
i	1	Index of species
i	A·m^{-2}	Area-specific current (with respect to A_{e})
i^0	A·m^{-2}	Exchange current density
i^{00}	A·m^{-2}	Exchange current density factor
i_m	A·m^{-3}	Area-specific current of representative electrode pair *m*
$i_{\mathrm{DL}}^{\mathrm{V}}$	A·m^{-3}	Volume-specific current due to double layer
i_F^{V}	A·m^{-3}	Volume-specific Faradaic current
$i_{\mathrm{lim,c}}$	A·m^{-2}	Cathodic limiting current
I_{cell}	A	Current of the cell
j	1	Index of volumes (Chapter 6)
j_{q}	W·m^{-2}	Heat flux from cell surface
j_i	mol·m^{-2}·s^{-1}	Molar flux of species *i*
$j_{\mathrm{Li[AM},i]}$	mol·m^{-2}·s^{-1}	Boundary flux at the particle/electrolyte interface
$j_{\mathrm{V,Li}}$	A·m^{-3}	Volumetric current density (plating reaction)
j_{tot}	A·m^{-3}	Volumetric current density (total)
k_{b}	eV·K^{-1}	Boltzmann constant
k_{f}	mol, m, s (*)	Reaction rate constant of forward reaction
k_{f}^0	mol, m, s (*)	Pre-exponential factor of forward reaction
k_{r}	mol, m, s (*)	Reaction rate constant of reverse reaction
L_{EP}	m	Thickness of electrode pair
$L_{\mathrm{electrode}}$	m	Thickness of electrode
M_i	kg·mol^{-1}	Molar mass of species *i*
$M_{\mathrm{Li[AM},i]}$	kg·mol^{-1}	Molar mass of lithiated active material

$M_{\mathrm{V[AM},i]}$	kg·mol^{-1}	Molar mass of delithiated active material
m	1	Index of electrode pair
n	1	Index of chemical reactions
N_{AM}	1	Number of active materials
N_{EP}	1	Number of electrode pairs
N_{gas}	1	Number of gas-phase species
N_{P}	1	Number of products participating in reaction
N_{R}	1	Number of reactants participating in reaction
N_{r}	1	Number of reactions
p_{gas}	kg·m^{-1}·s^{-2}	Pressure of gas phase
$\dot{q}^{\mathrm{V}}$	W·m^{-3}	Volume-specific heat source
$\dot{q}^{\mathrm{A}}$	W·m^{-2}	Heat source specific to active electrode area
$\dot{q}_{\mathrm{chem}}$	W·m^{-2}	Heat source due to chemical reactions
$\dot{q}_{\mathrm{ohm}}$	W·m^{-2}	Heat source due to ohmic losses
r	mol·m^{-2}·s^{-1}	Interfacial reaction rate
$r_{\mathrm{AM},i}$	m	Radius of active material particle
r_n	mol·m^{-2}·s^{-1}	Interfacial reaction rate of reaction *n*
$r_{n,\mathrm{SEI}}$	mol·m^{-1}·s^{-1}	SEI growth rate of reaction *n* (Chapter 6)
r_{P}	m	Radius of active material particle
R	J·K^{-1}·mol^{-1}	Ideal gas constant
R	Ω	Total internal resistance
R_{cc}	Ω·m^2	Area-specific ohmic resistance of current collection system
R_{ct}	Ω·m^2	Area-specific charge transfer resistance
R_{film}	Ω·m^2	Area-specific ohmic resistance of the surface film
$R_{\mathrm{SEI}}^{\mathrm{V}}$	Ω·m^3	Volume-specific ohmic resistance of SEI film
R_{Ohm}	Ω·m^2	Area-specific ohmic part of the impedance
R_{sep}	Ω·m^2	Area-specific electrolyte resistance in the separator
$\dot{s}_i$	mol·m^{-1}·s^{-1}	Species source term (Chapter 6)
$\dot{s}_i^{\mathrm{V}}$	mol·m^{-3}·s^{-1}	Volumetric species source term
$\dot{s}_{\mathrm{e}}^{\mathrm{V}}$	mol·m^{-3}·s^{-1}	Volumetric species source term of electrons
$\dot{s}_{i,\mathrm{DL}}^{\mathrm{V}}$	mol·m^{-3}·s^{-1}	Volumetric species source term due to double layer charge/discharge
$\dot{s}_i^{\mathrm{gas}}$	mol·s^{-1}	Gas-phase species source term
$\dot{s}_i^{\mathrm{gas,V}}$	mol·m^{-3}·s^{-1}	Volumetric species source term in gas phase
$\dot{s}_{\mathrm{Li[AM},i]}^{\mathrm{V}}$	mol·m^{-3}·s^{-1}	Volumetric source term of lithium in active material
$\dot{s}_{\mathrm{V[AM},i]}^{\mathrm{V}}$	mol·m^{-3}·s^{-1}	Volumetric source term of vacancies in active material
s_i	J·mol^{-1}·K^{-1}	Molar entropy of species *i*

$s^0_{\mathrm{Li[AM},i]}$	J·mol^{-1}·K^{-1}	Molar entropy of intercalated lithium in active material
$\mathrm{SOC_{elde}}$	1	Overall State-Of-Charge of an electrode
t	s	Time
t_i^0	1	Transference number of species *i*
t_+^0	1	Transference number of cation
t_-^0	1	Transference number of anion
T	K	Temperature
T_{amb}	K	Ambient temperature (cell surrounding)
T_{m}	K	Temperature of hollow cylinder V_m of the cell
V	m³	Volume of electrode
V^0	V	Open-circuit voltage
V_i	m^3·mol^{-1}	Molar volume (Chapter 6)
V_{cell}	m³	Volume of cell
V_m	m³	Volume of representative electrode pair
V_{void}	m³	Void (gas-phase) volume of cell
x	m	Spatial position in dimension of battery thickness
X_i	1	Initial mole fraction
$X_{\mathrm{Li[AM},i]}$	1	Lithium mole fraction
$X^{\mathrm{SOC=0}}_{\mathrm{Li[AM},i]} \dots X^{\mathrm{SOC=1}}_{\mathrm{Li[AM},i]}$	1	Stoichiometry range of lithium in the active material
y	m	Spatial position in dimension of electrode-pair thickness
Y_i	1	Mass fraction of species i
z	m	Spatial position in dimension of particle thickness
z	1	Number of electron transferred in charge-transfer reaction
Δz	m	Thickness of the control volume *j* (Chapter 6)
z_i	1	Charge number of species *i*
z_+	1	Charge number of cation
z_-	1	Charge number of anion
α	W·m^{-2}·K^{-1}	Heat transfer coefficient
$\alpha_{\mathrm{a}}, \alpha_{\mathrm{c}}$	1	Anodic and cathodic transfer coefficients of electrochemical reaction
α_{f}	1	Symmetry factor of forward reaction
δ_{SEI}	m	Thickness of SEI layer
ΔG	J·mol^{-1}	Gibbs free reaction energy
ΔG^0	J·mol^{-1}	Standard Gibbs free reaction energy
ΔH	J·mol^{-1}	Reaction enthalpy
ΔH_n	J·mol^{-1}	Reaction enthalpy of reaction *n*
$\Delta\phi$	V	Electric-potential difference between electrode and electrolyte

$\Delta\phi^{\mathrm{eff}}$	V	Effective electric-potential difference
$\Delta\phi^{\mathrm{eq}}$	V	Equilibrium potential difference
$\Delta\phi_n$	V	Electric potential difference of reaction *n*
$\phi_{\mathrm{s}}, \phi_{\mathrm{elyt}}$	V	Electric potential in the solid phase and in the electrolyte
$\Delta\phi_{\mathrm{an}}$	V	Electric potential of the anode electrode
$\Delta\phi_{\mathrm{Li}}^{\mathrm{eq}}$	V	Equilibrium potential of plating reaction
$\Delta\phi_{\mathrm{n}}$	V	Electric potential difference of reaction *n*
ΔS	J·mol^{-1}·K^{-1}	Reaction entropy
ϕ_{elde}	V	Electric potential of the electrode
ϕ_{elyt}	V	Electric potential of the electrolyte
ϵ	1	Emissivity of the cell surface
ε	1	Volume fraction
$\varepsilon_{\mathrm{elyt}}$	1	Volume fraction of the electrolyte
$\varepsilon_{\mathrm{AM}}$	1	Volume fraction of the active material
$\varepsilon_{\mathrm{SEI}}$	1	Volume fraction of the SEI
η_{act}	V	Activation Overpotential
λ	W·m^{-1}·K^{-1}	Thermal conductivity
μ_i^0	J·mol^{-1}	Standard-state chemical potentials of all species i
ν	1	CST lumped activity parameter
ν_i	1	Stoichiometric coefficient of species *i*
$\nu_{\mathrm{e},n}$	1	Stoichiometric coefficient of electrochemical reaction *n*
ρ	kg·m^{-3}	Density
ρ_{gas}	kg·m^{-3}	Density of the gas
$\rho_{\mathrm{Li[AM},i]}$	kg·m^{-3}	Density of the lithiated active material
$\rho_{\mathrm{AM},i}$	kg·m^{-3}	Density of the delithiated active material
σ	S·m^{-1}	Electrolyte conductivity
σ_{SB}	W·m^{-2}·K^{-4}	Stefan-Boltzmann constant
σ_{SEI}	S·m^{-1}	Electrical conductivity of SEI
$\sigma_{\mathrm{elec},j}$	S·m^{-1}	Electronic conductivity for a volume *j* (Chapter 6)
τ	1	Geometric tortuosity
τ'	1	Geometric tortuosity with Bruggeman approximation
τ_{elyt}	1	Geometric tortuosity of the electrolyte
Θ_I	1	Simulated degradation factor ($\Delta\phi_{\mathrm{an}} < 0$)
Θ_{Φ}	1	Simulated degradation factor ($\Delta\phi_{\mathrm{an}} < \Delta\phi_{\mathrm{Li}}^{\mathrm{eq}}$)
Θ_{Li}	1	Simulated degradation factor ($\dot{s}_{\mathrm{Li}} > 0$)

$*$ units of mol, m and s depending on reaction stoichiometry

10 PUBLICATIONS LIST

Published papers

1. "Modeling and experimental yalidation of a high-power lithium-ion pouch cell with LCO/NCA blend cathode." S. Carelli, M. Quarti, M. C. Yagci and W. G. Bessler, *J. Electrochem. Soc.,* **166**(13), A2990-A3003 (2019). [Ref. [111]]
2. "Identification of stoichiometric and microstructural parameters of a lithium-ion cell with blend electrode." M. Mayur, M. C. Yagci, S. Carelli, P. Margulies, D. Velten and W. G. Bessler, *Physical chemistry chemical physics : PCCP,* **21**(42), 23672–23684 (2019). [Ref. [34]]
3. "Prediction of reversible lithium plating with a pseudo-3D lithium-ion battery model." S. Carelli and W. G. Bessler, *J. Electrochem. Soc.,* **167**(100515) (2020). [Ref. [78]]

Conference posters and presentations

1. S. Carelli and W.G. Bessler: Mechanistic modeling of electrochemical ageing reactions at the anode of lithium-ion batteries (LIB), Poster presentation, German-Israeli Battery School (GIBS – Hadera IL, 09/2017)
2. S. Carelli, M. Quarti, M. Mayur, W.G. Bessler: Experimental and modeling study of a lithium-ion pouch cell with LCO/NCA blend cathode. Part 2: Model development and validation, Poster presentation, Kraftwerk Batterie (Münster, 04/2018)
3. S. Carelli, C. Kupper, W.G. Bessler: End-of-life prediction of a lithium-ion battery cell based on mechanistic ageing models of the graphite electrode, Poster presentation, 19th International Meeting on Lithium Batteries (IMLB – Kyoto JP, 06/2018)
4. S. Carelli and W.G. Bessler: An extended pseudo-3D model of a lithium-ion battery with lithium plating, Poster presentation, Modval '19 (Braunschweig, 03/2019)
5. S. Carelli and W.G. Bessler: Prediction of reversible lithium plating with a pseudo-3D lithium-ion battery model, Poster presentation, OBMS20 (Oxford UK, 03/2020) CANCELLED DUE TO COVID19
6. S. Carelli and W.G. Bessler: Lithium plating: How mathematics can help to identify fast-charging limits, Oral presentation, 237th ECS Meeting (Montreal CA, 05/2020) CANCELLED DUE TO COVID19

Extras

1. Guest scientist at Colorado School of Mines, USA (05.07.2019 – 16.08.2019)
2. Member of SiMET – Simulation of Mechanical, Electrical and Thermal effects in Li-ion batteries

11 REFERENCES

(1) Zito, R.; Ardibili, H. *Energy storage: A new approach*, Second edition; Wiley; Scrivener Publishing: Hoboken, NJ, Beverly, MA, 2019.

(2) Scrosati, B. History of lithium batteries. *J Solid State Electrochem* **2011**, *15*, 1623–1630.

(3) Whittingham, M. S. History, Evolution, and Future Status of Energy Storage. *Proc. IEEE* **2012**, *100*, 1518–1534.

(4) Bagotsky, V. S. Fuel cells, batteries, and the development of electrochemistry. *J Solid State Electrochem* **2011**, *15*, 1559–1562.

(5) Whittingham, M.S. Chemistry of intercalation compounds: Metal guests in chalcogenide hosts. Progress in Solid State Chemistry, 12(1), 41-99 [Online early access]. DOI: 10.1016/0079-6786(78)90003-1.

(6) Dunn, B.; Kamath, H.; Tarascon, J.-M. Electrical Energy Storage for the Grid: A Battery of Choices. *Science* **2011**, *334*, 928–935.

(7) Huo, H.; Cai, H.; Zhang, Q.; Liu, F.; He, K. Life-cycle assessment of greenhouse gas and air emissions of electric vehicles: A comparison between China and the U.S. *Atmospheric Environment* **2015**, *108*, 107–116.

(8) Egbue, O.; Long, S. Barriers to widespread adoption of electric vehicles: An analysis of consumer attitudes and perceptions. *Energy Policy* **2012**, *48*, 717–729.

(9) Lu, L.; Han, X.; Li, J.; Hua, J.; Ouyang, M. A review on the key issues for lithium-ion battery management in electric vehicles. *J. Power Sources* **2013**, *226*, 272–288.

(10) Wen, J.; Yu, Y.; Chen, C. A Review on Lithium-Ion Batteries Safety Issues: Existing Problems and Possible Solutions. *Mat Express* **2012**, *2*, 197–212.

(11) Bandhauer, T. M.; Garimella, S.; Fuller, T. F. A Critical Review of Thermal Issues in Lithium-Ion Batteries. *J. Electrochem. Soc.* **2011**, *158*, R1.

(12) Franco, A. A.; Doublet, M. L.; Bessler, W. G., Eds. *Physical Multiscale Modeling and Numerical Simulation of Electrochemical Devices for Energy Conversion and Storage: From Theory to Engineering to Practice*; Green Energy and Technology; Springer: London, Heidelberg, New York, Dordrecht, 2016.

(13) Ecker, M.; Kabitz, S.; Laresgoiti, I.; Sauer, D. U. Parameterization of a Physico-Chemical Model of a Lithium-Ion Battery: II. Model Validation. *J. Electrochem. Soc.* **2015**, *162*, A1849-A1857.

(14) Franco, A. A. Multiscale Modelling and Numerical Simulation of Rechargeable Lithium Ion Batteries: Concepts, Methods and Challenges. *RSC Adv.* **2013**, *3*, 13027–13058.

(15) Doyle, M.; Fuller, T. F.; Newman, J. Modeling of Galvanostatic Charge and Discharge of the Lithium/Polymer/Insertion Cell. *J. Electrochem. Soc.* **1993**, *140*, 1526–1533.

(16) Kim, G.-H.; Smith, K.; Lee, K.-J.; Santhanagopalan, S.; Pesaran, A. Multi-Domain Modeling of Lithium-Ion Batteries Encompassing Multi-Physics in Varied Length Scales. *J. Electrochem. Soc.* **2011**, *158*, A955.

(17) Tippmann, S.; Walper, D.; Balboa, L.; Spier, B.; Bessler, W. G. Low-temperature charging of lithium-ion cells part I: Electrochemical modeling and experimental investigation of degradation behavior. *J. Power Sources* **2014**, *252*, 305–316.

(18) Prada, E.; Di Domenico, D.; Creff, Y.; Bernard, J.; Sauvant-Moynot, V.; Huet, F. Simplified Electrochemical and Thermal Model of $LiFePO_4$ -Graphite Li-Ion Batteries for Fast Charge Applications. *J. Electrochem. Soc.* **2012**, *159*, A1508-A1519.

(19) Kupper, C.; Bessler, W. G. Multi-Scale Thermo-Electrochemical Modeling of Performance and Aging of a $LiFePO_4$ /Graphite Lithium-Ion Cell. *J. Electrochem. Soc.* **2017**, *164*, A304-A320.

(20) Northrop, P. W. C.; Pathak, M.; Rife, D.; De, S.; Santhanagopalan, S.; Subramanian, V. R. Efficient Simulation and Model Reformulation of Two-Dimensional Electrochemical Thermal Behavior of Lithium-Ion Batteries. *J. Electrochem. Soc.* **2015**, *162*, A940-A951.

(21) Awarke, A.; Pischinger, S.; Ogrzewalla, J. Pseudo 3D Modeling and Analysis of the SEI Growth Distribution in Large Format Li-Ion Polymer Pouch Cells. *J. Electrochem. Soc.* **2012**, *160*, A172-A181.

(22) Christensen, J.; Cook, D.; Albertus, P. An Efficient Parallelizable 3D Thermoelectrochemical Model of a Li-Ion Cell. *J. Electrochem. Soc.* **2013**, *160*, A2258-A2267.

(23) Greco, A.; Cao, D.; Jiang, X.; Yang, H. A theoretical and computational study of lithium-ion battery thermal management for electric vehicles using heat pipes. *J. Power Sources* **2014**, *257*, 344–355.

(24) Smith, K. A.; Rahn, C. D.; Wang, C.-Y. Control oriented 1D electrochemical model of lithium ion battery. *Energy Conversion and Management* **2007**, *48*, 2565–2578.

(25) Xiao, X.; Wu, W.; Huang, X. A multi-scale approach for the stress analysis of polymeric separators in a lithium-ion battery. *J. Power Sources* **2010**, *195*, 7649–7660.

(26) Danner, T.; Singh, M.; Hein, S.; Kaiser, J.; Hahn, H.; Latz, A. Thick electrodes for Li-ion batteries: A model based analysis. *J. Power Sources* **2016**, *334*, 191–201.

(27) Winter, M.; Brodd, R. J. What are batteries, fuel cells, and supercapacitors? *Chem. Rev.* **2004**, *104*, 4245–4269.

(28) Yue, Y.; Liang, H. 3D Current Collectors for Lithium-Ion Batteries: A Topical Review. *Small Methods* **2018**, *2*, 1800056.

(29) Gao, J.; Shi, S.-Q.; Li, H. Brief overview of electrochemical potential in lithium ion batteries. *Chinese Phys. B* **2016**, *25*, 18210.

(30) Arora, P.; Zhang, Z. Battery Separators. *Chem. Rev.* **2004**, *104*, 4419–4462.

(31) Mebarki, B.; Draoui, B.; Allaou, B.; Rahmani, L.; Benachour, E. Impact of the Air-Conditioning System on the Power Consumption of an Electric Vehicle Powered by Lithium-Ion Battery. *Modelling and Simulation in Engineering* **2013**, *2013*, 1–6.

(32) Marcicki, J. M. Modeling, Parametrization, and Diagnostics for Lithium-Ion Batteries with Automotive Applications. PhD Thesis, The Ohio State University, 2012.

(33) Li, A. Experimental analysis and modelling of battery cells and their packs : application to electric and hybrid vehicles. PhD Thesis, Université Claude Bernard - Lyon I, 2013.

(34) Mayur, M.; Yagci, M. C.; Carelli, S.; Margulies, P.; Velten, D.; Bessler, W. G. Identification of stoichiometric and microstructural parameters of a lithium-ion cell with blend electrode. *Physical Chemistry Chemical Physics* **2019**, *21*, 23672–23684.

(35) Bessler, W. G.; Gewies, S.; Vogler, M. A New Framework For Physically Based Modeling of Solid Oxide Fuel Cells. *Electrochim. Acta* **2007**, *53*, 1782–1800.

(36) Epstein, N. On tortuosity and the tortuosity factor in flow and diffusion through porous media. *Chem. Eng. Sci.* **1989**, *44*, 777–779.

(37) Bruggeman, D. A. G. Berechnung verschiedener physikalischer Konstanten von heterogenen Substanzen. I. Dielektrizitätskonstanten und Leitfähigkeiten der Mischkörper aus isotropen Substanzen. *Ann. Phys.* **1935**, *416*, 636–664.

(38) Neidhardt, J. P.; Fronczek, D. N.; Jahnke, T.; Danner, T.; Horstmann, B.; Bessler, W. G. A Flexible Framework for Modeling Multiple Solid, Liquid and Gaseous Phases in Batteries and Fuel Cells. *J. Electrochem. Soc.* **2012**, *159*, A1528-A1542.

(39) Valøen, L. O.; Reimers, J. N. Transport Properties of $LiPF_6$-Based Li-Ion Battery Electrolytes. *J. Electrochem. Soc.* **2005**, *152*, A882-A891.

(40) Veth, C.; Dragicevic, D.; Pfister, R.; Arakkan, S.; Merten, C. 3D Electro-Thermal Model Approach for the Prediction of Internal State Values in Large-Format Lithium Ion Cells and Its Validation. *J. Electrochem. Soc.* **2014**, *161*, A1943-A1952.

(41) Fuller, T. F.; Doyle, M.; Newman, J. Simulation and Optimization of the Dual Lithium Ion Insertion Cell. *J. Electrochem. Soc.* **1994**, *141*, 1–10.

(42) Goodwin, D.; Moffat, H. K.; Speth, R. L.; Goodwin, D. G.; Weber, B. W. *Cantera: An Object-Oriented Software Toolkit For Chemical Kinetics, Thermodynamics, And Transport Processes. Version 2.5.0*; www.cantera.org; Zenodo, 2019.

(43) Atkins, P. W. *Physical chemistry*, 6th; Oxford University Press: Oxford, UK, 1998.

(44) Newman, J.; Thomas-Alyea, K. E. *Electrochemical Systems*, 3rd ed.; John Wiley & Sons: Hoboken, New Jersey, USA, 2004.

(45) Bockris, J. O.'M.; Reddy, A. K.N.; Gamboa-Aldeco, M. E. *Modern Electrochemistry: Fundamentals of Electrodics*, 2nd ed.; Kluver Academic/Plenum Publishers: New York, USA, 2000.

(46) Grübl, D.; Janek, J.; Bessler, W. G. Electrochemical Pressure Impedance Spectroscopy (EPIS) as Diagnostic Method for Electrochemical Cells with Gaseous Reactants: A Model-Based Analysis. *J. Electrochem. Soc.* **2016**, *163*, A599-A610.

(47) Mayur, M.; DeCaluwe, S. C.; Kee, B. L.; Bessler, W. G. Modeling and simulation of the thermodynamics of lithium-ion battery intercalation materials in the open-source software Cantera. *Electrochim. Acta* **2019**, *323*, 134797.

(48) Danzer, M. A.; Liebau, V.; Maglia, F. Aging of lithium-ion batteries for electric vehicles. *Advances in Battery Technologies for Electric Vehicles*; Elsevier, 2015; pp 359–387.

(49) Anseán, D.; Dubarry, M.; Devie, A.; Liaw, B. Y.; García, V. M.; Viera, J. C.; González, M. Operando lithium plating quantification and early detection of a commercial $LiFePO_4$ cell cycled under dynamic driving schedule. *Journal of Power Sources* **2017**, *356*, 36–46.

(50) Birkl, C. R.; Roberts, M. R.; McTurk, E.; Bruce, P. G.; Howey, D. A. Degradation diagnostics for lithium ion cells. *J. Power Sources* **2017**, *341*, 373–386.

(51) Vetter, J.; Novák, P.; Wagner, M. R.; Veit, C.; Möller, K.-C.; Besenhard, J. O.; Winter, M.; Wohlfahrt-Mehrens, M.; Vogler, C.; Hammouche, A. Ageing mechanisms in lithium-ion batteries. *J. Power Sources* **2005**, *147*, 269–281.

(52) Keil, P. Aging of Lithium-Ion Batteries in Electric Vehicles. PhD Thesis, Technische Universität München, 2017.

(53) Ratnakumar, B. V.; Smart, M. C.; Surampudi, S. Effects of SEI on the kinetics of lithium intercalation. *J. Power Sources* **2001**, *97-98*, 137–139.

(54) Aurbach, D. Review of selected electrode–solution interactions which determine the performance of Li and Li ion batteries. *J. Power Sources* **2000**, *89*, 206–218.

(55) Li, D.; Danilov, D.; Zhang, Z.; Chen, H.; Yang, Y.; Notten, P. H. L. Modeling the SEI-Formation on Graphite Electrodes in $LiFePO_4$ Batteries. *J. Electrochem. Soc.* **2015**, *162*, A858-A869.

(56) Laresgoiti, I.; Käbitz, S.; Ecker, M.; Sauer, D. U. Modeling mechanical degradation in lithium ion batteries during cycling: Solid electrolyte interphase fracture. *J. Power Sources* **2015**, *300*, 112–122.

(57) Ning, G.; White, R. E.; Popov, B. N. A generalized cycle life model of rechargeable Li-ion batteries. *Electrochim. Acta* **2006**, *51*, 2012–2022.

(58) Guan, P.; Liu, L.; Lin, X. Simulation and Experiment on Solid Electrolyte Interphase (SEI) Morphology Evolution and Lithium-Ion Diffusion. *J. Electrochem. Soc.* **2015**, *162*, A1798-A1808.

(59) Chagnes, A.; Swiatowsk, J. Electrolyte and Solid-Electrolyte Interphase Layer in Lithium-Ion Batteries. In *Lithium ion batteries: New developments*; Belharouak, I., Ed.; InTech: Rijeka, Croatia, 2012.

(60) Peled, E.; Golodnitsky, D. SEI on lithium, graphite, disordered carbons and tin-based alloys. In *Lithium-ion batteries: Solid-electrolyte interphase,* [Repr.]; Balbuena, P. B., Wang, Y., Eds.; Imperial College Press: London, 2007; pp 1–69.

(61) Tang, M.; Lu, S.; Newman, J. Experimental and Theoretical Investigation of Solid-Electrolyte-Interphase Formation Mechanisms on Glassy Carbon. *J. Electrochem. Soc.* **2012**, *159*, A1775-A1785.

(62) Single, F.; Horstmann, B.; Latz, A. Dynamics and morphology of solid electrolyte interphase (SEI). *Physical chemistry chemical physics : PCCP* **2016**, *18*, 17810–17814.

(63) Single, F.; Karaca, E.; Horstmann, B.; Latz, A. Simulation and Modelling of the Solid Electrolyte Interphase with Varying Porosity. *ECS Transactions* **2015**, *69*, 129–131.

(64) Single, F.; Latz, A.; Horstmann, B. Identifying the Mechanism of Continued Growth of the Solid-Electrolyte Interphase. *ChemSusChem* **2018**, *11*, 1950–1955.

(65) DeCaluwe, S. Open Software for Chemical and Electrochemical Modeling: Opportunities and Challenges. *The Electrochemical Society Interface* **2019**, 47–50.

(66) Single, F.; Horstmann, B.; Latz, A. Revealing SEI Morphology: In-Depth Analysis of a Modeling Approach. *J. Electrochem. Soc.* **2017**, *164*, E3132-E3145.

(67) Andersson, A.M.; Henningson, A.; Siegbahn, H.; Jansson, U.; Edström, K. Electrochemically lithiated graphite characterised by photoelectron spectroscopy. *J. Power Sources* **2003**, *119-121*, 522–527.

(68) Horstmann, B.; Single, F.; Latz, A. Review on multi-scale models of solid-electrolyte interphase formation. *Current Opinion in Electrochemistry* **2019**, *13*, 61–69.

(69) Ploehn, H. J.; Ramadass, P.; White, R. E. Solvent diffusion model for aging of Lithium-ion battery cells. *J. Electrochem. Soc.* **2004**, *151*, A456.

(70) Pinson, M. B.; Bazant, M. Z. Theory of SEI Formation in Rechargeable Batteries: Capacity Fade, Accelerated Aging and Lifetime Prediction. *J. Electrochem. Soc.* **2013**, *160*, A243-A250.

(71) Broussely, M.; Herreyre, S.; Biensan, P.; Kasztejna, P.; Nechev, K.; Staniewicz, R.J. Aging mechanism in Li ion cells and calendar life predictions. *J. Power Sources* **2001**, *97-98*, 13–21.

(72) Christensen, J.; Newman, J. A Mathematical Model for the Lithium-Ion Negative Electrode Solid Electrolyte Interphase. *J. Electrochem. Soc.* **2004**, *151*, A1977-A1988.

(73) Röder, F.; Braatz, R. D.; Krewer, U. Multi-Scale Simulation of Heterogeneous Surface Film Growth Mechanisms in Lithium-Ion Batteries. *J. Electrochem. Soc.* **2017**, *164*, E3335-E3344.

(74) Soto, F. A.; Ma, Y.; La Martinez de Hoz, J. M.; Seminario, J. M.; Balbuena, P. B. Formation and Growth Mechanisms of Solid-Electrolyte Interphase Layers in Rechargeable Batteries. *Chem. Mater.* **2015**, *27*, 7990–8000.

(75) Shi, S.; Lu, P.; Liu, Z.; Qi, Y.; Hector, L. G.; Li, H.; Harris, S. J. Direct calculation of Li-ion transport in the solid electrolyte interphase. *J. Am. Chem. Soc.* **2012**, *134*, 15476–15487.

(76) Kolzenberg, L. von; Latz, A.; Horstmann, B. Solid-Electrolyte Interphase During Battery Cycling: Theory of Growth Regimes. *ChemSusChem* [Online early access]. DOI: 10.1002/cssc.202000867.

(77) Kupper, C.; Weißhar, B.; Rißmann, S.; Bessler, W. G. End-of-Life Prediction of a Lithium-Ion Battery Cell Based on Mechanistic Aging Models of the Graphite Electrode. *J. Electrochem. Soc.* **2018**, *165*, A3468-A3480.

(78) Carelli, S.; Bessler, W. G. Prediction of reversible lithium plating with a pseudo-3D lithium-ion battery model. *J. Electrochem. Soc.* **2020**, *167*.

(79) Remmlinger, J.; Tippmann, S.; Buchholz, M.; Dietmayer, K. Low-temperature charging of lithium-ion cells Part II: Model reduction and application. *J. Power Sources* **2014**, *254*, 268–276.

(80) Harris, S. J.; Timmons, A.; Baker, D. R.; Monroe, C. Direct in situ measurements of Li transport in Li-ion battery negative electrodes. *Chemical Physics Letters* **2010**, *485*, 265–274.

(81) Hein, S. Modeling of lithium plating in lithium-ionbatteries. PhD Thesis, Fakultät für Naturwissenschaften der Universität Ulm, 2017.

(82) Arora, P. Mathematical Modeling of the Lithium Deposition Overcharge Reaction in Lithium-Ion Batteries Using Carbon-Based Negative Electrodes. *J. Electrochem. Soc.* **1999**, *146*, 3543.

(83) Li, Z.; Huang, J.; Yann Liaw, B.; Metzler, V.; Zhang, J. A review of lithium deposition in lithium-ion and lithium metal secondary batteries. *J. Power Sources* **2014**, *254*, 168–182.

(84) Waldmann, T.; Hogg, B.-I.; Wohlfahrt-Mehrens, M. Li plating as unwanted side reaction in commercial Li-ion cells – A review. *J. Power Sources* **2018**, *384*, 107–124.

(85) Bitzer, B.; Gruhle, A. A new method for detecting lithium plating by measuring the cell thickness. *Journal of Power Sources* **2014**, *262*, 297–302.

(86) Petzl, M.; Kasper, M.; Danzer, M. A. Lithium plating in a commercial lithium-ion battery – A low-temperature aging study. *J. Power Sources* **2015**, *275*, 799–807.

(87) Uhlmann, C.; Illig, J.; Ender, M.; Schuster, R.; Ivers-Tiffée, E. In situ detection of lithium metal plating on graphite in experimental cells. *J. Power Sources* **2015**, *279*, 428–438.

(88) Ratnakumar, B. V.; Smart, M. C. Lithium Plating Behavior in Lithium-Ion Cells. *ECS Transactions* **2010**, *25*, 241–252.

(89) Smart, M. C.; Ratnakumar, B. V. Effects of Electrolyte Composition on Lithium Plating in Lithium-Ion Cells. *J. Electrochem. Soc.* **2011**, *158*, A379.

(90) Smart, M. C.; Ratnakumar, B. V.; Whitcanack, L.; Chin, K.; Rodriguez, M.; Surampudi, S. Performance characteristics of lithium ion cells at low temperatures. *IEEE Aerosp. Electron. Syst. Mag.* **2002**, *17*, 16–20.

(91) Petzl, M.; Danzer, M. A. Nondestructive detection, characterization, and quantification of lithium plating in commercial lithium-ion batteries. *J. Power Sources* **2014**, *254*, 80–87.

(92) Zinth, V.; Lüders, C. von; Hofmann, M.; Hattendorff, J.; Buchberger, I.; Erhard, S.; Rebelo-Kornmeier, J.; Jossen, A.; Gilles, R. Lithium plating in lithium-ion batteries at sub-ambient temperatures investigated by in situ neutron diffraction. *J. Power Sources* **2014**, *271*, 152–159.

(93) Lu, W.; López, C. M.; Liu, N.; Vaughey, J. T.; Jansen, A.; Dennis W., D. Overcharge Effect on Morphology and Structure of Carbon Electrodes for Lithium-Ion Batteries. *J. Electrochem. Soc.* **2012**, *159*, A566-A570.

(94) Lüders, C. von; Zinth, V.; Erhard, S. V.; Osswald, P. J.; Hofmann, M.; Gilles, R.; Jossen, A. Lithium plating in lithium-ion batteries investigated by voltage relaxation and in situ neutron diffraction. *J. Power Sources* **2017**, *342*, 17–23.

(95) Ecker, M. Lithium Plating in Lithium-Ion batteries: An experimental and simulation approach. PhD Thesis, RWTH Aachen University, 2016.

(96) Schindler, S.; Bauer, M.; Petzl, M.; Danzer, M. A. Voltage relaxation and impedance spectroscopy as in-operando methods for the detection of lithium plating on graphitic anodes in commercial lithium-ion cells. *J. Power Sources* **2016**, *304*, 170–180.

(97) Whitehead, A. H. A Graphical Aid to Evaluation of Carbon-Based Li-Ion Electrodes. *J. Electrochem. Soc.* **1997**, *144*, L92.

(98) Fan, J.; Tan, S. Studies on Charging Lithium-Ion Cells at Low Temperatures. *Electrochim. Acta* **2006**, *153*, A1081.

(99) Lin, H.-P.; Chua, D.; Salomon, M.; Shiao, H.-C.; Hendrickson, M.; Plichta, E.; Slane, S. Low-Temperature Behavior of Li-Ion Cells. *J. Electrochem. Soc.* **2001**, *4*, A71.

(100) Gallagher, K. G.; Trask, S. E.; Bauer, C.; Woehrle, T.; Lux, S. F.; Tschech, M.; Lamp, P.; Polzin, B. J.; Ha, S.; Long, B.*; et al.* Optimizing Areal Capacities through Understanding the Limitations of Lithium-Ion Electrodes. *J. Electrochem. Soc.* **2016**, *163*, A138-A149.

(101) Campbell, I. D.; Marzook, M.; Marinescu, M.; Offer, G. J. How Observable Is Lithium Plating? Differential Voltage Analysis to Identify and Quantify Lithium Plating Following Fast Charging of Cold Lithium-Ion Batteries. *J. Electrochem. Soc.* **2019**, *166*, A725-A739.

(102) Wohlfahrt-Mehrens, M.; Vogler, C.; Garche, J. Aging mechanisms of lithium cathode materials. *J. Power Sources* **2004**, *127*, 58–64.

(103) Edström, K.; Gustafsson, T.; Thomas, J. O. The cathode–electrolyte interface in the Li-ion battery. *Electrochim. Acta* **2004**, *50*, 397–403.

(104) Arora, P.; White, R. E.; Doyle, M. Capacity fade mechanisms and side reactions in Lithium-ion batteries // Capacity Fade Mechanisms and Side Reactions in Lithium-Ion Batteries. *J. Electrochem. Soc.* **1998**, *145*, 3647–3667.

(105) Abraham, D. P.; Kawauchi, S.; Dees, D. W. Modeling the Impedance versus Voltage Characteristics of $LiNi_{0.8}Co_{0.15}Al_{0.05}O_2$. *Electrochim. Acta* **2008**, *53*, 2121–2129.

(106) Ding, M. S.; Xu, K.; Zhang, S. S.; Amine, K.; Henriksen, G. L.; Jow, T. R. Change of Conductivity with Salt Content, Solvent Composition, and Temperature for Electrolytes of $LiPF_6$ in Ethylene Carbonate-Ethyl Methyl Carbonate. *J. Electrochem. Soc.* **2001**, *148*, A1196.

(107) Broussely, M.; Biensan, P.; Bonhomme, F.; Blanchard, P.; Herreyre, S.; Nechev, K.; Staniewicz, R. J. Main aging mechanisms in Li ion batteries. *Journal of Power Sources* **2005**, *146*, 90–96.

(108) Waldmann, T.; Gorse, S.; Samtleben, T.; Schneider, G.; Knoblauch, V.; Wohlfahrt-Mehrens, M. A Mechanical Aging Mechanism in Lithium-Ion Batteries. *J. Electrochem. Soc.* **2014**, *161*, A1742-A1747.

(109) Guenther, C.; Schott, B.; Hennings, W.; Waldowski, P.; Danzer, M. A. Model-based investigation of electric vehicle battery aging by means of vehicle-to-grid scenario simulations. *J. Power Sources* **2013**, *239*, 604–610.

(110) Saxena, S.; Le Floch, C.; MacDonald, J.; Moura, S. Quantifying EV battery end-of-life through analysis of travel needs with vehicle powertrain models. *J. Power Sources* **2015**, *282*, 265–276.

(111) Carelli, S.; Quarti, M.; Yagci, M. C.; Bessler, W. G. Modeling and Experimental Validation of a High-Power Lithium-Ion Pouch Cell with LCO/NCA Blend Cathode. *J. Electrochem. Soc.* **2019**, *166*, A2990-A3003.

(112) Chikkannanavar, S. B.; Bernardi, D. M.; Liu, L. A review of blended cathode materials for use in Li-ion batteries. *J. Power Sources* **2014**, *248*, 91–100.

(113) Heubner, C.; Liebmann, T.; Schneider, M.; Michaelis, A. Recent insights into the electrochemical behavior of blended lithium insertion cathodes: A review. *Electrochim. Acta* **2018**, *269*, 745–760.

(114) Albertus, P.; Christensen, J.; Newman, J. Experiments on and Modeling of Positive Electrodes with Multiple Active Materials for Lithium-Ion Batteries. *J. Electrochem. Soc.* **2009**, *156*, A606.

(115) Rodríguez, A.; Plett, G. L. Controls-oriented models of lithium-ion cells having blend electrodes. Part 2: Physics-based reduced-order models. *Journal of Energy Storage* **2017**, *11*, 219–236.

(116) Jung, S. Mathematical model of lithium-ion batteries with blended-electrode system. *J. Power Sources* **2014**, *264*, 184–194.

(117) Appiah, W. A.; Park, J.; van Khue, L.; Lee, Y.; Choi, J.; Ryou, M.-H.; Lee, Y. M. Comparative study on experiments and simulation of blended cathode active materials for lithium ion batteries. *Electrochim. Acta* **2016**, *187*, 422–432.

(118) Mao, Z.; Farkhondeh, M.; Pritzker, M.; Fowler, M.; Chen, Z. Multi-Particle Model for a Commercial Blended Lithium-Ion Electrode. *J. Electrochem. Soc.* **2016**, *163*, A458-A469.

(119) Karthikeyan, D. K.; Sikha, G.; White, R. E. Thermodynamic Model Development for Lithium Intercalation Electrodes. *J. Power Sources* **2008**, *185*, 1398–1407.

(120) Ménétrier, M.; Saadoune, I.; Levasseur, S.; Delmas, C. The insulator-metal transition upon lithium deintercalation from $LiCoO_2$: electronic properties and 7Li NMR study. *J. Mater. Chem.* **1999**, *9*, 1135–1140.

(121) Reynier, Y.; Graetz, J.; Swan-Wood, T.; Rez, P.; Yazami, R.; Fultz, B. Entropy of Li intercalation in Li_xCoO_2. *Phys. Rev. B* **2004**, *70*, 753.

(122) Hall, F.; Wußler, S.; Buqa, H.; Bessler, W. G. Asymmetry of Discharge/Charge Curves of Lithium-Ion Battery Intercalation Electrodes. *J. Phys. Chem. C* **2016**, *120*, 23407–23414.

(123) Basu, S.; Patil, R. S.; Ramachandran, S.; Hariharan, K. S.; Kolake, S. M.; Song, T.; Oh, D.; Yeo, T.; Doo, S. Non-isothermal electrochemical model for lithium-ion cells with composite cathodes. *J. Power Sources* **2015**, *283*, 132–150.

(124) Ecker, M.; Tran, T. K. D.; Dechent, P.; Kabitz, S.; Warnecke, A.; Sauer, D. U. Parameterization of a Physico-Chemical Model of a Lithium-Ion Battery: I. Determination of Parameters. *J. Electrochem. Soc.* **2015**, *162*, A1836-A1848.

(125) Reynier, Y. F.; Yazami, R.; Fultz, B. Thermodynamics of Lithium Intercalation into Graphites and Disordered Carbons. *J. Electrochem. Soc.* **2004**, *151*, A422.

(126) McBride, B. J.; Zehe, M. J.; Gordon, S. *NASA Glenn Coefficients for Calculating Thermodynamic Properties of Individual Species*; NASA Glenn Research Center, Cleveland, Ohio, USA, 2002.

(127) Almar, L.; Joos, J.; Weber, A.; Ivers-Tiffée, E. Microstructural feature analysis of commercial Li-ion battery cathodes by focused ion beam tomography. *J. Power Sources* **2019**, *427*, 1–14.

(128) Kwon, K.; Kong, F.; McLarnon, F.; Evans, J. W. Characterization of the SEI on a Carbon Film Electrode by Combined EQCM and Spectroscopic Ellipsometry. *J. Electrochem. Soc.* **2003**, *150*, A229.

(129) Lide, D. R., Ed. *CRC Handbook of Chemistry and Physics*; CRC press: Boca Raton, Florida, USA, 2006.

(130) Haynes, W. M.; Lide, D. R.; Bruno, T. J. *CRC Handbook of Chemistry and Physics: A Ready-Reference Book of Chemical and Physical Data: 2013-2014*, 94th edition; CRC press: Boca Raton (Fla.), London, New York, 2013.

(131) Loges, A.; Herberger, S.; Werner, D.; Wetzel, T. Thermal characterization of Li-ion cell electrodes by photothermal deflection spectroscopy. *J. Power Sources* **2016**, *325*, 104–115.

(132) Loges, A.; Herberger, S.; Seegert, P.; Wetzel, T. A study on specific heat capacities of Li-ion cell components and their influence on thermal management. *J. Power Sources* **2016**, *336*, 341–350.

(133) Wen, C.-D.; Mudawar, I. Emissivity characteristics of roughened aluminum alloy surfaces and assessment of multispectral radiation thermometry (MRT) emissivity models. *International Journal of Heat and Mass Transfer* **2004**, *47*, 3591–3605.

(134) Nyman, A.; Behm, M.; Lindbergh, G. Electrochemical characterisation and modelling of the mass transport phenomena in $LiPF_6$–EC–EMC electrolyte. *Electrochim. Acta* **2008**, *53*, 6356–6365.

(135) Zhang, S.S.; Xu, K.; Allen, J.L.; Jow, T.R. Effect of propylene carbonate on the low temperature performance of Li-ion cells. *J. Power Sources* **2002**, *110*, 216–221.

(136) Capiglia, C.; Saito, Y.; Kageyama, H.; Mustarelli, P.; Iwamoto, T.; Tabuchi, T.; Tukamoto, H. 7Li and 19F diffusion coefficients and thermal properties of non-aqueous electrolyte solutions for rechargeable lithium batteries. *J. Power Sources* **1999**, *81-82*, 859–862.

(137) Gantenbein, S.; Weiss, M.; Ivers-Tiffée, E. Impedance based time-domain modeling of lithium-ion batteries: Part I. *J. Power Sources* **2018**, *379*, 317–327.

(138) Van der Ven, A. Lithium Diffusion in Layered Li_xCoO_2. *Electrochem. Solid-State Lett.* **1999**, *3*, 301.

(139) Okubo, M.; Tanaka, Y.; Zhou, H.; Kudo, T.; Honma, I. Determination of activation energy for Li ion diffusion in electrodes. *The Journal of Physical Chemistry B* **2009**, *113*, 2840–2847.

(140) Dees, D. W.; Gallagher, K. G.; Abraham, D. P.; Jansen, A. N. Electrochemical Modeling the Impedance of a Lithium-Ion Positive Electrode Single Particle. *J. Electrochem. Soc.* **2013**, *160*, A478-A486.

(141) Amin, R.; Ravnsbaek, D. B.; Chiang, Y.-M. Characterization of Electronic and Ionic Transport in $Li_{1-x}Ni_{0.8}Co_{0.15}Al_{0.05}O_2$ (NCA). *J. Electrochem. Soc.* **2015**, *162*, A1163-A1169.

(142) Levi, M. D.; Aurbach, D. Diffusion Coefficients of Lithium Ions during Intercalation into Graphite Derived from the Simultaneous Measurements and Modeling of Electrochemical Impedance and Potentiostatic Intermittent Titration Characteristics of Thin Graphite Electrodes. *J. Phys. Chem. B* **1997**, *101*, 4641–4647.

(143) H. Xia, Y. S. Meng, L. Lu and G. Ceder. Electrochemical Behavior and Li Diffusion Study of $LiCoO_2$ Thin Film Electrodes Prepared by PLD **2007**, http://hdl.handle.net/1721.1/35827, last accessed: 02/02/2021.

(144) Doyle, M.; Fuentes, Y. Computer Simulations of a Lithium-Ion Polymer Battery and Implications for Higher Capacity Next-Generation Battery Designs. *J. Electrochem. Soc.* **2003**, *150*, A706.

(145) H. Sato, D. Takahashi, T. Nishina and I. Uchida. Electrochemical characterization of thin-film $LiCoO_2$ electrodes in propylene carbonate solutions. *J. Power Sources* **1997**, *68*, 540–544.

(146) Mizushima, K.; Jones, P.; Wiseman, P.; Goodenough, J. Li_xCoO_2 ($0<x\leqslant 1$): A new cathode material for batteries of high energy density. *Solid State Ionics* **1981**, *3-4*, 171–174.

(147) Honders, A.; Derkinderen, J.; Vanheeren, A.; Dewit, J.; Broers, G. Bounded diffusion in solid solution electrode powder compacts. Part II. The simultaneous measurement of the chemical diffusion coefficient and the thermodynamic factor in Li_xTiS_2 and Li_xCoO_2. *Solid State Ionics* **1985**, *15*, 265–276.

(148) Thomas, M.; Bruce, P.; Goodenough, J. Lithium mobility in the layered oxide $Li_{1-x}CoO_2$. *Solid State Ionics* **1985**, *17*, 13–19.

(149) Barker, J.; Pynenburg, R.; Koksbang, R.; Saidi, M. Y. An electrochemical investigation into the lithium insertion properties of Li_xCoO_2. *Electrochim. Acta* **1996**, *41*, 2481–2488.

(150) Jang, Y.-I.; Neudecker, B. J.; Dudney, N. J. Lithium Diffusion in Li_xCoO_2 ($0.45 < x < 0.7$) Intercalation Cathodes. *J. Electrochem. Soc.,* 2001, A74.

(151) Kleiner, K.; Melke, J.; Merz, M.; Jakes, P.; Nagel, P.; Schuppler, S.; Liebau, V.; Ehrenberg, H. Unraveling the Degradation Process of $LiNi_{0.8}Co_{0.15}Al_{0.05}O_2$ Electrodes in Commercial Lithium Ion Batteries by Electronic Structure Investigations. *ACS Appl. Mater. Interfaces* **2015**, *7*, 19589–19600.

(152) Yu, P. Determination of the Lithium Ion Diffusion Coefficient in Graphite. *J. Electrochem. Soc.* **1999**, *146*, 8.

(153) Persson, K.; Sethuraman, V. A.; Hardwick, L. J.; Hinuma, Y.; Meng, Y. S.; van der Ven, Anton; Srinivasan, V.; Kostecki, R.; Ceder, G. Lithium Diffusion in Graphitic Carbon. *J. Phys. Chem. Lett.* **2010**, *1*, 1176–1180.

(154) Kulova, T. L.; Skundin, A. M.; Nizhnikovskii, E. A.; Fesenko, A. V. Temperature effect on the lithium diffusion rate in graphite. *Russ J Electrochem* **2006**, *42*, 259–262.

(155) Doyle, M. Comparison of Modeling Predictions with Experimental Data from Plastic Lithium Ion Cells. *J. Electrochem. Soc.* **1996**, *143*, 1890.

(156) Funabiki, A.; Inaba, M.; Ogumi Zempachi; Yuasa, S.-i.; Otsuji, J.; Tasaka, A. Impedance Study on the Electrochemical Lithium Intercalation into Natural Graphite Powder. *J. Electrochem. Soc.* **1998**, 172–178.

(157) Nag, A.; Mukhopadhyay, S. C.; Kosel, J. Interdigitated Sensing and Electrochemical Impedance Spectroscopy. In *Printed flexible sensors: Fabrication, characterization and implementation*; Mukhopadhyay, S. C., Ed.; Smart Sensors, Measurement and Instrumentation volume 33; Springer International Publishing: Cham, 2019; pp 83–89.

(158) Deniz, H.; Onur, Z. Impedimetric Biosensors for Label-Free and Enzymless Detection. In *Love Wave Biosensors: A Review*; Rinken, T., Ed.; INTECH Open Access Publisher, 2013.

(159) Skoog, S.; David, S. Parameterization of linear equivalent circuit models over wide temperature and SOC spans for automotive lithium-ion cells using electrochemical impedance spectroscopy. *Journal of Energy Storage* **2017**, *14*, 39–48.

(160) Reniers, J. M.; Mulder, G.; Howey, D. A. Review and Performance Comparison of Mechanical-Chemical Degradation Models for Lithium-Ion Batteries. *J. Electrochem. Soc.* **2019**, *166*, A3189-A3200.

(161) Tanim, T. R.; Dufek, E. J.; Dickerson, C. C.; Wood, S. M. Electrochemical Quantification of Lithium Plating: Challenges and Considerations. *J. Electrochem. Soc.* **2019**, *166*, A2689-A2696.

(162) Greenwood, N. N.; Earnshaw, A. *Chemie der Elemente*, 1. Aufl., 1. korr. Nachdr. 1990 der 1. Aufl. 1988; VCH: Weinheim, 1990.

(163) Liu, Q.; Du, C.; Shen, B.; Zuo, P.; Cheng, X.; Ma, Y.; Yin, G.; Gao, Y. Understanding undesirable anode lithium plating issues in lithium-ion batteries. *RSC Adv* **2016**, *6*, 88683–88700.

(164) McBride, B. J.; Gordon, S.; Reno, M. A. *Coefficients for Calculating Thermodynamic and Transport Properties of Individual Species*; Ohio, USA, 1993.

(165) Lampinen, M. J. Analysis of Free Energy and Entropy Changes for Half-Cell Reactions. *J. Electrochem. Soc.* **1993**, *140*, 3537.

(166) Bhattacharyya, R.; Chandra Lahiri, S. The Determination of Absolute Values of Entropies of Hydration [ΔS_{abs}^0 $(H^+)_h$] and Aquation [ΔS_{abs}^0 $(H^+)_{aq}$] and The Thermodynamics of Proton in Solutions. *Zeitschrift für Physikalische Chemie* **2017**, *231*, 304.

(167) Wagman, D. D. *The NBS tables of chemical thermodynamic properties: Selected values for inorganic and C1 and C2 organic substances in SI units*; Journal of physical and chemical reference data Supplement 11,2; American Chemical Soc.: New York, NY, 1982.

(168) Yamada, Y.; Yamada, A. Review—Superconcentrated Electrolytes for Lithium Batteries. *J. Electrochem. Soc.* **2015**, *162*, A2406-A2423.

(169) Moon, H.; Tatara, R.; Mandai, T.; Ueno, K.; Yoshida, K.; Tachikawa, N.; Yasuda, T.; Dokko, K.; Watanabe, M. Mechanism of Li Ion Desolvation at the Interface of Graphite Electrode and Glyme–Li Salt Solvate Ionic Liquids. *J. Phys. Chem. C* **2014**, *118*, 20246–20256.

(170) Tao, R.; Bi, X.; Li, S.; Yao, Y.; Wu, F.; Wang, Q.; Zhang, C.; Lu, J. Kinetics Tuning the Electrochemistry of Lithium Dendrites Formation in Lithium Batteries through Electrolytes. *ACS Appl. Mater. Interfaces* **2017**, *9*, 7003–7008.

(171) Meibuhr, S. G. Electrode Studies in Nonaqueous Electrolytes. *J. Electrochem. Soc.* **1970**, *117*, 56.

(172) Lee, S.-I.; Jung, U.-H.; Kim, Y.-S.; Kim, M.-H.; Ahn, D.-J.; Chun, H.-S.: A study of electrochemical kinetics of lithium ion in organic electrolytes. *Korean J. Chem. Eng.* **2002**, 19 (4), 638–644.

(173) Verbrugge, M. W.; Koch, B. J. Microelectrode investigation of ultrahigh-rate lithium deposition and stripping. *J. Electroanal. Chem.* **1994**, *367*, 123–129.

(174) Bieker, G.; Winter, M.; Bieker, P. Electrochemical in situ investigations of SEI and dendrite formation on the lithium metal anode. *Physical chemistry chemical physics : PCCP* **2015**, *17*, 8670–8679.

(175) Jasinski, R. *Advances in Electrochemistry and Electrochemical Engineering*; P. Delahay and C. W. Tobias, Editors,Wiley-Interscience: New York, 1971.

(176) Ge, H.; Aoki, T.; Ikeda, N.; Suga, S.; Isobe, T.; Li, Z.; Tabuchi, Y.; Zhang, J. Investigating Lithium Plating in Lithium-Ion Batteries at Low Temperatures Using Electrochemical Model with NMR Assisted Parameterization. *J. Electrochem. Soc.* **2017**, *164*, A1050-A1060.

(177) Perkins, R. D.; Randall, A. V.; Zhang, X.; Plett, G. L. Controls oriented reduced order modeling of lithium deposition on overcharge. *J. Power Sources* **2012**, *209*, 318–325.

(178) Lueth, S. Untersuchung des Einflusses der Mikrostruktur von Kathoden auf das Entladeverhalten von Lithiumionenhalbzellen, PhD Thesis, Stuttgart University, 2015.

(179) Tippmann, S. Modellierung und experimentelle Charakterisierung des Degradationsverhaltens durch Lithium-Plating an Lithium-Ionen-Zellen unter automobilen Betriebsbedingungen. PhD Thesis, Stuttgart University, 2016.

(180) Hein, S.; Latz, A. Influence of local lithium metal deposition in 3D microstructures on local and global behavior of Lithium-ion batteries. *Electrochim. Acta* **2016**, *201*, 354–365.

(181) Chandrasekaran, R.; Fuller, T. F. Analysis of the Lithium-Ion Insertion Silicon Composite Electrode/Separator/Lithium Foil Cell. *J. Electrochem. Soc.* **2011**, *158*, A859.

(182) Doyle, M.; Fuller, T. F.; Newman, J. Modeling of Galvanostatic Charge and Discharge of the Lithium/Polymer/Insertion Cell. *J. Electrochem. Soc.* **1993**, *140*, 1526–1533.

(183) Jow, T. R.; Marx, M. B.; Allen, J. L. Distinguishing Li + Charge Transfer Kinetics at NCA/Electrolyte and Graphite/Electrolyte Interfaces, and NCA/Electrolyte and LFP/Electrolyte Interfaces in Li-Ion Cells. *J. Electrochem. Soc.* **2012**, *159*, A604-A612.

(184) Sequeira, C.; Hooper, A. The study of lithium electrode reversibility against $(PEO)_xLiF_3CSO_3$ polymeric electrolytes. *Solid State Ionics* **1983**, *9-10*, 1131–1138.

(185) Yang, X.-G.; Ge, S.; Liu, T.; Leng, Y.; Wang, C.-Y. A look into the voltage plateau signal for detection and quantification of lithium plating in lithium-ion cells. *J. Power Sources* **2018**, *395*, 251–261.

(186) Yang, X.-G.; Leng, Y.; Zhang, G.; Ge, S.; Wang, C.-Y. Modeling of lithium plating induced aging of lithium-ion batteries: Transition from linear to nonlinear aging. *J. Power Sources* **2017**, *360*, 28–40.

(187) Backes, D. Mikroskopische, strukturelle und chemische Analyse von Elektroden einer Lithium-Ionen-Batteriezelle. BSc Thesis, Hochschule Offenburg, 2019.

(188) Kupper, C.; Spitznagel, S.; Döring, H.; Danzer, M. A.; Gutiérrez, C.; Kvasha, A.; Bessler, W. G. Combined modeling and experimental study of the high-temperature behavior of a lithium-ion cell: differential scanning calorimetry, accelerating rate calorimetry and external short circuit. *Electrochimica Acta* **2019**, *306*, 209–219.

(189) Lee, C. H.; Dura, J. A.; LeBar, A.; DeCaluwe, S. C. Direct, operando observation of the bilayer solid electrolyte interphase structure: Electrolyte reduction on a non-intercalating electrode. *J. Power Sources* **2019**, *412*, 725–735.

(190) Nie, M.; Abraham, D. P.; Chen, Y.; Bose, A.; Lucht, B. L. Silicon Solid Electrolyte Interphase (SEI) of Lithium Ion Battery Characterized by Microscopy and Spectroscopy. *J Phys Chem C Nanomater Interfaces* **2013**, *117*, 13403–13412.

(191) Colclasure, A. M.; Smith, K. A.; Kee, R. J. Modeling detailed chemistry and transport for solid-electrolyte-interface (SEI) films in Li–ion batteries. *Electrochim. Acta* **2011**, *58*, 33–43.

(192) Safari, M.; Morcrette, M.; Teyssot, A.; Delacourt, C. Multimodal Physics-Based Aging Model for Life Prediction of Li-Ion Batteries. *J. Electrochem. Soc.* **2009**, *156*, A145-A153.

(193) Ramadass, P.; Haran, B.; Gomadam, P. M.; White, R.; Popov, B. N. Development of First Principles Capacity Fade Model for Li-Ion Cells. *J. Electrochem. Soc.* **2004**, *151*, A196.

(194) Ning, G.; Popov, B. N. Cycle Life Modeling of Lithium-Ion Batteries. *J. Power Sources* **2004**, *151*, A1584.

(195) Waldmann, T.; Wilka, M.; Kasper, M.; Fleischhammer, M.; Wohlfahrt-Mehrens, M. Temperature dependent ageing mechanisms in Lithium-ion batteries – A Post-Mortem study. *J. Power Sources* **2014**, *262*, 129–135.

(196) Yang, X.-G.; Wang, C.-Y. Understanding the trilemma of fast charging, energy density and cycle life of lithium-ion batteries. *J. Power Sources* **2018**, *402*, 489–498.